

**QUASISTATIC AND ULTRAFAST MAGNETIZATION  
DYNAMICS IN MAGNETIC NANOSTRUCTURES**

Thesis submitted for the degree of  
**Doctor of Philosophy (Science)**

in

**Physics (Experimental)**

by

**Bivas Rana**

**Department of Physics**

**University of Calcutta**

**2013**

*Dedicated to my parents . . . . .*

## Acknowledgement

At first, I would like to express my sincere gratitude to my supervisor Dr. Anjan Barman for giving me a wonderful opportunity to work under his supervision. It was a great pleasure and excitement to conduct research under his supervision in a competitive and yet a friendly environment. He first introduced me to the real world of magnetism, spintronics, magnetization dynamics and nanotechnology. When I joined under him as a Ph.D. student in 2009, there was nothing except the available empty place for the laboratory. Subsequently, he started to build up the laboratory with me and my colleague Milan and following that Semanti and Dheeraj joined our group. From there, the journey of starting from scratch to work in a world class laboratory full of state of the art equipment, students, postdocs and innovative ideas within few years was amazing. My supervisor taught me every steps of research starting from setting up and maintenance of a laboratory to do most rigorous experiment, simulation and analysis for research problems. He helped me profoundly to improve my writing and presentation skills. He tirelessly trained me about the safety protocols and to keep the laboratory always clean and ordered. He always motivated me to work hard and think independently. I have learnt much from his optimistic and meticulous approach. He sent me to UK, Japan and US for various collaborative research works and to attend international conferences so that I can get international exposure in broad fields of research. In a word, he solely converted me to a researcher from an ordinary human being.

I am also thankful to Dr. Saswati Barman for the mentoring, particularly in the numerical analysis of my results and for offering me with valuable suggestions. She taught me the numerical calculation methods using LLG micromagnetic simulator. She also gave me the opportunity to use her computers and LLG micromagnetic solver to perform those analyses.

I am indebted to my family, my parents and brother for the sacrifice they have made for my study. They always encouraged me to go forward with my research career even though there was financial hardship in the family. Without their constant support, I would not have been a researcher. I must thank to my wife, Moumita, who gave her constant mental support during last one year of my Ph.D. study. Also, special thanks to my uncle who always motivated me to become a scientist.

Thanks to my friend and colleague Milan, who taught me how to deal with tough situations. Thanks to Semanti, my best lab partner during my Ph. D. study, for her constant support and valuable suggestions. Without her help, my experiments would not have been completed. I have also learnt many software related issues from her, which were very helpful during simulation and data analysis. At the beginning of my Ph.D. work, she helped me a lot in maintaining the laboratory.

Thanks to Dheeraj for a valuable contribution in the development of the Dotmag software. This was used in great detail during the analysis and understanding of spin wave mode profiles of ferromagnetic nanodot arrays described in this thesis.

Thanks to my other lab-mates Bipul, Susmita, Ruma, Arnab, Debanjan, Chandrima and Shreyasi for their helps and valuable suggestions during different stages of my research. Susmita and Ruma helped me during some of the static and time-resolved magneto-optical measurements, whereas Arnab and Shreyasi assisted me during the synthesis of magnetic nanoparticles. Also, thanks to Drs. P. Sabareesan, Pinaki Laha and Arabinda Haldar of our group, who helped me to gain more insight to my research problems. Thanks to all the lab members for making the lab such an enjoyable place to work.

I would like to express my sincere gratitude to Prof. YoshiChika Otani of Quantum Nano-Scale Magnetism Laboratory, RIKEN, Japan for giving me an opportunity to work in his lab under the DST-JST collaborative project. I learnt the electron beam lithography technique at RIKEN with the help of Mr. Satoshi Sugimoto, a Ph.D. student of Prof. Otani. I must also thank Dr. Yasuhiro Fukuma, for providing me with the first set of lithographically patterned permalloy dot array samples. I also had some stimulating discussions with them, which not only helped me to gain more insight to my research problems but also to broaden my view towards research.

I would also like to express my sincere gratitude to Prof. R. J. Hicken of University of Exeter, UK for giving me an opportunity to work in his lab under the DST-UKIERI collaborative project. This helped me to improve my experimental skills in magneto-optics. I would like to thank Drs. Uday Al-Jarah, Prim Gangmei, Paul Keatley and Oleksandr Dmytriiev for their helps and for making my stay enjoyable at Exeter.

I would like to express my heartfelt regards to all my respected teachers involved throughout my academic career for their proper guidance and influential teaching, which

helped me achieve my goals. I also thank to my friends and seniors outside my research group who always encouraged me during my academic career. Without their helps, I would not have been able to cross the long hurdles of my life.

Finally, I thank the S. N. Bose National Centre for Basic Sciences for giving me such an opportunity to work here. The common research facilities under the *Technical Cell* were very helpful for initial characterization of my samples. Thanks to University Grant Commission for providing me with junior and senior research fellowships. I must thank various funding agencies including Department of Science and Technology, Government of India under Grant Nos. SR/NM/NS-09/2007, INT/EC/CMS (24/233552) and INT/JP/JST/P-23/09; and Department of Information Technology, Govt. of India under Grant No. 1(7)2010/M & C for their funding towards development of the experimental set ups that I used during my Ph.D. study.

Bivas Rana,  
S. N. Bose National Centre for Basic Sciences,  
Salt Lake, Kolkata, India.

## List of Publications

**This thesis is based upon the following publications and manuscript:**

1. **B. Rana**, M. Agrawal, S. Pal, and A. Barman, "Magnetization Reversal Dynamics in Clusters of Single Domain Ni Nanoparticles," *J. Appl. Phys.* **107**, 09B513 (2010).
2. M. Agrawal, **B. Rana**, and A. Barman, "Magnetization Reversal in Chains and Clusters of Exchange-Coupled Nickel Nanoparticles," *J. Phys. Chem. C* **114**, 11115 (2010).
3. **B. Rana**, A. Ganguly, and A. Barman, "Magnetic Shape Anisotropy in Chemically Synthesized Chains of Nickel Nanoparticles," *IEEE Trans. Magn.* **47**, 2859 (2011).
4. **B. Rana**, S. Pal, S. Barman, Y. Fukuma, Y. Otani, and A. Barman, "All-Optical Excitation and Detection of Picosecond Dynamics of Ordered Arrays of Nanomagnets with Varying Areal Density," *Appl. Phys. Expr.* **4**, 113003 (2011).
5. **B. Rana**, D. Kumar, S. Barman, S. Pal, Y. Fukuma, Y. Otani, and A. Barman, "Detection of Picosecond Magnetization Dynamics of 50 nm Magnetic Dots down to the Single Dot Regime," *ACS Nano* **5**, 9559 (2011).
6. **B. Rana**, D. Kumar, S. Barman, S. Pal, R. Mandal, Y. Fukuma, Y. Otani, S. Sugimoto, and A. Barman, "Anisotropy in Collective Precessional Dynamics in Arrays of Ni<sub>80</sub>Fe<sub>20</sub> Nanoelements," *J. Appl. Phys.* **111**, 07D503 (2012).
7. **B. Rana** and A. Barman, "Magneto-Optical Measurements of Collective Spin Dynamics of Two-dimensional Arrays of Ferromagnetic Nanoelements," *SPIN* **3**, 1330001 (2013).
8. **B. Rana** and A. Barman, "Ultrafast Magnetization Dynamics of Magnetic Nanoparticles with Different Clustering Geometry," (manuscript to be submitted).

**The following publications are not included in this thesis:**

1. S. Pal, **B. Rana**, O. Hellwig, T. Thomson, and A. Barman, "Tunable Magnonic Frequency and Damping in [Co/Pd]<sub>8</sub> Multilayers with Variable Co Layer Thickness," *Appl. Phys. Lett.* **98**, 082501 (2011).
2. S. Pal, **B. Rana**, S. Saha, R. Mandal, O. Hellwig, J. Romero-Vivas, S. Mamica, J. W. Klos, M. Mruczkiewicz, M. L. Sokolovskyy, M. Krawczyk, and A. Barman, "Time-

- resolved Measurement of Spin-wave Spectra in CoO Capped  $[\text{Co}(t)/\text{Pt}(7\text{\AA})]_{n-1}\text{Co}(t)$  Multilayer Systems,” *J. Appl. Phys.* **111**, 07C507 (2012).
3. B. K. Mahato, A. Ganguly, **B. Rana**, and A. Barman, “Magnetization Reversal in Chemically Synthesized Hexagonal Cobalt Microplatelets,” *J. Phys. Chem. C* **116**, 22057 (2012).
  4. O. Dmytriiev, U. A. S. Al-Jarah, P. Gangmei, V. V. Kruglyak, R. J. Hicken, B. K. Mahato, **B. Rana**, M. Agrawal, A. Barman, M. Mátéfi-Tempfli, L. Piraux, and S. Mátéfi-Tempfli, “Static and Dynamic Magnetic Properties of Densely Packed Magnetic Nanowire Arrays,” *Phys. Rev. B* **87**, 174429 (2013).
  5. B. K. Mahato, **B. Rana**, R. Mandal, D. Kumar, S. Barman, Y. Fukuma, Y. Otani, and A. Barman, “Configurational Anisotropic Spin Waves in Cross-shaped  $\text{Ni}_{80}\text{Fe}_{20}$  Nanoelements,” *Appl. Phys. Lett.* **102**, 192402 (2013).
  6. S. Saha, R. Mandal, S. Barman, D. Kumar, **B. Rana**, Y. Fukuma, S. Sugimoto, Y. Otani, and A. Barman, “Tunable Magnonic Spectra in Two-Dimensional Magnonic Crystals with Variable Lattice Symmetry,” *Adv. Funct. Mater.* **23**, 2378 (2013).
  7. D. Mahesh, S. K. Mandal, B. K. Mahato, **B. Rana**, and A. Barman, “Pronounced Multiferroicity in Oleic Acid Stabilized  $\text{BiFeO}_3$  Nanocrystals at Room Temperature,” *J. Nanosci. Nanotechnol.* **12**, 4090 (2013).
  8. A. K. Ghosh, G. D. Dwivedi, B. Chatterjee, **B. Rana**, A. Barman, S. Chatterjee, and H. D. Yang, “Role of Codoping on Multiferroic Properties at Room Temperature in  $\text{BiFeO}_3$  Ceramic,” *Solid State Commun.* **166**, 22 (2013).

## Abstract

Nanomagnets are interesting systems for future applications in nanotechnology including in patterned magnetic media, magnetic data storage, magnonic crystals, magnetic logic, sensors and biomedical applications. All applications require the knowledge base of the magnetization processes of nanomagnets and their arrays at various time and length scales. In this thesis, we have studied the quasistatic and ultrafast magnetization dynamics of lithographically patterned magnetic nanodot arrays and chemically synthesized clusters and chains of magnetic nanoparticles. The quasistatic magnetization reversal dynamics is studied by static magneto-optical Kerr effect (SMOKE) measurement and vibrating sample magnetometer (VSM), whereas the ultrafast magnetization dynamics is studied by an all optical time-resolved magneto-optical Kerr effect (TRMOKE) microscope with collinear pump-probe geometry. The experimental results are explained with the aid of numerical micromagnetic simulations. We have investigated the magnetization dynamics of two-dimensional periodic arrays of Ni<sub>80</sub>Fe<sub>20</sub> (permalloy) nanodots of two different shapes (square and circular), with varying sizes between 200 nm and 50 nm, and with varying interelement separations of the arrays between 50 nm and 400 nm. The quasistatic magnetization reversal dynamics of arrays of 200 nm square permalloy dots show a systematic transition from a strongly collective magnetization reversal to a non-collective reversal dynamics as the interdot separation ( $S$ ) increases from 50 to 400 nm. A significant but non-systematic variation of the magnetization relaxation times are observed with dot size, shape and areal density of array due to the random size distribution and defects in the dots and variation of physical contacts of the dots with the Si substrates, whereas the femtosecond demagnetization times remain unchanged. The collective precessional magnetization dynamics of arrays of 200 nm dots shows a systematic transition from uniform collective regime to non-collective regime via different weakly collective regimes as the interdot separation ( $S$ ) increases from 50 nm to 400 nm. Consequently, the effective damping ( $a_{eff}$ ) value also increases and saturates starting from a lower value same as a blanket thin film. The strongly collective dynamics for array of 200 nm dots with 50 nm edge-to-edge separation undergoes a transition to a weakly collective regime with the decrease in the bias field magnitude and consequently the  $a_{eff}$  also increases. The collective dynamics is found to be anisotropic with the variation in the azimuthal angle of in-plane bias magnetic field and a systematic transition from a strongly collective to non-collective dynamics is observed in strongly ( $S = 50$  nm) and weakly ( $S = 100$  nm) coupled regimes. As the dot size decreases from 200 nm down to 50 nm, an increase

in the resonant frequency is observed for the intrinsic dynamics as well as for the collective dynamics. With the decrease in dot size, the centre mode (CM) and the mixed edge mode-Damon Eshbach (EM-DE) mode of the dots are suppressed by dominating edge modes (EM) of the dots and consequently, a crossover from upper branch to lower branch of resonance frequency is observed for the intrinsic and collective magnetization dynamics. The dynamics of 50 nm square dot arrays reveals one dominant edge mode in the single nanodot regime with slightly higher damping than that of the blanket thin film. With the increase in areal density of the array both the precession frequency and damping increase significantly due to the increase in magnetostatic interactions between the nanodots, and a mode splitting and sudden jump in apparent damping are observed at an edge-to-edge separation of 50 nm. The main contribution to the magnetostatic interaction is found to be quadrupolar in nature. The intrinsic and collective precessional dynamics of circular dots are significantly different than that of the square dots due to the modification in the ground state of magnetization as well as the stray field profiles for the circular dots. However, a crossover from higher frequency branch to lower branch is also observed here as the dot size decreases down to 50 nm. The magnetization reversal for clusters of randomly arranged Ni nanoparticles occurs through the appearance of various collective domain states including C-state, vortex-state and flower-like state, although the constituent particles in the cluster maintain primarily single domain states. In case of parallel chains, the overall geometry controls the reversal mechanism and the magnetic hysteresis loops with magnetic field applied along the long-axis and short-axis of the chains show magnetic easy-axis and hard-axis like behaviours. A comparative study of the reversal behaviour of chains and clusters of exchange-coupled Ni nanoparticles with four distinct geometries shows that the magnetization reversal of the clusters and chains is dominated by the interparticle exchange and the shape anisotropy of the overall clusters and occurs through the formation of various local magnetic configurations. In chain-like structures, the fanning- and curling-like modes of magnetization reversal cause the smallest saturation field, and the largest coercive field and remanence. However, in more entangled structures such as branched chains and random clusters, formation of more stable magnetic configurations such as vortices causes a larger saturation field, but a smaller coercive field and remanence. The ultrafast magnetization dynamics shows that the femtosecond demagnetization time does not depend on the sample geometry, whereas a significant variation in the fast and slow relaxation time is observed due to the finite size and shape distributions and variation in the surface and interface properties of the nanoparticles. The picosecond precessional dynamics for long chains with single particle along the width shows

a systematic decrease in the resonant frequency of nonuniform collective mode with the decrease in the bias field magnitude, whereas the precessional frequency spectra for samples with different geometries also show various nonuniform collective modes, where the mode frequencies vary with sample geometry due to the variation in the magnetic ground state configurations.

# List of Contents

<b>List of Figures</b>	<b>xvii</b>
<b>1. Introduction</b>	<b>1</b>
Bibliography	9
<b>2. Theoretical Background</b>	<b>17</b>
2.1 Magnetism	17
2.1.1 Classical Theory of Diamagnetism: Langevin's Theory	17
2.1.2 Quantum Theory of Paramagnetism	18
2.1.3 Ferromagnetism and Exchange Interaction.	19
2.1.4 Antiferromagnetism and Ferrimagnetism	21
2.2 Magnetic Energies	22
2.2.1 Zeeman Energy	22
2.2.2 Magnetostatic Self-energy	22
2.2.3 Exchange Energy	24
2.2.4 Magnetocrystalline Anisotropy Energy	25
2.3 Magnetic Domains	26
2.4 Stoner-Wohlfarth Model	28
2.5 Magnetization Reversal Modes	30
2.6 Magnetization Dynamics	33
2.6.1 Landau-Lifshitz-Gilbert Equation	33
2.6.2 Time Scales of Magnetization Dynamics	36
2.6.3 Ultrafast Magnetization Dynamics Induced by Ultrashort Laser Pulses	37
2.6.4 Ferromagnetic Resonance	39
2.6.5 Macrospin Model of Ferromagnetic Resonance: Kittel Formula	39
2.6.6 Effective Demagnetizing Factors: Two-fold and Four-fold Anisotropy	42
2.7 Spin Waves	45
2.7.1 Introduction	45
2.7.2 Exchange Spin Wave: Dispersion Relation	45
2.7.3 Exchange Spin Waves in Thin Films	47

2.7.4	Magnetostatic Modes in Thin Films . . . . .	48
2.7.5	Magnetostatic Modes in Confined Thin Ferromagnetic Elements. . . . .	51
2.8	Magneto-optical Kerr Effect . . . . .	51
2.8.1	Introduction . . . . .	51
2.8.2	Physical Origin of Magneto-optical Effects . . . . .	52
2.8.3	Phenomenological Theory . . . . .	54
	Bibliography . . . . .	58
<b>3.</b>	<b>Fabrication, Synthesis and Characterization Techniques</b>	<b>61</b>
3.1	Fabrication . . . . .	61
3.1.1	Introduction . . . . .	61
3.1.2	Optical Lithography . . . . .	62
3.1.3	Electron Beam Lithography . . . . .	63
3.2	Synthesis . . . . .	64
3.3	Sample Characterization . . . . .	66
3.3.1	Introduction . . . . .	66
3.3.2	Scanning Electron Microscope (SEM) . . . . .	66
3.3.3	Energy Dispersive X-ray (EDX) Analysis . . . . .	68
3.3.4	X-ray Diffraction (XRD) . . . . .	69
3.3.5	Vibrating Sample Magnetometer (VSM) . . . . .	70
3.3.6	Atomic Force Microscope (AFM) . . . . .	71
	Bibliography . . . . .	74
<b>4.</b>	<b>Static and Time-resolved Magneto-optical Kerr Effect (MOKE) Measurements</b>	<b>75</b>
4.1	Introduction . . . . .	75
4.2	MOKE Geometries . . . . .	75
4.3	All Optical Time-resolved Magneto-optical Kerr Effect (TRMOKE) Microscope . . . . .	77
4.3.1	Components Required for Construction of TRMOKE Microscope. . . . .	77
4.3.2	Descriptions of Lasers . . . . .	79
4.3.3	Description of the Set up . . . . .	89
4.3.4	Construction of the TRMOKE Microscope and Alignment Procedure	95

4.3.5	Some Routine Alignments . . . . .	102
4.4	Static Magneto-optical Kerr Effect (SMOKE) Microscope . . . . .	105
	Bibliography . . . . .	107
<b>5.</b>	<b>Micromagnetic Simulations</b>	<b>109</b>
5.1	Introduction . . . . .	109
5.2	Free Energies of a Ferromagnetic Element in Micromagnetics . . . . .	110
5.3	Micromagnetic Simulation Methods and Solvers . . . . .	112
5.3.1	Introduction: Different LLG Solvers . . . . .	112
5.3.2	Object oriented Micromagnetic Framework (OOMMF) . . . . .	113
5.3.3	NMAG . . . . .	115
5.3.4	LLG Micromagnetic Simulator . . . . .	116
5.4	Methods of Calculating Power and Phase Profiles of Resonant Modes . . . . .	117
	Bibliography . . . . .	120
<b>6.</b>	<b>Collective Magnetization Dynamics of Arrays of Square Ni<sub>80</sub>Fe<sub>20</sub> Dots With Varying Areal Density</b>	<b>121</b>
6.1	Background . . . . .	121
6.2	Sample Fabrication, Characterization and Experimental Techniques . . . . .	124
6.3	Quasistatic Magnetization Dynamics of 10 × 10 μm <sup>2</sup> Permalloy Blanket Thin Film and Arrays of 200 nm Square Permalloy Dots . . . . .	126
6.4	Ultrafast Magnetization Dynamics of 10 × 10 μm <sup>2</sup> Permalloy Blanket Thin Film . . . . .	128
6.5	Ultrafast Magnetization Dynamics of Arrays of 200 nm Square Permalloy Dots as a Function of Areal Density . . . . .	132
6.5.1	Ultrafast Demagnetization and Remagnetization . . . . .	132
6.5.2	Time-resolved Precessional Dynamics: Experimental Results . . . . .	134
6.5.3	Micromagnetic Simulations . . . . .	135
6.5.4	Numerical Calculation of Magnetostatic Field Distribution . . . . .	137
6.5.5	Power and Phase Profiles of Resonant Modes . . . . .	138

6.6	Damping as a Function of Areal Density. . . . .	141
6.7	Collective Magnetization Dynamics as a Function of Bias Field . . . . .	142
6.7.1	Magnetic Ground State as a Function of Bias Field . . . . .	142
6.7.2	Precessional Dynamics as a Function of Bias Field . . . . .	143
6.8	Damping as a Function of Bias Field . . . . .	144
6.9	Summary . . . . .	145
	Bibliography . . . . .	147
<b>7.</b>	<b>Magnetization Dynamics of Arrays of 50 nm Ni<sub>80</sub>Fe<sub>20</sub> Dots Down to the Single Nanodot Regime</b>	<b>150</b>
7.1	Background . . . . .	150
7.2	Sample Fabrication, Characterization and Measurement Technique . . . . .	152
7.3	Results and Discussions . . . . .	154
7.3.1	Variation of Precession Frequency with Areal Density of the Arrays .	154
7.3.2	Variation of Damping of Precession with Areal Density of the Arrays	158
7.3.3	Micromagnetic Analysis of the Observed Precessional Dynamics . . . .	159
7.4	Summary . . . . .	161
	Bibliography . . . . .	163
<b>8.</b>	<b>Collective Magnetization Dynamics of Ni<sub>80</sub>Fe<sub>20</sub> Nanodot Arrays with Varying Dot Size and Shape</b>	<b>166</b>
8.1	Background . . . . .	166
8.2	Sample Fabrication, Characterization and Measurement Technique . . . . .	167
8.3	Precessional Magnetization Dynamics of Square Permalloy Dot Arrays with Varying Dot Size . . . . .	169
8.3.1	Static Magnetic Configurations . . . . .	169
8.3.2	Intrinsic Magnetization Dynamics of Single Dots as a Function of dot Size . . . . .	170
8.3.3	Collective Magnetization Dynamics of Array of Dots with Varying Dot Size . . . . .	171

8.4	Ultrafast Magnetization Dynamics of Circular Permalloy Dot Arrays with Varying Dot Size . . . . .	175
8.4.1	Static Magnetic Configurations . . . . .	175
8.4.2	Intrinsic and Collective Magnetization Dynamics of Circular Permalloy Nanodots with Varying Dot Size . . . . .	176
8.4.3	Power and Phase Profiles of the Resonant Modes . . . . .	179
8.5	Summary . . . . .	180
	Bibliography . . . . .	182
<b>9.</b>	<b>Role of Configurational Magnetic Anisotropy in Collective Magnetization Dynamics of Ni<sub>80</sub>Fe<sub>20</sub> Nanodot Arrays</b>	<b>184</b>
9.1	Background . . . . .	184
9.2	Sample Fabrication, Characterization and Measurement Technique . . . . .	185
9.3	Static Magnetization Configuration and Magnetostatic Field Profiles as a Function of the Azimuthal Angle of the Bias Magnetic Field . . . . .	186
9.4	Results and Discussions. . . . .	187
9.5	Summary . . . . .	193
	Bibliography . . . . .	194
<b>10.</b>	<b>Quasistatic Magnetization Reversal Dynamics of Ni Nanoparticles</b>	<b>196</b>
10.1	Background . . . . .	196
10.2	Magnetization Reversal in Clusters of Ni Nanoparticles. . . . .	198
10.2.1	Sample Preparation and Characterization . . . . .	198
10.2.2	Results and Discussions . . . . .	199
10.3	Magnetization Reversal of Ni Nanoparticles Assembled in Different Geometries . . . . .	203
10.3.1	Sample Preparation and Characterization . . . . .	203
10.3.2	Results and Discussions . . . . .	204
10.4	Magnetization Shape Anisotropy in Chains of Ni Nanoparticles . . . . .	208
10.4.1	Sample Preparation and Characterization . . . . .	208
10.4.2	Results and Discussions . . . . .	209

10.5 Summary .....	214
Bibliography .....	216
<b>11. Ultrafast Magnetization Dynamics of Ni Nanoparticles</b>	<b>218</b>
11.1 Background .....	218
11.2 Sample Preparation, Characterization and Experimental Technique .....	220
11.3 Demagnetization and Relaxation of Ni Nanoparticles .....	222
11.4 Precessional Magnetization Dynamics of Ni Nanoparticles .....	225
11.4.1 Precessional Dynamics as a Function of Bias Field .....	225
11.4.2 Precessional Dynamics as a Function of Sample Geometry .....	227
11.5 Summary .....	228
Bibliography .....	230
<b>12. Summary and Future Perspectives</b>	<b>232</b>
12.1 Summary .....	232
12.2 Future Perspectives .....	235

## List of Figures

Figure	Description	Page
2.1	Spin orientations in ferromagnet, antiferromagnet and ferrimagnet.	22
2.2	Structures of Néel and Bloch walls are shown between two domains.	27
2.3	(a) Schematic diagram of a prolate ellipsoidal particle with magnetization ( $\mathbf{M}$ ) in a magnetic field ( $\mathbf{H}$ ). The hysteresis loops of a prolate ellipsoidal particle for (b) applied field along easy axis ( $\theta = 0^\circ$ ) and (c) applied field along hard axis ( $\theta = 90^\circ$ ).	29
2.4	Coherent rotation and incoherent rotation or curling-like rotation are schematically shown for a sphere and a disc.	31
2.5	Schematics of ‘curling’ and ‘buckling’ modes are shown for a cylinder. The ‘fanning’ mode is shown for chains of spherical nanoparticles.	32
2.6	Precession of magnetization vector ( $\mathbf{M}$ ) around magnetic field ( $\mathbf{H}$ ) (a) in absence of damping term and (b) in presence of a damping term.	34
2.7	Characteristic times scales of various kinds of magnetization dynamics.	36
2.8	A schematic diagram of sequence of mechanisms in ultrafast magnetization dynamics.	38
2.9	The schematic diagrams of orthogonal coordinates are shown for (a) a ferromagnetic specimen with plane surface ( $y = 0$ ) and (b) an ellipsoid with principle axes parallel to $x$ , $y$ and $z$ axes.	40
2.10	Geometry of the magnetization and applied magnetic field is shown in an orthogonal coordinate system ( $a, b, c$ ).	43
2.11	(a) Schematics of perpendicular standing spin wave (PSSW) and magnetostatic surface spin wave (MSSW) modes are shown for a ferromagnetic thin film. (b) The calculated dispersions of three different magnetostatic spin wave modes are shown for a permalloy thin film with $4\pi M_S = 10.8$ kOe. The values of applied bias field were chosen as 1 kOe for MSSW & backward volume magnetostatic (BWVMS) modes and 11 kOe for forward volume magnetostatic (FWVMS) modes in the calculation.	48
3.1	Schematic diagram of optical and electron beam lithography.	62
3.2	Schematic diagram of synthesis of Ni nanoparticles by hydrazine reduction method.	65
3.3	Schematic diagram of scanning electron microscope (SEM).	67
3.4	Interaction of accelerated electrons with sample and emission of X-rays is shown schematically.	68
3.5	Schematic diagrams of (a) X-ray diffraction with illustration of the conditions required for Bragg’s diffraction to occur and (b) X-ray diffractometer are shown.	69
3.6	Schematic diagram of Vibrating Sample Magnetometer (VSM).	70
3.7	Schematic diagram of an atomic force microscope (AFM).	72

4.1	Schematic diagrams of (a) polar (b) longitudinal and (c) transverse MOKE are shown. (d) Geometry of the Kerr rotation ( $\theta_k$ ) and Kerr ellipticity ( $\varepsilon_k$ ) is demonstrated.	76
4.2	A photograph of the all optical time-resolved magneto-optical Kerr effect (TRMOKE) microscope with collinear pump-probe geometry in our laboratory at the S. N. Bose Centre. The important components in the set up are labeled in the figure.	77
4.3	(a) Energy bands and various absorption and emission spectra for $\text{Nd}^{3+}$ ion are shown. (b) The absorption spectra of $\text{Nd}^{3+}$ are compared to the emission spectra of a diode laser. The figures are reproduced from Ref. [18].	81
4.4	(a) Schematic diagram of mode matching between diode laser mode volume and $\text{TEM}_{00}$ mode volume of Millennia. (b) Schematic diagram of Millennia laser head. The figures are reproduced from Ref. [18].	81
4.5	(a) Energy band diagram of the Ti-sapphire crystal. (b) Absorption and emission spectra of Ti-sapphire. The figures are reproduced from Ref. [19].	83
4.6	A schematic of the beam path inside the folded cavity of Tsunami. The figure is reproduced from Ref. [19].	83
4.7	(a) Schematic diagram of an acousto-optic modulator (AOM). (b) The configuration of the electronics for regenerative mode locking. The figure is reproduced from Ref. [19].	86
4.8	The sequence of four prism used for dispersion compensation in Tsunami laser.	87
4.9	A schematic diagram of the SHG unit and the optical path inside it are shown. The figure is reproduced from Ref. [20].	88
4.10	A schematic diagram of an all optical time-resolved magneto-optical Kerr effect (TRMOKE) microscope with collinear pump-probe geometry.	89
4.11	(a) Schematic diagram showing the collinear geometry of pump and probe beams focused by a microscope objective (MO) on the sample surface. (b) The longitudinal and polar Kerr rotations of the left and right portions of the incident probe beam. When the intensities of the two halves of the beam cross-section are added, the longitudinal Kerr components cancel each other leaving only the polar Kerr component.	92
4.12	Schematic diagram of the optical bridge detector unit is shown along with the electronics circuit, which amplifies and processes (A + B) and (A – B) signals.	92
4.13	A schematic representation of the comparison of the spatio-temporal resolution of different techniques for the measurements of the time-resolved magnetization dynamics of single (isolated) nanomagnets.	94
4.14	(a) A photograph of the femtosecond oscillator (Tsunami) showing different external laser head controls. (b) A typical mode-locked power spectrum of the output beam from Tsunami. (c) A photograph of the SHG showing the external micrometer screw for adjusting the BBO crystal angle.	96
4.15	(a) Alignment procedure of the retro-reflector is shown schematically. (b) The schematic diagram of a kinematic mirror mount along with the screws on it is shown. Alignment procedure of probe beam is shown schematically (c) just after the retro-reflector and (d) after the polarizer.	98
4.16	A schematic diagram showing the alignment procedure of the microscope objective.	101

4.17	The reflectivity signal ( $A + B$ ) from a Si(100) wafer as function of the time delay between the pump and the probe beams. The decay of the reflectivity signal after the zero delay has been fitted with a double exponential decay function. The time constant of the longer decay is 210 ps.	104
4.18	A schematic diagram of static magneto-optical Kerr effect (SMOKE) microscope.	106
5.1	The schematic diagrams show the discretization of a rectangular sample into a number of (a) cuboidal cells with equal size and (b) tetrahedral cells with varying size. The second figure is reproduced from Ref. [8].	114
5.2	The diagrams show the discretization of a spherical nanoelement with (a) cuboidal cells and (b) tetrahedral cells. The figures are reproduced from Ref. [8].	115
5.3	(a) Simulated spatially averaged magnetization ( $M_z$ ) vs time is shown for a 20 nm thick and 200 nm wide single permalloy square shaped dot with a bias field ( $H_b$ ) of 1.25 kOe applied along the horizontal edge ( $x$ -axis) of the dot. (b) The spatial distribution of the $z$ -component of magnetization is shown for two different times ('a' and 'b') marked by red solid dots on the curve. The colour scale is shown on top of the figure. (c) The fast Fourier transform (FFT) of simulated time-resolved magnetization curve is shown. It shows three well resolved resonant peaks. (d) The calculated power and phase distributions corresponding to three resonant modes are shown. The corresponding colour scales are shown inside the box.	118
6.1	(a) A typical scanning electron micrograph (SEM) and (b) atomic force microscope (AFM) image of $10 \times 10 \mu\text{m}^2$ blanket permalloy thin film is shown. The sample surface is in $x$ - $y$ plane. The geometry of magnetic field is shown on top of the SEM image. (c) Scanning electron micrographs of arrays of square permalloy dots with width ( $W$ ) = 200 nm, thickness ( $t$ ) = 20 nm and with varying edge-to-edge interelement separations ( $S$ ) from 50 nm to 400 nm. (d) AFM image of array of 200 nm square dots with $S = 100$ nm.	125
6.2	(a) Normalized static MOKE loops for a $10 \times 10 \mu\text{m}^2$ blanket permalloy thin film and array of 200 nm wide permalloy square shaped dots with $S = 50$ nm are shown. (b) Normalized static MOKE loops for arrays of 200 nm wide permalloy square shaped dots are shown for four different interdot separations $S = 50$ nm, 75 nm, 100 nm and 200 nm.	127
6.3	(a) The geometry of bias magnetic field and schematics of the pump and the probe beams are shown on the top of an AFM image of $10 \times 10 \mu\text{m}^2$ blanket permalloy thin film. (b) A typical time-resolved reflectivity data is plotted as a function of the time delay between the pump and the probe. (c) A typical Kerr rotation data from the blanket thin film with a bias field magnitude ( $H_b$ ) of 1.4 kOe, applied along the positive $x$ -axis. The time-resolved Kerr rotation shows four distinct regions, marked by numbers (1, 2, 3 and 4). The corresponding time scale is also written on top of the graph. The solid grey line in regions 3 and 4 are the bi-exponential fitting to the data, which gives the relaxation times $\tau_1 = 5.75$ ps and $\tau_2 = 200$ ps.	129
6.4	(a) The time-resolved Kerr rotation from the blanket permalloy thin film with a bias magnetic field $H_b = 1.4$ kOe, applied along the positive $x$ -axis. The solid line is only a guide to the eyes. (b) The oscillatory part of the time-resolved Kerr rotation (symbol) with a bi-exponential fit (solid line). (c) The background subtracted time-resolved Kerr rotation data and (d) the corresponding FFT power spectra showing the resonant mode.	130

- 6.5 (a) Left panel (solid circles) shows the background subtracted time-resolved Kerr rotation signals measured from a  $10 \times 10 \mu\text{m}^2$  blanket permalloy film as function of the bias magnetic field applied along  $x$ -axis. Solid black lines are fits with Eq. 6.4.3. Right panel shows the FFT power spectra of the time-resolved data. (b) Frequencies of the uniform precessional mode as a function of the bias magnetic field (solid circles) and the fit with the Kittel formula (solid line) are shown. 131
- 6.6 Time-resolved Kerr rotation for the first 25 ps is shown for arrays of 200 nm square shaped permalloy dots with interdot separation  $S = 50$  nm, 100 nm and 200 nm. The ultrafast demagnetization time is between 500 and 600 fs, while the fast relaxation time  $\tau_1$  is shown next to each time-resolved trace. 133
- 6.7 (a) Experimental time-resolved Kerr rotations and (b) corresponding FFT spectra are shown for arrays of permalloy square dots with width ( $W$ ) = 200 nm, thickness ( $t$ ) = 20 nm, and varying interdot separations ( $S$ ) at  $H_b = 1.25$  kOe. (c) FFT spectra of simulated time-domain magnetization for  $7 \times 7$  array of dots with same specifications as in the experiment. 135
- 6.8 Profiles of the simulated magnetostatic field distribution ( $x$ -component) for  $3 \times 3$  arrays of permalloy dots with  $W = 200$  nm and with varying  $S$  values are shown for  $H_b = 1.25$  kOe. The magnetostatic fields were calculated for array of  $7 \times 7$  elements, out of which  $3 \times 3$  elements from the centre have been shown. The arrows inside the dots represent the magnetization states of the dots. The strength of the stray magnetic field is presented by a contour map with a colour bar as shown at the bottom right corner of the figure. 137
- 6.9 (a) Linescans of the magnetostatic fields from arrays of 200 nm square permalloy dots with  $S = 50$  nm, 100 nm, 200 nm and 400 nm are shown. The linescans were taken along the dotted lines (parallel to  $x$ -axis) as shown in Fig. 6.8. (b) The magnitudes of the  $x$ -component of the stray magnetic field at the centre of the gap between two consecutive dots are plotted as a function of  $S$ . The values of  $B_x$  were taken along the dotted line as shown in (a). 138
- 6.10 Simulated mode spectra for a  $10 \times 10 \mu\text{m}^2$  permalloy blanket film and a single permalloy dot with  $W = 200$  nm are shown (1st column) along with their static magnetization states (2nd column) and mode profiles (3rd, 4th and 5th column) for  $H_b = 1.25$  kOe applied parallel to the horizontal edge of the elements. The colour scale for power profile is shown in the first row. 139
- 6.11 Power and phase distributions of the simulated modes for arrays of 200 nm dots with varying interdot separation  $S$  at  $H_b = 1.25$  kOe. The colour scales for power and phase are shown in the top row. 140
- 6.12 (a) Simulated power spectra for arrays of 200 nm permalloy dots with varying interdot separation  $S$ , illustrating the effect of the array on the edge mode of the single 200 nm permalloy dot. The corresponding mode (power) profiles are shown next to each spectrum. (b) Simulated power spectra from arrays of 200 nm permalloy dots for  $50 \text{ nm} \leq S \leq 100 \text{ nm}$  are shown with smaller steps of  $S$  to reveal the precise value of  $S$ , at which the mode splitting occurs. 141
- 6.13 Variation of the effective damping coefficient  $\alpha_{\text{eff}}$  for arrays of 200 nm permalloy dots at  $H_b = 1.25$  kOe is plotted as a function of the interdot separation  $S$ . The dotted horizontal line shows the damping coefficient of the uniform mode of a  $10 \times 10 \mu\text{m}^2$  blanket permalloy thin film at  $H_b = 1.25$  kOe. 142

6.14	Simulated static magnetization states for a single 200 nm square permalloy dot and an array of 200 nm square permalloy dots with $S = 50$ nm are shown at different values of $H_b$ . The colour scale (orange-white-green) which indicates the $y$ -component of magnetization, is shown at the bottom of figure. ‘F’, ‘S’ and ‘C’ denote flower-like, S-like and C-like states.	143
6.15	(a) Experimental time-resolved Kerr rotations at different bias fields (left panel) and the corresponding FFT spectra (right panel) are shown for the array of 200 nm dots with $S = 50$ nm. (b) Plot of the frequencies of the experimentally observed resonant peaks and simulated resonant peaks for different bias field magnitudes. The plotted modes are fitted with the Kittel mode with similar parameters obtained from the $10 \times 10 \mu\text{m}^2$ blanket permalloy film.	144
6.16	Variation of the effective damping coefficient $\alpha_{eff}$ as a function of the bias magnetic field ( $H_b$ ) for an array of 200 nm square permalloy dots with interdot separation $S = 50$ nm. The dotted horizontal line shows the damping of the uniform mode of a $10 \times 10 \mu\text{m}^2$ blanket permalloy thin film.	145
7.1	(a) Scanning electron micrographs of 50 nm permalloy dots with edge-to-edge separations ( $S$ ) varying from 50 to 200 nm are shown. The direction of the applied bias field is also shown on top of the image for $S = 150$ nm. (b) Atomic force microscope (AFM) image of an array of 50 nm permalloy dots with $S = 100$ nm is shown.	153
7.2	(a) Time-resolved reflectivity and (b) Kerr rotation data for an array of 50 nm permalloy dots with interdot separation $S = 50$ nm at $H_b = 2.5$ kOe. (c) The initial part of the dynamics is shown with a greater time resolution to illustrate the ultrafast demagnetization and the fast relaxation.	155
7.3	(a) Experimental time-resolved Kerr rotations and (b) the corresponding FFT spectra are shown for arrays of permalloy dots with width = 50 nm, thickness = 20 nm and with varying interdot separation $S$ at $H_b = 2.5$ kOe. (c) The FFT spectra of the simulated time-resolved magnetization are shown. The peak numbers are assigned to the FFT spectra. The dotted line in panel ‘c’ shows the simulated precession frequency of a single permalloy dot with width = 50 nm, thickness = 20 nm.	157
7.4	(a) The precession frequency is plotted as a function of $W/a$ . The circular and square symbols correspond to the experimental and simulated results, respectively, while the solid curves correspond to the fit to Eq. 7.3.1. (b) The damping coefficient $\alpha$ is plotted as a function of $S$ . The symbols correspond to the experimental data, while the solid line corresponds to a linear fit. The dashed line corresponds to the measured value of $\alpha$ for a continuous permalloy film grown under identical conditions.	158
7.5	Simulated magnetostatic field distributions ( $x$ -component) are shown for arrays of permalloy dots with $S = 50, 75, 100, 150$ and 200 nm at $H_b = 2.5$ kOe. The arrows inside the dots represent the magnetization states of the dots, while the strengths of the stray magnetic fields are represented by the colour bar at the bottom right corner of the figure.	160
7.6	The power and phase maps corresponding to different resonant frequencies are shown for the arrays with (a) $S = 50$ nm and (b) $S = 200$ nm. We have also simulated the power maps for a single 50 nm dot with 20 nm thickness with different cell sizes as (c) $2.5 \times 2.5 \times 20 \text{ nm}^3$ , (d) $1 \times 1 \times 20 \text{ nm}^3$ , and (e) $2.5 \times 2.5 \times 5 \text{ nm}^3$ and compared it with (f) the central dot from the $7 \times 7$ array with $S = 200$ nm. The colour bars at the top of the images represent the power and phase values within the images.	160

8.1	Scanning electron micrographs for (a) arrays of square permalloy dots with fixed edge-to-edge separation ( $S$ ) of 50 nm and varying sizes ( $W$ ) from 200 nm to 50 nm and (b) arrays of circular permalloy dots with fixed edge-to-edge separation ( $S$ ) of 50 nm and varying sizes $W = 200$ nm, 100 nm and 50 nm. The geometry of the bias field ( $H_b$ ) is shown on top of the SEM image of arrays with 50 nm dot size.	167
8.2	Simulated static magnetic configurations for single square permalloy dots with varying widths ( $W$ ) at bias field $H_b = 1.25$ kOe applied parallel to the horizontal edges of the dots. The colour map shows the $z$ -component (out-of-plane) of the magnetization. The figures are not in the same length scale. The colour scale of magnetization is shown at right-bottom corner of the figure.	169
8.3	Frequencies of the simulated resonant modes of single permalloy square dots with varying sizes ( $W = 50, 75, 100, 150$ and $200$ nm) are plotted as a function of the dot size. The mode (power) profiles for all modes are shown. The three different background colours show three different regions of interest. Different branches of frequencies are assigned with different coloured symbols. The colour scale of power is shown at right-bottom corner of the figure.	171
8.4	(a) Time-resolved Kerr rotation data measured from arrays of square permalloy dots with varying dot size and with fixed interdot separation $S = 50$ nm and (b) the corresponding FFT spectra. (c) FFT spectra of simulated magnetization dynamics for $7 \times 7$ arrays of dots with same specifications as mentioned above.	172
8.5	Simulated resonant mode frequencies for arrays of square permalloy dots with $S = 50$ nm and thickness ( $t$ ) = 20 nm are plotted as a function of dot size. The overall area of the graph has been divided into three different regions of interest by using different background colours. A crossover from the higher frequency branch to lower frequency branches is shown by an arrow.	173
8.6	The power and phase maps for the resonant modes for arrays of square permalloy dots with varying dot size ( $W$ ) and with $S = 50$ nm and thickness ( $t$ ) = 20 nm are shown. The whole range is split into three regions. The colour map for power is shown in region 1. The colour map for phase for first two rows in region 1 is shown within that region, while the phase colour map for the last row in region 1, and regions 2 and 3 are shown in region 3.	174
8.7	(a) Simulated static magnetic states for single circular permalloy dots with varying size ( $W$ ) at bias field $H_b = 2.0$ kOe. The colour map shows the $z$ -component (out-of-plane) of magnetization. The figures are not in the same length scale. The colour scales of magnetization are same to those in Fig. 8.2. (b) The ultrafast demagnetization and fast relaxation for array of 200 nm circular dots with $S = 50$ nm is shown.	176
8.8	(a) Time-resolved Kerr rotations measured from arrays of circular permalloy dots with interdot separation $S = 50$ nm and varying dot size ( $W = 200, 100$ and $50$ nm) and (b) the corresponding FFT power spectra. (c) The FFT power spectra of simulated time-resolved magnetization for $7 \times 7$ arrays of circular dots with same specifications as the experimental samples. (d) The FFT power spectra of simulated time-resolved magnetization for single circular dots with dot size $W = 200, 100$ and $50$ nm.	177
8.9	The experimental resonant frequencies for arrays of circular permalloy dots and simulated resonant frequencies for single and arrays of circular permalloy dots are plotted as function of dot size. The overall area of the graph has been divided into two different regions of interest by using different background colours. A crossover from higher frequency branch to lower frequency branch is shown by an arrow.	178

8.10	Simulated power and phase profiles of intrinsic and collective resonant modes of circular permalloy dots with sizes $W = 200, 100$ and $50$ nm. For the array, the edge-to-edge separation is fixed at $S = 50$ nm. The colour scales for power and phase are shown at the bottom of the figure.	179
9.1	(a) Scanning electron micrographs for arrays of square permalloy dots with size ( $W$ ) = $200$ nm and separation ( $S$ ) = $50$ nm and $100$ nm. The geometry of the applied bias field is shown on top of the SEM image of the array with $S = 100$ nm. (b) Simulated static magnetization states are shown for a single $200$ nm square dot of thickness ( $t$ ) = $20$ nm at a bias field ( $H_b$ ) of $1.15$ kOe applied at different azimuthal angles ( $\phi$ ).	186
9.2	Contour plots of magnetostatic fields at different azimuthal angles ( $\phi$ ) of the in-plane bias field of magnitude $H_b = 1.15$ kOe for arrays of $200$ nm square shaped permalloy dots with interdot separations ( $S$ ) of (a) $50$ nm and (b) $100$ nm. The arrows inside the dots show the magnetization states of the dots and the colour map as shown in the extreme right side of figure represents the $x$ -component of the magnetostatic field.	187
9.3	(a) Experimentally measured time-resolved Kerr rotations at $H_b = 1.15$ kOe applied at different azimuthal angles ( $\phi$ ) and (b) the corresponding FFT power spectra are shown. (c) FFT spectra of the simulated time-domain magnetization obtained from a $7 \times 7$ array of $200$ nm magnetic dots with $50$ nm edge-to-edge separation are shown for different values of $\phi$ .	188
9.4	(a) The experimental and (b) simulated resonant mode frequencies for array of $200$ nm magnetic dots with $S = 50$ nm are plotted as a function of the azimuthal angle ( $\phi$ ) of the applied bias field. The solid lines correspond to fit to Eq. 9.4.1.	189
9.5	(a) Simulated precession frequencies as a function of the azimuthal angle ( $\phi$ ) of the applied bias field and fit to Eq. 9.4.1 (solid lines) are shown for a single square permalloy dot with width = $200$ nm and thickness = $20$ nm. (b) The simulated power and phase profiles of the resonant modes are shown. The azimuthal angle $\phi$ is shown in the first column.	190
9.6	Power and phase distributions of the resonant modes for an array of $200$ nm square permalloy dots with $50$ nm interdot separation are shown (extreme left and extreme right columns) along with the FFT power spectra (middle column) for four different values of $\phi$ . The scales of the colour maps are same as in Fig. 9.5.	191
9.7	(a) Simulated resonant mode frequencies for array of $200$ nm square dots with $100$ nm interdot separation are plotted as a function of the azimuthal angle ( $\phi$ ) of the bias field. (b) Power and phase distributions of the simulated modes are shown for four different values of $\phi$ . The scales of the colour maps are same to those in Fig. 9.5.	192
10.1	The EDX spectra obtained from Ni nanoparticles samples [(a) sample A, (b) sample B and (c) sample C] are shown. The corresponding scanning electron micrographs are shown in the inset.	198
10.2	(a) The XRD patterns from all three samples are shown. (b) The experimental results of magnetization ( $M$ ) vs applied magnetic field ( $H$ ) data are shown for all three samples.	199
10.3	(a) The simulated $M$ - $H$ curves are shown for single Ni nanoparticles of $48$ nm and $200$ nm diameters. (b) The simulated $M$ - $H$ loops with increasing number of overlapped ( $10\%$ ) particles in cluster. (c) The simulated $M$ - $H$ loops for three different clusters (cluster 1, cluster 2 and cluster 3) composed of $5 \times 5 \times 3$ particles.	200

10.4	Simulated magnetization images at various applied magnetic field ( $H$ ) values for (a) 48 nm single spherical particle, (b) 200 nm single spherical particle, (c) periodic cluster of $5 \times 5 \times 3$ particles (cluster 2) and (d) random cluster of 75 particles (cluster 3). The constituent particles are spherical with 48 nm in diameter.	202
10.5	(a) The scanning electron micrographs from four different samples ( $S_1$ , $S_2$ , $S_3$ and $S_4$ ) are shown. The (b) EDX spectrum and the (c) XRD pattern from sample $S_1$ are shown.	204
10.6	(a) The experimental data of normalized magnetization ( $M/M_S$ ) as a function of the applied magnetic field ( $H$ ) are shown for samples $S_1$ , $S_2$ , $S_3$ and $S_4$ . (b) Typical discretizations of the simulated samples used in the finite element method based micromagnetic simulations are shown. Due to clarity, enlarged views from the specific regions of simulated microstructures $S_3$ and $S_4$ are shown. (c) Simulated normalized magnetization ( $M/M_S$ ) is plotted as a function of the applied magnetic field ( $H$ ) for four samples. The insets show the geometries of the simulated microstructures. The dimensions of the unit spheres in the microstructures are not in scale.	205
10.7	The spatial maps of the simulated magnetization (arrows) and the energy due to the external field (colour map) for samples (a) $S_1$ , (b) $S_2$ , (c) $S_3$ and (d) $S_4$ at specific values of the external magnetic fields are shown. The dashed arrows are given as a guide to the eye to follow the spatial variation of magnetization.	207
10.8	Scanning electron micrograph of (a) single Ni chain and (b) a number of parallel chains of Ni nanoparticles are shown. The geometry of applied field is shown on top of Fig. (a). (c) EDX spectrum and (d) XRD pattern are shown for same sample.	209
10.9	(a) The VSM results of Ni chains are shown with different angles ( $\theta$ ) of the applied magnetic field with the axes of the chains. Inset shows the expanded view of the $M$ - $H$ curves. (b) The geometry of the applied magnetic field for simulation is shown schematically.	210
10.10	(a) The simulated $M$ vs $H$ curves of single Ni chain for three different angles ( $\theta$ ) of the applied magnetic field <i>w.r.t.</i> the length of the chain. (b) The schematic of a single chain for simulation is shown. Spatial maps of magnetization at different magnetic field values for (c) $\theta = 0^\circ$ , (d) $\theta = 45^\circ$ , (e) $\theta = 90^\circ$ . The colour map (red-white-blue) indicates the projection of vector magnetization on the image plane.	212
10.11	Hysteresis loops of three parallel Ni nanochains with separation (a) $S = 5$ nm and (b) $S = 50$ nm for three different angles ( $\theta$ ) of the applied magnetic field <i>w.r.t.</i> the length of the chains.	212
10.12	(a) Simulated hysteresis loops of three parallel chains with separation $S = 10$ nm. (b) The schematic of the array of chains for simulation. The spatial maps of magnetization at different values of $H$ for (c) $\theta = 0^\circ$ , (d) $\theta = 45^\circ$ , (e) $\theta = 90^\circ$ .	213
11.1	(a) Ultrafast demagnetization and fast relaxation of samples $S_1$ , $S_2$ , $S_3$ and $S_4$ . (b) Only the relaxation parts of the Kerr ellipticities are shown. The grey solid lines are the fittings with a single exponential decay function (Eq. 11.1). (c) Typical scanning electron micrographs of the samples are shown.	222
11.2	(a) The time-resolved Kerr ellipticity data for samples $S_1$ , $S_3$ and $S_4$ are shown for a longer time scale (up to 1500 ps). (b) The data are fitted with the bi-exponential decay function (grey solid lines) and the extracted long relaxation times ( $\tau_2$ ) are shown in the graphs.	225

- 11.3 (a) Scanning electron micrograph of sample  $S_1$ . The geometry of the bias field and the pump and the probe spots are shown schematically on top of the figure. (b) Hysteresis loop ( $M-H$ ) of the sample is shown. Solid circular points on top of the hysteresis loop denote the static magnetization values of the sample at different bias field values, for which the precessional dynamics were measured. (c) In left column, background subtracted Kerr ellipticity signals are shown for the same sample as a function of  $H_b$ . The right column shows corresponding FFT power spectra. The peak numbers are assigned to the FFT power spectra. (d) The frequencies of the observed resonant modes are plotted as a function of  $H_b$ . 226
- 11.4 The FFT spectra of background subtracted time-resolved Kerr ellipticity data are shown for three samples ( $S_1$ ,  $S_3$  and  $S_4$ ) at a fixed value of  $H_b = 1$  kOe applied in plane of the samples. 228

# CHAPTER 1

---

## Introduction

---

Though magnetism is a very old topic of research among different scientific disciplines, nanomagnetism has become a topic of interest for modern scientific research during past few decades. The reason behind that is not only the fundamental scientific interest but also the tremendous potential to use the nanomagnets in modern and future nanotechnology. The scientific communities have already proved the potential of nanomagnets to use them as the building blocks for a range of multidisciplinary applications like nonvolatile magnetic memory [1-3], magnetic data storage [4-6], magnetic recording heads [7], magnetic resonance imaging [8], biomedicine and biotechnology [9-10]. They also have potential applications in spin logic devices [11-13], spin torque nano-oscillators (STNOs) [14-15] and magnonic crystals [16-19].

Magnetic recording was invented more than hundred years ago by Valdemar Poulsen [20]. Since then, it has played a key role in development of different kinds of nonvolatile storage devices like data, audio and video storage. The first magnetic hard disk drive of storage capacity 5 MB was developed by IBM in 1956. In modern disk drives, the storage capacity has increased by more than 20 million-fold in the quest to increase the storage density and to reduce the cost. Conventional recording media uses a single layer thin granular film of *hcp* Co-based alloys where the easy axis of magnetization lies in the plane of the film [21]. As the storage capacity increases, the grain size also decreases and the magnetization of the grains becomes unstable due to superparamagnetic effects [22-23]. Thermal stability can be improved by reducing crystallographic defects and introducing materials with higher anisotropy. Now, in a longitudinal magnetic media the magnetization of grains are oriented randomly, which decreases the signal-to-noise ratio. To reduce this kind of effect, sometimes the easy axes of the grains are set along a track direction. This is called oriented longitudinal media [24]. Antiferromagnetically coupled (AFC) media are another kind of novel magnetic media. AFC media consist of two magnetic layers, which are antiferromagnetically coupled

through a thin nonmagnetic layer [25-26]. In AFC media, the writing field is lower than the longitudinal media and stability can be optimized by controlling the thickness of the layers. In a perpendicular recording media, the easy axis of magnetization is perpendicular to the film surface [27]. The thermal stability of perpendicular media is greater than the longitudinal media. Therefore, the storage density can be increased by decreasing the grain size. The heat-assisted magnetic recording (HAMR) can be used for longitudinal recording or perpendicular recording. In HAMR, The switching fields of the grains are reduced by heating them with a laser. Then the medium is quickly cooled back to the normal temperature to store the data [24]. In all the above recording media a number of grains are used as a single bit [28-29]. In patterned magnetic media, each bit consists of a lithographically patterned island, which has much larger volume than a single grain. Therefore, their thermal stability is higher than the granular media.

Giant magnetoresistance (GMR) is observed in thin film structures composed of alternating ferromagnetic and nonmagnetic conductive layers [30-31]. Modern recording head of hard-disk drives (HDD) are based on the phenomenon of GMR with current-in-plane (CIP) geometry [7]. In CIP geometry, current flows parallel to the layers. To overcome few limitations of CIP, a new type of sensor geometry called Current-perpendicular-to-plane (CPP) geometry can be used. In CPP geometry, current flow perpendicular to the plane of the layers. Magnetic tunnel junction (MTJ), where two ferromagnetic thin film layers are separated by a thin insulating nonmagnetic barrier, also makes read-head sensors because of the large signal at room temperature [32], which comes from large tunnel-magnetoresistance (TMR) ratios. However, MTJs are accompanied by large noise [33]. The conventional solid state memories like Dynamic Random Access Memory (DRAM) and the Static Random Access Memory (SRAM) rely on the electric charges. Therefore, they are volatile in nature and capable of nanosecond access times in both read and write operations [1]. The major nonvolatile memory used today is FLASH but it has slow write access time and poor bit cyclability. Ferroelectric RAM (FeRAM) is another kind of nonvolatile memory, which has the potential to have high speed performance similar to DRAM. But it has many process integration complexities [1, 3]. Magnetoresistive random access memory (MRAM) is a nonvolatile memory, which offers very high read-write speed by consuming very low power [34]. They are based on GMR elements or MTJs. However, the basic MRAM bits suffer from half-select problem, which limits the bit size to about 180 nm. In order for MRAM to be a productive technology, bit size needs to reduce down to 65 nm, which requires the spin

transfer torque (STT) switching and a thorough investigation of the dynamics of arrays of sub-100 nm MRAM bits at various time scales is required for further advancement of this technology.

Conventional logic devices are based on transistors. The ongoing increment of the numbers of devices per unit area needs shrinkage of metal-oxide-semiconductor field effect transistor (MOSFET). This will cause the power dissipation problem and will increase the difficulties in interconnection wiring [35]. A new type of technology called “spintronics” are promising an alternative route as a solution to this problem [36]. In spintronics, both the spin and charge of electrons are used for logic and memory operations. The spintronic devices promise high-speed and nonvolatile operations with lower power consumption [36-37]. There are many reports on magnetic logic devices. Few reports have been published on magnetic logic based on a single electron transistor architecture [38]. The logic devices can also be fabricated using MTJs [39-40]. Magnetic nanowires show very high shape anisotropy where the magnetization prefers to align along the long axis of the wire. Binary data can be stored on the basis of direction of magnetization. During the change in the magnetization direction, the domain wall propagates through nanowires. The propagation of domain wall can be controlled by an externally applied magnetic field. Logic devices based on the domain walls have also been reported [11]. Spin waves can also be used in logic devices as was reported by Kostylev *et al.* [41]. The properties of spin wave interference are used in a Mach–Zehnder-type current-controlled spin wave interferometer. Different kinds of spin wave gates have been demonstrated by using spin wave amplitude [42-43] and phase [44].

The concept of spin waves in a periodic medium was first introduced by Bloch [45]. Spin waves are basically collective excitation of spins in a continuous or confined magnetic medium. Magnons are the particle counterpart of spin waves. The periodically modulated magnetic medium may be considered as an artificial crystal where spin waves or magnons are the carriers, and are therefore called as the “magnonic crystal” analogous to the “photonic crystal”, where the light or photons are the carriers. Following this, a newly born and rapidly evolving research area called “magnonics” has been introduced [16-19]. The periodic modulation of the magnetic parameters tailors the magnonic band structure with the creation of magnonic band gaps. The aim of the modern research in magnonics is to investigate and manipulate the magnonic band structure [46-48] by varying various physical and material parameters of the magnonic crystals as well as the external magnetic fields. Ordered arrays of magnetostatically coupled magnetic nanoparticles, nanodots or nanostripes have the potential

to serve as magnonic crystals. The dots or nanostripes can be made of a single component (element), bi-component or multilayered structure. Magnetic antidot lattices, which are basically arrays of holes on a magnetic thin film are also showing promises as magnonic crystals, which show larger spin wave propagation velocity (steeper dispersion) than magnetic dot lattices.

The successful applications of spin waves in future technology strongly rely upon their generation, controlled propagation, and detection mechanisms. The challenge is to generate controlled spin waves at well defined frequencies. The spin waves can be generated by picosecond magnetic field pulses either launched from a photoconductive switch [49] or generated by a pulsed electric field [50]. Harmonic [51] or pulsed [49] magnetic fields can be applied in this case. One can also use ultrashort laser pulses [52-53] to generate the spin waves. The spin transfer torque (STT), a recently discovered physical phenomenon, are recently being used to excite spin waves with the help of spin polarized current [54]. The spin waves are generally guided by one dimensional magnetic stripes [55-57] and detected by probing optically [58], electrically [59-60] or by inductive method [61-62]. The future technology demands various spin wave based nanoscale microwave components and devices. Consequently, devices such as spin wave amplifier [63], phase shifter [64], splitter, frequency filter and interferometer [42] have become subjects of intense research. Different properties of spin waves like reflection and refraction [65-68], interference and diffractions [69-72], tunneling [73-74] and focusing and self-focusing [75-78] have been studied theoretically and experimentally in last few decades.

Beyond the applications in spintronics and magnonics, nanomagnets have opened new windows for biomedical and biotechnological applications. Magnetic nanoparticles show new promising applications in improved contrast enhanced magnetic resonance imaging [79-80], targeted drug delivery [81], manipulation of cell membrane [82] and hyperthermic treatment for malignant cells [83-84]. Since ferromagnetic nanoparticles could be harmful for the biological cells, superparamagnetic nanoparticles are used for biomedical treatments as they do not retain any net magnetization in absence of magnetic field.

For most of the potential applications mentioned above, the nanomagnets should be arranged in an ordered array such that they can be addressed easily. Therefore, in recent years fabrication and the study of magnetization dynamics of ordered arrays of nanomagnets have attracted much attention of the nanomagnetism community [85-95]. Modern data storage and

memory technologies also demand higher operational speed along with the higher storage density. The conventional storage technology depends upon the slow magnetic domain wall dynamics, which limits the data writing and reading speed in the nanosecond regime. The faster speed demands the operation of nanomagnets far beyond the gigahertz regime. The picosecond precessional magnetization dynamics of nanomagnets may fulfill the above requirement. The ultrafast precessional switching [96-98], where the magnetization reversal is triggered by a large angle precessional dynamics can be used for high speed data storage and memory devices. However, a thorough understanding and control of the precessional dynamics including the precession frequency and the damping coefficient of the nanomagnets are required for its application in technology.

The quasistatic and ultrafast magnetization dynamics of confined magnetic structures are different from their bulk counterparts and continuous thin films. Magnetization dynamics of nanomagnets strongly depends upon their static magnetization states, which depend not only on their intrinsic material parameters such as exchange stiffness constant, saturation magnetization and magnetocrystalline anisotropy, but also on their physical structures including the shape, size and aspect ratio [99-102] as well as the external parameters like the strength and direction of the bias magnetic field [103]. For an array of nanomagnets, the static magnetization state depends also upon the physical parameters of the arrays such as the lattice constant and the lattice symmetry. The quasistatic magnetization reversal of nanomagnets can be of various types. For an isolated single or quasi-single domain nanomagnet, the reversal may occur through the coherent rotation of magnetization or through the formation of curling, buckling, fanning, vortex, onion, flower, leaf, C- and S-states depending upon the shape, size and aspect ratio of the nanomagnet [89, 104-111]. On the other hand, multidomain structures reverse through domain wall dynamics [109]. In contrary, the reversal for clusters and arrays of dipolar or exchange coupled nanomagnets may occur through the formation of different collective modes, where the flux flows through a number of nanomagnets to form the minimum energy configuration and various reversal modes as above may also be observed [108, 112-114]. While the shape, size and aspect ratio of the individual nanomagnets control the nonuniform demagnetizing field within them, lattice periodicity and lattice constant and the external magnetic field control the strength and type of the interactions among the nanomagnets. The static magnetization states of non-ellipsoidal nanomagnets are generally nonuniform due to the nonuniform nature of the demagnetizing field. The nonuniform static magnetization states may trap spin waves locally

or quantize them [90, 115-121]. Magnetic vortices are very interesting nonuniform ground state of magnetization, which are found in micro and nano-disks when the aspect ratio defined by thickness/diameter is much less than one and both thickness and diameter exceed the exchange length in that material. The vortex dynamics is dominated by gyration of the core and radial and azimuthal spin wave modes of the chiral spins, which are much different from the dynamics of a single domain nanomagnet. Magnetic vortices are also potential candidates for future nonvolatile memory and logic devices [122-123].

The key challenges to study the physical phenomenon mentioned above are the synthesis or fabrication of high quality magnetic nanostructures and their characterization. Technology demands fabrication of nanomagnets with narrow size dispersion and in an ordered array over a macroscopic length scale. These led to the development of a number of ‘top-down’ and ‘bottom-up’ approaches in nanofabrication methods and more recently a combination of the two. The solution phase colloidal chemistry is applied in ‘bottom-up’ approach to synthesize monodisperse nanocrystals of uniform shapes and sizes [124]. There are many colloidal chemistry based methods like reduction, nonhydrolytic sol-gel and thermal decomposition processes [125]. In reduction method, various kinds of reductants are used to synthesize metallic nanoparticles, whereas nonhydrolytic sol-gel process is mainly used to synthesize metal oxide nanoparticles. In thermal decomposition methods, the decomposition of organometallic compounds is performed in hot surfactant solutions to synthesize nanoparticles of various materials. Reverse micelle methods are also very efficient to synthesize various kinds of nanocrystals. On the other hand, the physical methods are utilized in ‘top-down’ approach, which includes different kinds of lithographic techniques such as photolithography [126], electron beam lithography (EBL) [127], deep ultraviolet (DUV) lithography [128], X-ray lithography [129], interference or holographic lithography (IL) [130], nanoimprint lithography (NIL) [131] and ion beam lithography (IBL) [132]. Scanning probe lithography [133], step growth method [134], shadow masks [135], laser or ion irradiation [136] are also very promising techniques. Other different techniques for preparing ordered nanostructures are self-assembly mechanism like heterogeneous nucleation of magnetic atoms on metallic surfaces [137], seeded growth [138], and nanotemplate fabrication technique using templates such as diblock copolymers [139], anodized alumina membranes [140] and nuclear-track etched membranes [141].

To study the quasistatic and ultrafast dynamic properties of nanomagnets, different kinds of sensitive characterization techniques have been developed in last few decades [58].

Magnetic force microscopy (MFM) [142-143] and Lorentz force microscopy [144] are now commonly used microscopies, which are very efficient to map the stray magnetic field and the sample magnetization, respectively with a spatial resolution better than 10 nm. The contrast of the images come from magnetic force between the scanning magnetic tip and the stray field gradient from the sample in case of MFM and the deflection of the accelerated electrons by Lorentz force after transmitting through the sample in case of Lorentz microscopy. The main drawback for both techniques is the difficulty of extracting quantitative information directly from the images. Electron holography [145] is another electron transmission method based on the electron interference. The amplitude as well as the phase information of the magnetic domains and stray magnetic field can be mapped with a very high spatial resolution close to 2 nm. Magneto-optical Kerr effect (MOKE) microscopy [146] is widely used to map the sample magnetization with a spatial resolution of about few hundreds of nanometer. The photoemission electron microscopy (PEEM) [147] is used with much better spatial resolution than visible light imaging. Spin polarized low energy electron microscopy (SPLEEM) [148], scanning electron microscopy with polarization analysis (SEMPA) [149], spin polarized scanning tunneling microscopy (SP-STM) [150] and ballistic electron magnetic microscopy (BEMM) [151] are other imaging techniques, which give spatial resolution close to 10 nm or better. These techniques use the spin dependent transmission, scattering or tunneling for image contrast. The imaging methods mentioned above in this paragraph are used to map static magnetization state with very high spatial resolution but with poor temporal resolution. To investigate fast magnetization dynamics different kinds of techniques have emerged. The conventional ferromagnetic resonance (FMR) [152] or vector network analyzer – ferromagnetic resonance (VNA – FMR) [153] techniques are very efficient to measure the high frequency magnetic response from MHz to GHz regime with a very good frequency resolution. The poor spatial resolution of FMR techniques pushed to develop spatially resolved FMR [154]. Pulsed inductive microwave magnetometry (PIMM) [155] is another technique to measure the dynamics in the time-domain with tens of picoseconds temporal resolution. The Brillouin light scattering (BLS) is a very efficient technique to study the spin waves in the wave-vector-domain [92]. The frequency dispersion of the spin waves with their wave-vector can be measured directly by using this technique. Recently space-resolved and time-resolved BLS techniques have been developed to obtain sub- $\mu\text{m}$  spatial resolution and few ns temporal resolution [156]. The best spatio-temporal resolution is obtained from time-resolved magneto-optical Kerr effect (TRMOKE) microscope [99]. They are used to probe the ultrafast magnetization dynamics in the time-

domain with sub-hundred femtosecond time resolution limited by the pulse width of the laser. The magnetoresistive methods [157] and X-ray microscopy [158] also have the potential to achieve very good spatio-temporal resolution like TRMOKE. Time-resolved scanning Kerr microscopy (TRSKM) is another variant of TRMOKE, which is used to image the time evolution of magnetization excited by a time-dependent magnetic field [159-161].

## Bibliography:

1. S. Tehrani, E. Chen, M. Durlam, M. DeHerrera, J. M. Slaughter, J. Shi, and G. Kerszykowski, *J. Appl. Phys.* **85**, 5822 (1999).
2. J. Åkerman, *Science* **308**, 508 (2005).
3. R. C. Sousa and I. L. Prejbeanu, *C. R. Physique* **6**, 1013 (2005).
4. T. Thomson, G. Hu, and B. D. Terris, *Phys. Rev. Lett.* **96**, 257204 (2006).
5. B. D. Terris, T. Thomson, and G. Hu, *Microsyst. Technol.* **13**, 189 (2007).
6. O. Hellwig, A. Berger, T. Thomson, E. Dobisz, Z. Z. Bandic, H. Yang, D. S. Kercher, and E. E. Fullerton, *Appl. Phys. Lett.* **90**, 162516 (2007).
7. J. R. Childress and R. E. Fontana Jr, *C. R. Physique* **6**, 997 (2005).
8. S. H. Chung, A. Hoffmann, S. D. Bader, C. Liu, B. Kay, L. Makowski, and L. Chen, *Appl. Phys. Lett.* **85**, 2971 (2004).
9. M. Arruebo, R. Fernández-Pacheco, M. R. Ibarra, and J. Santamaría, *Nano Today* **2**, 22 (2007).
10. A. K. Gupta and M. Gupta, *Biomaterials* **26**, 3995 (2005).
11. D. A. Allwood, G. Xiong, C. C. Faulkner, D. Atkinson, D. Petit, and R. P. Cowburn, *Science* **309**, 1688 (2005).
12. A. Imre, G. Csaba, L. Ji, A. Orlov, G. H. Bernstein, and W. Porod, *Science* **311**, 205 (2006).
13. D. B. Carlton, N. C. Emley, E. Tuchfeld, and J. Bokor, *Nano Lett.* **8**, 4173 (2008).
14. S. Kaka, M. R. Pufall, W. H. Rippard, T. J. Silva, S. E. Russek, and J. A. Katine, *Nature* **437**, 389 (2005).
15. A. Slavin and V. Tiberkevich, *IEEE Trans. Magn.* **45**, 1875 (2009).
16. V. V. Kruglyak and R. J. Hicken, *J. Magn. Magn. Mater.* **306**, 191 (2006).
17. S. Neusser and D. Grundler, *Adv. Mater.* **21**, 2927 (2009).
18. V. V. Kruglyak, S. O. Demokritov, and D. Grundler, *J. Phys. D: Appl. Phys.* **43**, 264001 (2010).
19. B. Lenk, H. Ulrichs, F. Garbs, and M. Münzenberg, *Phys. Rep.* **507**, 107 (2011).
20. E. D. Daniel, C. D. Mee, and M. H. Clark, "Magnetic Recording: The First 100 Years," *IEEE Press*, New York (1998).
21. B. D. Terris and T. Thomson, *J. Phys. D: Appl. Phys.* **38**, R199 (2005).

22. S. H. Charap, L. Pu-Ling, and H. Yanjun, *IEEE Trans. Magn.* **33**, 978 (1997).
23. D. Weller and A. Moser, *IEEE Trans. Magn.* **35**, 4423 (1999).
24. A. Moser, K. Takano, D. T. Margulies, M. Albrecht, Y. Sonobe, Y. Ikeda, S. Sun, and E. E. Fullerton, *J. Phys. D: Appl. Phys.* **35**, R157 (2002).
25. E. N. Abarra, A. Inomata, H. Sato, I. Okamoto, and Y. Mizoshita, *Appl. Phys. Lett.* **77**, 2581 (2000).
26. E. E. Fullerton, D. T. Margulies, M. E. Schabes, M. Carey, B. Gurney, A. Moser, M. Best, G. Zeltzer, K. Rubin, H. Rosen, and M. Doerner, *Appl. Phys. Lett.* **77**, 3806 (2000).
27. S.-i. Iwasaki, *J. Magn. Magn. Mater.* **235**, 227 (2001).
28. G. F. Hughes, *IEEE Trans. Magn.* **36**, 521 (2000).
29. M. Todorovic, S. Schultz, J. Wong, and A. Scherer, *Appl. Phys. Lett.* **74**, 2516 (1999).
30. M. N. Baibich, J. M. Broto, A. Fert, F. N. Van Dau, F. Petroff, P. Etienne, G. Creuzet, A. Friederich, and J. Chazelas, *Phys. Rev. Lett.* **61**, 2472 (1988).
31. S. S. P. Parkin, Z. G. Li, and D. J. Smith, *Appl. Phys. Lett.* **58**, 2710 (1991).
32. J. S. Moodera, L. R. Kinder, T. M. Wong, and R. Meservey, *Phys. Rev. Lett.* **74**, 3273 (1995).
33. K. B. Klaassen, X. Xinzhi, and J. C. L. van Peppen, *IEEE Trans. Magn.* **40**, 195 (2004).
34. J. M. Daughton, *Thin Solid Films* **216**, 162 (1992).
35. J. A. Davis, R. Venkatesan, A. Kaloyeros, M. Beylansky, S. J. Souri, K. Banerjee, K. C. Saraswat, A. Rahman, R. Reif, and J. D. Meindl, *Proc. IEEE* **89**, 305 (2001).
36. S. A. Wolf, D. D. Awschalom, R. A. Buhrman, J. M. Daughton, S. von Molnár, M. L. Roukes, A. Y. Chtchelkanova, and D. M. Treger, *Science* **294**, 1488 (2001).
37. G. A. Prinz, *Science* **282**, 1660 (1998).
38. R. P. Cowburn and M. E. Welland, *Science* **287**, 1466 (2000).
39. A. Ney, C. Pampuch, R. Koch, and K. H. Ploog, *Nature* **425**, 485 (2003).
40. R. Richter, H. Boeve, L. Bär, J. Bangert, G. Rupp, G. Reiss, and J. Wecker, *Solid State Electron.* **46**, 639 (2002).
41. M. P. Kostylev, A. A. Serga, T. Schneider, B. Leven, and B. Hillebrands, *Appl. Phys. Lett.* **87**, 153501 (2005).
42. T. Schneider, A. A. Serga, B. Leven, B. Hillebrands, R. L. Stamps, and M. P. Kostylev, *Appl. Phys. Lett.* **92**, 022505 (2008).
43. K. S. Lee and S. K. Kim, *J. Appl. Phys.* **104**, 053909 (2008).

44. A. Khitun, M. Bao, and K. L. Wang, *J. Phys. D: Appl. Phys.* **43**, 264005 (2010).
45. F. Bloch, *Z. Physik* **61**, 206 (1930).
46. J. O. Vasseur, L. Dobrzynski, B. Djafari-Rouhani, and H. Puszkarski, *Phys. Rev. B* **54**, 1043 (1996).
47. Z. K. Wang, V. L. Zhang, H. S. Lim, S. C. Ng, M. H. Kuok, S. Jain, and A. O. Adeyeye, *Appl. Phys. Lett.* **94**, 083112 (2009).
48. D. Kumar, O. Dmytriiev, S. Ponraj, and A. Barman, *J. Phys. D: Appl. Phys.* **45**, 015001 (2012).
49. M. R. Freeman, R. R. Ruf, and R. J. Gambino, *IEEE Trans. Magn.* **27**, 4840 (1991).
50. S. Tamaru, J. A. Bain, R. J. M. van de Veerdonk, T. M. Crawford, M. Covington, and M. H. Kryder, *Phys. Rev. B* **70**, 104416 (2004).
51. R. W. Damon and H. van de Vaart, *Phys. Rev. Lett.* **12**, 583 (1964).
52. A. V. Kimel, A. Kirilyuk, F. Hansteen, R. V. Pisarev, and T. Rasing, *J. Phys.: Condens. Matter* **19**, 043201 (2007).
53. G. M. Müller, G. Eilers, Z. Wang, M. Scherff, R. Ji, K. Nielsch, C. A. Ross, and M. Münzenberg, *New J. Phys.* **10**, 123004 (2008).
54. S. I. Kiselev, J. C. Sankey, I. N. Krivorotov, N. C. Emley, R. J. Schoelkopf, R. A. Buhrman, and D. C. Ralph, *Nature* **425**, 380 (2003).
55. V. E. Demidov, J. Jersch, S. O. Demokritov, K. Rott, P. Krzysteczko, and G. Reiss, *Phys. Rev. B* **79**, 054417 (2009).
56. V. E. Demidov, J. Jersch, K. Rott, P. Krzysteczko, G. Reiss, and S. O. Demokritov, *Phys. Rev. Lett.* **102**, 177207 (2009).
57. S.-K. Kim, *J. Phys. D: Appl. Phys.* **43**, 264004 (2010).
58. M. R. Freeman and B. C. Choi, *Science* **294**, 1484 (2001).
59. J. C. Sankey, P. M. Braganca, A. G. F. Garcia, I. N. Krivorotov, R. A. Buhrman, and D. C. Ralph, *Phys. Rev. Lett.* **96**, 227601 (2006).
60. S. Petit, C. Baraduc, C. Thirion, U. Ebels, Y. Liu, M. Li, P. Wang, and B. Dieny, *Phys. Rev. Lett.* **98**, 077203 (2007).
61. S. Zhang, S. A. Oliver, N. E. Israeloff, and C. Vittoria, *Appl. Phys. Lett.* **70**, 2756 (1997).
62. J. Podbielski, D. Heitmann, and D. Grundler, *Phys. Rev. Lett.* **99**, 207202 (2007).
63. Y. Acremann, X. W. Yu, A. A. Tulapurkar, A. Scherz, V. Chembrolu, J. A. Katine, M. J. Carey, H. C. Siegmann, and J. Stohr, *Appl. Phys. Lett.* **93**, 102513 (2008).
64. R. Hertel, W. Wulfhekel, and J. Kirschner, *Phys. Rev. Lett.* **93**, 257202 (2004).

65. F. Goedsche, *Phys. Stat. Sol. B* **39**, K29 (1970).
66. J. Gouzerh, A. A. Stashkevich, N. G. Kovshikov, V. V. Matyushev, and J. M. Desvignes, *J. Magn. Magn. Mater.* **101**, 189 (1991).
67. Y. I. Gorobets and S. A. Reshetnyak, *Tech. Phys.* **43**, 188 (1998).
68. A. V. Vashkovsky and E. H. Lock, *Phys. Usp.* **49**, 389 (2006).
69. V. K. Dugaev, P. Bruno, B. Canals, and C. Lacroix, *Phys. Rev. B* **72**, 024456 (2005).
70. S. K. Choi, K. S. Lee, and S. K. Kim, *Appl. Phys. Lett.* **89**, 062501 (2006).
71. K. Perzlmaier, G. Woltersdorf, and C. H. Back, *Phys. Rev. B* **77**, 054425 (2008).
72. D. R. Birt, B. O'Gorman, M. Tsoi, X. Q. Li, V. E. Demidov, and S. O. Demokritov, *Appl. Phys. Lett.* **95**, 122510 (2009).
73. S. O. Demokritov, A. A. Serga, A. André, V. E. Demidov, M. P. Kostylev, B. Hillebrands, and A. N. Slavin, *Phys. Rev. Lett.* **93**, 047201 (2004).
74. A. Kozhanov, D. Ouellette, M. Rodwell, S. J. Allen, A. P. Jacob, D. W. Lee, and S. X. Wang, *J. Appl. Phys.* **105**, 07D311 (2009).
75. F. Morgenthaler, *IEEE Trans. Magn.* **8**, 550 (1972).
76. M. Bauer, C. Mathieu, S. O. Demokritov, B. Hillebrands, P. A. Kolodin, S. Sure, H. Dötsch, V. Grimalsky, Y. Rapoport, and A. N. Slavin, *Phys. Rev. B* **56**, R8483 (1997).
77. R. Khomeriki, *Eur. Phys. J. B* **41**, 219 (2004).
78. V. E. Demidov, S. O. Demokritov, K. Rott, P. Krzysteczko, and G. Reiss, *Phys. Rev. B* **77**, 064406 (2008).
79. J. Halavaara, P. Tervahartiala, H. Isoniemi, and K. Höckerstedt, *Acta radiologica (Stockholm, Sweden : 1987)* **43**, 180 (2002).
80. A. Mühler, X. Zhang, H. Wang, R. Lawaczeck, and H. J. Weinmann, *Invest. Radiol.* **30**, 98 (1995).
81. A. S. Lübbe, C. Alexiou, and C. Bergemann, *J. Surg. Res.* **95**, 200 (2001).
82. S. M. Mijailovich, M. Kojic, M. Zivkovic, B. Fabry, and J. J. Fredberg, *J. Appl. Physiol.* **93**, 1429 (2002).
83. R. K. Gilchrist, R. Medal, W. D. Shorey, R. C. Hanselman, J. C. Parrott, and C. B. Taylor, *Ann. Surg.* **146**, 596 (1957).
84. M. Babincová, D. Leszczynska, P. Sourivong, and P. Babinec, *Med. Hypotheses* **54**, 177 (2000).
85. C. Elachi, *IEEE Trans. Magn.* **11**, 36 (1975).
86. R. L. Stamps and R. E. Camley, *Phys. Rev. B* **60**, 12264 (1999).

87. J. Jorzick, S. O. Demokritov, B. Hillebrands, B. Bartenlian, C. Chappert, D. Decanini, F. Rousseaux, and E. Cambril, *Appl. Phys. Lett.* **75**, 3859 (1999).
88. S. Jung, B. Watkins, L. DeLong, J. B. Ketterson, and V. Chandrasekhar, *Phys. Rev. B* **66**, 132401 (2002).
89. A. Barman, V. V. Kruglyak, R. J. Hicken, J. Scott, A. Kundrotaite, and M. Rahman, *J. Appl. Phys.* **95**, 6998 (2004).
90. V. V. Kruglyak, A. Barman, R. J. Hicken, J. R. Childress, and J. A. Katine, *Phys. Rev. B* **71**, 220409(R) (2005).
91. L. Giovannini, F. Montoncello, and F. Nizzoli, *Phys. Rev. B* **75**, 024416 (2007).
92. G. Gubbiotti, S. Tacchi, G. Carlotti, N. Singh, S. Goolaup, A. O. Adeyeye, and M. Kostylev, *Appl. Phys. Lett.* **90**, 092503 (2007).
93. A. Barman and S. Barman, *Phys. Rev. B* **79**, 144415 (2009).
94. J. M. Shaw, T. J. Silva, M. L. Schneider, and R. D. McMichael, *Phys. Rev. B* **79**, 184404 (2009).
95. S. Tacchi, M. Madami, G. Gubbiotti, G. Carlotti, H. Tanigawa, T. Ono, and M. P. Kostylev, *Phys. Rev. B* **82**, 024401 (2010).
96. C. H. Back, R. Allenspach, W. Weber, S. S. P. Parkin, D. Weller, E. L. Garwin, and H. C. Siegmann, *Science* **285**, 864 (1999).
97. T. Gerrits, H. A. M. van den Berg, J. Hohlfeld, L. Bar, and T. Rasing, *Nature* **418**, 509 (2002).
98. H. W. Schumacher, C. Chappert, R. C. Sousa, P. P. Freitas, and J. Miltat, *Phys. Rev. Lett.* **90**, 017204 (2003).
99. A. Barman, S. Wang, J. D. Maas, A. R. Hawkins, S. Kwon, A. Liddle, J. Bokor, and H. Schmidt, *Nano Lett.* **6**, 2939 (2006).
100. A. O. Adeyeye and N. Singh, *J. Phys. D: Appl. Phys.* **41**, 153001 (2008).
101. L. Thevenard, H. T. Zeng, D. Petit, and R. P. Cowburn, *J. Appl. Phys.* **106**, 063902 (2009).
102. E. Sirotkin and F. Y. Ogrin, *IEEE Trans. Magn.* **46**, 1840 (2010).
103. V. V. Kruglyak, P. S. Keatley, R. J. Hicken, J. R. Childress, and J. A. Katine, *Phys. Rev. B* **75**, 024407 (2007).
104. R. Skomski, J. P. Liu, and D. J. Sellmyer, *Phys. Rev. B* **60**, 7359 (1999).
105. M. Kläui, J. Rothman, L. Lopez-Diaz, C. A. F. Vaz, J. A. C. Bland, and Z. Cui, *Appl. Phys. Lett.* **78**, 3268 (2001).

106. S. P. Li, D. Peyrade, M. Natali, A. Lebib, Y. Chen, U. Ebels, L. D. Buda, and K. Ounadjela, *Phys. Rev. Lett.* **86**, 1102 (2001).
107. R. Skomski, *J. Phys.: Condens. Matter* **15**, R841 (2003).
108. B. Rana, M. Agrawal, S. Pal, and A. Barman, *J. Appl. Phys.* **107**, 09B513 (2010).
109. S. Pal, S. Saha, D. Polley, and A. Barman, *Solid State Commun.* **151**, 1994 (2011).
110. E. H. Frei, S. Shtrikman, and D. Treves, *Phys. Rev.* **106**, 446 (1957).
111. I. S. Jacobs and C. P. Bean, *Phys. Rev.* **100**, 1060 (1955).
112. S. Goolaup, N. Singh, A. O. Adeyeye, V. Ng, and M. B. A. Jalil, *Eur. Phys. J. B* **44**, 259 (2005).
113. L. J. Heyderman, H. H. Solak, C. David, D. Atkinson, R. P. Cowburn, and F. Nolting, *Appl. Phys. Lett.* **85**, 4989 (2004).
114. R. Skomski, *J. Appl. Phys.* **91**, 7053 (2002).
115. P. H. Bryant, J. F. Smyth, S. Schultz, and D. R. Fredkin, *Phys. Rev. B* **47**, 11255 (1993).
116. J. Jorzick, S. O. Demokritov, B. Hillebrands, M. Bailleul, C. Fermon, K. Y. Guslienko, A. N. Slavin, D. V. Berkov, and N. L. Gorn, *Phys. Rev. Lett.* **88**, 047204 (2002).
117. J. P. Park, P. Eames, D. M. Engebretson, J. Berezovsky, and P. A. Crowell, *Phys. Rev. Lett.* **89**, 277201 (2002).
118. G. Gubbiotti, M. Conti, G. Carlotti, P. Candeloro, E. D. Fabrizio, K. Y. Guslienko, A. Andre, C. Bayer, and A. N. Slavin, *J. Phys.: Condens. Matter* **16**, 7709 (2004).
119. V. V. Kruglyak, A. Barman, R. J. Hicken, J. R. Childress, and J. A. Katine, *J. Appl. Phys.* **97**, 10A706 (2005).
120. M. Bailleul, R. Höllinger, and C. Fermon, *Phys. Rev. B* **73**, 104424 (2006).
121. G. Gubbiotti, M. Madami, S. Tacchi, G. Carlotti, and T. Okuno, *J. Appl. Phys.* **99**, 08C701 (2006).
122. R. P. Cowburn, D. K. Koltsov, A. O. Adeyeye, M. E. Welland, and D. M. Tricker, *Phys. Rev. Lett.* **83**, 1042 (1999).
123. T. Shinjo, T. Okuno, R. Hassdorf, K. Shigeto, and T. Ono, *Science* **289**, 930 (2000).
124. A. L. Rogach, D. V. Talapin, E. V. Shevchenko, A. Kornowski, M. Haase, and H. Weller, *Adv. Funct. Mater.* **12**, 653 (2002).
125. J. Park, J. Joo, S. G. Kwon, Y. Jang, and T. Hyeon, *Angew. Chem. Int. Ed.* **46**, 4630 (2007).
126. J. Aizenberg, J. A. Rogers, K. E. Paul, and G. M. Whitesides, *Appl. Phys. Lett.* **71**, 3773 (1997).

127. P. B. Fischer and S. Y. Chou, *Appl. Phys. Lett.* **62**, 2989 (1993).
128. N. Singh, S. Goolaup, and A. O. Adeyeye, *Nanotechnology* **15**, 1539 (2004).
129. F. Rousseaux, D. Decanini, F. Carcenac, E. Cambril, M. F. Ravet, C. Chappert, N. Bardou, B. Bartenlian, and P. Veillet, *J. Vac. Sci. Technol. B* **13**, 2787 (1995).
130. E. F. Wassermann, M. Thielen, S. Kirsch, A. Pollmann, H. Weinforth, and A. Carl, *J. Appl. Phys.* **83**, 1753 (1998).
131. J. Moritz, S. Landis, J. C. Toussaint, R. Bayle-Guillemaud, B. Rodmacq, G. Casali, A. Lebib, Y. Chen, J. P. Nozires, and B. Dieny, *IEEE Trans. Magn.* **38**, 1731 (2002).
132. R. Mandal, S. Saha, D. Kumar, S. Barman, S. Pal, K. Das, A. K. Raychaudhuri, Y. Fukuma, Y. Otani, and A. Barman, *ACS Nano* **6**, 3397 (2012).
133. K. Bessho, Y. Iwasaki, and S. Hashimoto, *J. Appl. Phys.* **79**, 5057 (1996).
134. A. Dallmeyer, C. Carbone, W. Eberhardt, C. Pampuch, O. Rader, W. Gudat, P. Gambardella, and K. Kern, *Phys. Rev. B* **61**, R5133 (2000).
135. F. Marty, A. Vaterlaus, V. Weich, C. Stamm, U. Maier, and D. Pescia, *J. Appl. Phys.* **85**, 6166 (1999).
136. T. Devolder, C. Chappert, Y. Chen, E. Cambril, H. Bernas, J. P. Jamet, and J. Ferre, *Appl. Phys. Lett.* **74**, 3383 (1999).
137. H. Takeshita, Y. Suzuki, H. Akinaga, W. Mizutani, K. Tanaka, T. Katayama, and A. Itoh, *Appl. Phys. Lett.* **68**, 3040 (1996).
138. K. L. Lee, R. R. Thomas, A. Viehbeck, and E. J. M. O'Sullivan, *J. Vac. Sci. Technol. B* **11**, 2204 (1993).
139. Y. Kamata, A. Kikitsu, H. Hieda, M. Sakurai, and K. Naito, *J. Appl. Phys.* **95**, 6705 (2004).
140. H. Masuda, H. Yamada, M. Satoh, H. Asoh, M. Nakao, and T. Tamamura, *Appl. Phys. Lett.* **71**, 2770 (1997).
141. W. D. Williams and N. Giordano, *Phys. Rev. B* **33**, 8146 (1986).
142. Y. Martin and H. K. Wickramasinghe, *Appl. Phys. Lett.* **50**, 1455 (1987).
143. L. Folks, M. E. Best, P. M. Rice, B. D. Terris, D. Weller, and J. N. Chapman, *Appl. Phys. Lett.* **76**, 909 (2000).
144. J. N. Chapman, *J. Phys. D: Appl. Phys.* **17**, 623 (1984).
145. M. S. Cohen, *J. Appl. Phys.* **38**, 4966 (1967).
146. B. E. Argyle and J. G. McCord, *J. Appl. Phys.* **87**, 6487 (2000).
147. J. Stohr, Y. Wu, B. D. Hermsmeier, M. G. Samant, G. R. Harp, S. Koranda, D. Dunham, and B. P. Tonner, *Science* **259**, 658 (1993).

148. H. Pinkvos, H. Poppa, E. Bauer, and J. Hurst, *Ultramicroscopy* **47**, 339 (1992).
149. K. Koike and K. Hayakawa, *Jpn. J. Appl. Phys.* **23**, L187 (1984).
150. M. Johnson and J. Clarke, *J. Appl. Phys.* **67**, 6141 (1990).
151. W. H. Rippard and R. A. Buhrman, *Appl. Phys. Lett.* **75**, 1001 (1999).
152. G. N. Kakazei, Y. G. Pogorelov, M. D. Costa, T. Mewes, P. E. Wigen, P. C. Hammel, V. O. Golub, T. Okuno, and V. Novosad, *Phys. Rev. B* **74**, 060406(R) (2006).
153. V. P. Denysenkov and A. M. Grishin, *Rev. Sci. Instrum.* **74**, 3400 (2003).
154. S. Tamaru, J. A. Bain, R. J. M. van de Veerdonk, T. M. Crawford, M. Covington, and M. H. Kryder, *J. Appl. Phys.* **91**, 8034 (2002).
155. T. J. Silva, C. S. Lee, T. M. Crawford, and C. T. Rogers, *J. Appl. Phys.* **85**, 7849 (1999).
156. S. O. Demokritov, B. Hillebrands, and A. N. Slavin, *Phys. Rep.* **348**, 441 (2001).
157. I. N. Krivorotov, N. C. Emley, J. C. Sankey, S. I. Kiselev, D. C. Ralph, and R. A. Buhrman, *Science* **307**, 228 (2005).
158. Y. Acremann, J. P. Strachan, V. Chembrolu, S. D. Andrews, T. Tyliczszak, J. A. Katine, M. J. Carey, B. M. Clemens, H. C. Siegmann, and J. Stöhr, *Phys. Rev. Lett.* **96**, 217202 (2006).
159. W. K. Hiebert, A. Stankiewicz, and M. R. Freeman, *Phys. Rev. Lett.* **79**, 1134 (1997).
160. Y. Acremann, C. H. Back, M. Buess, O. Portmann, A. Vaterlaus, D. Pescia, and H. Melchior, *Science* **290**, 492 (2000).
161. A. Barman, V. V. Kruglyak, R. J. Hicken, A. Kundrotaite, and M. Rahman, *Appl. Phys. Lett.* **82**, 3065 (2003).

## CHAPTER 2

---

# Theoretical Background

---

### 2.1 Magnetism

In this section, we will discuss about the basic theory of magnetism. There are mainly three different sources of magnetic moment of a free atom. Out of them change in orbital moment induced by external magnetic field is responsible for diamagnetism, whereas spin and orbital angular momentum are responsible for other types of magnetism including paramagnetism, ferromagnetism, antiferromagnetism and ferrimagnetism. Ferromagnetism arises from the exchange interaction among the atomic magnetic moments. To explain the origin of all the magnetic phenomena, a quantum mechanical treatment is required. Though some of the magnetic effects can be described with semi-classical models, in which magnetic moments are viewed as originated from circulating electric charges, but ordered permanent magnetic moments do not have any classical analogue.

#### 2.1.1 Classical Theory of Diamagnetism: Langevin's Theory

From classical point of view, when an electron moves around an atom in a closed orbit, a magnetic moment ( $\boldsymbol{\mu}$ ) is generated, which is given as [1]

$$\boldsymbol{\mu} = -\frac{e}{2mc}\mathbf{I}, \quad (2.1.1)$$

where  $\mathbf{I}$  is the angular momentum.

In presence of a magnetic field ( $\mathbf{H}$ ) a torque will be produced on  $\boldsymbol{\mu}$ , which is given by

$$\frac{d\mathbf{I}}{dt} = \boldsymbol{\mu} \times \mathbf{H} = -\frac{e}{2mc}(\mathbf{I} \times \mathbf{H}). \quad (2.1.2)$$

The above equation signifies that  $\mathbf{I}$  will be precessing around  $\mathbf{H}$  at Larmor Frequency ( $\omega_L$ ), given by

$$\omega_L = eH/2mc. \quad (2.1.3)$$

This induces a magnetic moment ( $\mu$ ) given by

$$\mu_i = -\left(\frac{e^2}{6mc^2}\right)\mathbf{H}\overline{r^2}, \quad (2.1.4)$$

where  $\overline{r^2}$  is the mean square distance of electrons from nucleus. If an atom contains  $z$  electrons, then the susceptibility per unit volume can be written as [2]

$$\chi = -\frac{Ne^2}{6mc^2} \sum_{i=1}^z \overline{r_i^2}, \quad (2.1.5)$$

where  $N$  is the number of atoms per unit volume. Diamagnetic susceptibility is always negative and a temperature independent property of all material. The order of magnitude of  $\chi$  is  $10^{-6}$  cm<sup>3</sup>/mol.

## 2.1.2 Quantum Theory of Paramagnetism

A paramagnetic material contains permanent magnetic moments ( $\mu$ ). According to quantum mechanics, a magnetic moment  $\mu$  of total angular momentum  $\mathbf{J}$  (where  $\mu = g\mu_B\mathbf{J}$ ) can have  $J(J + 1)$  different values along the direction of  $\mathbf{B}$ . The component of magnetic moment along the direction of  $\mathbf{B}$  can be written as [2]

$$\mu = m_J g \mu_B, \quad (2.1.6)$$

where  $g$  is the Landé g-factor,  $\mu_B$  is the Bohr magneton and  $m_J$  is the azimuthal quantum number and has values  $J, J - 1, \dots, -J$ .

The energy of this system in the magnetic field will be

$$E = -\mu \cdot \mathbf{B} = -m_J g \mu_B B. \quad (2.1.7)$$

At room temperature (where  $m_J g \mu_B JH/kT \ll 1$ ), the magnetization of the system which is determined by Boltzmann distribution can be written as [2]

$$M = \frac{Ng^2 J(J+1)\mu_B^2 H}{3kT}. \quad (2.1.8)$$

Therefore, paramagnetic susceptibility will be

$$\chi_p = M/H = \frac{Ng^2 J(J+1)\mu_B^2}{3kT} = \frac{N\mu^2}{3kT} = \frac{C}{T}. \quad (2.1.9)$$

This is the Curie's law for paramagnetism, where  $C = \frac{Ng^2 J(J+1)\mu_B^2}{3k}$ .

Paramagnetic susceptibility is inversely proportional to temperature and independent of bias magnetic field. For a magnetic moment of one Bohr magneton ( $\mu_B$ ),  $\chi \approx 1/30T$ . At room temperature ( $T = 300$  K),  $\chi \approx 10^{-4}$  cm<sup>3</sup>/mol [2].

### 2.1.3 Ferromagnetism and Exchange Interaction

The spontaneous magnetization in ferromagnetic material implies that there is a strong interaction among the permanent atomic dipoles. According to Weiss, the average molecular field acting on a dipole can be written as [1]

$$\mathbf{H}_m = \mathbf{H} + \gamma\mathbf{M}, \quad (2.1.10)$$

where  $\mathbf{H}$  is the applied field,  $\mathbf{M}$  is the magnetization and  $\gamma$  is the Weiss constant. The paramagnetic susceptibility given by Curie's law is  $\chi_p = C/T$  [3]. Substituting it in Eq. 2.1.10 we find

$$\chi_p = \frac{M}{H_m} = \frac{M}{H + \gamma M} = C/T.$$

This gives,

$$\chi_f = \frac{C}{(T - C\gamma)} = \frac{C}{(T - T_c)}. \quad (2.1.11)$$

Equation 2.1.11 is called Curie-Weiss law, where  $T_c$  is Curie temperature. Below Curie temperature ( $T_c$ ), ferromagnetic materials show spontaneous magnetization.

Though Weiss was correct, but he did not give any explanation for the source of this molecular field. Heisenberg's explained that this molecular field comes from quantum

mechanical exchange interaction. Heisenberg theory is based on Heitler-London model for hydrogen molecule. According to this theory, the wavefunction of two electrons can be written as  $\psi(r_1, s_1)$  and  $\psi(r_2, s_2)$ , where  $r_i$  is the spatial coordinate and  $s_i$  is the spin coordinate. When two electrons are brought closer, their wavefunctions overlap and the combined wavefunction can be written in antisymmetric or symmetric form. However, Pauli exclusion principle imposes a restriction on the wavefunction, that it must be antisymmetric. Now, the electron wavefunction can be written as

$$\psi = \phi(r)\chi, \quad (2.1.12)$$

where  $\phi(r)$  is a function of spatial coordinate and  $\chi$  is a function of spin coordinate only. Therefore, the antisymmetric wavefunctions can be written in the following two ways [2, 4]:

$$\psi_{anti} = \phi_{sym}(r_1, r_2)\chi_{anti}(s_1, s_2) \quad (2.1.13)$$

$$\text{or } \psi_{anti} = \phi_{anti}(r_1, r_2)\chi_{sym}(s_1, s_2). \quad (2.1.14)$$

More explicitly one can write Eq. 2.1.12 in the following two forms:

$$\psi_S = A[\phi_a(r_1)\phi_b(r_2) + \phi_a(r_2)\phi_b(r_1)][\chi_\alpha(s_1)\chi_\beta(s_2) - \chi_\alpha(s_2)\chi_\beta(s_1)] \quad (2.1.15)$$

$$\psi_T = B[\phi_a(r_1)\phi_b(r_2) - \phi_a(r_2)\phi_b(r_1)] \begin{bmatrix} \chi_\alpha(s_1) & \chi_\alpha(s_2) \\ \chi_\alpha(s_1)\chi_\beta(s_2) + \chi_\alpha(s_2)\chi_\beta(s_1) \\ \chi_\beta(s_1) & \chi_\beta(s_2) \end{bmatrix}. \quad (2.1.16)$$

Here,  $\psi_S$  and  $\psi_T$  refer to singlet and triplet states, respectively. In singlet state the spins are antiparallel and total spin quantum number  $S = 0$ , whereas for triplet state total spin quantum number  $S = 1$  and therefore there are  $(2S + 1)$  degenerate states.

The Hamiltonian  $H_{12}$  for the hydrogen molecule with two nuclei  $a$  and  $b$  can be written as

$$H_{12} = \frac{e^2}{r_{ab}} + \frac{e^2}{r_{12}} - \frac{e^2}{r_{1b}} - \frac{e^2}{r_{2a}}, \quad (2.1.17)$$

where  $r_{ab}$ ,  $r_{12}$ ,  $r_{1b}$ ,  $r_{2a}$  are separation between two nuclei, separation between electrons and separation between nuclei and electrons. The energies for singlet and triplet states are

$$E_S = A^2(K_{12} + J_{12}) \quad (2.1.18)$$

$$\text{and } E_T = B^2(K_{12} - J_{12}), \quad (2.1.19)$$

where  $K_{12}$  is the average Coulomb interaction energy and  $J_{12}$  is the exchange integral. They can be expressed by the following two integrals:

$$K_{12} = \int \phi_a^*(r_1)\phi_b^*(r_2)H_{12}\phi_a(r_1)\phi_b(r_2)d\tau_1d\tau_2 \quad (2.1.20)$$

$$\text{and } J_{12} = \int \phi_a^*(r_1)\phi_b^*(r_2)H_{12}\phi_a(r_2)\phi_b(r_1)d\tau_1d\tau_2. \quad (2.1.21)$$

For parallel alignment of spins,  $J_{12}$  must be positive. It can be shown by qualitative analysis that the exchange integral is positive when the interatomic spacing  $r_{ab}$  is large compared to the radii of the orbitals. This condition is fulfilled for  $d$  and  $f$  wavefunctions for some iron group elements and rare earth metals. In the above description, the direct interaction between two overlapping wavefunctions has been considered. This is known as direct exchange. But direct exchange may not always be a significant mechanism in ferromagnetic materials. In rare earth ferromagnets, the  $4f$  electrons are strongly localized and are not involved in bonding. In these cases some form of indirect exchange must exist. In some antiferromagnetic oxides (for nanoparticles, nanodots a metal oxide layer is always formed), the antiferromagnetic coupling between metal ions (like Ni, Fe, Co) is mediated by the oxygen ion in a process known as superexchange. In metals, the exchange interaction can also be carried by the conduction electrons (RKKY interaction).

#### 2.1.4 Antiferromagnetism and Ferrimagnetism

In antiferromagnetic material, the exchange integral  $J_{12}$  is negative. Hence neighboring spins are antiparallel, which gives rise to zero or negligible magnetization (Fig. 2.1). With the increment of the temperature, the susceptibility increases and the ferromagnetic order disappears above a certain temperature, known as Néel temperature. Above Néel temperature, the change in susceptibility with temperature becomes similar to paramagnet.

Ferrimagnets consist of two sublattices, in which the magnetic moments are different. This can happen when sublattices are made of two different materials or two different ions of same material. In ferrimagnetic material, the antiferromagnetic coupling between two sublattices causes partial cancellation of magnetic moment (Fig. 2.1). This leads to a total

magnetization equals to the difference in magnetization of two sublattices at low temperature [3].

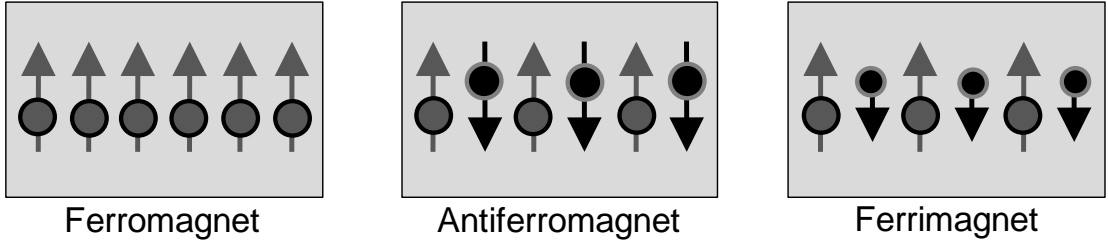


Fig. 2.1: Spin orientations in ferromagnet, antiferromagnet and ferrimagnet.

## 2.2 Magnetic Energies

The total free energy of a ferromagnetic material in presence of an external magnetic field can be written as sum of different free energies.

$$E_{total} = E_Z + E_d + E_e + E_K, \quad (2.2.1)$$

where  $E_Z$  is interaction energy of the magnetization with the external magnetic field. It is also called Zeeman energy.  $E_d$  is the magnetostatic self-energy of ferromagnetic material,  $E_e$  is the exchange energy and  $E_K$  is magnetocrystalline anisotropy energy.

### 2.2.1 Zeeman Energy

In presence of external magnetic field  $\mathbf{H}$ , the Zeeman energy can be written in the following form

$$E_Z = -\int \mathbf{M} \cdot \mathbf{H} \, dv, \quad (2.2.2)$$

where  $\mathbf{M}$  is the magnetization. Zeeman energy becomes minimum when the magnetization is aligned parallel to the applied magnetic field.

### 2.2.2 Magnetostatic Self-energy

When a ferromagnetic material is magnetized, then the classical dipolar or magnetostatic interaction among the magnetic dipoles is observed. The corresponding energy is called the magnetostatic self-energy. This is also known as the demagnetizing energy or shape anisotropy energy. Gauss's law of magnetostatics gives

$$\begin{aligned}
& \nabla \cdot \mathbf{B} = 0 \\
& \Rightarrow \nabla \cdot (\mathbf{H} + 4\pi\mathbf{M}) = 0 \\
& \Rightarrow \nabla \cdot \mathbf{H} = -4\pi(\nabla \cdot \mathbf{M})
\end{aligned} \tag{2.2.3}$$

Thus the stray magnetic field can be expressed as the divergence of magnetization. The demagnetizing energy is expressed as

$$E_d = -\frac{1}{2} \int \mathbf{M} \cdot \mathbf{H}_d d^3r . \tag{2.2.4}$$

The stray field ( $\mathbf{H}_d$ ) can be expressed as

$$\mathbf{H}_d = -\mathbf{N} \cdot \mathbf{M} , \tag{2.2.5}$$

where  $\mathbf{N}$  is the demagnetizing tensor. For uniform magnetization,  $\mathbf{N}$  becomes diagonal and it can be expressed as a constant. In that case the demagnetizing energy can be simplified as

$$E_d = \frac{1}{2} \int N M^2 d^3r . \tag{2.2.6}$$

The stray field energy can also be determined from the volume ( $\rho_v$ ) and surface ( $\sigma_s$ ) charge densities, which are given by

$$\begin{aligned}
& \rho_v = -\nabla \cdot \mathbf{M} \\
& \text{and } \sigma_s = \mathbf{M} \cdot \mathbf{n} ,
\end{aligned} \tag{2.2.7}$$

where  $\mathbf{n}$  is the normal direction to the surface. The potential energy associated with the stray field is given by [5]

$$U_d(\mathbf{r}) = \frac{M_s}{4\pi} \left( \int_v \frac{\rho_v(\mathbf{r}')}{|\mathbf{r} - \mathbf{r}'|} d^3\mathbf{r}' + \int_s \frac{\sigma_s(\mathbf{r}')}{|\mathbf{r} - \mathbf{r}'|} d^2\mathbf{r}' \right) . \tag{2.2.8}$$

The stray field or demagnetizing field can be determined by

$$\mathbf{H}_d(\mathbf{r}) = -\nabla U_d(\mathbf{r}) . \tag{2.2.9}$$

With the help of volume charge and surface charge, the demagnetizing field can be written as [5]

$$\mathbf{H}_d(\mathbf{r}) = \frac{1}{4\pi} \left( \int_V \frac{\rho_v(\mathbf{r}')(\mathbf{r}-\mathbf{r}')}{|\mathbf{r}-\mathbf{r}'|^3} d^3r' + \int_S \frac{\sigma_s(\mathbf{r}')(\mathbf{r}-\mathbf{r}')}{|\mathbf{r}-\mathbf{r}'|^3} d^2r' \right). \quad (2.2.10)$$

The demagnetizing energy becomes

$$E_d(\mathbf{r}) = \mu_0 M_s \left( \int_V \rho_v(\mathbf{r}) U_d(\mathbf{r}) d^3\mathbf{r} + \int_S \sigma_s(\mathbf{r}) U_d(\mathbf{r}) d^2\mathbf{r} \right). \quad (2.2.11)$$

### 2.2.3 Exchange Energy

Let us consider two atoms denoted by  $i$  and  $j$  and they have one electron each with spins  $s_i$  and  $s_j$ , respectively. The exchange Hamiltonian can be expressed in the following form [2]

$$\mathbf{H} = -2J_{ij} \mathbf{s}_i \cdot \mathbf{s}_j, \quad (2.2.12)$$

where  $J_{ij}$  is the exchange integral of two electrons. If we consider that both atoms have more than one electrons, then the exchange Hamiltonian can be expressed as

$$\mathbf{H} = -2J_{ij} \sum_{i,j}' \mathbf{s}_i \cdot \mathbf{s}_j. \quad (2.2.13)$$

Assuming all electrons have same exchange integral and omitting the exchange energy between the electrons in the same atom, one can write

$$\mathbf{H} = -2J_{ij} \sum_i \mathbf{s}_i \cdot \sum_j \mathbf{s}_j = -2J_{ij} \mathbf{S}_i \cdot \mathbf{S}_j, \quad (2.2.14)$$

where  $\mathbf{S}_i$  and  $\mathbf{S}_j$  are total spin of atom  $i$  and  $j$ , respectively. Considering nearest neighbour interaction only, the exchange Hamiltonian of an atom  $i$  with its neighbors can be written as

$$\mathbf{H} = -2 \sum_j J_{ij} \mathbf{S}_i \cdot \mathbf{S}_j. \quad (2.2.15)$$

If the exchange is isotropic and equal to a constant value  $J_e$ , then

$$\mathbf{H} = -2J_e \sum_j \mathbf{S}_i \cdot \mathbf{S}_j. \quad (2.2.16)$$

For a whole crystal, the exchange Hamiltonian or exchange energy will be

$$E_e = -2J_e \sum_{ij} \mathbf{S}_i \cdot \mathbf{S}_j . \quad (2.2.17)$$

The Hamiltonian mentioned above is called Heisenberg Hamiltonian.

Under a continuum model, the summation in Eq. 2.2.17 may be replaced by integration over the ferromagnetic sample.

$$E_e = A \int_V (\nabla \mathbf{m})^2 d^3 r , \quad (2.2.18)$$

where  $\mathbf{m}$  is a continuous vector quantity and  $A$  is called the exchange stiffness constant and defined as

$$A = \frac{2J_e S^2}{a} , \quad (2.2.19)$$

where  $a$  is the lattice constant. The values of  $A$  for Ni, Co, Fe and permalloy ( $\text{Ni}_{80}\text{Fe}_{20}$ ) are  $9 \times 10^{-12}$  J/m,  $30 \times 10^{-12}$  J/m,  $21 \times 10^{-12}$  J/m and  $13 \times 10^{-12}$  J/m, respectively.

## 2.2.4 Magnetocrystalline Anisotropy Energy

Though Heisenberg exchange energy is isotropic, magnetization of ferromagnetic materials tends to align along certain crystallographic axis. The crystallographic axes, along which the magnetization tends to align, are called easy axes and other axes, along which it is very difficult to saturate the magnetization are called hard axes. Magnetocrystalline anisotropy originates from spin-orbit coupling. The electronic orbits depend upon the crystallographic axes and the spin-orbit coupling forces the electronic spins to be aligned along certain crystallographic axes. Usually, anisotropy energy is expressed as a function of the power of trigonometric functions of angle made by magnetization with the easy axis.

For hexagonal close packed (*hcp*) crystal, the anisotropy energy is expressed as a function of the angle  $\theta$  made by the magnetization with *c*-axis. This kind of anisotropy is called uniaxial anisotropy. Uniaxial anisotropy is generally expressed as [2]

$$E_K = K_1 \sin^2 \theta + K_2 \sin^4 \theta , \quad (2.2.20)$$

where  $K_1$  and  $K_2$  are constants and functions of temperature. For most of the ferromagnetic materials,  $|K_1| \gg |K_2|$ . For most of the *hcp* crystals, the easy axis lies along the *c*-axis ( $K_1 >$

0). However, there are certain materials for which  $K_I < 0$  and easy axis lies perpendicular to the  $c$ -axis. Co has  $hcp$  structure and the easy axis is along the  $c$ -axis, whereas the hard axis is perpendicular to the  $c$ -axis [2].

For cubic anisotropy, the anisotropy energy can be expressed by direction cosines  $\alpha_1, \alpha_2$  and  $\alpha_3$  of the direction of magnetization with the cube edges [2]:

$$E_K = K'_1(\alpha_1^2\alpha_2^2 + \alpha_2^2\alpha_3^2 + \alpha_3^2\alpha_1^2) + K'_2\alpha_1^2\alpha_2^2\alpha_3^2. \quad (2.2.21)$$

Ni has  $fcc$  and Fe has  $bcc$  crystal structure. Therefore, both have cubic anisotropy [2]. For Ni, the easy axes are along body diagonals [111] and hard axes are along cube edges [110 and 100], whereas for Fe, cube edges [100 and 110] are easy axes and body diagonals are hard axes [111]. Permalloy has  $fcc$  crystal structure, therefore it also has cubic anisotropy. The values of magnetocrystalline anisotropy constants for Co, Ni and Fe are listed below (at  $T = 293$  K), whereas permalloy has negligible magnetocrystalline anisotropy [2].

**Table: 2.1**

Metal	Crystal Structure	Easy axis	Hard axis	$K_1$ or $K'_1$ (J/m <sup>3</sup> )	$K_2$ or $K'_2$ (J/m <sup>3</sup> )
Co	$hcp$	$C_{\parallel}$	$C_{\perp}$	$4.1 \times 10^5$	$1 \times 10^5$
Ni	$fcc$	[111]	[110], [100]	$-5.0 \times 10^3$	-
Fe	$bcc$	[100], [110]	[111]	$4.6 \times 10^4$	$1.5 \times 10^4$

## 2.3 Magnetic Domains

The exchange interaction between two nearest neighbour spins is roughly  $10^3$  times larger than the dipolar interaction between them. However, the exchange interaction is a short range interaction (decays exponentially with distance), whereas dipolar interaction is a long range interaction ( $\propto 1/r^3$ ). In larger samples, the competition between exchange and dipolar interactions may lead to formation of magnetic domains. Within a magnetic domain, the exchange interaction dominates and the spins are aligned parallel along a certain direction. However, for a ferromagnet with dimension greater than the dimension of a domain, the long

range dipolar interaction dominates over the exchange interaction. This leads to the formation of a number of domains separated by domain walls. Magnetic domains reduce the magnetostatic stray field energy associated with the uncompensated free charges on the surface of ferromagnets.

In general the ferromagnetic materials consist of several domains. But under certain conditions they can be single domain also. If a ferromagnet is saturated by applying a large enough magnetic field, the material becomes single domain. If the dimension of the material is small enough, the short range exchange interaction dominates over the demagnetizing field even in the absence of an external magnetic field. Then also the element can be in a single domain state.

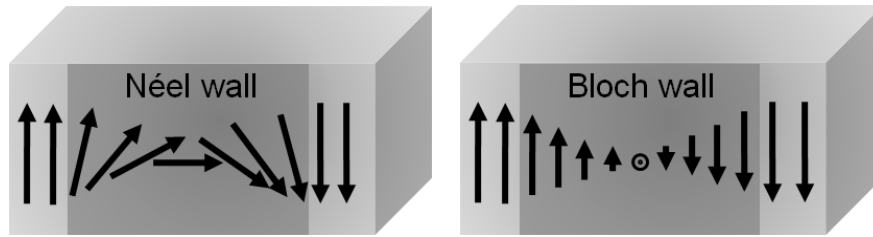


Fig. 2.2: Structures of Néel and Bloch walls are shown between two domains.

The domains are separated by domain walls where the direction of magnetic moment changes gradually to minimize the total energy associated with the domain wall. The calculated thickness of domain wall from a simple model can be expressed as [4]

$$\delta = \sqrt{\frac{J_e \pi^2 S^2}{Ka}}, \quad (2.3.1)$$

where  $J_e$  is the exchange integral,  $K$  is the anisotropy constant and  $a$  is lattice constant. A variety of domain walls are observed in magnetic materials, out of which Bloch wall and Néel wall are very common. When the magnetization from one domain to its neighbouring domain rotates along the axis that is perpendicular to the plane of the wall, it is called Bloch wall (Fig. 2.2). For Néel wall, the rotation axis is parallel to the plane of the wall (Fig. 2.2). The typical domain wall width for Co, Ni and permalloy are about 10 nm, 60 nm and 57 nm [6-7].

## 2.4 Stoner-Wohlfarth Model

This model is named after Stoner and Wohlfarth, who made pioneering theoretical study on the mechanism of magnetization reversal in single domain ferromagnetic particle [8]. In single domain ferromagnet, the exchange interaction holds all the spins parallel to each other. Therefore, the exchange energy is minimized in this case. The magnetic hysteresis loops and the reversal mechanism of single domain particles can be calculated by using Stoner-Wohlfarth model. In this model, the particles are assumed to be non-interacting. Let us consider a prolate ellipsoid with negligible magnetocrystalline and strain energy. The total energy is then composed of demagnetizing energy ( $E_d$ ) and Zeeman energy ( $E_Z$ ), and can be expressed as [2]

$$E = C - \frac{1}{4}(D_b - D_a)M^2V \cos 2\alpha - HMV \cos \phi, \quad (2.4.1)$$

where  $C$  is a constant,  $a$  and  $b$  are polar semiaxis and equatorial semiaxis of the ellipsoid.  $D_a$  and  $D_b$  are the demagnetizing factors along  $a$  and  $b$ . The angles  $\theta$ ,  $\alpha$  and  $\phi$  are shown in Fig. 2.3(a). In equilibrium,

$$\begin{aligned} \frac{\partial E}{\partial \phi} &= \frac{1}{2}(D_b - D_a)M^2 \sin 2\alpha + HM \sin \phi = 0 \\ \Rightarrow \frac{1}{2} \sin 2(\phi - \theta) + h \sin \phi &= 0, \end{aligned} \quad (2.4.2)$$

$$\text{where } h = \frac{H}{(D_b - D_a)M}.$$

For minimum energy condition,

$$\begin{aligned} \frac{\partial^2 E}{\partial^2 \phi} &= (D_b - D_a)M^2 \cos 2\alpha + HM \cos \phi > 0 \\ \Rightarrow \cos 2(\phi - \theta) + h \cos \phi &> 0 \end{aligned} \quad (2.4.3)$$

For a given value of  $h$  and  $\theta$ , Eq. 2.4.3 always has more than one solution. It is also possible to have more than one energy minima. For  $\theta = 0^\circ$ , Eqs. 2.4.2 and 2.4.3 become

$$\begin{aligned} (h + \cos \phi) \sin \phi &= 0 \\ \text{and } h \cos \phi + \cos 2\phi &> 0 \end{aligned} \quad (2.4.4)$$

For minimum condition,  $\sin \phi = 0$  and  $1 + h \cos \phi > 0$ .

The necessary condition is  $\phi = 0$  for  $h > -1$  and  $\phi = \pi$  for  $h < -1$ . Therefore, an unique solution is observed for  $|h| > 1$ , whereas in region  $|h| < 1$ , there are two valid energy minima for  $\phi = 0^\circ$  and  $\phi = 180^\circ$ . If the field is reduced to zero from a large enough positive value and then increased to opposite direction, the system stay in the branch of the solution  $\phi = 0^\circ$  till the field reaches to  $h = -1$ . Though for negative values of  $h$ , the minimum energy state is  $\phi = 0^\circ$ , the magnetization can not flip due to the presence of an energy barrier. For  $h = -1$ , the Zeeman energy becomes equal to the barrier energy and the system jumps from  $\phi = 0^\circ$  state to  $\phi = 180^\circ$  state. The reversal mechanism is shown in Fig. 2.3(b).

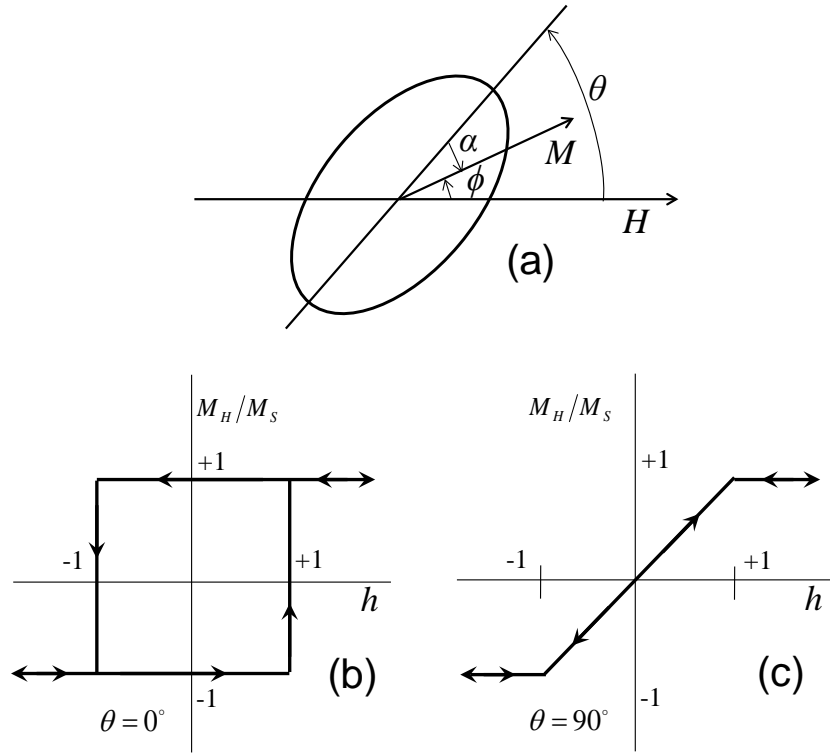


Fig. 2.3: (a) Schematic diagram of a prolate ellipsoidal particle with magnetization ( $\mathbf{M}$ ) in a magnetic field ( $\mathbf{H}$ ). The hysteresis loops of a prolate ellipsoidal particle for (b) applied field along easy axis ( $\theta = 0^\circ$ ) and (c) applied field along hard axis ( $\theta = 90^\circ$ ).

When the field is applied perpendicular to the easy axis, then

$$(h - \cos \phi) \sin \phi = 0$$

$$h \cos \phi - \cos 2\phi > 0 \quad (2.4.5)$$

The solution for minimum energy is  $\cos \phi = h$  and this will be valid only if  $|h| < 1$ . In this case, magnetization is proportional to the applied field. For  $|h| > 1$ , the second solution *i.e.*,  $\sin \phi = 0$  gives the energy minima, and the system is saturated as shown in Fig. 2.3(c).

For  $\theta = 0^\circ$ , the reversal mechanism is irreversible, whereas for  $\theta = 90^\circ$  the reversal mechanism is reversible. For other cases, the reversal is partly reversible and partly irreversible. We have just seen that a finite magnetic field ( $h$ ) is required to saturate the magnetization for  $\theta = 0^\circ$  and  $90^\circ$ . For other cases, an infinite field is required for saturation. This is because when  $\phi \rightarrow 0^\circ$ , the torque arises from the external field also approaches to zero for a finite value of  $H$ . If an opposing torque is present due to the finite shape anisotropy, the magnetization is aligned along  $H$  only when  $H$  approaches to infinity. Practically particles are arranged randomly. Therefore, the coercive field of individual particles also varies from  $h = 0$  to 1. Hence, the coercive field of powder sample becomes roughly around 0.5.

## 2.5 Magnetization Reversal Modes

Magnetocrystalline anisotropy, exchange stiffness constant ( $A$ ) and spontaneous magnetization of a ferromagnetic material are intrinsic properties and these effects originate from atomic structures. The extrinsic properties like remanence, coercive field and reversal mechanism are determined by the magnetic hysteresis loops. Hysteresis is basically the trace of average magnetization with the external applied field *i.e.*, Zeeman field. It is a very complex, non-equilibrium, nonlinear and non-local phenomenon, which is caused by rotation of magnetization [9]. The rotation of magnetization occurs in the mesoscopic length scale, which is better known as micromagnetism. Different kinds of magnetic energies like Zeeman energy, magnetostatic self-energy, exchange energy and magnetic anisotropy energy contribute to the rotation of magnetization. The micromagnetic free energy can be written as [9]

$$E = \int \left\{ A \left[ \nabla \left( \frac{\mathbf{M}}{M_s} \right) \right]^2 - K_1 \frac{(\mathbf{n} \cdot \mathbf{M})^2}{M_s^2} - \mu_0 \mathbf{M} \cdot \mathbf{H} - \frac{\mu_0}{2} \mathbf{M} \cdot \mathbf{H}_d(\mathbf{M}) \right\} dV, \quad (2.5.1)$$

where  $\mathbf{n}$  is the unit vector along local anisotropy direction,  $\mathbf{H}$  is the external field and  $\mathbf{H}_d$  is magnetostatic self-field. The most important parameter of hysteresis loop is the coercive field ( $H_C$ ). The phenomenological expression of coercive field is [10]

$$H_C = \alpha_K \frac{2K_1}{\mu_0 M_s} - D_{eff} M_s - \Delta H, \quad (2.5.2)$$

where  $\alpha_K$  is known as real-structure-dependent Kronmüller parameter,  $D_{eff}$  is related to magnetostatic interaction and  $\Delta H$  is a correction term, which depends upon temperature and the sweep rate of the external field. In a small single domain nanomagnet, the magnetization is uniform throughout the magnet and  $\nabla M$  is zero in Eq. 2.5.1. The magnetization reversal occurs through the coherent rotation as shown in Fig. 2.4. For an ellipsoid with symmetry axis parallel to the applied field, magnetostatic self-field in Eq. 2.5.1 can be written as [9]

$$H_d = (1-3D)M_s. \quad (2.5.3)$$

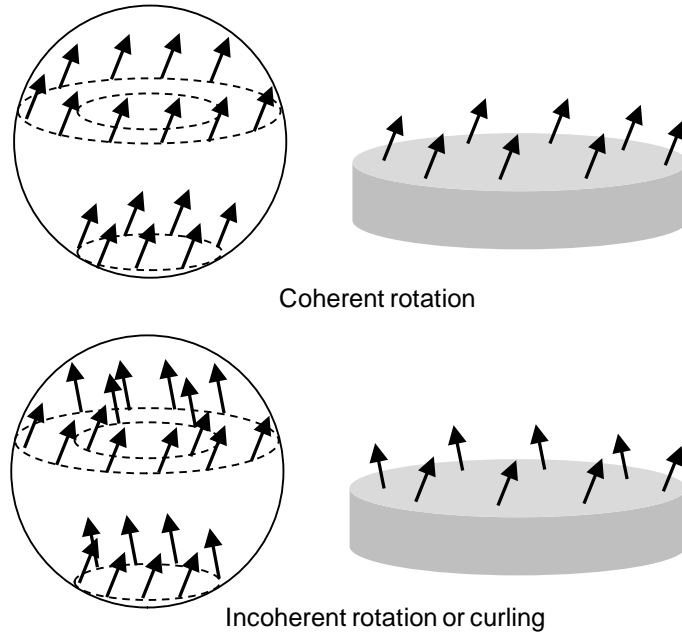


Fig. 2.4: Coherent rotation and incoherent rotation or curling-like rotation are schematically shown for a sphere and a disc.

Magnetostatic self-field is proportional to the magnetization and the factor  $D$  is called the demagnetizing factor. The Eq. 2.5.1 becomes [9]

$$\frac{E}{V} = K_1 \sin^2 \theta + \frac{\mu_0}{2} (1-3D) M_s^2 \sin^2 \theta - \mu_0 M_s H \cos \theta. \quad (2.5.4)$$

Subsequently, the coercive field can be expressed as [9]

$$H_C = \frac{2K_1}{\mu_0 M_s} + \frac{1}{2} (1-3D) M_s. \quad (2.5.5)$$

The Stoner–Wohlfarth model is valid only for very small particles, where the spins are exchange coupled and  $\nabla M \approx 0$ . This model can also be applicable for non-interacting small particles. In larger particles, the magnetization often becomes nonuniform and the coercive field is generally called as nucleation field ( $H_n$ ). In these cases the reversal occurs through incoherent and localized modes, which are irreversible processes.

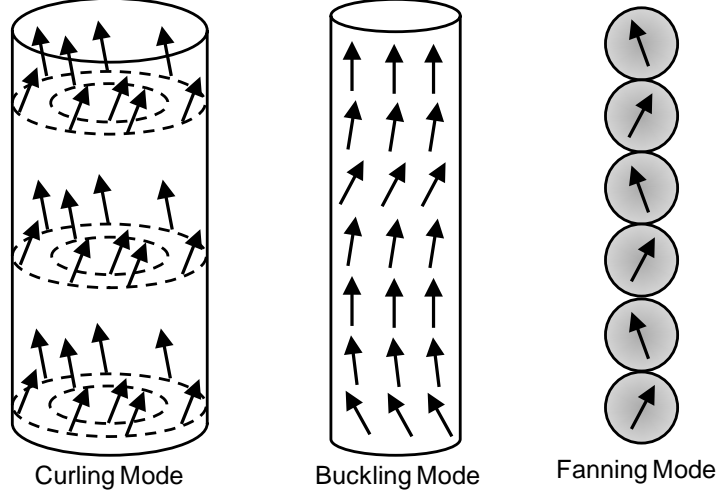


Fig. 2.5: Schematics of ‘curling’ and ‘buckling’ modes are shown for a cylinder. The ‘fanning’ mode is shown for chains of spherical nanoparticles.

The exchange length of a ferromagnetic material can be expressed as [9]

$$l_{ex} = \sqrt{\frac{A}{\mu_0 M_s^2}}. \quad (2.5.6)$$

The exchange length ( $l_{ex}$ ) is the length, below which atomic exchange interactions dominate over magnetostatic interactions. The calculated typical values of  $l_{ex}$  for Co, Ni and permalloy are 4.93 nm, 7.72 nm, 5.29 nm, respectively. A transition from coherent rotation to incoherent rotation is observed at a radius called the coherent radius of nanomagnet ( $R_{coh}$ ) [11]. Above the coherent radius the reversal is dominated by incoherent or localized modes or flux closure structure. The coherent radius depends upon the exchange length and the shape of the ferromagnet. For spheres,  $R_{coh} = 5.099l_{ex}$  [9] and for wires,  $R_{coh} = 3.655l_{ex}$  [11]. When  $R > R_{coh}$ , ‘curling’ mode is observed in sphere, disc (Fig. 2.4), ellipsoid (not shown) and also in infinite cylinder (Fig. 2.5). For cylinder with smaller diameter, ‘buckling’ mode is observed (Fig. 2.5) [12]. Magnetic nanoparticles often form chains and clusters to minimize magnetostatic self-energy. If a magnetic field is applied parallel to the axis of the chain then the reversal occurs through the ‘fanning’ mode as shown in Fig. 2.5 [13].

The magnetization reversal in magnetic nanowires is mediated through domain wall movement. There are basically two different fundamental reversal modes observed in magnetic nanowires depending upon their thickness [14-15]. They are called ‘transverse wall mode’ and the ‘vortex wall mode’. For a very thin wire, the magnetization becomes homogeneous along the radial cross-section of the wire. A head-to-head domain wall is formed during the reversal. The domain wall walks along the axis of the wire along with a characteristic spiral motion. This spiral motion of the wall is super-imposed with the propagation along the wire axis. This kind of reversal modes are called ‘corkscrew’ mode. As the diameter of nanomagnet increases, the magnetization becomes inhomogeneous along radial direction. The reversal of magnetization starts with the nucleation of a vortex state at the end of the wire. The vortex is then propagated along the wire axis. This mode is known as ‘vortex wall mode’ or ‘localized curling mode’ [15].

The reversal modes or the nucleation modes of soft nanomagnets embedded in a hard single crystalline magnetic material are very interesting. It can be of different types. The nucleation field in this case can be expressed as [9]

$$H_N = H_a \frac{3\delta_B^2 M_h}{L^2 M_S}, \quad (2.5.7)$$

where  $H_a$  is the anisotropy field of the hard magnet,  $M_S$  is the magnetization of the hard magnet and  $\delta_B$  is the Bloch wall width of the hard magnet. For a very small sphere, coherent rotation is observed when the soft magnet is isolated. However, when a soft magnet is placed inside a hard magnet, ‘clamped mode’ is observed where  $m(r) = 0$  at the hard–soft interface [16]. For smaller diameter of soft magnet, ‘bulging’ type nucleation mode is observed, whereas for larger diameter ‘clamped curling’ mode is observed.

## 2.6 Magnetization Dynamics

### 2.6.1 Landau-Lifshitz-Gilbert Equation

The dynamics of a spin can be described mathematically by an equation of motion. The equation of motion can be derived from quantum mechanics [5, 17]. The commutation of spin observable  $S$  with Hamiltonian operator ( $H$ ) gives the time evolution of  $S$ .

$$i\hbar \frac{d}{dt} \langle \mathbf{S} \rangle = [\mathbf{S}, \mathbf{H}] \quad (2.6.1)$$

The interaction of  $\mathbf{S}$  with the magnetic induction vector  $\mathbf{B}$  can be written as

$$\mathbf{H} = -\frac{g\mu_B}{\hbar} \mathbf{S} \cdot \mathbf{B}, \quad (2.6.2)$$

Using commutation rule for spin operators [5]

$$[S_i, S_j] = i\hbar \varepsilon_{ijk} S_k, \quad (2.6.3)$$

and using Eq. 2.6.2, we can write

$$[\mathbf{S}, \mathbf{H}] = ig\mu_B (\mathbf{S} \times \mathbf{B}). \quad (2.6.4)$$

Substituting (2.6.4) in (2.6.1) we can write

$$\frac{d}{dt} \langle \mathbf{S} \rangle = \frac{g\mu_B}{\hbar} (\mathbf{S} \times \mathbf{B}). \quad (2.6.5)$$

The above equation of motion is for a single spin. In the macrospin model, the magnetization  $\mathbf{M}$  is supposed to be uniform throughout the sample. The relation between  $\mathbf{S}$  and  $\mathbf{M}$  can be written as

$$\mathbf{M} = \frac{g\mu_B}{\hbar} \langle \mathbf{S} \rangle. \quad (2.6.6)$$

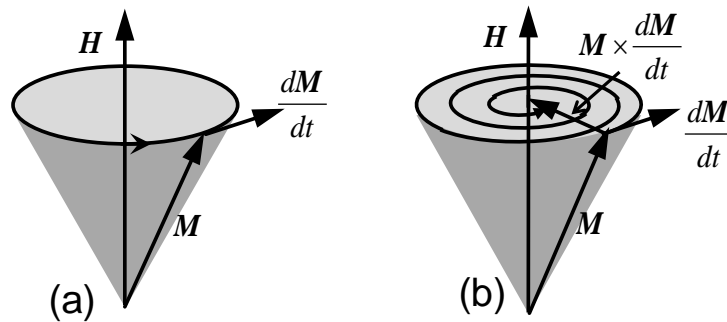


Fig. 2.6: Precession of magnetization vector ( $\mathbf{M}$ ) around magnetic field ( $\mathbf{H}$ ) (a) in absence of damping term and (b) in presence of a damping term.

Therefore, equation of motion of magnetization in presence of an external magnetic field will be

$$\frac{d\mathbf{M}}{dt} = -\frac{g\mu_B}{\hbar}(\mathbf{M} \times \mathbf{H})$$

or  $\frac{d\mathbf{M}}{dt} = -\gamma(\mathbf{M} \times \mathbf{H}).$  (2.6.7)

The above equation is called the Landau-Lifshitz equation (without damping), where  $\gamma = \frac{g\mu_B}{\hbar}$  is the gyromagnetic ratio.

The above equation can be generalized by replacing  $\mathbf{H}$  by  $\mathbf{H}_{eff}$ . This equation implies that the tip of the magnetization vector precesses around the effective magnetic field in a circular orbit as shown in Fig. 2.6(a) for infinitely long time with an angular frequency  $\omega = \gamma H_{eff}$ . Practically the precession amplitude of magnetization decreases with time and the tip of the magnetization vector follows a spiral path (Fig. 2.6(b)). Therefore, a damping or relaxation term ( $R$ ) should be added with the Landau-Lifshitz equation [18].

$$\frac{d\mathbf{M}}{dt} = -\gamma(\mathbf{M} \times \mathbf{H}_{eff}) + R(\mathbf{M}, \mathbf{H}_{eff})$$
 (2.6.8)

Landau-Lifshitz suggested [19]

$$R = -\frac{\lambda}{M_s^2} \mathbf{M} \times (\mathbf{M} \times \mathbf{H}_{eff}).$$
 (2.6.9)

Gilbert suggested [20-21]

$$R = \frac{\alpha}{M_s} \left( \mathbf{M} \times \frac{d\mathbf{M}}{dt} \right).$$
 (2.6.10)

With the above expression, the equation of motion of magnetization vector in presence of damping is expressed by the following equation:

$$\frac{d\mathbf{M}}{dt} = -\gamma(\mathbf{M} \times \mathbf{H}_{eff}) + \frac{\alpha}{M_s} \left( \mathbf{M} \times \frac{d\mathbf{M}}{dt} \right).$$
 (2.6.11)

The Eq. 2.6.11 is known as Landau-Lifshitz-Gilbert (LLG) equation. Here  $\alpha$  is the Gilbert damping parameter. The value of  $\alpha$  is much less than 1 for transition metals, which ensures that the magnetization precesses a number of times around the effective field before coming

to the equilibrium position. The values of  $\alpha$  for Ni, Fe, Co and permalloy are 0.064, 0.0019, 0.011 and 0.008, respectively [22-24].

## 2.6.2 Time Scales of Magnetization Dynamics

Magnetization dynamics can occur over a wide range of time scale. Figure 2.7 shows various kinds of magnetization dynamics with their characteristic time scales [25]. The time scales ( $\tau$ ) are determined by the interaction energies ( $E$ ) via Heisenberg relation  $\tau = h/E$ .

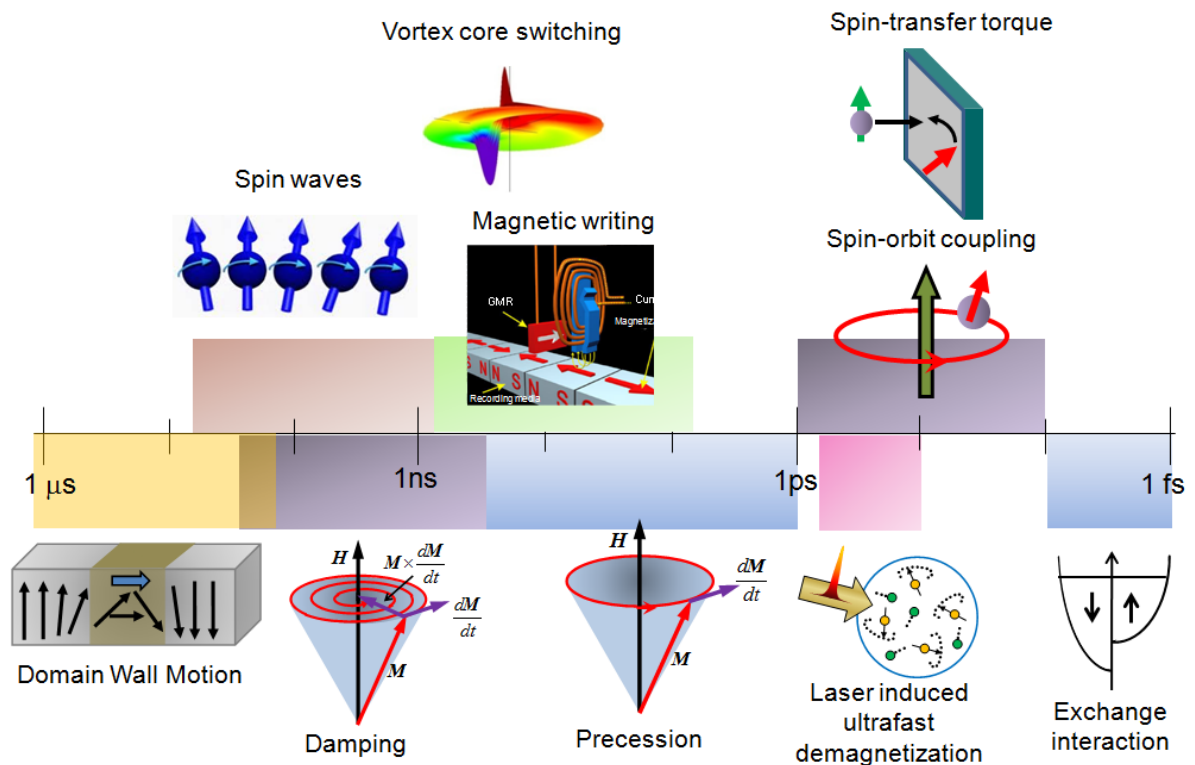


Fig. 2.7: Characteristic time scales of various kinds of magnetization dynamics.

The fastest process is the fundamental exchange interaction, which occurs within 10 fs. The spin-orbit coupling and spin transfer torque occurs in the time scale of 10 fs – 1 ps. Laser induced ultrafast demagnetization occurs within few hundreds of fs. The fast remagnetization time following the ultrafast demagnetization covers the time scale of 1-10 ps. The magnetic writing, which is done via reversal of spin has a time scale of few ps to few hundreds of ps, whereas vortex core switching occurs from few tens of ps to several ns time scale. The precession of magnetization occurs in few ps to few hundreds of ps whereas the Gilbert damping associated with magnetization precession occurs from sub-ns to tens of ns time scale. The spin waves in ferromagnetic material can propagate in a time scale of few

hundreds of ps to tens of ns before it dies out. The slowest process is the domain wall motion, which has the time scale from few ns to hundreds of  $\mu\text{s}$ .

### **2.6.3 Ultrafast Magnetization Dynamics Induced by Ultrashort Laser Pulses**

The researchers have been attracted to the question: what happens when an ultrashort laser pulse interacts with a ferromagnetic material. The breakthrough in this research topic occurred since the pioneering work by Beaurepaire *et al.* in 1996 [26]. They found that a Ni thin film can be demagnetized in a sub-picosecond time scale after the excitation with a sub-100 fs pulsed laser beam. A number of studies on all elementary ferromagnetic transition metals (Co, Ni, Fe) and several alloys thereof have confirmed the above result [27]. Then the question came how the magnetic moment of a system can be quenched so rapidly, while its total angular momentum is conserved? Before laser excitation, the angular momentum is mainly carried by the aligned electron spins. Thus, a transfer of angular momentum to another degree of freedom, such as electrons or lattice, is required to compensate the loss of magnetic order [28]. Below, we have described a sequence of phenomena observed when a ferromagnetic material interacted with ultrashort laser pulses (Fig. 2.8). We have discussed the underlying mechanism by considering the transfer of angular momentum among different degrees of freedom.

A number of processes occur when a femtosecond laser pulse interacts with an ordered ferromagnetic material. First of all, the photon field of the laser beam interacts with spin degrees of freedom of electrons. The angular momentum of light is modified nonlinearly within first 50 fs. The electronic distribution is not initially thermalized. The electrons are excited above the Fermi level because of electron–electron scattering [29]. The excited electrons are called ‘hot electrons’ [30]. In this time the electronic temperature may be increased up to  $10^3$  K [29]. Shortly after that the thermalization of spin population occurs as the ‘hot electrons’ excite the spins by electron-magnon interaction [31-32]. So, there is a difference between the thermalization times of charges ( $\tau_e$ ) and spins ( $\tau_s$ ). During the thermalization of charges and spins, the electronic wavefunction loses its phase memory (incoherent process) *w.r.t.* the excitation, which leads to the demagnetization of the ferromagnet. However, the underlying mechanism of demagnetization is a subject of intense debate.

Most of the scientists in magnetism community believe that during the excitation and thermalization of the electrons, Stoner pairs with a large kinetic energy are excited in ferromagnetic metals like Ni or Co [29]. Therefore, most of the published reports on the ultrafast demagnetization state that ultrafast spin-flip scatterings play important role for demagnetization. The first one is the Elliott-Yafet type of scattering, which says that an electron flips its spin due to the influence of impurity centers and phonons and emits or absorbs a phonon [28, 33]. Other kinds of scattering processes such as electron-magnon spin-flip scattering [34], Coulomb exchange spin-flip scattering [35] and relativistic electromagnetic radiation induced spin-flip scattering [36] have also claimed to be responsible for the ultrafast demagnetization. However, few reports also claim that other kinds of physical mechanisms like spin-orbit coupling [37], the coupling with the electromagnetic field via a terahertz emission [38] are responsible for ultrafast demagnetization. Moreover, some recent reports show that the superdiffusive spin transport rather than spin-flip plays the major role in magnetic processes on the femtosecond time scale [39-40].

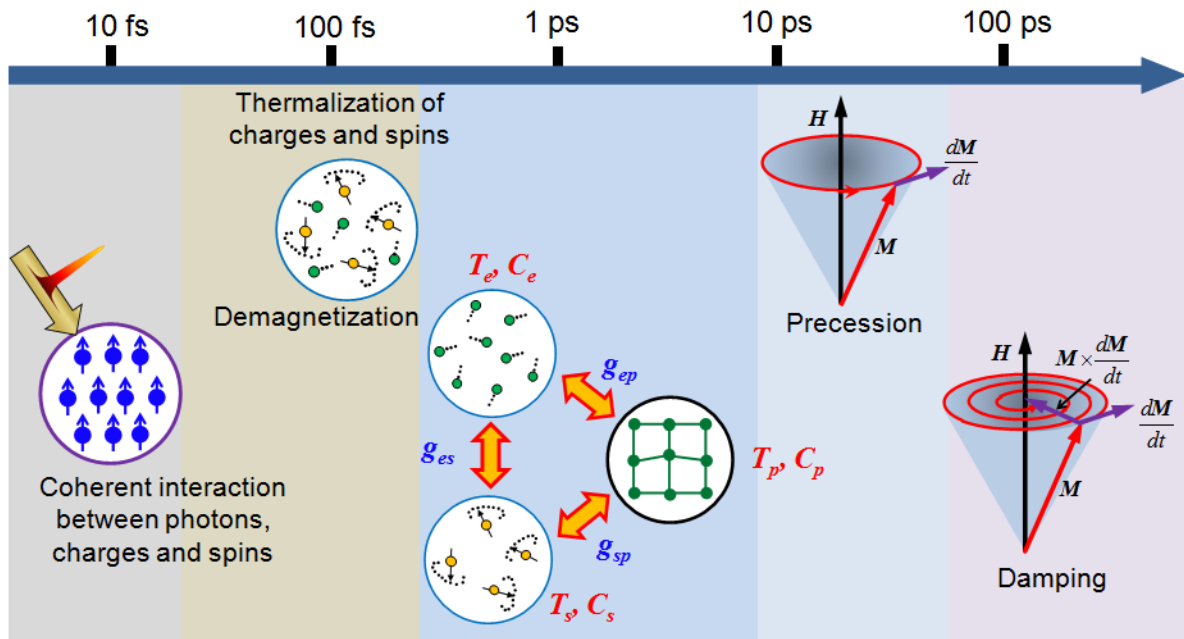


Fig. 2.8: A schematic diagram of the sequence of mechanisms in ultrafast magnetization dynamics.

After the demagnetization, the electronic charges and spins start to relax. This relaxation occurs in two different time scales (few ps and hundreds of ps). Therefore, the reflectivity (depends on the population of charges above Fermi level) and also magnetization of the system decays bi-exponentially. The faster relaxation time ( $\tau_l$ ) of the hot electrons and

spins occurs, because they exchange energy with the lattice and this is mediated by the electron–phonon interaction.  $\tau_l$  may vary from sub-ps to several ps depending on the electron–phonon coupling and also the specific heat of the electrons and phonons [29, 41-42]. The relaxation time also depends on the density of laser excitation [41-42] and magneto-crystalline anisotropy [29] to some extent. In this time scale, the thermodynamic quantities such as specific heat and temperature come into play. Therefore, one may talk about phenomenological three temperature model (3TM) [26, 43]. In 3TM, heat capacities and temperatures are assigned to the reservoirs of electron charge ( $e$ ), spin ( $s$ ) and lattice/phonon ( $p$ ) as  $(C_e; T_e)$ ,  $(C_s; T_s)$  and  $(C_p; T_p)$ , respectively. Furthermore, coupling constants between charge-spin, spin-lattice, charge-lattice are defined as  $g_{es}$ ,  $g_{sp}$  and  $g_{ep}$ . They describe the rate of energy exchange between the participating sub-systems. Thus, the overall dynamics is phenomenologically described by a set of three coupled differential equations. By exchanging heats, spins come to an equilibrium temperature with charge and lattice. Therefore, the lattice temperature changes. The magnetocrystalline anisotropy, which is a function of lattice temperature also changes rapidly. This rapid change in magnetocrystalline anisotropy acts as an internal pulse field and triggers the precession of magnetization. The second or longer relaxation time ( $\tau_2$ ) corresponds to the diffusion of electron and lattice heat to the surroundings (such as substrate) [41-42]. In this time scale, the precession of magnetization also starts to damp out. These mechanisms can be described by Landau-Lifshitz-Gilbert formalism.

## 2.6.4 Ferromagnetic Resonance

In section 2.6.1, we have seen that when a steady magnetic field is applied to a ferromagnetic material, the magnetization start to precess around the effective magnetic field with an angular frequency  $\omega = \gamma H_{eff}$ . If an alternating magnetic field with same angular frequency ( $\omega$ ) is applied in transverse direction to the steady field, then resonance will occur and the magnetization will precess in the resonant frequency absorbing power from the alternating field. This phenomenon is called ferromagnetic resonance.

## 2.6.5 Macrospin Model of Ferromagnetic Resonance: Kittel Formula

In macrospin model, the magnetization of a ferromagnetic element is considered to be uniform throughout the element. Therefore, the magnetic moment of the whole element may be represented by a giant magnetic moment. In this situation the resonance condition of a

ferromagnetic element can be derived theoretically. J. H. E. Griffiths first experimentally reported the ferromagnetic resonance phenomenon in 1946 [44]. Griffiths observed that the resonance frequencies were two to six times greater than the calculated Larmor frequencies for electron spin. Later (1947), C. Kittel explained that the dynamic coupling caused by the demagnetizing field normal to the specimen surface should be taken into account [45]. Let us consider a ferromagnetic specimen with a plane surface ( $y = 0$ ) (Fig. 2.9(a)). A steady bias field  $H_z$  is applied along  $z$ -axis and rf field  $H_x$  is applied along the  $x$ -axis. Now, considering the divergence relation

$$B_y = H_y + 4\pi M_y = 0, \quad (2.6.12)$$

the components of magnetic fields can be written as  $H_x, -4\pi M_y, H_z$ .

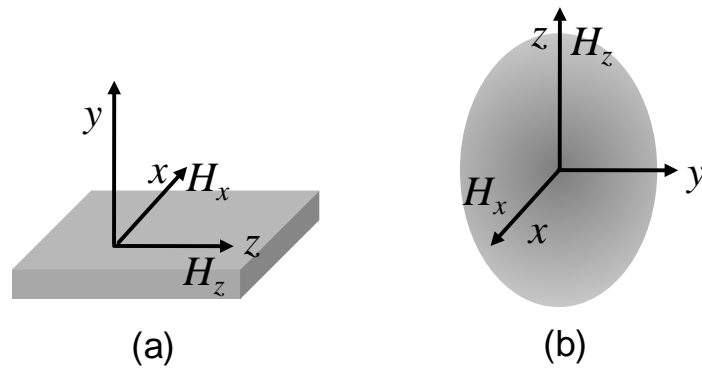


Fig. 2.9: The schematic diagrams of orthogonal coordinates are shown for (a) a ferromagnetic specimen with plane surface ( $y = 0$ ) and (b) an ellipsoid with principle axes parallel to  $x, y$  and  $z$  axes.

Using Eq. 2.6.7 and neglecting products of small quantities, we can write

$$\begin{aligned} \frac{\partial M_x}{\partial t} &= \gamma(H_z + 4\pi M_z)M_y = \gamma B_z M_y \\ \frac{\partial M_y}{\partial t} &= \gamma(M_z H_x - M_x H_z) \\ \frac{\partial M_z}{\partial t} &\cong 0 \end{aligned} \quad (2.6.13)$$

Solving these equations by considering time dependent variation of  $\mathbf{M}$  and  $\mathbf{H}$  ( $\exp(j\omega t)$ ), the resonant frequency comes out to be

$$\omega_0 = \gamma(B_z H_z)^{1/2}. \quad (2.6.14)$$

The above resonant frequency is derived for plane surface. The resonant frequencies for other shapes will be different, because demagnetizing field depends upon the shape of the specimen. Kittel generalized the expression for resonant frequency after taking into account the demagnetizing factors along three coordinate axes. Let us now consider a specimen of ellipsoidal shape. The principal axes are parallel to  $x$ ,  $y$  and  $z$  axes (Fig. 2.9(b)). The effective magnetic field values inside the specimen can be written as [46]

$$\begin{aligned} H_x^i &= H_x - N_x M_x; \\ H_y^i &= -N_y M_y; \\ H_z^i &= H_z - N_z M_z. \end{aligned} \quad (2.6.15)$$

Here  $N_x$ ,  $N_y$ ,  $N_z$  are the demagnetizing factors. Substituting effective field values in Eq. 2.6.7, the components can be written as

$$\begin{aligned} \frac{\partial M_x}{\partial t} &= \gamma [H_z + (N_y - N_z) M_z] M_y; \\ \frac{\partial M_y}{\partial t} &= \gamma [M_z H_x - (N_x - N_z) M_x M_z - M_x H_z]; \\ \frac{\partial M_z}{\partial t} &\cong 0. \end{aligned} \quad (2.6.16)$$

In this case, the resonant frequency becomes

$$\omega_0 = \gamma \left[ (H_z + (N_y - N_z) M_z) \times (H_z + (N_x - N_z) M_z) \right]^{1/2}. \quad (2.6.17)$$

The demagnetizing factors and resonant frequencies for few standard shapes are listed below [18, 46]:

**Table: 2.2**

Shape	Magnetization direction	Demagnetizing Factors			Eigen frequencies
		$N_x$	$N_y$	$N_z$	
Infinitely thin plane	Tangential	0	$4\pi$	0	$\omega_0 = \gamma [H_z (H_z + 4\pi M_z)]^{1/2}$
	Normal	0	0	$4\pi$	$\omega_0 = \gamma [H_z - 4\pi M_z]$

Infinitely thin cylinder	Longitudinal	$2\pi$	$2\pi$	0	$\omega_0 = \gamma(H_z + 2\pi M_z)$
	Transverse	$2\pi$	0	$2\pi$	$\omega_0 = \gamma[H_z(H_z - 2\pi M_z)]^{1/2}$
Sphere	-	$4\pi/3$	$4\pi/3$	$4\pi/3$	$\omega_0 = \gamma H_z$

Till now we have not considered the magnetocrystalline anisotropy or any other kind of anisotropy, which may be present in the system. If anisotropy terms are expressed as effective demagnetizing factors  $(N_x^e, N_y^e, N_z^e)$ , then the components of the anisotropy field can be written by the following equations,

$$\begin{aligned} H_x^e &= -N_x^e M_x; \\ H_y^e &= -N_y^e M_y. \end{aligned} \quad (2.6.18)$$

The resonant frequency can then be written in the following form:

$$\omega_0 = \gamma \left[ H_z + (N_y + N_y^e - N_z) M_z \right] \times \left[ H_z + (N_x + N_x^e - N_z) M_z \right]^{1/2}. \quad (2.6.19)$$

The Eq. 2.6.19 is called the Kittel formula, which gives the resonant frequency of magnetization for a uniformly magnetized ferromagnetic element.

### 2.6.6 Effective Demagnetizing Factors: Two-fold and Four-fold Anisotropy

Now we will find out the effective demagnetizing factors for two- and four-fold anisotropy. We consider here an orthogonal system with  $a$ ,  $b$  and  $c$  axes [47]. The magnetic field ( $\mathbf{H}$ ) is inclined by an angle  $\theta$  with the  $c$ -axis and its projection in the  $a$ - $b$  plane makes an angle  $\phi$  (azimuthal angle) with the  $a$ -axis. The  $x$ ,  $y$  and  $z$  axes are chosen in such a way that the direction of  $\mathbf{M}$  is along  $z$ -axis. The directions of  $x$  and  $y$  axes are shown in Fig. 2.10.

If  $F$  represents the anisotropy energy, then we can write [47]

$$\nabla F = \left( \frac{\partial F}{\partial \theta} \right) \hat{\theta} + \frac{1}{\sin \theta} \left( \frac{\partial F}{\partial \phi} \right) \hat{\phi}. \quad (2.6.20)$$

$$\text{Torque, } \mathfrak{T} = -\hat{r} \times \nabla F$$

$$= -\left(\frac{\partial F}{\partial \theta}\right)\hat{\phi} + \frac{1}{\sin \theta}\left(\frac{\partial F}{\partial \theta}\right)\hat{\theta}. \quad (2.6.21)$$

The torque along  $y$  or  $\phi$  direction can be written as

$$\begin{aligned} \mathfrak{T}_y \hat{\phi} &= \mathbf{M}_S \times \mathbf{H}_x^e \\ \mathfrak{T}_y \hat{\phi} &= \mathbf{M}_S \times \mathbf{H}_x^e \\ &= \mathbf{M}_S \times (-N_x^e \mathbf{M}_x) \\ &= \mathbf{M}_S \times (-N_x^e M_z \sin \alpha) \hat{\theta} \\ &= (-N_x^e M_S^2 \sin \alpha) \hat{\phi}. \end{aligned} \quad (2.6.22)$$

Similarly, the torque along  $x$  or  $\theta$  direction can be written as

$$\mathfrak{T}_x \hat{\theta} = N_y^e M_S^2 \sin \theta \left[1 - (\sin^2 \theta \cos \beta + \cos^2 \theta)^2\right]^{1/2} \hat{\theta}. \quad (2.6.23)$$

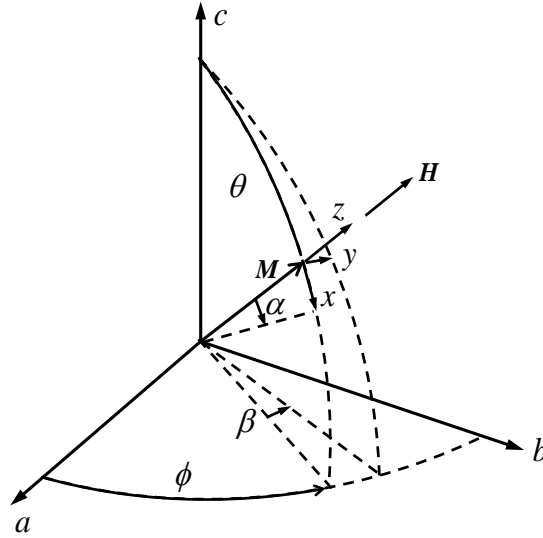


Fig. 2.10: Geometry of the magnetization and applied magnetic field is shown in an orthogonal coordinate system  $(a, b, c)$ .

Let us now consider a film with in-plane uniaxial or two-fold anisotropy. The film is considered to be in the  $a$ - $b$  plane and the magnetic field is applied in the plane of the film ( $\theta = \pi/2$ ).

$$\left(\frac{\partial F}{\partial \theta}\right)_{\frac{\pi}{2}+\alpha} - \left(\frac{\partial F}{\partial \theta}\right)_{\frac{\pi}{2}} = N_x^e M_S^2 \sin \alpha;$$

$$\text{Hence, } \left( \frac{\partial F}{\partial \theta} \right)_{\frac{\pi}{2} + \alpha} - \left( \frac{\partial F}{\partial \theta} \right)_{\frac{\pi}{2}} = N_x^e M_S^2 \sin \alpha ; \quad (2.6.24)$$

$$\left[ \left( \frac{\partial F}{\partial \theta} \right)_{\phi + \beta} - \left( \frac{\partial F}{\partial \theta} \right)_{\phi} \right]_{\theta = \frac{\pi}{2}} = N_y^e M_S^2 \sin \beta . \quad (2.6.25)$$

If the anisotropy energy is considered to be along the  $a$ -axis, then it can be written as

$$F_2 = -K_2 \sin \theta \cos^2 \phi . \quad (2.6.26)$$

Substituting (2.6.26) in (2.6.24) and (2.6.25), we get

$$N_x^e M_S = \frac{2K_2}{M_S} \cos^2 \phi ; \quad (2.6.27)$$

$$N_y^e M_S = \frac{2K_2}{M_S} \cos 2\phi . \quad (2.6.28)$$

For four-fold anisotropy, the free energy can be written as

$$F_4 = K_4 (\sin^4 \theta \cos^4 \phi + \sin^4 \theta \sin^4 \phi) . \quad (2.6.29)$$

After performing simple algebra we can write,

$$F_4 = \frac{K_4}{4} \sin^4 \theta (3 + \cos 4\phi) . \quad (2.6.30)$$

Substituting (2.6.30) in (2.6.24) and (2.6.25)

$$N_x^e M_S = -\frac{K_4}{M_S} (3 + \cos 4\phi) ; \quad (2.6.31)$$

$$N_y^e M_S = -\frac{4K_4}{M_S} \cos 4\phi . \quad (2.6.32)$$

Here,  $\phi$  is the angle made by magnetization with the four-fold easy axis.

Substituting (2.6.27) and (2.6.28) into (2.6.19), we get the resonant frequency for two-fold anisotropy as

$$\omega_0 = \gamma \left( \left[ H_z + \left( N_y - N_z + \frac{2K_2}{M_S^2} \cos 2\phi \right) M_z \right] \times \left[ H_z + \left( N_x - N_z + \frac{2K_2}{M_S^2} \cos^2 \phi \right) M_z \right] \right)^{\frac{1}{2}} .$$

(2.6.33).

Similarly, substituting (2.6.31) and (2.6.32) into (2.6.19), we get the resonant frequency for four-fold anisotropy as

$$\omega_0 = \gamma \left( \left[ H_z + \left( N_y - N_z - \frac{4K_4}{M_S^2} \cos 4\phi \right) M_z \right] \times \left[ H_z + \left( N_x - N_z - \frac{K_4}{M_S^2} (3 + \cos 4\phi) \right) M_z \right] \right)^{1/2}. \quad (2.6.34)$$

## 2.7 Spin Waves

### 2.7.1 Introduction

The concept of spin wave was first introduced by Bloch [48]. If an array of spins is disturbed locally by some external perturbation then the disturbance propagates as a wave. This wave is generated by collective phase coherent precession of magnetization or spins in the ferromagnetic medium. The quanta of spin waves are called magnons. Classically magnetization dynamics is governed by Landau-Lifshitz (neglecting damping) equation (Eq. 2.6.7), which shows that the time rate of change of magnetization is proportional to the torque exerted by the effective magnetic field ( $H_{eff}$ ) on the magnetization. Both dipolar and exchange interaction contribute to effective magnetic field.

### 2.7.2 Exchange Spin Wave: Dispersion Relation

The spin wave is dominated by exchange interaction when the wavelength ( $\lambda$ ) of a spin wave becomes is very short (*i.e.*, the wave vector ( $k$ ) is very large). In this section we will derive the dispersion relation of purely exchange spin wave. In the ground state, all the spins are parallel to each other. Let us consider a chain of  $N$  spins and each of them has magnitude ‘ $S$ ’. Considering Heisenberg interaction, the exchange interaction energy of  $p^{\text{th}}$  spin will be [3]

$$-2JS_p \cdot (S_{p-1} + S_{p+1}). \quad (2.7.1)$$

Now the magnetic moment of  $p^{\text{th}}$  spin is  $\mu_p = -g\mu_B S_p$ .

Substituting the value of magnetic moment into Eq. 2.7.1, we get the energy of  $p^{\text{th}}$  spin

$$-\boldsymbol{\mu}_p \cdot \left[ \left( -\frac{2J}{g\mu_B} \right) (\mathbf{S}_{p-1} + \mathbf{S}_{p+1}) \right] = -\boldsymbol{\mu}_p \cdot \mathbf{B}_p, \quad (2.7.2)$$

where  $\mathbf{B}_p = \left( -\frac{2J}{g\mu_B} \right) (\mathbf{S}_{p-1} + \mathbf{S}_{p+1})$  is the total exchange field on  $p^{\text{th}}$  spin. The torque on the  $p^{\text{th}}$  spin can be written as

$$\begin{aligned} \hbar \frac{d\mathbf{S}_p}{dt} &= \boldsymbol{\mu}_p \times \mathbf{B}_p \\ \Rightarrow \frac{d\mathbf{S}_p}{dt} &= -\frac{g\mu_B}{\hbar} \mathbf{S}_p \times \left( -\frac{2J}{g\mu_B} \right) (\mathbf{S}_{p-1} + \mathbf{S}_{p+1}) \\ &= \left( \frac{2J}{\hbar} \right) (\mathbf{S}_p \times \mathbf{S}_{p-1} + \mathbf{S}_p \times \mathbf{S}_{p+1}) \end{aligned} \quad (2.7.3)$$

For small amplitude of excitation,  $S_p^x, S_p^y \ll S$  and  $S_p^z \cong S$ . Neglecting the product of small terms, the linearized equations can be written as [3]

$$\begin{aligned} \frac{dS_p^x}{dt} &= \left( \frac{2JS}{\hbar} \right) (2S_p^y - S_{p-1}^y - S_{p+1}^y); \\ \frac{dS_p^y}{dt} &= -\left( \frac{2JS}{\hbar} \right) (2S_p^x - S_{p-1}^x - S_{p+1}^x); \\ \frac{dS_p^z}{dt} &= 0. \end{aligned} \quad (2.7.4)$$

Let the solutions are of sinusoidal form *i.e.*,

$$S_p^x = m e^{i(pka - \omega t)}, S_p^y = n e^{i(pka - \omega t)}. \quad (2.7.5)$$

Substituting these in the above equations (Eq. 2.7.4)

$$\begin{aligned} -i\omega m &= \left( \frac{2JS}{\hbar} \right) (2 - e^{-ika} - e^{ika}) n \\ &= \left( \frac{4JS}{\hbar} \right) (1 - \cos ka) n \\ \text{and } -i\omega n &= -\left( \frac{2JS}{\hbar} \right) (2 - e^{-ika} - e^{ika}) m \end{aligned} \quad (2.7.6)$$

$$= -\left(\frac{4JS}{\hbar}\right)(1 - \cos ka)m \quad (2.7.7)$$

The determinant of coefficients of Eqs. 2.7.6 and 2.7.7 should be zero to have solution for  $m$  and  $n$ .

$$\begin{vmatrix} i\omega & \left(\frac{4JS}{\hbar}\right)(1 - \cos ka) \\ -\left(\frac{4JS}{\hbar}\right)(1 - \cos ka) & i\omega \end{vmatrix} = 0 \quad (2.7.8)$$

This gives

$$\hbar\omega = 4JS(1 - \cos ka). \quad (2.7.9)$$

At long wavelength limit,  $ka \ll 1$ .

Then,

$$\hbar\omega = (2JSa^2)k^2. \quad (2.7.10)$$

The dispersion of spin wave frequency ( $\omega$ ) with wave vector ( $k$ ) is quadratic in nature for long wavelength limit *i.e.*, in the small  $k$  limit. The dispersion of exchange spin wave is isotropic.

### 2.7.3 Exchange Spin Waves in Thin Films

In the section above, we have seen that the dispersion of exchange dominated spin wave is proportional to the square of the wave vector. We can write [49]

$$\omega(k) = \gamma(H + Dk^2), \quad (2.7.11)$$

where  $D = 2A/M_s$  and  $A$  is the exchange stiffness constant.

Perpendicular standing spin wave (PSSW) mode observed in a thin film is an example of the exchange spin wave. The spin wave propagates along the direction perpendicular to the plane of the film and reflects back to form standing spin wave. The wave vector is quantized for pinned or unpinned boundary condition. The wave vector can have the value  $n(\pi/d)$ ,

where  $d$  is the film thickness and  $n$  is a positive integer. In Fig. 2.11(a), the pattern of PSSW mode is shown for  $n = 0$  and  $n = 1$ .

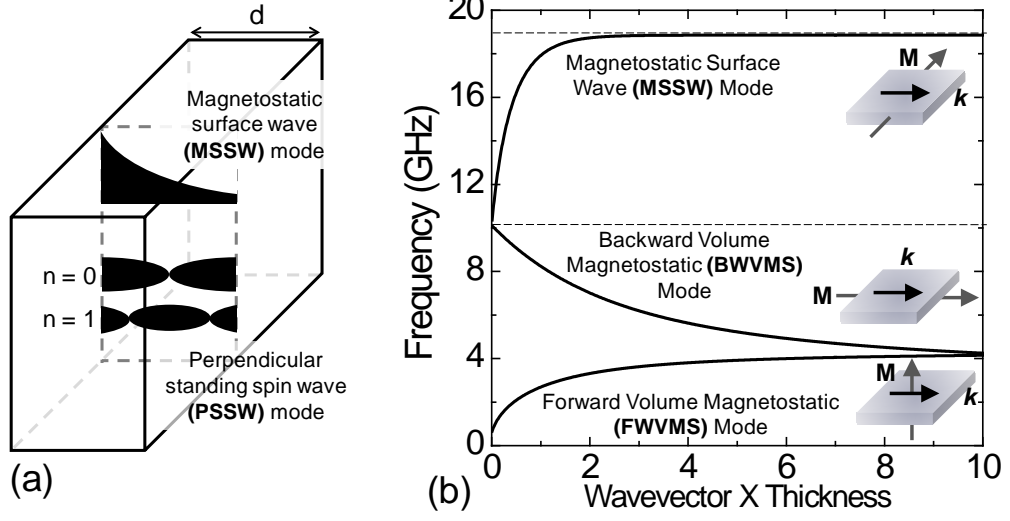


Fig. 2.11: (a) Schematics of perpendicular standing spin wave (PSSW) and magnetostatic surface spin wave (MSSW) modes are shown for a ferromagnetic thin film. (b) The calculated dispersions of three different magnetostatic spin wave modes are shown for a permalloy thin film with  $4\pi M_s = 10.8$  kOe. The values of applied bias field were chosen as 1 kOe for MSSW & backward volume magnetostatic (BWVMS) modes and 11 kOe for forward volume magnetostatic (FWVMS) modes in the calculation.

## 2.7.4 Magnetostatic Modes in Thin Films

If an in-plane magnetic field is applied to an infinite ferromagnetic thin film, the magnetic moments are aligned in the plane of the film. Now, the wavelength of excited spin waves depends upon the characteristic length scale of uniformity of the internal magnetic field. As the magnetization and hence the internal field for an infinite thin film is very uniform, the large wavelength spin waves ( $\lambda \geq 1 \mu\text{m}$ ) are observed for such thin films. The spin waves observed in this case are governed by dipolar interaction. The dispersion relations of dipolar modes can be calculated numerically by solving Landau-Lifshitz equation (Eq. 2.6.7) after considering Maxwell's equations in magnetostatic limit:

$$\begin{aligned}\nabla \times \mathbf{H} &= 0 \\ \nabla \cdot (\mathbf{H} + 4\pi\mathbf{M}_s) &= 0.\end{aligned}\quad (2.7.12)$$

The magnetization can be written as [50]

$$\mathbf{M}(\mathbf{r}, t) = \mathbf{M}_s + \mathbf{m}(\mathbf{r}, t). \quad (2.7.13)$$

In the above equation  $M_S$  is saturation magnetization and  $\mathbf{m}$  is the small variation of magnetization due to the precession of magnetization. For small angle precession,  $m \ll M_S$ . In this case  $\mathbf{m}(\mathbf{r}, t)$  can be written as a sum of a series of plane waves.

$$\mathbf{m}(\mathbf{r}, t) = \sum_k \mathbf{m}_k e^{i(\omega t - \mathbf{k} \cdot \mathbf{r})} \quad (2.7.14)$$

Under this condition the nonlinear Landau-Lifshitz equation can be linearized and solved. The dispersion relation of dipole-exchange spin wave in an infinite ferromagnetic material can be written by Herring-Kittel formula [51]

$$\omega = \gamma \left[ \left( H + \frac{2A}{M_S} k^2 \right) \left( H + \frac{2A}{M_S} k^2 + 4\pi M_S \sin^2 \theta_k \right) \right]^{1/2}, \quad (2.7.15)$$

where  $\theta_k$  is the angle between  $k$  and  $M_S$ . For a thin film of thickness  $d$ , this dispersion relation is modified due to the broken translational symmetry at the interface. Let the Zeeman field is applied along the  $z$ -axis, which is essentially in the plane of the film and  $x$ -axis is normal to the direction of the film. Damon and Eshbach first calculated the dispersions of dipolar modes for a thin magnetic film [52]. They found two kinds of modes: surface or Damon Eshbach (DE) mode and volume mode. The surface modes exist up to an angle (called critical angle  $\theta_c$ ) *w.r.t.* the perpendicular direction of magnetization. The expression for the critical angle is given by

$$\theta_c = \tan^{-1} \sqrt{\frac{4\pi M_S}{H}}. \quad (2.7.16)$$

The amplitude of the surface mode decays exponentially away from the surface and most of the power in this mode is distributed in the vicinity of the film surface (Fig. 2.11(a)). The penetration depth ( $\delta$ ) decreases with the increase in angle  $\theta$  and becomes exactly zero at  $\theta = \theta_c$ . At this angle the surface mode is localized strictly at the surface.

Again,  $\delta$  is inversely proportional to wave vector along that direction [53]. As  $k_y \rightarrow 0$ , the penetration depth  $\delta \rightarrow \infty$ , *i.e.*, the surface mode is transferred to Kittel mode. The penetration depth is independent of the film thickness and therefore DE mode is converted to bulk mode when film thickness becomes comparable to the penetration depth. In general when the surface mode propagates perpendicular to the magnetization, it is called the

magnetostatic surface wave (MSSW) mode. Considering negligible anisotropy, the dispersion relation of MSSW mode (Fig. 2.11(b)) is given by [49]

$$\omega_{DE} = \gamma \left[ H(H + 4\pi M_s) + (2\pi M_s)^2 (1 - e^{-2kd}) \right]^{1/2}. \quad (2.7.17)$$

At  $k = 0$ , the frequency of the DE mode becomes

$$(\omega_{DE})_{k=0} = \gamma [H(H + 4\pi M_s)]^{1/2}. \quad (2.7.18)$$

The above frequency is same as the frequency of Kittel mode or uniform mode.

At  $k \rightarrow \infty$ , the frequency of MSSW mode becomes

$$(\omega_{DE})_{k=\infty} = \gamma(H + 2\pi M_s). \quad (2.7.19)$$

The frequencies of MSSW mode always remain in between two frequency values as described by Eqs. 2.7.18 and 2.7.19.

There is a manifold of volume or bulk modes. Volume modes form standing wave pattern along the film thickness. Each volume mode corresponds to a mode number. The volume modes are degenerate along the propagation direction perpendicular to  $\mathbf{M}$ . The degeneracy is lifted when  $\mathbf{k}$  becomes parallel to  $\mathbf{M}$ . For  $\mathbf{k} \perp \mathbf{M}$ , the volume mode becomes dispersionless, while for other directions negative dispersion is observed. When the direction of  $\mathbf{M}$  and  $\mathbf{k}$  are the same and both lie in the plane of the film, the spin wave is called backward volume magnetostatic (BWVMS) mode. Considering negligible anisotropy the dispersion relation of the lowest order BWVMS mode is given by [49-50]

$$\left( \frac{\omega_B}{\gamma} \right)^2 = H \left[ H + 4\pi M_s \left( \frac{1 - e^{-2kd}}{kd} \right) \right]. \quad (2.7.20)$$

The negative slope of dispersion implies that the phase velocity and group velocity are in opposite directions. At  $k \rightarrow 0$ , the frequency of BWVMS mode becomes the same as the Kittel mode (Eq. 2.7.18).

Another kind of magnetostatic spin wave mode is observed when the magnetization is along the perpendicular direction to the film and the propagation direction is in the plane of the film. This is called the forward volume magnetostatic (FWVMS) mode. In the long

wavelength limit, the dispersion relation of the FWVMS mode can be expressed after neglecting anisotropy as

$$\left(\frac{\omega_F}{\gamma}\right)^2 = (H - 4\pi M_s) \left[ H - 4\pi M_s \left( \frac{1 - e^{-kd}}{kd} \right) \right]. \quad (2.7.21)$$

In the magnetostatic modes, the exchange interaction is generally neglected. This is a valid approximation for the materials with a very weak exchange stiffness constant such as Yttrium Iron Garnet (YIG). But for permalloy (used as a material for thin films and nanodot arrays in this thesis) the value of  $A$  is much larger and hence the contribution of exchange interaction cannot be neglected. The frequency of dipole-exchange modes therefore becomes larger than the dipolar modes. The contribution from exchange interaction becomes more for higher wave vector as the exchange has a quadratic contribution to the dispersion relation.

### 2.7.5 Magnetostatic Modes in Confined Thin Ferromagnetic Elements

In section 2.7.3, we have seen that the quantized standing spin wave (PSSW) mode is observed across the thickness of thin film due to the physical boundary. The spin wave can also be quantized in the plane of the film due to confinement of ferromagnetic element. Stripes and dots are the examples of confined magnetic nanostructures. If  $w$  is the width of the nanostructure then the values of quantized wave vector spin waves may be written as [49]

$$k_n = \frac{2\pi}{\lambda_n} = \frac{n\pi}{w}. \quad (2.7.22)$$

However, the analysis of the quantized spin waves cannot be done by only considering the allowed wave vector in the DE modes, but one has to take into account of the nonuniform demagnetizing field and the edge effects [54]. The quantized spin waves can be solved easily by solving Landau-Lifshitz equation in the micromagnetic framework [55].

## 2.8 Magneto-optical Kerr Effect

### 2.8.1 Introduction

Magneto-optical effect is a very old and well known phenomenon. In 1854 Michael Faraday first invented magneto-optical phenomenon in a piece of glass placed in between two magnetic pole pieces. He observed that with the magnetic field applied along the propagation

direction of light, the axis of polarization is rotated. The angle of rotation is a function of the strength of the magnetic field and the distance traveled in the medium. In 1877 John Kerr also observed a magneto-optical effect in reflection from the polished metallic pole of an electromagnet [56]. Both of these effects originate from the interaction of light with the applied magnetic field and magnetization of the material. In 1884 Kundt observed that magneto-optical effect is greatly enhanced when light is reflected from or transmitted through a ferromagnetic material [57]. The magneto-optical rotation is linearly proportional to the magnetization. Magneto-optical effects have proved to be a very efficient and sensitive technique for imaging magnetic domains and probing magnetization dynamics at various time scales. Magneto-optical effect depends on the complex dielectric tensor. A plane polarized light is converted into an elliptically polarized light due to the magneto-optical effect where the major axis of the ellipse is rotated from the plane of polarization of the plane polarized light.

## 2.8.2 Physical Origin of Magneto-optical Effects

The origin of magneto-optical effect can be explained by Zeeman effect. Let us consider a system of electrons bound harmonically in an oscillating electric field and a static magnetic field. The equation of motion of each electron can be written as

$$m\ddot{\mathbf{r}} + b\dot{\mathbf{r}} + k\mathbf{r} = -e\mathbf{E}_0 e^{j\omega t} - e\mu_0\dot{\mathbf{r}} \times \mathbf{H}, \quad (2.8.1)$$

where  $b$  is the damping coefficient,  $m$  is the electron mass and  $(k/m)^{1/2} = \omega_0$  is the natural frequency of electron. The last term in this equation is the Lorentz force. The above equation can easily be solved. The electric dipole moment ( $-er_0$ ) is proportional to the electric field ( $E_0$ ). The proportionality tensor is called the polarizability tensor. For an assembly of  $N$  oscillators the polarizability can be expressed as [58]

$$\begin{aligned} \chi_{xx} = \chi_{yy} &= \frac{Ne^2}{\epsilon_0 m} \frac{\omega_0^2 - \omega^2 + j\omega\gamma}{(\omega_0^2 - \omega^2 + \omega\gamma)^2 - 4\omega^2\omega_L^2} \\ \chi_{xy} = -\chi_{yx} &= \frac{Ne^2}{\epsilon_0 m} \frac{-2j\omega\omega_L}{(\omega_0^2 - \omega^2 + \omega\gamma)^2 - 4\omega^2\omega_L^2} \end{aligned} \quad (2.8.2)$$

where  $\omega_L = e\mu_0 H/2m$  is the Larmor precession frequency and  $\gamma = b/m$  is the width of the resonance.  $\chi$  is a symmetric and scalar quantity in an isotropic medium. Therefore the off-diagonal terms of the dielectric tensor are zero. The anisotropy in the medium may be

generated from the magnetic field or the magnetization of the ferromagnetic material. For a circularly polarized light, the polarizability can be written as [58]

$$\begin{aligned}\chi_{\pm} = \chi_{xx} \pm \chi_{xy} &= \frac{Ne^2}{\epsilon_0 m} \frac{(\omega_0^2 - \omega^2 + j\omega\gamma) \pm 2\omega\omega_L}{(\omega_0^2 - \omega^2 + j\omega\gamma)^2 - 4\omega^2\omega_L^2} \\ &\approx \frac{Ne^2}{\epsilon_0 m} \frac{1}{\omega_0^2 - (\omega \pm \omega_L)^2 + j\omega\gamma}.\end{aligned}\quad (2.8.3)$$

The upper sign refers to the right circularly polarized (RCP) light, whereas the lower sign to the left circularly polarized (LCP) light. Larmor's theorem says that if the refractive index in absence of magnetic field is  $n(\omega)$ , then in presence of a field the refractive indices can be written as

$$n_{\pm}(\omega) = n(\omega \pm \omega_L). \quad (2.8.4)$$

Therefore, the refractive indices of RCP and LCP are different in presence of a magnetic field.

Let us now consider a linearly polarized light propagating along  $+z$  direction in a circularly birefringent medium. If the polarization direction is along  $+x$  axis then the linearly polarized light can be expressed as

$$E = \hat{e}_x E_0 e^{j(\omega t - kz)}, \quad (2.8.5)$$

where  $k$  is the wave vector and  $\omega$  is the angular frequency. In a non-birefringent medium the expression (2.8.5) of linearly polarized light can be written as a linear combination of RCP and LCP in the following way:

$$E = \frac{E_0}{2} (\hat{e}_x + j\hat{e}_y) e^{j(\omega t - kz)} + \frac{E_0}{2} (\hat{e}_x - j\hat{e}_y) e^{j(\omega t - kz)}. \quad (2.8.6)$$

In a circularly birefringent medium, the above expression will be modified as

$$E = \frac{E_0}{2} (\hat{e}_x + j\hat{e}_y) e^{j(\omega t - 2\pi z / \lambda_0)} + \frac{E_0}{2} (\hat{e}_x - j\hat{e}_y) e^{j(\omega t - 2\pi z / \lambda_0)}, \quad (2.8.7)$$

where  $\lambda_0$  is the wavelength of the linearly polarized light in vacuum. The above expression can be rewritten as

$$E = \frac{E_0}{2} e^{j(\omega t - 2\pi \bar{n} z / \lambda_0)} \left[ \hat{e}_x \cos \frac{\delta}{2} + \hat{e}_y \sin \frac{\delta}{2} \right], \quad (2.8.8)$$

where

$$\bar{n} = \frac{1}{2}(n_+ + n_-), \quad (2.8.9)$$

and

$$\delta = \frac{2\pi(n_+ - n_-)z}{\lambda_0}, \quad (2.8.10)$$

is the phase difference introduced between the components by the birefringence of the medium. Equation 2.8.8 states that the direction of polarization of linearly polarized light is being rotated through an angle of  $\delta/2$ .

For an absorptive medium  $n_{\pm}$  is a complex quantity and can be written as [58]

$$n_{\pm} = N_{\pm} - jK_{\pm}, \quad (2.8.11)$$

where  $N_{\pm}$  and  $K_{\pm}$  both are real quantities. In this case the linearly polarized light will be converted to an elliptically polarized light with the major axis of the ellipse rotated through an angle

$$\theta_K = \Re\left(\frac{\delta}{2}\right) = \Re\left[\frac{\pi l}{\lambda_0}(n_+ - n_-)\right], \quad (2.8.12)$$

where  $l$  is the distance of propagation.

The ellipticity is expressed as

$$\varepsilon_K = -\tanh \Im\left(\frac{\delta}{2}\right) = -\tanh \Im\left[\frac{\pi l}{\lambda_0}(n_+ - n_-)\right]. \quad (2.8.13)$$

### 2.8.3 Phenomenological Theory

The optical properties of material can be given by Maxwell's equations and the corresponding relations, which describe the specific material properties. We need two equations:

$$\nabla \times \mathbf{E} = -\mu_0 \frac{\partial \mathbf{H}}{\partial t}, \quad (2.8.14)$$

$$\nabla \times \mathbf{H} = \varepsilon_0 \frac{\partial \mathbf{E}}{\partial t} + \mathbf{J}. \quad (2.8.15)$$

where  $\mathbf{E}$ ,  $\mathbf{H}$ ,  $\mathbf{J}$ ,  $\mu_0$ ,  $\varepsilon_0$  are electric field, magnetic field, electrical current density, permeability and permittivity of free space, respectively. The current density can be expressed as [58]

$$\mathbf{J} = \varepsilon_0 \frac{\partial \mathbf{P}}{\partial t} = \chi \frac{\partial \mathbf{E}}{\partial t}, \quad (2.8.16)$$

where  $\chi$  is the polarizability. Again dielectric constant ( $\kappa$ ) and polarizability ( $\chi$ ) are related by the relation

$$\kappa = \mathbf{I} + \chi. \quad (2.8.17)$$

$\kappa$  and  $\chi$  are the tensorial quantities and depends on the applied magnetic field and magnetization of the material. Their non-scalar nature gives rise to the magneto-optical effect. Now we consider a plane propagating wave propagating through a medium. The electric and magnetic fields may be written as

$$\mathbf{E} = E_0 e^{j(\omega t - \mathbf{k} \cdot \mathbf{r})}, \mathbf{H} = H_0 e^{j(\omega t - \mathbf{k} \cdot \mathbf{r})}. \quad (2.8.18)$$

Taking curl of (2.8.14) and using (2.8.15) & (2.8.17), one can write [58]

$$\{n^2 \mathbf{I} - \mathbf{k} \cdot \mathbf{k} / k_0^2 - \kappa\} \cdot \mathbf{E}_0 = 0. \quad (2.8.19)$$

Equation 2.8.19 posses a nontrivial solution for  $E_0$  only if the determinant of coefficient vanishes. We have not said anything about the magneto-optical effect so far. Let us consider a cubic crystal with dc magnetic field applied along the  $z$ -axis. Then, the dielectric constant can be written as

$$\kappa = \begin{bmatrix} \kappa_1 & \kappa_2 & 0 \\ -\kappa_2 & \kappa_1 & 0 \\ 0 & 0 & \kappa_3 \end{bmatrix}. \quad (2.8.20)$$

In the above equation,  $\kappa_2$  is the odd function of  $\mathbf{H}$  or  $\mathbf{M}$ , whereas  $\kappa_1$  and  $\kappa_3$  even functions. With the above form of  $\kappa$ , the secular determinant for (2.8.19) becomes [58]

$$n^4 \{ \kappa_1 + (\kappa_3 - \kappa_1) \cos^2 \theta' \} - n^2 \{ (\kappa_1^2 + \kappa_2^2 + \kappa_1 \kappa_3) - (\kappa_1^2 + \kappa_2^2 - \kappa_1 \kappa_3) \cos \theta' \} + \kappa_3 (\kappa_1^2 + \kappa_2^2) = 0, \quad (2.8.21)$$

where

$$\cos \theta' = k_z / k = k_z / nk_0. \quad (2.8.22)$$

Let us now consider the simplest case. A homogeneous wave (real and imaginary part of  $k$  are parallel) with propagation direction along  $\mathbf{H}$  or  $\mathbf{M}$ . In this case,  $\cos \theta' = 1$ . Therefore the solutions of (2.8.21) are

$$n_{\pm} = \kappa_1 \pm j\kappa_2. \quad (2.8.23)$$

For simplicity, we now consider the polar Kerr effect at normal incidence. Let  $k_0$ ,  $k_1$  and  $k_2$  are the incident, reflected and transmitted wave vectors, respectively. The reflected amplitude can be written as

$$r = E_1 / E_0 = -\frac{n-1}{n+1}. \quad (2.8.24)$$

If we write the reflectivity as

$$r = |r| e^{i\phi}, \quad (2.8.25)$$

then

$$\frac{r_+}{r_-} = \left| \frac{r_+}{r_-} \right| e^{i(\phi_+ - \phi_-)}. \quad (2.8.26)$$

The above relation says that the linearly polarized light will be converted to elliptically polarized light upon reflection because the circular components (RCP & LCP) will not have equal amplitudes. The major axis of the ellipse will be rotated from the original direction of polarization of the incident light because of the phase introduced between the two circular vibrations. The Kerr rotation and ellipticity can be expressed as [58]

$$\theta_K = \frac{1}{2}(\phi_+ - \phi_-) \quad (2.8.27)$$

$$\text{and } \varepsilon_K = -\frac{r_+ - r_-}{r_+ + r_-}. \quad (2.8.28)$$

Now, expressing the refractive index as a complex quantity (like Eq. 2.8.11), the complex Kerr rotation can be written as

$$\theta_K = \frac{2}{1 - \varepsilon} [-(k_- - k_+) + i(n_- - n_+)]. \quad (2.8.29)$$

The real component of  $\theta_K$  gives the Kerr rotation and imaginary component of  $\theta_K$  gives the Kerr ellipticity. The Kerr rotation depends upon the circular dichroism, whereas Kerr ellipticity depends upon the circular birefringence of the medium. It can also be shown qualitatively that the Kerr rotation and Kerr ellipticity both are proportional to the magnetization of ferromagnetic material.

## Bibliography

1. A. J. Dekker, "Solid State Physics," *Macmillan Publishers India Ltd.*, New Delhi, India (1981).
2. A. H. Morrish, "The Physical Principles of Magnetism," *IEEE Press*, New York, United States (2001).
3. C. Kittel, "Introduction to Solid State Physics," Seventh edition, *Wiley India*, New Delhi, India (2009).
4. S. Chikazumi, "Physics of Ferromagnetism," *Oxford University Press*, New York, United States (1997).
5. M. D. Kaufmann, "Magnetization Dynamics in All-optical Pump-probe Experiments: Spin-wave Modes and Spin-current Damping," Ph.D Thesis, Georg-August-Universität, Göttingen, Germany (2006).
6. J. Silcox, *Philos. Mag.* **8**, 7 (1963).
7. T. Suzuki, *J. Phys. Colloques* **32**, C1 134 (1971).
8. E. C. Stoner and E. P. Wohlfarth, *Phil. Trans. R. Soc. London. Ser. A* **240**, 599 (1948).
9. R. Skomski, *J. Phys.: Condens. Matter* **15**, R841 (2003).
10. D. Givord and M. F. Rossignol, "Rare-Earth Iron Permanent Magnets," *Oxford University Press*, New York, United States (1996).
11. A. Aharoni, "Introduction to the Theory of Ferromagnetism," Second Edition, *Oxford University Press*, New York, United States (2000).
12. E. H. Frei, S. Shtrikman, and D. Treves, *Phys. Rev.* **106**, 446 (1957).
13. I. S. Jacobs and C. P. Bean, *Phys. Rev.* **100**, 1060 (1955).
14. R. Hertel, *J. Magn. Magn. Mater.* **249**, 251 (2002).
15. R. Hertel and J. Kirschner, *Physica B* **343**, 206 (2004).
16. R. Skomski, J. P. Liu, and D. J. Sellmyer, *Phys. Rev. B* **60**, 7359 (1999).
17. A. T. J. Miltat and G. Albuquerque, "Spin dynamics in confined magnetic structures I," *Springer*, Berlin, Heidelberg (2002).
18. A. G. Gurevich and G. A. Melkov, "Magnetization Oscillations and Waves," *CRC Press*, Boca Raton (1996).
19. L. D. Landau and E. M. Lifshitz, *Phys. Zs. der Sowjetunion.* **8**, 153 (1935).
20. T. L. Gilbert, *Phys. Rev.* **100**, 1243 (1955).

21. T. L. Gilbert, *IEEE Trans. Magn.* **40**, 3443 (2004).
22. M. Oogane, T. Wakitani, S. Yakata, R. Yilgin, Y. Ando, A. Sakuma, and T. Miyazaki, *Jpn. J. Appl. Phys.* **45**, 3889 (2006).
23. S. Trudel, O. Gaier, J. Hamrle, and B. Hillebrands, *J. Phys. D: Appl. Phys.* **43**, 193001 (2010).
24. C. Scheck, L. Cheng, and W. E. Bailey, *Appl. Phys. Lett.* **88**, 252510 (2006).
25. S.-K. Kim, *J. Phys. D: Appl. Phys.* **43**, 264004 (2010).
26. E. Beaurepaire, J. C. Merle, A. Daunois, and J.-Y. Bigot, *Phys. Rev. Lett.* **76**, 4250 (1996).
27. B. Koopmans, "Handbook of Magnetism and Advanced Magnetic Materials," Vol. 3, Wiley, (2007).
28. B. Koopmans, *Nat. Mater.* **6**, 715 (2007).
29. J.-Y. Bigot, M. Vomir, L. H. F. Andrade, and E. Beaurepaire, *Chem. Phys.* **318**, 137 (2005).
30. E. Carpena, E. Mancini, C. Dallera, M. Brenna, E. Puppini, and S. De Silvestri, *Phys. Rev. B* **78**, 174422 (2008).
31. L. Guidoni, E. Beaurepaire, and J.-Y. Bigot, *Phys. Rev. Lett.* **89**, 017401 (2002).
32. P. M. Oppeneer and A. Liebsch, *J. Phys. Cond. Matt.* **16**, 5519 (2004).
33. B. Koopmans, J. J. M. Ruigrok, F. D. Longa, and W. J. M. de Jonge, *Phys. Rev. Lett.* **95**, 267207 (2005).
34. M. Krauß, T. Roth, S. Alebrand, D. Steil, M. Cinchetti, M. Aeschlimann, and H. C. Schneider, *Phys. Rev. B* **80**, 180407 (2009).
35. G. P. Zhang, W. Hubner, G. Lefkidis, Y. Bai, and T. F. George, *Nat. Phys.* **5**, 499 (2009).
36. J.-Y. Bigot, M. Vomir, and E. Beaurepaire, *Nat. Phys.* **5**, 515 (2009).
37. G. P. Zhang and W. Hübner, *Phys. Rev. Lett.* **85**, 3025 (2000).
38. E. Beaurepaire, G. M. Turner, S. M. Harrel, M. C. Beard, J.-Y. Bigot, and C. A. Schmuttenmaer, *Appl. Phys. Lett.* **84**, 3465 (2004).
39. M. Battiato, K. Carva, and P. M. Oppeneer, *Phys. Rev. Lett.* **105**, 027203 (2010).
40. A. Eschenlohr, M. Battiato, P. Maldonado, N. Pontius, T. Kachel, K. Holldack, R. Mitzner, A. Föhlich, P. M. Oppeneer, and C. Stamm, *Nat. Mater.* **12**, 332 (2013).
41. A. Laraoui, V. Halté, M. Vomir, J. Vénuat, M. Albrecht, E. Beaurepaire, and J.-Y. Bigot, *Eur. Phys. J. D* **43**, 251 (2007).

42. A. Laraoui, J. Venuat, V. Halte, M. Albrecht, E. Beaurepaire, and J.-Y. Bigot, *J. Appl. Phys.* **101**, 09C105 (2007).
43. B. Koopmans, G. Malinowski, F. Dalla Longa, D. Steiauf, M. Fahnle, T. Roth, M. Cinchetti, and M. Aeschlimann, *Nat. Mater.* **9**, 259 (2010).
44. J. H. E. Griffiths, *Nature* **158**, 670 (1946).
45. C. Kittel, *Phys. Rev.* **71**, 270 (1947).
46. C. Kittel, *Phys. Rev.* **73**, 155 (1948).
47. O. Kohmoto, *J. Magn. Magn. Mater.* **262**, 280 (2003).
48. F. Bloch, *Z. Phys.* **61**, 206 (1930).
49. B. Hillebrands and J. Hamrle, “Handbook of Magnetism and Advanced Magnetic Materials,” *John Wiley & Sons, Ltd.*, (2007).
50. S. O. Demokritov, B. Hillebrands, and A. N. Slavin, *Phys. Rep.* **348**, 441 (2001).
51. C. Herring and C. Kittel, *Phys. Rev.* **81**, 869 (1951).
52. R. W. Damon and J. R. Eshbach, *J. Phys. Chem. Solids* **19**, 308 (1961).
53. P. A. Grünberg, *Prog. Surf. Sci.* **18**, 1 (1985).
54. P. H. Bryant, J. F. Smyth, S. Schultz, and D. R. Fredkin, *Phys. Rev. B* **47**, 11255 (1993).
55. M. Donahue and D. G. Porter, “OOMMF User’s guide, Version 1.0,” *NIST Interagency Report No. 6376, National Institute of Standard and Technology, Gaithersburg, MD, URL: <http://math.nist.gov/oommf>*, (1999).
56. J. Kerr, *Philos. Mag. Series 5* **3**, 321 (1877).
57. A. Kundt, *Philosophical Magazine Series 5* **18**, 308 (1884).
58. M. J. Freiser, *IEEE Trans. Magn.* **4**, 152 (1968).

## CHAPTER 3

---

# Fabrication, Synthesis and Characterization Techniques

---

## 3.1 Fabrication

### 3.1.1 Introduction

Nanofabrication is the first step of nanoscience and nanotechnology. The fabrication of good quality ordered arrays of nanostructures is required for advanced nanodevices. In addition to that, the nanostructures should be identical in shape and monodisperse in size. In some cases ordered array of nanostructures should be fabricated over macroscopic length scales. In these cases, the physical properties particularly magnetization dynamics for magnetic nanoelements have to be well studied prior to the desired applications. For different experimental studies, the nanostructures should be chemically pure with uniform chemical composition and physically less defective with good surface quality. Another hurdle is the development of cost effective fabrication techniques with a high yield. Various nanofabrication methods have been developed over the years, which we have already discussed in chapter 1. All of them are not able to produce good quality ordered nanostructures. However, good quality samples are always needed for scientific research, because sample quality plays an important role in the intrinsic properties of material. Lithographic methods are found to be the best option for precise fabrication of high quality sample in spite of being a slow and expensive method. In the next section, we will describe optical and electron beam lithography techniques used for fabrication of magnetic blanket thin film and nanodot arrays for our study [1].

### 3.1.2 Optical Lithography

In lithography, different kinds of radiation are used to expose a recording media called resist. Different kinds of lithography techniques have been developed over the decades based on the type of exposure radiation. Out of them optical, electron beam, X-ray and ion beam lithography are widely used for fabrication of ordered array of nanostructures efficiently and precisely. In optical lithography, a photo mask containing the desired pattern is generally used. Therefore, a parallel growth of all the nanostructures is possible. This reduces the fabrication time significantly. However, the main drawback of this process is that the resolution is limited by the diffraction of light. Therefore, it is very difficult to fabricate sub-micron nanostructures by optical lithography.

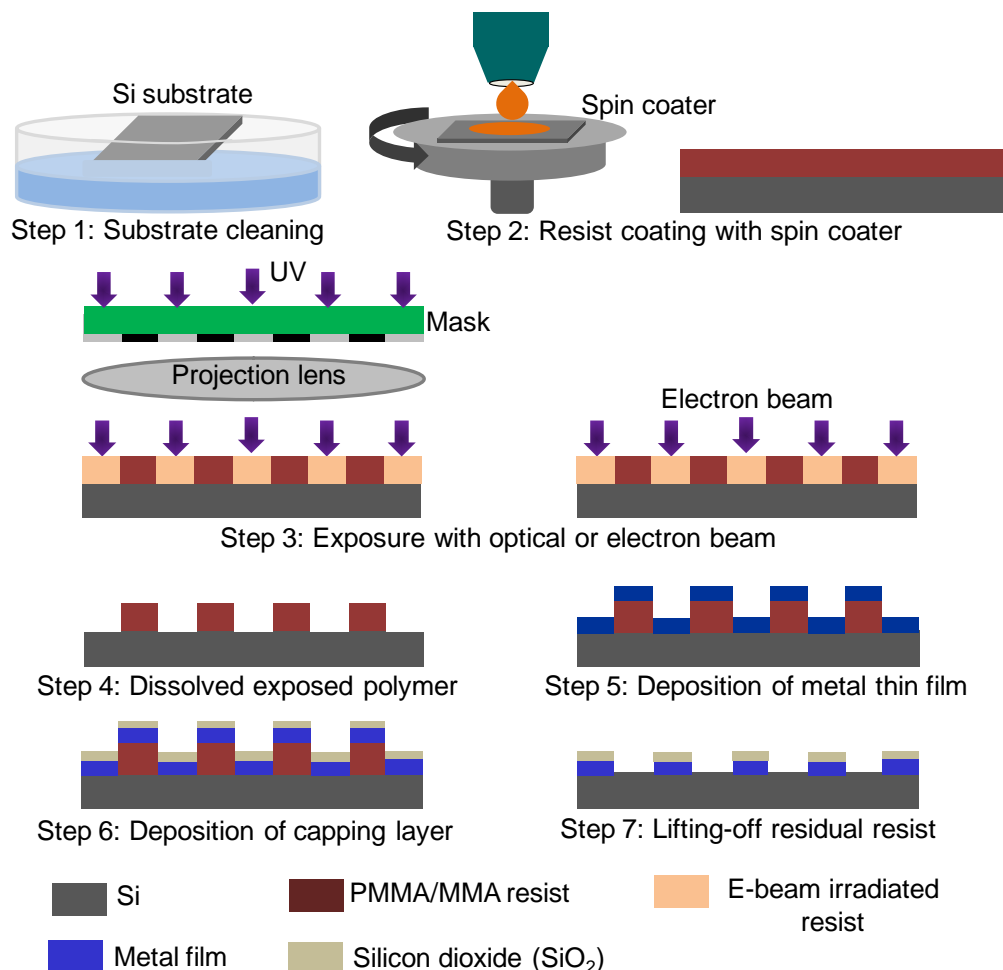


Fig. 3.1: Schematic diagram of optical and electron beam lithography.

We used ultraviolet (UV) photolithography to fabricate  $10 \times 10 \mu\text{m}^2$  Ni<sub>80</sub>Fe<sub>20</sub> (permalloy) blanket film [1-2]. First of all the Si(100) substrate was ultrasonicated in water and acetone for 20 minutes each to remove the inorganic and organic materials from the top

surface of the substrate (Fig. 3.1). The substrate was dried after cleaning by a dry nitrogen gas flow. A uniform layer of positive photoresist dissolved in an organic solvent was then coated on the substrate using a spin coater. The thickness of the photoresist layer was adjusted to about one micron depending upon the viscosity of the resist and the spinning speed [3]. A photo mask (chrome on glass) containing the square patterns to be fabricated was placed on top of the substrate. A convex lens was used in between the source and the mask for uniform illumination of the source on the mask. The polymer chains in the resist were broken at the exposed area after a sufficient amount of exposure. The exposed area was etched out by wet chemical process. The substrate was first put into distilled water at room temperature, rinsed for 60 s and dried using dry nitrogen gas flow. The substrate was then put into MIBK:IPA (1:3) (methyl isobutyl ketone : isopropyl alcohol) solution and rinsed for 30 s. Finally, the substrate was put into acetone, rinsed for 60 s and dried with dry nitrogen gas flow. Subsequently, the two dimensional pattern of the photomask was copied onto the resist as a three dimensional structure. After that a 20 nm thick permalloy film was deposited at a deposition rate of 0.3 nm/s by electron beam evaporation at a base pressure of  $2.0 \times 10^{-8}$  Torr. A thin ( $\leq 10$  nm) layer of silicon dioxide ( $\text{SiO}_2$ ) was also deposited on the permalloy layer by electron beam evaporation to protect it from oxidization or any kind of external damage. Finally, the film deposited on the resist was lifted-off along with the resist leaving only the desired structure onto the surface.

### 3.1.3 Electron Beam Lithography

As electron beams have very short wavelength at large enough accelerating voltage, they are widely used for fabrication of arrays of submicron elements [1, 3]. In our case, the square arrays of permalloy dots with different sizes (50 nm – 200 nm) and separations (50 nm – 400 nm) were fabricated by electron beam lithography. The schematic diagram of the process is shown in Fig. 3.1. At first the substrate was cleaned with water, acetone and IPA (2-propanol) by using an ultrasonicator as mentioned in the paragraph above. Polymethyl methacrylate (PMMA) resist was spin coated onto the cleaned Si(100) substrate for 40 s at a speed of 5000 rpm to prepare a 1.5  $\mu\text{m}$  thick layer of it. Another layer of 1  $\mu\text{m}$  thick methyl methacrylate (MMA) was prepared on the PMMA layer at a rotation speed of 1500 rpm for 90 s. In this way the Si substrate was coated with the bilayer (PMMA/MMA) resist. The reason behind this is to get an undercut edge profile of the resist after development of the pattern onto it. This is because the PMMA layer is developed faster than the MMA layer

forming an overhang structure. The scanning electron microscope (Elionix ELS-7700H) was used to expose the resist with focused electrons. At first, the desired structures were designed in a computer using commercially available design software (Auto CAD). The design files were then converted into the position coordinates defining CELL files and uploaded to the computer interfaced with the lithography system. Ultimately, the design patterns were written onto the resist layers by accelerated electron beam controlled by the attached PC. The beam current and dose time were optimized at 100 pA and 0.9 – 1.0  $\mu$ s. The substrate with the exposed resist was then dipped into the developer solutions, which helped to develop the required 3-D structure onto the resist after etching out the exposed material from the substrate. A 20 nm thick permalloy film was post deposited by electron beam evaporation with an optimized deposition rate of 0.3 nm/s at a base pressure of  $2.0 \times 10^{-8}$  Torr. A 10 nm thick protective layer of silicon dioxide ( $\text{SiO}_2$ ) was also deposited on top of the patterned dots and resist to protect the sample from further oxidization or degradation during the exposure of the laser beam during measurements. The lift-off technique was used to remove the unexposed resist along with the film deposited on it. A clean break-off of the film at the pattern edges of the resist was achieved because of the undercut structure of the edges. Ultimately, the substrate was dipped into acetone for 12 hrs to remove the residual resists.

## 3.2 Synthesis

Synthesis of nanoparticles is a bottom up method. We synthesized spherical Ni nanoparticles with different kinds of clustering geometries. The synthesis procedure is shown schematically in Fig. 3.2. In a typical synthesis of Ni nanoparticles, 45 mM nickel chloride ( $\text{NiCl}_2, 6\text{H}_2\text{O}$ ) was dissolved in ethylene glycol by stirring in a beaker using a magnetic stirrer. Then 0.9 M hydrazine hydrate ( $\text{N}_2\text{H}_5\text{OH}$ , 80%) and 0.1 M sodium hydroxide (NaOH) were added to that solution [4]. The molar ratio of  $\text{N}_2\text{H}_5\text{OH}$  and  $\text{NiCl}_2$  was kept around 20 and *pH* value of the final solution was maintained at around 10. The solution was continuously stirred at 70 – 80°C temperature. When  $\text{NiCl}_2$  is added to  $\text{N}_2\text{H}_5\text{OH}$ , a mixture of nickel hydrazine complex compounds like  $[\text{Ni}(\text{N}_2\text{H}_4)_2]\text{Cl}_2$  and  $[\text{Ni}(\text{N}_2\text{H}_4)_3]\text{Cl}_2$  are formed in aqueous solution [5]. Therefore, the colour of the solution is changed from light blue to light violet. After 30 to 40 minutes of magnetic stirring, the Ni nanoparticles are formed by the reduction of these compounds. Therefore, the colour of the solution turned to grey black indicating the formation of nanoparticles. The reaction can be described by an equation given as:

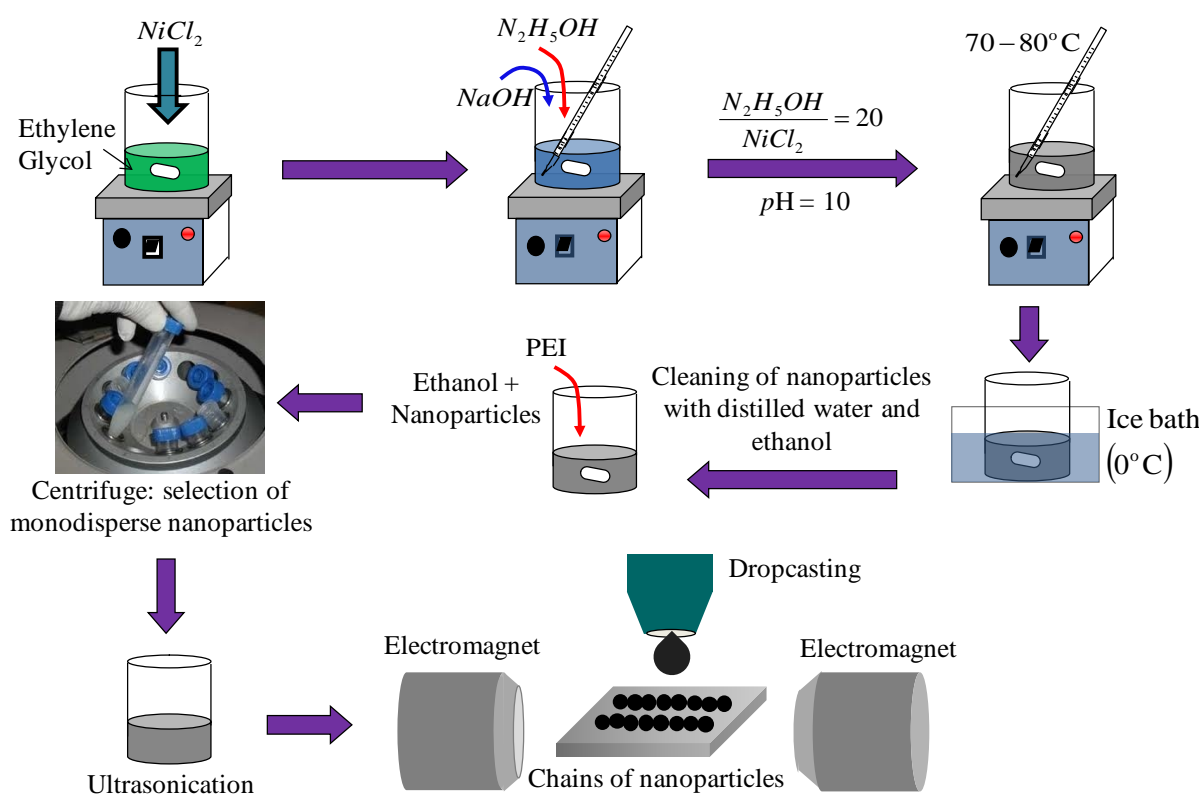
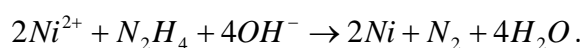


Fig. 3.2: Schematic diagram of synthesis of Ni nanoparticles by hydrazine reduction method.

The reaction was immediately stopped and the beaker was cooled at  $0^\circ C$  by placing it in an ice-bath to avoid random agglomeration of the nanoparticles. Then the uncoated nanoparticles were cleaned for several times using distilled water and ethanol. To coat the nanoparticles with polyethylenimine (PEI), the cleaned nanoparticles were dispersed in distilled water and 1 wt% of PEI was added to the dispersed nanoparticles. The solution was then thermostated for 30-45 minutes at  $25^\circ C$  using ultrasonic bath. The coated nanoparticles were magnetically recovered and dried at room temperature. For the preparation of Ni nanochain, the polymer coated nanoparticles were redispersed in ethanol and centrifuged to select monodispersed single domain nanoparticles. Then a drop of very dilute colloidal solution of monodispersed nanoparticles was placed on a cleaned Si substrate and a large magnetic field ( $> 6$  kOe) was applied in the plane of the Si substrate by an electromagnet. When the nanoparticles were in colloidal form, they were easily aligned along the magnetic lines of force to form one-dimensional chain like structures. When the solution was dried, the chain like structures were retained due to the magnetostatic forces between the constituent nanoparticles. The nanoparticles with different clustering geometries were prepared by

varying the molar concentrations of  $\text{NiCl}_2$ ,  $\text{N}_2\text{H}_5\text{OH}$ , PEI and applying a low magnetic field ( $\sim 250$  Oe) to assist the magnetic interactions between the particles during growth.

### **3.3 Sample Characterization**

#### **3.3.1 Introduction**

Sample characterization is an important step after fabrication. Though we use lithography method for synthesizing magnetic nanodots arrays, the dots deviate from their nominal shapes, dimensions and chemical purity to an extent. The deformation like rounded corners of the square dots is almost always found due to the finite spot size of the optical and electron beams. Sometimes this kind of defect may also appear during the lifting-off of the resist. The defects like inhomogeneity in the shapes and sizes of the dots in an array may appear while using un-optimized dose current and dose time. The edge roughness is another inherent problem, which comes from the roughness of the side walls of resist and arises during the lifting-off of the resist. The defects like inhomogeneity in the chemical composition of the thin film in case of alloy (for example  $\text{Ni}_{80}\text{Fe}_{20}$ ) and impurity come during the deposition of the film. Beyond all these defects, sometimes different kinds of mechanical defects may also come due to the mishandling of the samples. The top surface of sample may also get contaminated if they are not preserved in the vacuum dessicator. The defects are minimized by optimizing the dose current, dose time and lift-off procedure. The right choice of developer solution and time is also required in addition to that. The optimization of deposition parameters is also necessary for getting a good quality of film. The contamination of the sample is prevented by coating the sample with a transparent nonmagnetic material, which is generally unaffected by the environment. Finally, proper handling of sample is always required to keep the samples in a good condition. The characterization techniques for the samples studied in this thesis are described below along with their working principles.

#### **3.3.2 Scanning Electron Microscope (SEM)**

A scanning electron microscope (SEM) is used to investigate surface topography and morphology of samples. In a typical SEM, a stream of electron beam is emitted from a cathode either thermionically or by electric field. We have used both types of scanning electron microscopes. For first case, the electrons are emitted from an electron gun fitted with a tungsten filament cathode. In the second case, the electrons are emitted from a field

emission cathode. The field emission process produces narrower electron beam profile, which helps to get a better spatial resolution than the thermionic emission electrons. The energy of the electrons can be varied from few hundreds eV to few tens of keV. After emission, the electrons are accelerated by applying a gradient of electric field. The beam passes through two electromagnetic lenses, which are called condenser lens (Fig. 3.3). Finally, the beam passes through an electromagnetic scanning coil and is focused onto the sample [6]. The scanning coil deflects the beam in the  $x$  and  $y$  directions (in the plane of the sample) so that it scans in a raster fashion over a rectangular area of the sample surface. When high energetic electron beam interacts with the sample, different types of electrons are emitted or scattered from the sample due to the elastic and inelastic collision of accelerated electrons with the electrons present near the sample surface. The scattered electrons include secondary electrons, backscattered electrons, Auger electrons. The energy is also emitted in the form of characteristic X-rays and visible light (cathodo-luminescence). The secondary electrons are produced by inelastic scattering of incident electrons with the atoms of the sample. In a typical SEM, the secondary electrons are detected by a detector. An image of the sample surface is constructed by comparing the intensity of these secondary electrons to the scanning primary electron beam. Finally, the image is displayed on a monitor.

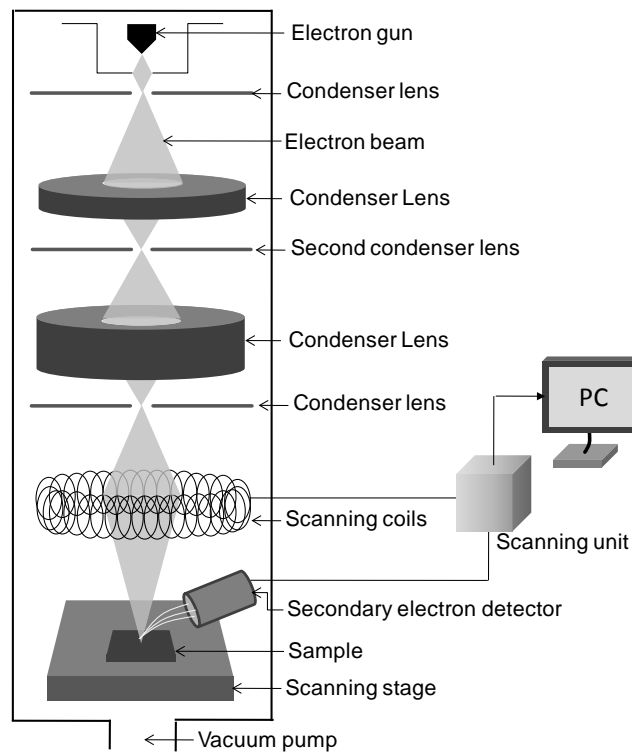


Fig. 3.3: Schematic diagram of scanning electron microscope (SEM).

SEM images have large depth of field due to a very narrow electron beam. Therefore, SEM is capable of producing three-dimensional images, which are very useful for understanding the surface structure of a sample. The samples are generally mounted rigidly on a specimen stub with carbon tape. The specimens should be electrically conductive at the surface and electrically grounded to prevent the accumulation of electrostatic charge at the surface. In our sample characterization “FEI QUANTA 200” and “FEI Helios NanoLab 600” SEM were used.

### 3.3.3 Energy Dispersive X-ray (EDX) Analysis

Energy dispersive X-ray (EDX) analysis is used for the elemental analysis or chemical characterization of a sample. In this technique, the sample is stimulated by a high energy beam of charged particles like electrons, protons or sometimes X-rays. At the ground state, an atom contains a number of electrons moving around the nuclei in different shells. The incident charged particles eject out electrons from an inner shell creating a hole. Consequently, electrons from outer shells (with higher energies) jump to the inner shell to fill up the hole and the difference of energy is radiated in the form of X-ray. Since the atomic structure of each element is unique, the energy of the emitted X-rays, which is basically the characteristics of an element’s atomic structure is also unique in nature. The energy and number of the X-ray are measured by an energy dispersive spectrometer, which is a Si (Li) detector. The energy values give the identification of elements and the relative heights of the peaks give the atomic percentage of the element. In general the EDX spectrometer is attached to SEM. We have used an EDX spectrometer from EDAX attached with “FEI QUANTA 200” SEM.

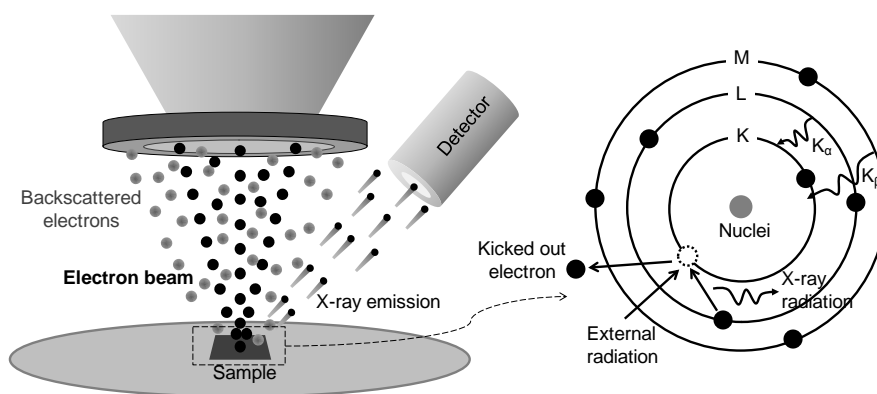


Fig. 3.4: Interaction of accelerated electrons with sample and emission of X-rays is shown schematically.

### 3.3.4 X-ray Diffraction (XRD)

When an electromagnetic radiation interacts with a periodic structure with the periodicity comparable to the wavelength of the incident radiation, diffraction occurs. X-rays have wavelengths in the order of one to few Å. Therefore, when X-ray is incident on the surface of a crystalline solid, the diffraction pattern gives the information about crystal structure. For the characterization of samples used in this thesis, we have used “PANALYTICAL EXPERT PRO” X-ray diffractometer. In this instrument, the  $K_{\alpha}$  radiation (X-ray) from a copper target with an average wavelength ( $\lambda$ ) of  $\sim 1.5418$  Å is used. When this X-ray is incident on the surface of a crystalline material, the atoms within the material elastically scatter the X-ray. In a typical X-ray diffractometer, the incident angle of X-ray is varied between a range of angles in small steps and the reflected intensities of X-rays are measured by a detector placed at the reflected angle. When glancing angle satisfies Bragg’s condition ( $2d \sin\theta = \lambda$ ) (Fig. 3.5(a)), then X-rays reflected from regular array of atoms constructively interfere and intensity peaks appear in the diffraction pattern [7]. In X-ray diffractometer, the intensities of the reflected X-rays are measured as a function of the angle of the reflected beam with respect to the direction of the incident beam. In our system X-ray source is kept fixed while the sample moves at half the rate of the detector to maintain the  $\theta$ - $2\theta$  geometry (Fig. 3.5(b)). Conversion of the diffraction peaks to  $d$ -spacings allows identification of the elements present in the sample because each element has a set of unique  $d$ -spacings. Typically, this is achieved by comparison of  $d$ -spacings with standard reference patterns (*i.e.*, ICSD or Inorganic Crystal Structure Database).

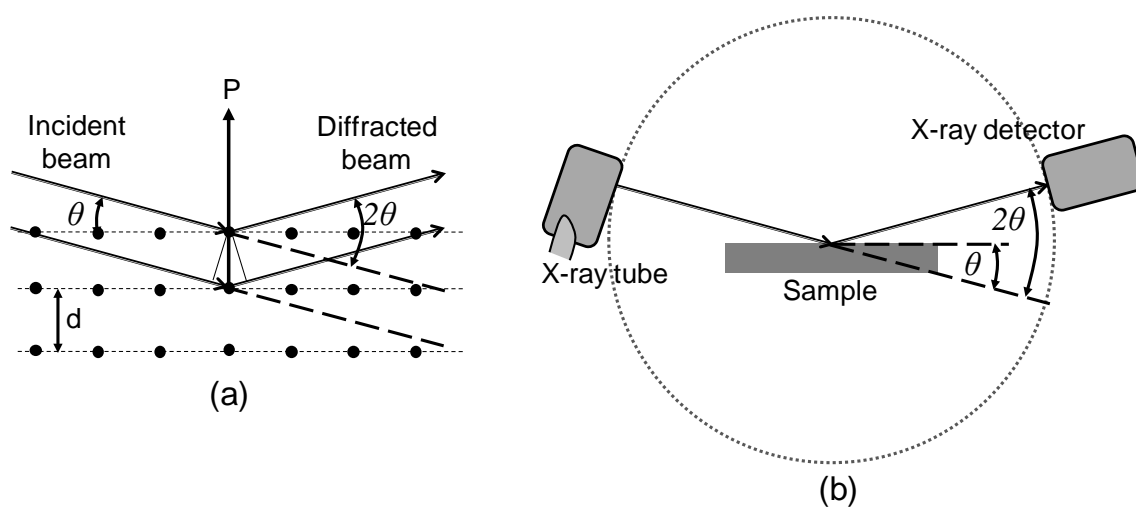


Fig. 3.5: Schematic diagrams of (a) X-ray diffraction with illustration of the conditions required for Bragg’s diffraction to occur and (b) X-ray diffractometer are shown.

### 3.3.5 Vibrating Sample Magnetometer (VSM)

Vibrating Sample Magnetometer (VSM) is used to measure the variation of magnetic moment (magnetization,  $M$ ) as a function of applied magnetic field ( $H$ ) or temperature ( $T$ ) [8]. The schematic diagram of a VSM is shown in Fig. 3.6. The working principle of VSM is based on the Faraday's law, which states that whenever there is a change in magnetic flux through a coil, an electromotive force ( $emf$ ) is induced in the coil. Mathematically,

$$V_{in} = -na \frac{dB}{dt}, \quad (3.3.1)$$

where  $V_{in}$  is the induced  $emf$ ,  $a$  is the area of coil and  $n$  is the number of turns in the coil. Using the relation  $\mathbf{B} = \mathbf{H} + 4\pi\mathbf{M}$ , one can write

$$V_{in} = -na \left( 4\pi \frac{dM}{dt} \right), \quad (3.3.2)$$

if  $H$  remains unchanged.

If the initial magnetization is negligible compared to the induced magnetization, then

$$V_{in} dt = -na(4\pi M). \quad (3.3.3)$$

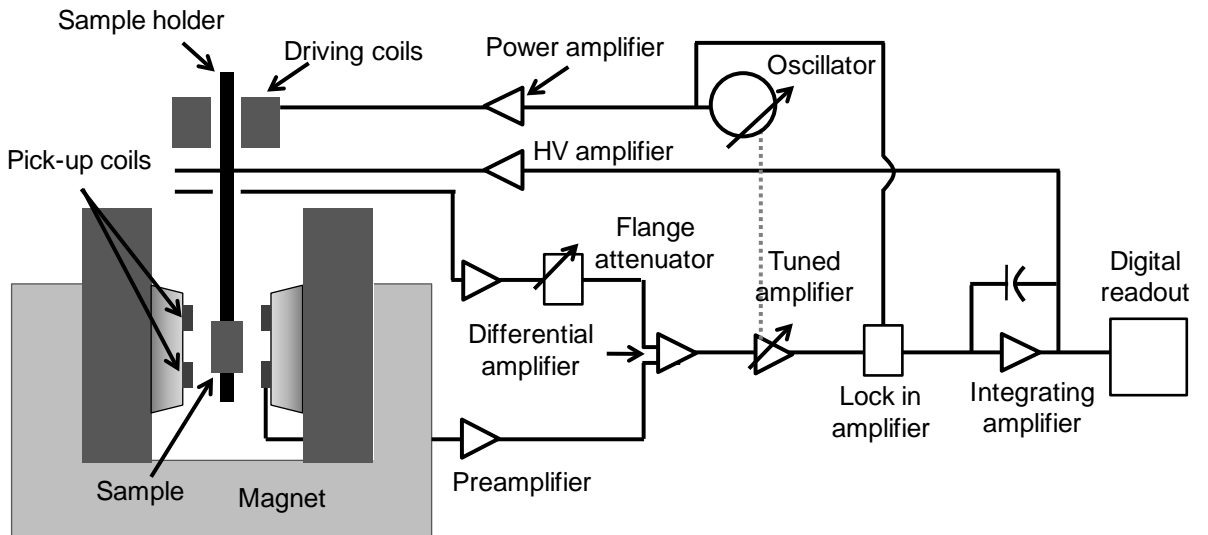


Fig. 3.6: Schematic diagram of Vibrating Sample Magnetometer (VSM).

Therefore, the induced  $emf$  is proportional to the magnetization of the sample. In VSM, the sample is placed inside a uniform magnetic field produced by two pole pieces of an

electromagnet (Fig. 3.6). A vertical nonmagnetic plastic/quartz rod is used to mount the sample. The rod is connected with a piezoelectric transducer assembly located above the magnet. The transducer converts a sinusoidal electric signal (generated by an oscillator/amplifier) into a sinusoidal vertical vibration of the sample rod. The sample then starts to oscillate sinusoidally. A voltage is induced in the stationary pickup coils located in between the pole pieces. The induced voltage in the pick-up coil is proportional to the sample's magnetic moment, but does not depend on the strength of the applied magnetic field as the magnetic field is stationary. In a typical setup, the induced voltage is measured through the use of a lock-in amplifier using the output of the piezoelectric signal as its reference signal. By measuring induced voltage as a function of magnetic field ( $H$ ) of an external electromagnet or temperature ( $T$ ) of the sample, it is possible to obtain the  $M-H$  or  $M-T$  curves of a ferromagnetic material.

### 3.3.6 Atomic Force Microscope (AFM)

Atomic force microscope (AFM) is a very high resolution ( $\sim 10$  nm) scanning probe microscope [9]. AFM is used to image the surface topography of any material. A typical AFM consists of a very tiny sharp tip at the end of a cantilever (Fig. 3.7). The cantilever is made of Si or SiN (silicon nitride) having a very low spring constant. The sharp tip with radius of curvature of few nanometers is fabricated using semiconductor processing techniques. The cantilever scans the sample surface by moving backward and forward across the surface. When the tip is approached to the sample surface, different types of forces, *viz.*, Van der Waals forces, capillary and adhesive forces and double layer forces are exerted on the tip. Among these, Van der Waals force is most commonly associated with AFM. The force exerted on the tip varies with the difference in the surface height and thus leads to the bending or deflection of the cantilever. According to Hooke's law, the bending is proportional to the force on the tip. To measure the bending or deflection a laser beam is reflected from the top surface of the cantilever head into an array of position sensitive photodiodes. When there is a change in the deflection of the cantilever due to the change in interaction force, the reflected laser beam is also deflected. This causes a change in the signal of the photodiode. The sample is mounted on a piezoelectric tube, which can move the sample in the  $z$  direction for maintaining a constant force, and the  $x$  and  $y$  directions for scanning the sample. A feedback mechanism is employed from photodiode to piezoelectric

tube to adjust the tip-to-sample distance to maintain a constant force between the tip and the sample.

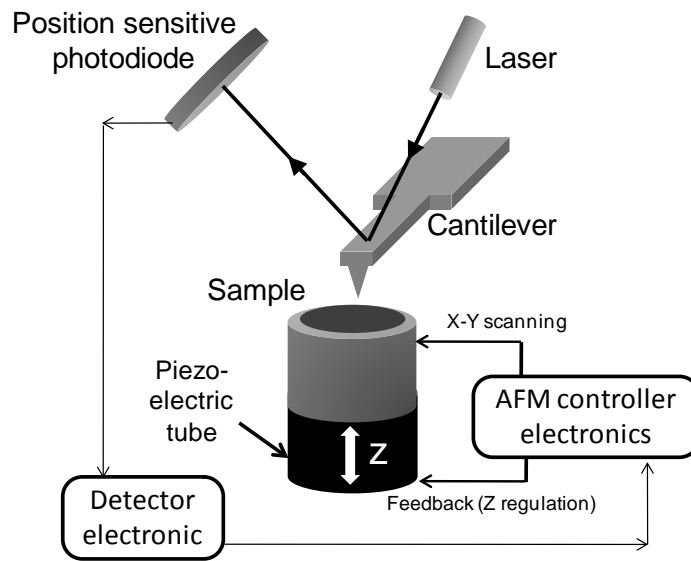


Fig. 3.7: Schematic diagram of an atomic force microscope (AFM).

Primarily, there are three modes of operation: contact mode, non-contact mode and tapping mode. Contact mode or repulsive mode is the simplest mode of operation for AFM. This mode of operation involves sideways scanning by the cantilever tip over the sample surface. The tip utilizes repulsive Van der Waals force with the sample and the scanner gently traces the tip across the sample. However, contact mode yields very low resolution with large soft samples. In the non-contact mode, the tip experiences an attractive Van der Waals force. The cantilever is oscillated at its resonant frequency, where the amplitude of oscillation is typically a few nanometers ( $< 10$  nm) down to a few picometers [10]. The Van der Waals forces, which are strongest from 1 nm to 10 nm above the surface, or any other long range force, which extends above the surface acts to decrease the resonance frequency of the cantilever. This decrease in resonant frequency combined with the feedback loop system maintains a constant oscillation amplitude or frequency by adjusting the average tip-to-sample distance. Measuring the tip-to-sample distance at each  $(x, y)$  data point allows the scanning software to construct a topographic image of the sample surface. In tapping mode, the cantilever is driven to oscillate up and down at near its resonance frequency by a piezoelectric element mounted in the AFM tip holder similar to non-contact mode. However, the amplitude of this oscillation is greater than 10 nm, typically 100 to 200 nm. The interaction forces acting on the cantilever when the tip comes close to the surface such as Van der Waals forces, dipole-dipole interactions, electrostatic forces, etc. cause the amplitude of

this oscillation to decrease or phase to be changed as the tip gets closer to the sample. An electronic servo uses the piezoelectric actuator to control the height of the cantilever above the sample to maintain a set cantilever oscillation amplitude or phase as the cantilever is scanned over the sample.

## Bibliography

1. B. Rana and A. Barman, *SPIN* **3**, 1330001 (2013).
2. A. O. Adeyeye and N. Singh, *J. Phys. D: Appl. Phys.* **41**, 153001 (2008).
3. J. I. Martín, J. Nogués, K. Liu, J. L. Vicent, and I. K. Schuller, *J. Magn. Magn. Mater.* **256**, 449 (2003).
4. S.-H. Wu and D.-H. Chen, *J. Colloid Interface Sci.* **259**, 282 (2003).
5. G.-y. Huang, S.-m. Xu, G. Xu, L.-y. Li, and L.-f. Zhang, *T. Nonferr. Metal. Soc.* **19**, 389 (2009).
6. D. McMullan, *Scanning* **17**, 175 (1995).
7. M. A. Moram and M. E. Vickers, *Rep. Prog. Phys.* **72**, 036502 (2009).
8. S. Foner, *Rev. Sci. Instrum.* **30**, 548 (1959).
9. G. Binnig, C. F. Quate, and C. Gerber, *Phys. Rev. Lett.* **56**, 930 (1986).
10. L. Gross, F. Mohn, N. Moll, P. Liljeroth, and G. Meyer, *Science* **325**, 1110 (2009).

## CHAPTER 4

---

# Static and Time-resolved Magneto-optical Kerr Effect (MOKE) Measurements

---

### 4.1 Introduction

In section 2.8, we have briefly discussed about the background of magneto-optical Kerr effect (MOKE) and the underlying phenomenological theory. Since the discovery in 1877 [1], MOKE has been used as an efficient tool for measuring the magnetic hysteresis loops and imaging of magnetic domains. Later, a variety of MOKE configurations have been developed in the static and dynamic regimes [2-3]. The first time-resolved MOKE measurement was performed by Freeman *et al.* [4] in 1991. Since then, different variants of time-resolved MOKE measurements have been reported over two decades. Some of the important developments are the introduction of time-resolved scanning Kerr microscope [5], all-optical time-resolved MOKE for measurement of ultrafast demagnetization [6] and coherent spin waves [7], application of time-resolved Kerr effect measurements to samples fabricated on opaque substrates [8-9], time-resolved cavity enhanced MOKE measurements [10] and more recently a benchtop time-resolved Kerr magnetometer [11-12]. Over the years, the time-resolved MOKE has emerged as a very powerful technique for non-invasive excitation and probing of ultrafast magnetization dynamics of magnetic thin films, multilayers, arrays of magnetic nanostructures and single magnetic nanodots in the time-domain with an excellent spatio-temporal resolution and measurement sensitivity.

### 4.2 MOKE Geometries

There are three kinds of MOKE geometries, namely the longitudinal, transverse and polar geometries depending upon the orientation of the magnetization vector *w.r.t.* the sample

surface and the plane of incidence of light [12]. In the polar geometry, the magnetization ( $\mathbf{M}$ ) lies perpendicular to the sample surface and parallel to the plane of incidence (Fig. 4.1(a)) whereas in longitudinal geometry,  $\mathbf{M}$  lies parallel to the sample surface and the plane of incidence (Fig. 4.1(b)). The Kerr rotation can be explained qualitatively by considering the interaction of the electric field ( $\mathbf{E}$ ) of the light with the magnetization of the material [13-14]. In a linearly polarized light (let us say  $p$ -polarized light), the electrons in the sample oscillate along the  $E$ -field of the light. For a  $p$ -polarized light, the oscillation is in the plane of incidence of the beam and also in the plane of the sample. Again, a regularly reflected light experiences a  $\pi$  phase change *w.r.t.* the incident beam. Therefore, the direction of  $E$  becomes opposite to the direction of the incident electric field. The Lorentz force ( $F_{Lor}$ ) on the oscillating electrons generates an additional small vibrational component ( $\mathbf{k}$ ) perpendicular to the plane of incidence [13] (Fig. 4.1(a)). The electric field of the reflected light is the vector sum of the original electric field vector ( $\mathbf{r}$ ) and the Lorentz field vector ( $\mathbf{k}$ ). Figure 4.1(a) shows that the vector sum of the reflected light *i.e.*, the resultant electric field of reflected light is rotated due to the magnetization of the sample.  $S$ -polarized light (electric field is perpendicular to the plane of incidence) gives a similar Kerr rotation for the polar effect.

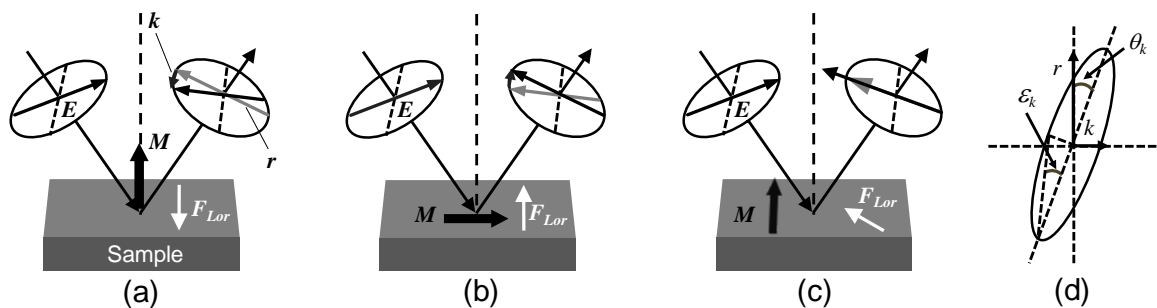


Fig. 4.1: Schematic diagrams of (a) polar (b) longitudinal and (c) transverse MOKE are shown. (d) Geometry of the Kerr rotation ( $\theta_k$ ) and Kerr ellipticity ( $\epsilon_k$ ) is demonstrated.

The longitudinal Kerr effect is not observed at normal incidence as the cross-product is zero. For other incident angles the longitudinal Kerr effect is observed for both  $p$ - and  $s$ -polarized lights (Fig. 4.1(b)). The Kerr rotation ( $\theta_k$ ) and ellipticity ( $\epsilon_k$ ) (Fig. 4.1(d)) are related to each other by a relation:  $\theta_k + i\epsilon_k = k/r$ , in the limit  $k \ll r$  [15]. The third MOKE geometry is called the transverse geometry where  $\mathbf{M}$  lies in the plane of the sample, but perpendicular to the plane of incidence of light (Fig. 4.1(c)). Only  $p$ -polarized light shows transverse Kerr effect. In this case, the reflected beam remains linearly polarized without any Kerr rotation, but the amplitude is changed as magnetization vector changes sign from  $+\mathbf{M}$  to  $-\mathbf{M}$ .

## 4.3 All Optical Time-resolved Magneto-optical Kerr Effect (TRMOKE) Microscope

### 4.3.1 Components Required for Construction of TRMOKE Microscope

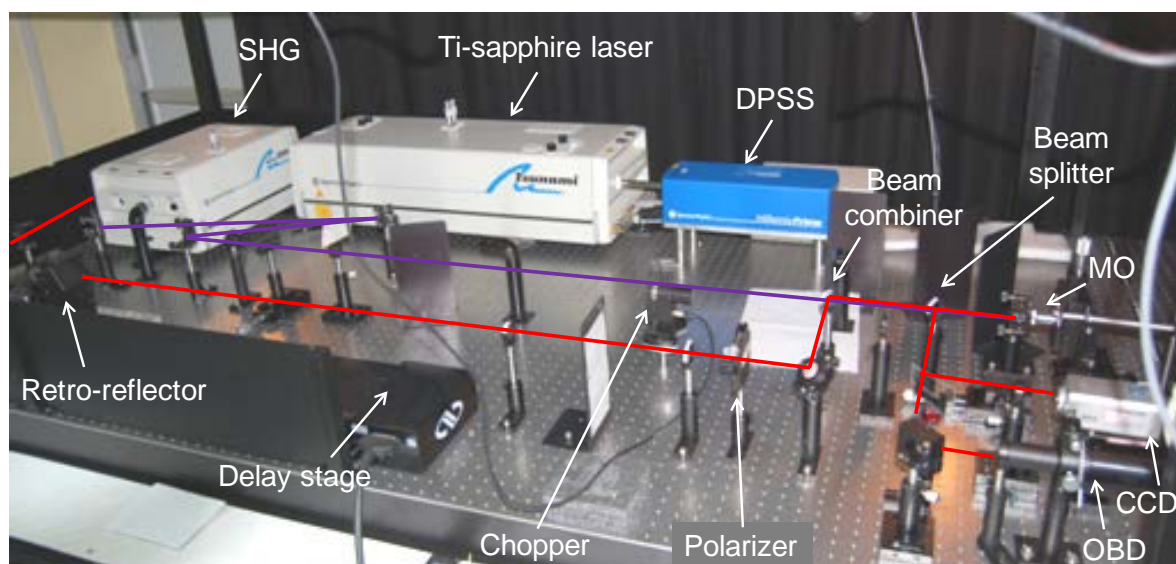


Fig. 4.2: A photograph of the all optical time-resolved magneto-optical Kerr effect (TRMOKE) microscope with collinear pump-probe geometry in our laboratory at the S. N. Bose Centre. The important components in the set up are labeled in the figure.

All optical TRMOKE is a very efficient tool to measure magnetization dynamics of magnetic nanostructures in the time domain. All the TRMOKE results presented in this thesis have been measured by using a TRMOKE set up with a collinear pump-probe geometry developed during the beginning of this thesis work. A photograph of the set up is shown in Fig. 4.2. The important components of the set up are labeled in the figure. The essential components used in general to build the set up are listed below. However, small changes are regularly made to meet the requirements of new types of measurements.

**Table 4.1**

Sl. No.	Name	Company	Model
1	Optical Table	Newport	RS 4000 <sup>TM</sup>
2	Optical Table Enclosure	Home Made	-

3	Diode Pumped Solid State (DPSS) Laser	Spectra Physics	Millenia Pro 10s (with diode laser: model J80)
4	Ti-sapphire Laser	Spectra Physics	Tsunami
5	Second Harmonic Generator	Spectra Physics	3980
6	Retro-reflector	Newport	UBBR1-2S
7	Delay Stage	Newport	(M-)IMS series
8	Motion Controller	Newport	EPS301
9	Optical chopper + Controller	Thorlabs	MC1F60, MC2000
10	Polarizer	Thorlabs	GTH5M
11	Microscope Objective (MO)	Newport	M-10X, M-40X, M-60X
12	Piezo Electric Controller + Piezo Electric $x$ - $y$ - $z$ stage	Thorlabs	BPC203, NanoMax-TS
13	CCD Camera & Monitor	Samsung	SDC-313B
14	Optical Bridge Detector (OBD)	Neoark Corporation	NDT-40110GTP
15	Dielectric Mirrors	Thorlabs	BB1-E02 BB1-E03
16	Optical Filters	Thorlabs	FGB37 FGL610
17	Attenuators, Neutral Density Filters	Thorlabs	NE40B NDL-10C-4
18	Beam Splitters (Non-polarized)	Thorlabs and Newport	EBS1 (50:50) EBP1 (70:30)
19	Lenses	Thorlabs	LA1608 LA1708
20	Lock-in Amplifiers	Stanford Research Laboratory	SR830

21	Mirror Mounts	Thorlabs	KS1, KM100
22	Lens Mounts	Thorlabs	LMR1/M
23	Polarizer Mounts	Holmarc	PMC-25
24	Linear Stage	Holmarc	TS-90-Mu10-01
25	X-Y Stages	Holmarc	TS-90-Mu10-02
26	Oscilloscope	Agilent	DS05032A
27	Digital Multimeter	Rishabh	RISH Multi 15S
28	Spectrometer	Ocean Optics	USB4000
29	IR Viewer	Newport	IRV2-1700
30	Beam Height	Home Made	-
31	Beam Block	Home Made	-
32	Power Meter	Newport, Coherent	407A, FieldMate

### 4.3.2 Description of Lasers

There are three lasers and a second harmonic generator (SHG) used in our TRMOKE set up (Fig. 4.2). The mode-locked Ti-sapphire laser or the Tsunami is pumped by a solid state laser (Millenia), which is again pumped by an array of diode lasers (diode laser array is not shown in the figure). Millenia is therefore called a diode pumped solid state laser (DPSS). Below we discuss the components and working principles of these lasers [16-20].

#### ➤ Diode Laser:

The diode laser can produce a CW output, which is specially designed for producing very high power with a smaller mode volume. The diode laser bars are made from a single

monolithic piece of semiconductor material which contains twenty diode lasers. These bars produce high output power along with the same high efficiency as the discrete diode laser devices. The output of the diode laser is collimated with a cylindrical microlens of high numerical aperture (NA) and the highly asymmetric output beam is coupled into a fiber bundle. This is a patented highly efficient method of coupling the output of diode laser in fiber. This patented method is called *FCbar* technology. The fiber bundle is made of several multimode fibers. Typically 85-90% light of diode laser is coupled into the fiber bundle. The fiber bundle is directly connected to Millenia [18].

➤ **Diode Pumped Solid State (DPSS) Laser or Millenia:**

*Working Principle*

In Millenia, the gain medium is composed of  $\text{Nd}^{3+}$  ions doped in a Yttrium Vanadate crystalline matrix ( $\text{Nd:YVO}_4$ ). The  $\text{Nd}^{3+}$  is a four level system with principal absorption bands in red and near infrared regime. The excited electrons from the lower energy levels go to the upper energy levels and quickly drop to the  $^4\text{F}_{3/2}$  level, which is a metastable state and also the upper level of the lasing transition (Fig. 4.3(a)). A photon of wavelength ( $\lambda$ ) = 1064 nm is emitted due to the transition of an electron from  $^4\text{F}_{3/2}$  level to  $^4\text{I}_{1/2}$  level. Electrons quickly relax to the ground state from  $^4\text{I}_{1/2}$  state. Therefore the population inversion is built up in between energy levels  $^4\text{F}_{3/2}$  and  $^4\text{I}_{1/2}$ . Though there are also transitions at 1319, 1338 and 946 nm, but at room temperature they have lower gain along with a higher threshold value than the 1064 nm transition. These factors and the wavelength selection optics limit the oscillation to 1064 nm [18].

Figure 4.3(b) shows that the monochromatic output of diode laser overlaps with the absorption spectra of the  $\text{Nd}^{3+}$  ion. Therefore, Millenia is efficiently pumped by the diode laser. The efficiency of Millenia is again optimized by focusing the diode laser output on a volume in the active medium of Millenia in such a way that it matches with the radius of  $\text{TEM}_{00}$  mode of Millenia (mode matching) (Fig. 4.4(a)).

The output of Millenia is sampled by using a beam splitter and a photodiode and a feedback is provided from photodiode to the pump laser driver to provide a constant output in power mode operation. A shutter placed outside the cavity acts as a beam blocker (Fig. 4.4(b)). It is opened by the controller. The  $90^\circ$  polarization rotation aligns the polarization axis of output beam vertically.

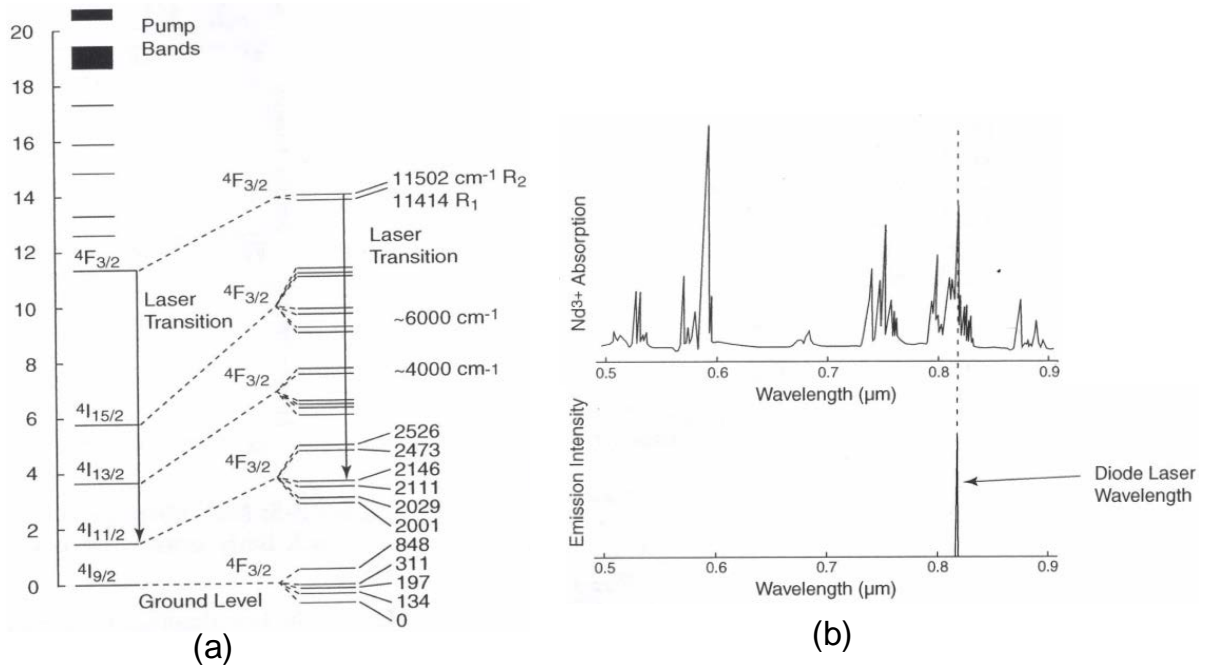


Fig. 4.3: (a) Energy bands and various absorption and emission spectra for  $\text{Nd}^{3+}$  ion are shown. (b) The absorption spectra of  $\text{Nd}^{3+}$  are compared to the emission spectra of a diode laser. The figures are reproduced from Ref. [18].

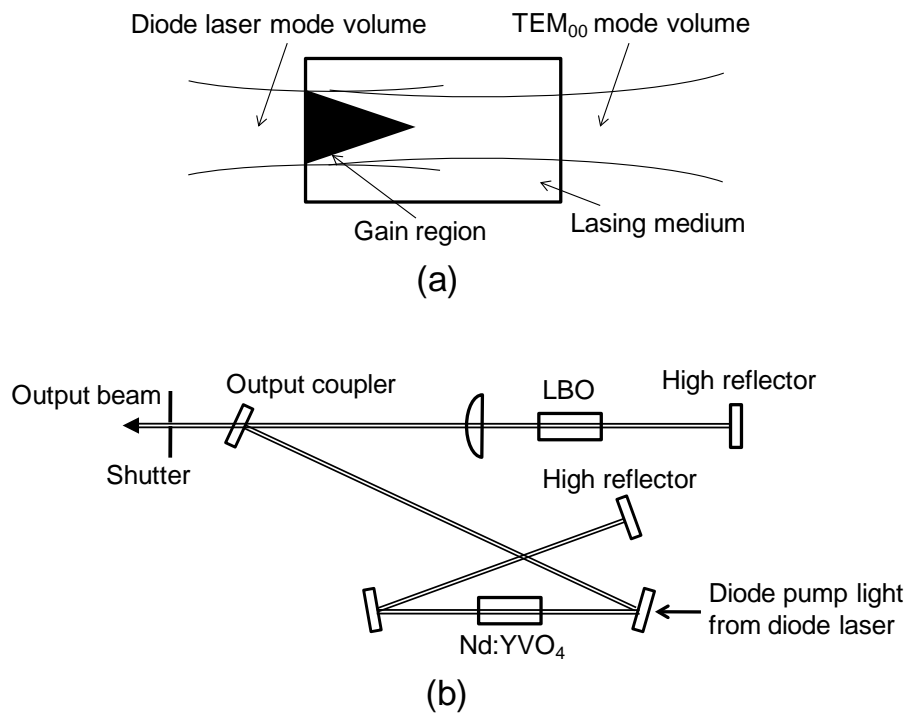


Fig. 4.4: (a) Schematic diagram of mode matching between diode laser mode volume and  $\text{TEM}_{00}$  mode volume of Millenia. (b) Schematic diagram of Millenia laser head. The figures are reproduced from Ref. [18].

### *Frequency Doubling*

The infrared output of Millenia (1064 nm) is converted to visible light (532 nm) by using a lithium triborate (LBO) nonlinear crystal. The efficiency of LBO crystal is a function of temperature. Therefore, a temperature regulating oven is used to maintain the crystal at the appropriate phase-matching temperature to keep the output wavelength fixed to 532 nm and also to optimize the efficiency. LBO keeps the fundamental and the second harmonic beams collinear (noncritically phase matched). For these reasons, the alignment of the laser cavity is not required. Again a large acceptance angle makes it insensitive to any slight misalignment of Millenia. Therefore, in spite of having lower nonlinear coefficient than other materials, LBO is used for frequency doubling in Millenia.

The second harmonic power can be expressed as the following form [18]:

$$P_{2\omega} \propto \frac{d_{eff}^2 P_{\omega}^2 l^2 [\phi]}{A}, \quad (4.3.1)$$

where  $d_{eff}$  is the effective nonlinear coefficient,  $P_{\omega}$  is the fundamental input power,  $l$  is the effective crystal length,  $[\phi]$  is the phase matching factor and  $A$  is the cross section area of the beam in the crystal. As the output power of second harmonic is proportional to the square of the peak power of the fundamental, therefore a high second harmonic power can be achieved by enhancing the intensity of the fundamental light.

#### ➤ **Mode Locked Ti-sapphire Laser or Tsunami:**

##### *Working Principle*

Ti-sapphire is a crystalline material produced by doping  $Ti^{3+}$  ions for a small percentage of  $Al^{3+}$  ions in  $Al_2O_3$  [16, 19]. The vibrational energy bands of electrons in  $Ti^{3+}$  ions are shown in Fig. 4.5(a). The absorption and emission spectra are shown in Fig. 4.5(b). Both absorption transition and fluorescence transition occur over a broad range of wavelength as shown in Fig. 4.5(b) but, the long wavelength side of absorption band overlaps with the short wavelength side of the fluorescence spectrum. Therefore the lasing action is possible only at wavelengths longer than 670 nm.

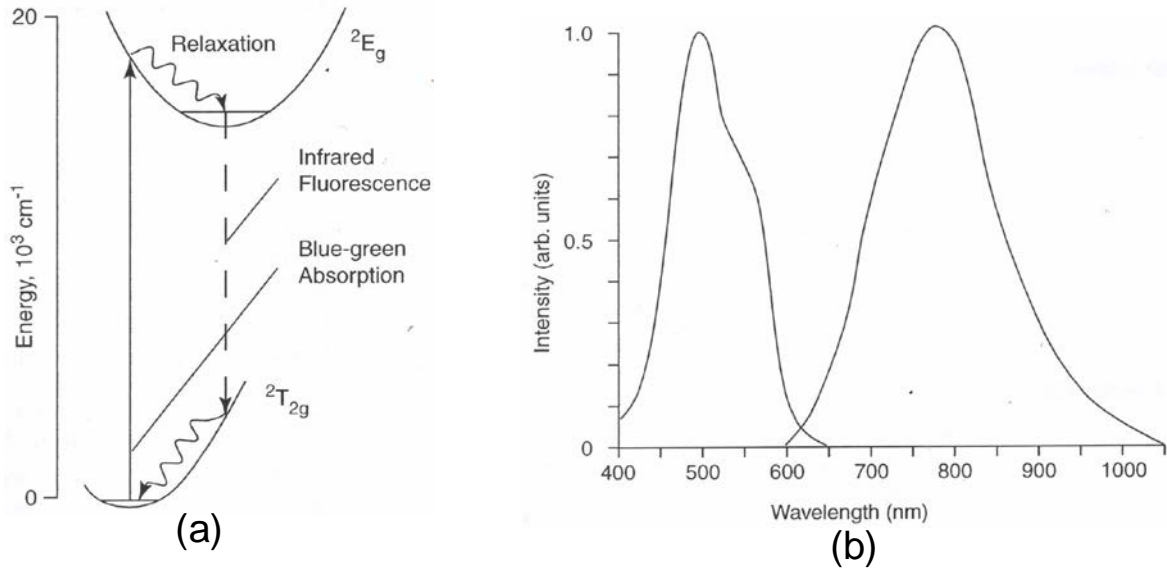


Fig. 4.5: (a) Energy band diagram of the Ti-sapphire crystal. (b) Absorption and emission spectra of Ti-sapphire. The figures are reproduced from Ref. [19].

*Ten-fold Mirror Cavity*

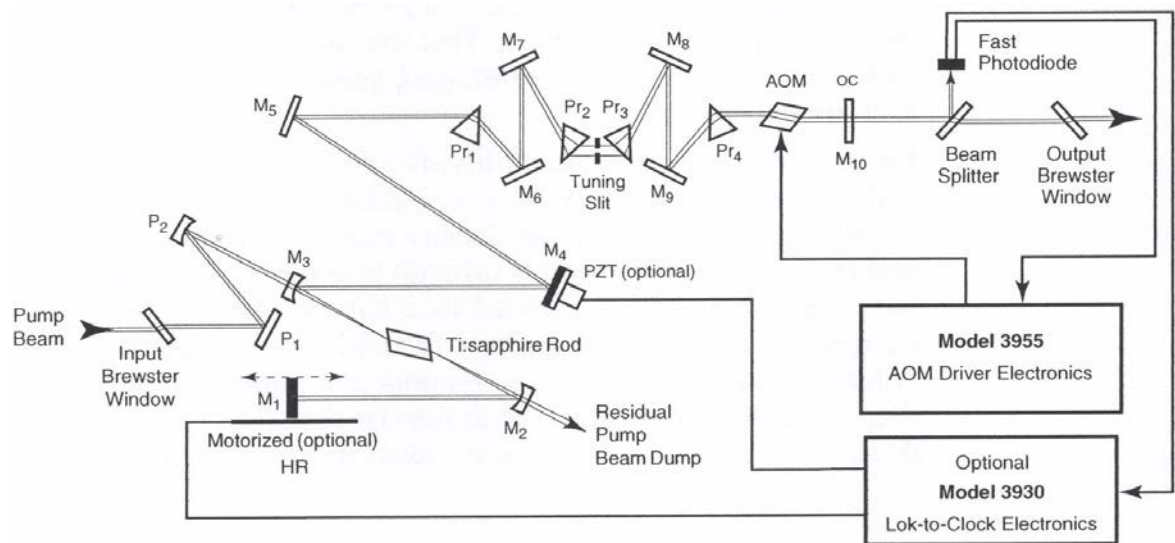


Fig. 4.6: A schematic of the beam path inside the folded cavity of Tsunami. The figure is reproduced from Ref. [19].

To run the Tsunami with a convenient repetition rate (near 80 MHz), the cavity length should be longer than that in a CW laser. Hence, a ten mirror folded cavity is used in Tsunami (Fig. 4.6) to achieve an optimum performance in minimal space. Therefore, an unavoidable problem like astigmatism in the beam may be present if the focusing mirror is

used at an angle other than the normal incidence. This is eliminated by accurately aligning the angles of the cavity focus mirrors and the rod length at Brewster's angle.

Clean and dry nitrogen gas (purity = 99.999%) is constantly purged to the laser head to remove dust and water vapour. A chiller unit keeps the Ti-sapphire rod at a constant temperature for long-term stable performance.

### *Regenerative Mode Locking*

In a CW laser, the longitudinal modes oscillate independently with no fixed phase relationship between each other and the interference among these modes produces constant output intensity. If the modes are locked in phase, then the output will comprise of periodic pulses with a repetition rate  $c/2\eta L$ , where  $c$  is the velocity of light in free space,  $\eta$  is the refractive index of the active medium and  $L$  is the laser cavity length. Let there are  $N$  modes in the laser cavity. The amplitude of the  $n^{\text{th}}$  mode can be expressed as [16]

$$E(t) = E_n e^{i(\omega_n t + \phi_n)}, \quad (4.3.2)$$

where  $\omega_n$  is the frequency and  $\phi_n$  is the phase of the  $n^{\text{th}}$  mode. Let all the modes are in same phase and they have same amplitude *i.e.*,

$$\phi_n = \phi_0 \ \& \ E_n = E_0 \ \text{for all } n.$$

Then, the total amplitude of all the modes can be expressed as

$$E(t) = E_0 \sum_{n=0}^{N-1} e^{i(\omega_n t + \phi_0)} = E_0 e^{i\phi_0} \sum_{n=0}^{N-1} e^{i\omega_n t}. \quad (4.3.3)$$

By defining  $\omega_n$  as

$$\omega_n = \omega_{N-1} - n\Delta\omega, \quad (4.3.4)$$

Eq. 4.3.3 can be written as

$$E(t) = E_0 e^{i\phi_0} \sum_{n=0}^{N-1} e^{i(\omega_{N-1} - n\Delta\omega)t}. \quad (4.3.5)$$

After performing few steps of mathematics the total electric field vector and intensity can be written as

$$E(t) = E_0 e^{i(\phi_0 + \omega_{N-t}t)} \left[ \frac{1 - e^{iN\Delta\omega t}}{1 - e^{-i\Delta\omega t}} \right], \quad (4.3.6)$$

$$\text{and } I(t) = E_0^2 \left[ \frac{1 - e^{iN\Delta\omega t}}{1 - e^{-i\Delta\omega t}} \right]^2 = E_0^2 \frac{\sin^2(N\Delta\omega t / 2)}{\sin^2(\Delta\omega t / 2)}. \quad (4.3.7)$$

The Eq. 4.3.7 can be simplified by taking limit for  $I(t)$  as  $\Delta\omega t/2$  approaching to zero:

$$I(t)_{\text{lim}} = \lim_{\Delta\omega t/2 \rightarrow 0} E_0^2 \frac{\sin^2 N\Delta\omega t / 2}{\sin^2 \Delta\omega t / 2} = N^2 E_0^2. \quad (4.3.8)$$

Therefore,

$$I(t)_{\text{max}} = N^2 E_0^2. \quad (4.3.9)$$

Equation 4.3.9 shows that  $I(t)_{\text{max}}$  is proportional to the square of the number of modes locked in phase. The pulse width can be expressed as

$$\Delta t_p = \frac{2\eta d}{Nc} = \frac{2\pi}{\Delta\omega N} = \frac{1}{\Delta\nu N} = \frac{1}{\text{gain bandwidth}}. \quad (4.3.10)$$

There are a number of techniques for mode locking, namely active mode locking, passive mode locking, additive pulse mode locking and self mode locking. Active mode locking is commonly used in solid state lasers. In Tsunami, acousto-optic modulator (AOM) is used for active mode locking [19]. The modulator is composed of a quartz with two highly polished surfaces that are parallel to the direction of the light propagation. A piezoelectric transducer is attached to one of the quartz surfaces. The transducer is driven by an rf frequency to generate an acoustic wave within the modulator. The acoustic wave is reflected back from the opposite surface of quartz and form standing waves (Fig. 4.7(a)). This introduces a time dependent refractive index grating along an axis perpendicular to the light propagation. If the rf drive is at a frequency  $\omega_{mL}$ , the acoustic grating generated by the standing wave will turn on and off at a frequency of  $2\omega_{mL}$ . The value for this is chosen to be the same as the laser repetition rate. The AOM diffracts light out of the cavity only when the

acoustic grating is present and thus functions as a time dependent loss. In frequency domain, this loss imparts modulation side bands when a wave passes through the modulator. In this manner the AOM communicates the phase between the longitudinal modes of the laser cavity. The main disadvantage of active mode locking is the mismatch between cavity length and the external driving frequency. Therefore, the mode locking becomes unstable quite often. To overcome this, the AOM is driven by the rf signal, which is again driven by a feedback from the laser cavity (Fig. 4.7(b)). If the laser cavity length is slightly changed, the drive signal to the modulator is changed accordingly. This is called regenerative mode locking.

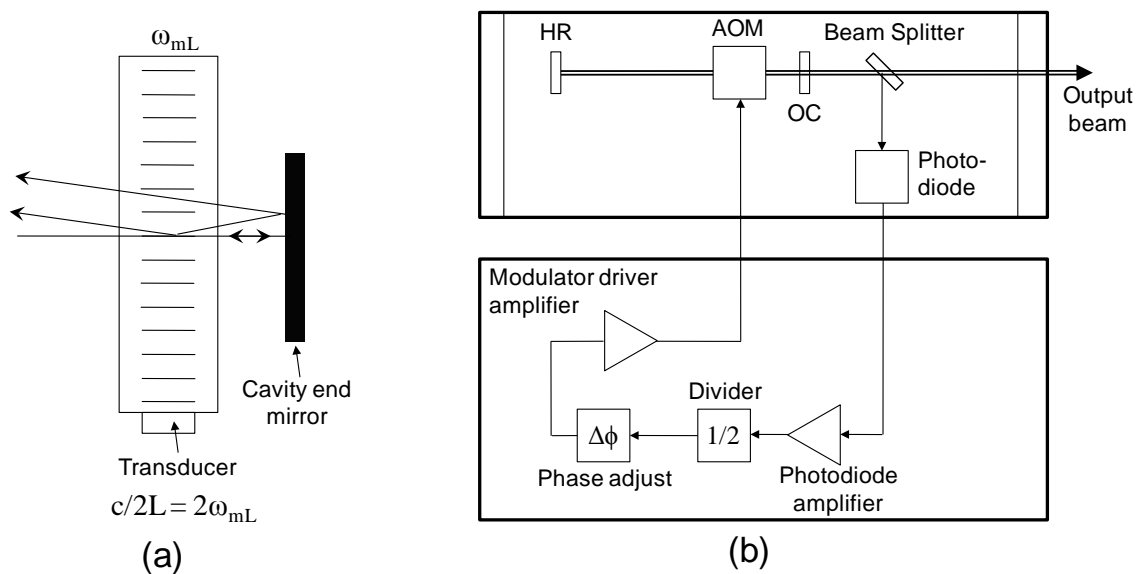


Fig. 4.7: (a) Schematic diagram of an acousto-optic modulator (AOM). (b) The configuration of the electronics for regenerative mode locking. The figure is reproduced from Ref. [19].

### *Group Velocity Dispersion and Wavelength Selection*

The Heisenberg uncertainty principle says that for a pulse of duration  $\Delta t_p$  and bandwidth  $\Delta\nu$ , the product ( $\Delta t_p \times \Delta\nu$ ) will always be greater than a constant value. Therefore, shorter the pulse, greater difference is found between lowest to highest frequency within a pulse. The refractive index of any material is a function of frequency. Therefore, each frequency in a pulse experiences a slightly different refractive index and hence a slightly different velocity. This causes a time separation between different frequencies of pulse. The variation of transit time as a function of wavelength is called as the group velocity dispersion (GVD). When lower frequencies travel faster than the higher frequencies, then that is called positive GVD. When a pulse experiences positive GVD, then the pulse is said to be positively

chirped. Pulses are generally positively chirped as they pass through normal dispersive materials at visible and near IR wavelengths. Again nonlinear index of refraction introduces an intensity dependent index at high intensities.

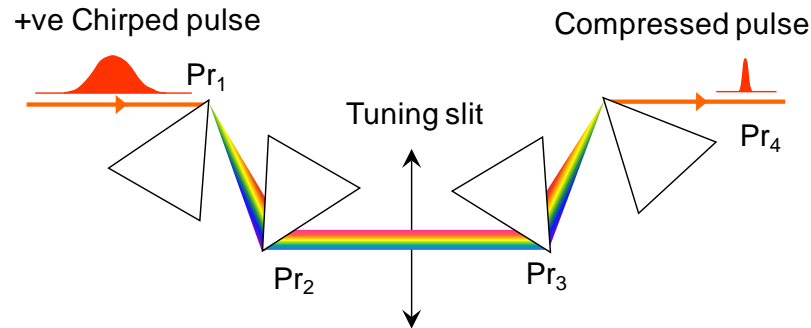


Fig. 4.8: The sequence of four prism used for dispersion compensation in Tsunami laser.

In Tsunami laser, four prism sequence configuration is used to compensate positive GVD (Fig. 4.8). The net intracavity GVD can be changed by translating prisms  $Pr_2$  and  $Pr_3$  perpendicular to their bases. This is achieved by using a single micrometer adjustment (not shown in figure). By translating  $Pr_2$  and  $Pr_3$  further into the intracavity beam, more optical material is inserted into the cavity and net intracavity GVD becomes less negative. The different spectral components of the pulse are spatially spread between prisms  $Pr_2$  and  $Pr_3$ . This allows wavelength selection to be conveniently accomplished by moving a slit between these two prisms in the direction of the spectral spread. Varying the slit width, the output bandwidth and hence the pulse width can be controlled.

### ➤ **Second Harmonic Generator (SHG):**

#### *Working Principle*

A second harmonic generator (SHG) is used to double the frequency of the fundamental beam from the Ti-sapphire laser. SHG uses a barium beta borate (BBO) crystal, which does not require any heater. A schematic diagram of SHG and the optical path inside it are shown in Fig. 4.9 [20]. It shows that mirrors  $M_1$  and  $M_2$  direct the output beam, while mirror  $M_3$  focuses the beam to a small waist into a critically phase matched (angle tuned) type I second harmonic generator. The BBO crystal produces horizontally polarized second harmonic beam, while leaving the residual fundamental vertically polarized. The beam is then passed through a prism ( $P_1$ ) to separate out the second harmonic and residual fundamental beams. The prism has a highly reflective coating at residual fundamental IR wavelength.



### 4.3.3 Description of the Set up

A photograph of our TRMOKE set up is shown in Fig. 4.2. The photograph shows that the entire set up is installed on an L-shaped optical table (two Newport *RS4000 series* tables are joined) with vibration isolation. The optical table is a very important part of any highly sensitive optical experiment like TRMOKE. Our optical table is made of vertically bonded closed cell honeycomb core sandwiched in between two sheets of ferromagnetic material (4.8 mm thick). In this way the stiffness constant of the table is increased and the mass is lowered to increase the resonant frequency of the table well above the external mechanical and acoustic vibration frequency. Therefore, the external vibrations can not resonate the table easily. The core of the table is filled up by broadband and tuned hydraulic dampers to damp out the vibrations and acoustic modes of the table very quickly. The table is placed on top of vibration isolation in floating condition. This isolates the table from the mechanical vibrations originates from the ground. The flatness of the table surface is  $\pm 0.1$  mm over  $600 \times 600$  mm<sup>2</sup> area. The square array of circular holes with 25 mm grid enables mounting of the laser, optics and detectors.

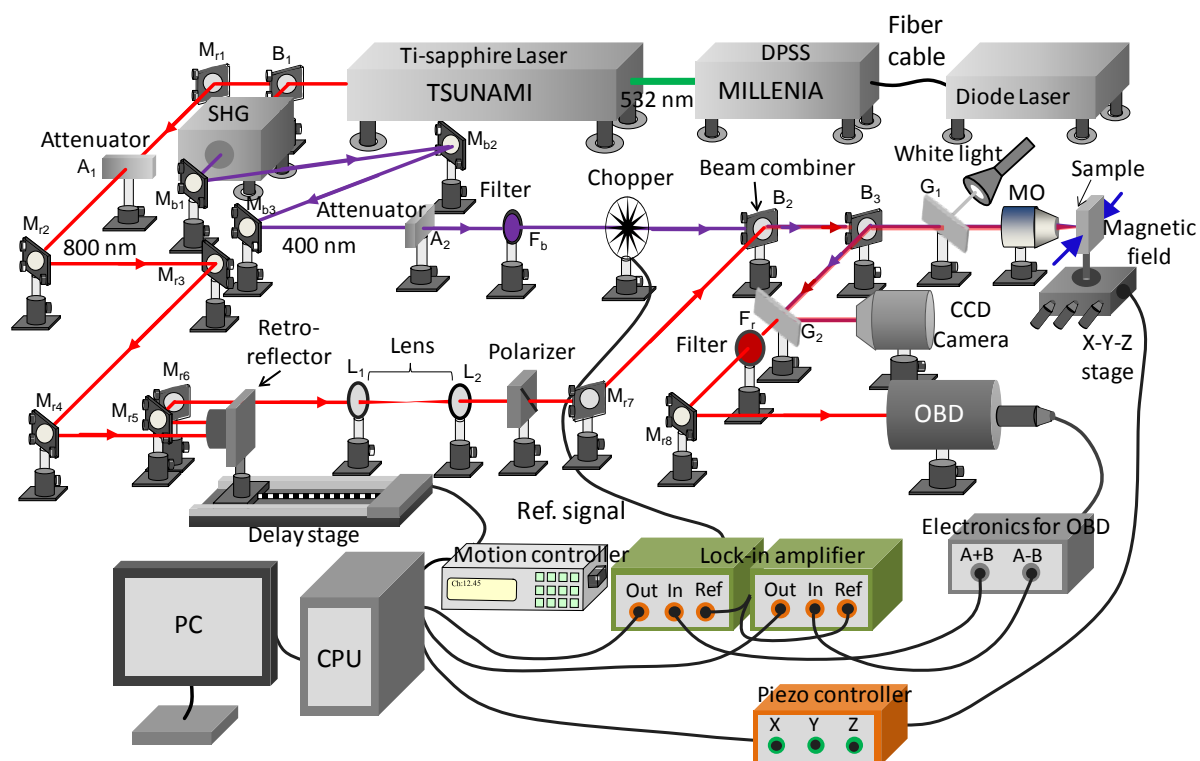


Fig. 4.10: A schematic diagram of an all optical time-resolved magneto-optical Kerr effect (TRMOKE) microscope with collinear pump-probe geometry.

A schematic diagram of the TRMOKE set up is shown in Fig. 4.10. It shows a solid state laser (Millenia) is pumped by an array diode lasers to produce a maximum output power of 10 W at  $\lambda = 532$  nm. The output of the DPSS is used to pump the Ti-sapphire laser (Tsunami). Regenerative mode locking mechanism produces a train of laser pulses with  $\sim 70$  fs pulse width and maximum average power of 2 W at a repetition rate of 80 MHz (25 nJ/pulse). Though, the output wavelength can be tuned from 690 nm to 1080 nm, the output is kept fixed at around 800 nm in our experiments for stable operation and for better spectral response of the Si based detectors at the wavelength.

The output beam from the Ti-sapphire oscillator is vertically polarized and has a spot size of  $\sim 2$  mm. This beam is divided into two parts (70:30) by a beam splitter ( $B_1$ ). The stronger part is frequency doubled ( $\lambda = 400$  nm) by passing into a second harmonic generator (SHG) with pulse width  $\sim 100$  fs. The second harmonic is used to pump the magnetization dynamics whereas the linearly polarized fundamental beam is used for probing. A spectral filter ( $F_b$ ) is placed outside the SHG to filter out the residual fundamental beam, because a trace amount of the fundamental beam mixed with the pump beam can produce a very noisy signal. The pump beam travels through a variable neutral density filter also called an attenuator ( $A_2$ ) and a mechanical chopper after getting reflected from three highly reflecting mirrors ( $M_{b1}$ ,  $M_{b2}$  and  $M_{b3}$ ). The attenuator is coated with a reflecting material such that the reflectivity of the material changes gradually from one end to other end causing a gradual change in the optical density. The transmitted pump fluence can be controlled by moving the attenuator horizontally. The chopper is used to modulate the pump beam at 1-2 kHz frequency, which is used as the reference signal for lock-in detection. The pump path is kept fixed. The fundamental or probe beam is first guided through a fixed optical path by using a set of highly reflecting mirrors ( $M_{r1}$ ,  $M_{r2}$ ,  $M_{r3}$  and  $M_{r4}$ ). A variable attenuator ( $A_1$ ) is also placed in its path to adjust its fluence. The probe beam is then reflected back from a broadband hollow retro-reflector placed on a motorized delay line. The retro-reflector reflects the incident beam in such a way that the reflected beam becomes parallel to the incident beam. The probe path can be varied by moving the retro-reflector back and forth on the delay stage. This is generally done by a motion controller and a PC interfaced with the delay stage through GPIB connection (Fig. 4.10). The beam is then passed through a pair of lenses  $L_1$  ( $f_1 = 75$  mm) and  $L_2$  ( $f_2 = 200$  mm) arranged in a telescopic arrangement, which collimates the beam and increases the beam diameter to  $\sim 5$  mm so that it fills the back-aperture of the microscope objective. The beam is then passed through a Glan-Thompson polarizer with

extinction coefficient of 100,000:1, which refines the polarization state of the probe beam to a very high quality.

After that, both the pump and probe beams are combined with the aid of a 50:50 non-polarized beam splitter set at  $45^\circ$  to the optical path of the probe beam, which acts as a beam combiner. The beams are made collinear from this point with the help of steering mirrors (particularly  $M_{r6}$ ,  $M_{r7}$ ,  $M_{b1}$ ,  $M_{b2}$  and  $M_{b3}$ ). The combined beams pass through a 50:50 non-polarized beam splitter  $B_3$  and a glass slide ( $G_1$ ) both set at  $45^\circ$  to the optical path before entering into a microscope objective (MO: M-40X) at normal incidence, which focuses the probe beam on the sample surface. The tilt of the sample is carefully adjusted so that it is precisely normal to the axis of the microscope objective and also to the directions of the pump and probe beams. The sample is generally hold by using a suitable sample holder, which is mounted on a computer controlled piezo-electric scanning  $x$ - $y$ - $z$  stage. The probe beam is focused to a diffraction limited spot size ( $\sim 800$  nm) at the sample surface with the help of the MO (N.A. = 0.65) and the  $z$ -travel of the piezoelectric stage. The pump beam is spatially overlapped with the probe beam after passing through the same MO in a collinear geometry. The probe beam is carefully placed at the centre of the pump beam, where the later is slightly defocused with a spot size of  $\sim 1$   $\mu\text{m}$  due to the chromatic aberration. The optical arrangement of the microscope objective, sample and the pump and probe beams is shown in Fig. 4.11(a).

Both the back-reflected pump and probe beams from the sample surface come out from the MO and are then reflected by the beam splitter  $B_3$  ( $B_3$  is placed in between the beam combiner  $B_2$  and the MO) by  $90^\circ$  angle *w.r.t.* the incident beam. Small fractions of the reflected pump and probe beams are sent (after reflection from a glass slide  $G_2$ ) to a CCD camera for viewing the pump and probe beams and the sample surface. A white light source is used to illuminate the sample surface. The white light is reflected by a glass slide ( $G_1$ ) placed in between  $B_3$  and MO and is focused onto the sample surface through the MO. The back-reflected white light from the sample enters into the CCD camera after reflection from  $B_3$  and the glass slide ( $G_2$ ). This arrangement enables us to view the sample structure with sub- $\mu\text{m}$  spatial resolution such that we can locate the exact position where the pump and probe beams are focused onto the sample. The CCD camera also helps to check the overlap of the pump and probe spots on the sample surface. The major parts of the pump and probe beams are sent through a spectral filter ( $F_r$ ) to filter out the pump beam before sending only the probe beam into the optical bridge detector (OBD).

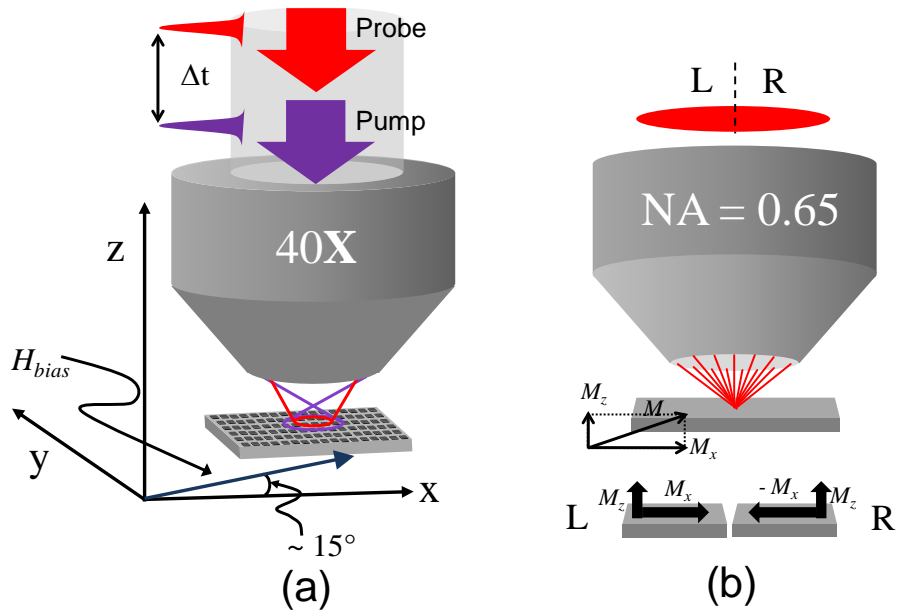


Fig. 4.11: (a) Schematic diagram showing the collinear geometry of pump and probe beams focused by a microscope objective (MO) on the sample surface. (b) The longitudinal and polar Kerr rotations of the left and right portions of the incident probe beam. When the intensities of the two halves of the beam cross-section are added, the longitudinal Kerr components cancel each other leaving only the polar Kerr component.

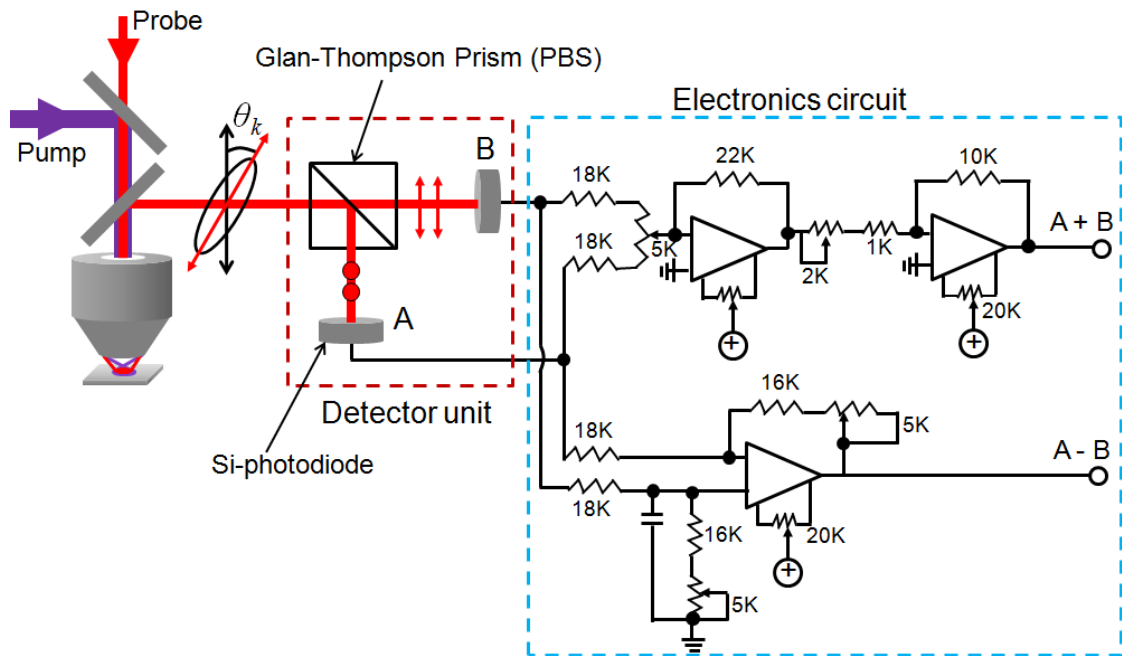


Fig. 4.12: Schematic diagram of the optical bridge detector unit is shown along with the electronics circuit, which amplifies and processes (A + B) and (A - B) signals.

The microscope objective has a numerical aperture of 0.65 with working distance 0.6 mm. This allows a cone of rays with varying angles of incidence up to  $40^\circ$  to incident on the

sample. All rays with non-zero angles of incidence will carry information about the longitudinal Kerr rotations, if any, present in the magnetization dynamics. The longitudinal Kerr rotation in the left and right halves of the cones will have equal magnitudes with opposite signs (Fig. 4.11(b)). However, since in our measurements we have not used split photodiodes to separately collect the two halves of the circular cross-section of the beam, the longitudinal Kerr effect gets averaged out to negligible net value and we primarily measure the polar Kerr rotation (Fig. 4.11(b)). If the incident beam is not perfectly normal to the sample/MO or the beam does not travel along the axis of the MO, there will be a finite longitudinal Kerr rotation component mixed with polar Kerr rotation.

The magnetization dynamics is measured by measuring the polar Kerr rotation by means of an OBD. The OBD splits the incident polarized beam into two orthogonally polarized components by a polarized beam splitter (PBS) (Fig. 4.12). The intensities of two beams are then measured by two Si-photodiodes A and B. The PBS is placed at  $45^\circ$  to the light incident on the OBD so that when a linearly polarized light (in the absence of Kerr rotation) passes through the PBS, the intensities of lights in two orthogonal components of polarization are identical, giving rise to a “balance” in the bridge ( $A - B = 0$ ). When the pump beam is incident on the sample, the sample magnetization changes with the time delay between the pump and the probe beams due to the ensuing magnetization dynamics. This causes a Kerr rotation ( $\theta_k$ ) of the reflected probe beam. This Kerr rotation modifies the intensities in the two orthogonal components of polarization and gives rise to a finite electronic signal at the output of the optical bridge detector ( $A - B \neq 0$ ). The signal ( $A - B$ ) can be calibrated to obtain the precise value of the Kerr rotation. Therefore, measurement of ( $A - B$ ) as a function of time delay gives information about the magnetization dynamics including ultrafast demagnetization, remagnetization, magnetization precession and damping. On the other hand, the sum of the readout signals from the two photodiodes ( $A + B$ ) gives the total reflectivity signal and gives information about the dynamics of the electronic state of the sample as well as the acoustic modes. The signals A and B from the photodiodes are sent to the electronic circuit as shown in Fig. 4.12. The electronic circuit amplifies the signals by two equal gain and low noise pre-amplifiers and processes the signals by sum and difference amplifiers to give outputs as A, B, ( $A - B$ ) and ( $A + B$ ). These outputs are regularly checked while aligning and optimizing the function of the OBD. In our set up the PBS and the two photodiodes A and B are mounted on a stage attached with a precision rotation mount, while the electronic signal processing is done in the circuit placed in a separate box, which

improved the stability of the signal and the ease of optical alignment. The Kerr rotation and the reflectivity signals are measured separately by two lock-in amplifiers (SR830) in a phase sensitive manner. The pump beam is modulated by a chopper at a fixed low frequency of 1-2 kHz and the frequency of the chopper is used as the reference signal for the lock-in detection.

The geometry of a dc bias magnetic field is shown in Fig. 4.11(a). The magnetic field is applied at a small angle ( $\sim 15^\circ$ ) to the sample plane. Initially the component of the applied magnetic field in the sample plane is well above the in-plane saturation field of the sample. The magnetic field strength is then reduced to the bias field value ( $H =$  projection of bias field in the plane of the sample), which ensures that the magnetization remains saturated along the bias field direction. The bias field is tilted by about  $15^\circ$  from the plane of the sample to have a finite demagnetizing field along the normal direction (along  $z$ -axis) to the sample. This demagnetizing field is eventually modified by the pump pulse to induce the magnetization precession within the sample and we measured the corresponding polar Kerr rotation for the out-of-plane component of the precession orbit of the tip of the magnetization vector.

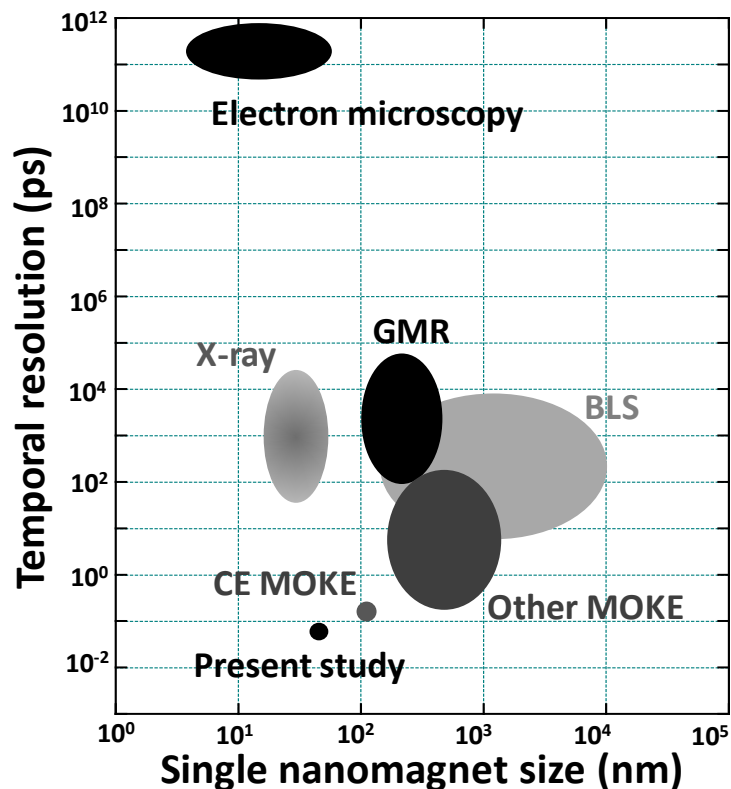


Fig. 4.13: A schematic representation of the comparison of the spatio-temporal resolution of different techniques for the measurements of the time-resolved magnetization dynamics of single (isolated) nanomagnets.

The collinear pump-probe geometry enables us to achieve a diffraction limited spatial resolution of about 800 nm simultaneously with a temporal resolution of about 100 fs limited by the cross-correlation between the pump and probe pulses. The balanced photodetector or OBD enables us to get a very high measurement sensitivity of Kerr signal ( $\sim \mu\text{deg}$ ) because a small variation of the Kerr rotation or ellipticity can be measured on top of a zero or negligible background. Figure 4.13 represents a schematic diagram of a comparison of temporal resolution and size of the individual dot measurement sensitivity among different measurement techniques. Among them the electron microscopy has very good spatial resolution but poor temporal resolution. Brillouin light scattering, X-ray microscopy and magnetoresistance based techniques have intermediate temporal and spatial resolution. Cavity enhanced magneto-optical Kerr effect (CE-MOKE) microscope has shown the best spatio-temporal sensitivity so far. Using the collinear micro-focused pump-probe techniques we have achieved a spatial sensitivity below 100 nm for the measurements of isolated dots along with a temporal resolution of  $\sim 100$  fs. We have achieved an overall improvement by a factor of about 3 than the previously published results.

#### **4.3.4 Construction of the TRMOKE Microscope and Alignment Procedure**

The important feature of our TRMOKE microscope is the collinear pump-probe geometry with a remarkable spatio-temporal sensitivity and resolution. However, it requires very high precision optical alignment of the set up to achieve the above. The TRMOKE set up was developed on top of high quality optical table by assembling a number of optics, precision mounts and motion controlled stages. The temperature, humidity and dust level in the laboratory is carefully controlled to avoid large long-term drift of the alignment. Yet, small amount of misalignment of the laser and the optical components lead to a lower spatial resolution and lower signal-to-noise ratio. A complete alignment was performed during the construction of the set up. In addition to that, systematic minor alignments are often required to achieve good quality signal from the set up. Below, a step by step systematic alignment procedure is described that were performed for the development and maintenance of the set up during this thesis.

##### **➤ Alignment of the Optical Table**

The alignment of the optical table was done during its installation. The routine alignment of the optical table is not necessary. The optical table was installed on the ground

floor of the laboratory in such a way that the flat surface becomes exactly parallel to the horizontal base of the ground. The tilt of the optical table was checked by spirit level and removed by adjusting the heights of the mounting legs. The table is kept under floating condition with a low noise air compressor attached to the air line manifold feeding air to each of the isolator legs. It uses a laminar flow damping, which employs many tiny orifices, resulting in greater damping efficiency. The hybrid chamber design minimizes air volume between piston motion and damper airflow. It has built in leveling indicators, which provide visual feedbacks ensuring the table is properly floating at the correct level.

➤ **Alignment of the Lasers**

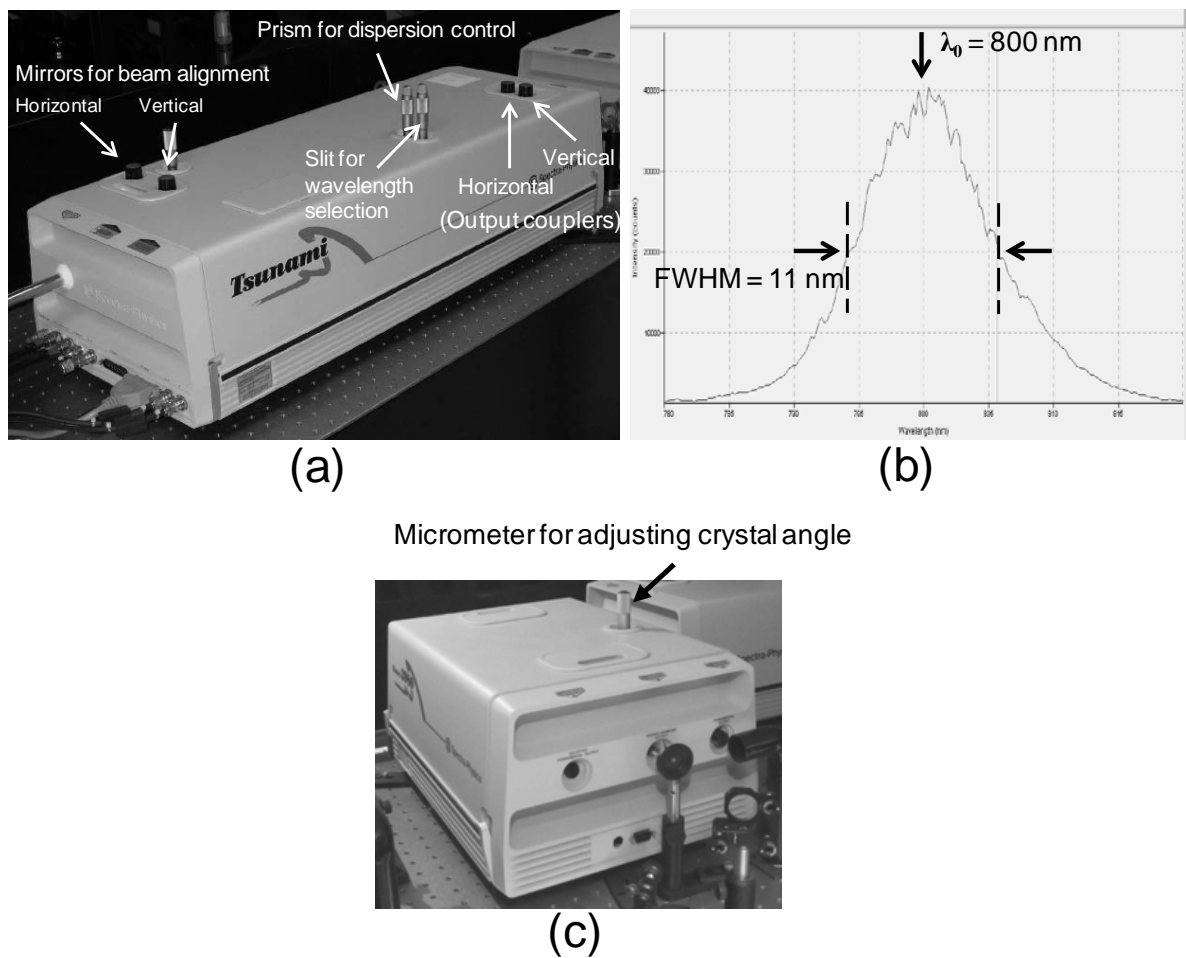


Fig. 4.14: (a) A photograph of the femtosecond oscillator (Tsunami) showing different external laser head controls. (b) A typical mode-locked power spectrum of the output beam from Tsunami. (c) A photograph of the SHG showing the external micrometer screw for adjusting the BBO crystal angle.

The lasers (Millenia, Tsunami) and SHG were installed on the optical table. For stable operation of Millenia an optimized diode current and temperatures of diode laser were set

first. However, routine alignments of the lasers are performed after switching on or before starting the experiment. While switched on, the cavity of Tsunami is continuously purged with ultra high pure (99.999%) dry N<sub>2</sub> gas, which protects the cavity optics from humidity and dust and gives a long-term stability of the output power and laser pulse width over several hours of the measurement. After the laser is switched ON and allowed a warm up time of about 45-60 minutes for a stable mode locking, we first monitor the power spectrum of the output beam from Tsunami by a fiber optic spectrometer (Ocean Optics model no. USB4000). The central wavelength ( $\lambda_0$ ) of the spectra is set close to 800 nm (Fig. 4.14 (b)) and the full width at half maxima (FWHM) is adjusted to greater than 10 nm by iteratively adjusting the micrometer drives for the slit for wavelength selection and the prisms for dispersion control as shown in Fig. 4.14(a). The laser output power is routinely optimized by primarily adjusting the cavity end mirrors and occasionally by the output couplers. The output beam from the Tsunami is divided into two parts (70:30) by the beam splitter (B<sub>1</sub>). The stronger part goes through the SHG. For an efficient conversion of the fundamental beam to its second harmonic, the input beam is guided through the path inside the SHG as shown in the Fig. 4.9. The beam path is controlled externally by aligning the beam splitter B<sub>1</sub> with the horizontal and vertical screws attached to it and by adjusting the phase matching angle of the BBO crystal inside the SHG through the external micrometer screw as shown in Fig. 4.14(c). If required, the internal optics of the SHG are also adjusted for a thorough alignment of the set up. A good spatial profile of the pump beam *i.e.*, output beam from SHG is required for better overlapping of pump and probe beams on the sample. A circular beam profile with uniform Gaussian distribution of the power within the beam profile (*i.e.*, close to TEM<sub>00</sub> mode) is desirable for both pump and probe beams. While for the fundamental laser coming out of the Tsunami a TEM<sub>00</sub> mode is almost always obtained, care has been taken in the alignment of the SHG to obtain this desirable beam profile.

#### ➤ **Alignment of Mirrors Before Retro-reflector**

The weaker part of the fundamental beam is guided by the mirrors M<sub>r1</sub>, M<sub>r2</sub>, M<sub>r3</sub> and M<sub>r4</sub> up to the retro-reflector (Fig. 4.10). The beam is made horizontal by keeping the beam height fixed at a certain value (14.4 cm, from the top surface of the optical table) with the help of four mirrors. A ‘beam height’ is used to aid the alignment. The beam is always aligned in a rectangular path cutting across a set of holes on the optical table for the convenience of alignment.

➤ **Alignment of Retro-reflector**

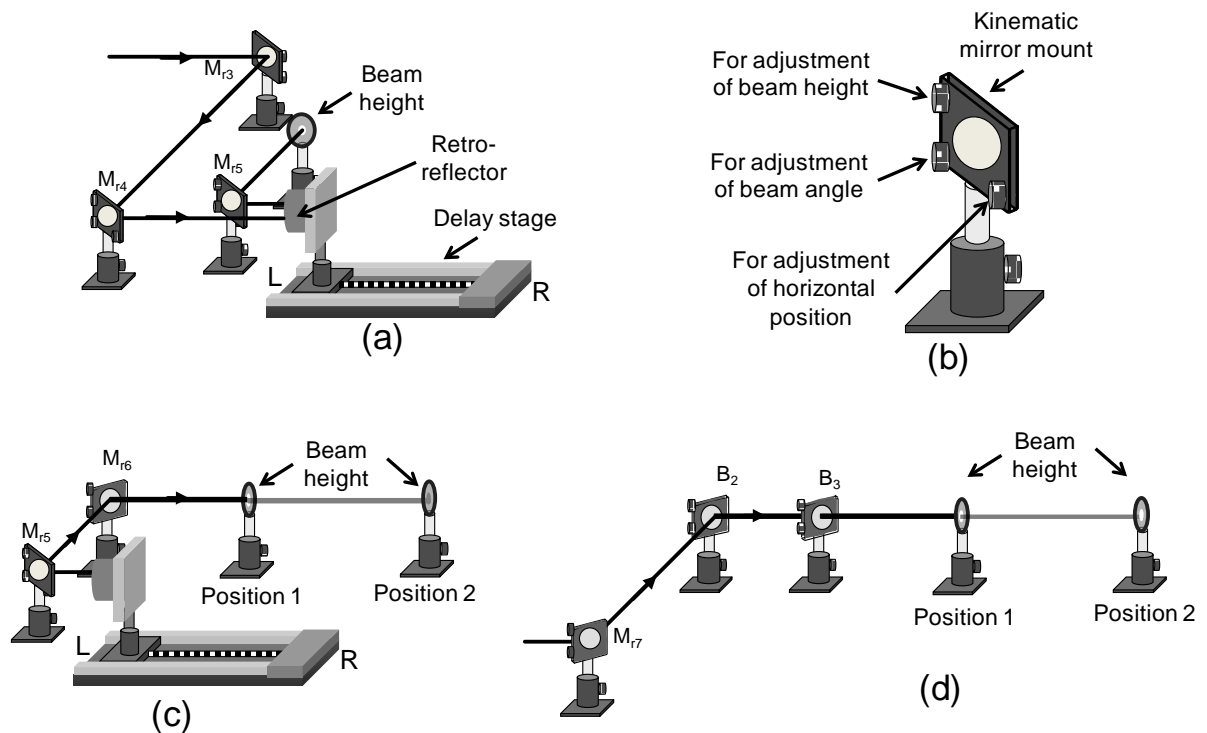


Fig. 4.15: (a) Alignment procedure of the retro-reflector is shown schematically. (b) The schematic diagram of a kinematic mirror mount along with the screws on it is shown. Alignment procedure of probe beam is shown schematically (c) just after the retro-reflector and (d) after the polarizer.

The alignment of retro-reflector is done by a simple method. The method is schematically shown in Fig. 4.15(a). The retro-reflector is mounted on a small table with set of M6 holes on the delay stage with the help of post and base mounts. The purpose is to align the axis of retro-reflector and the axis of motion of the delay stage exactly parallel to the incident beam path. At first the delay stage is placed on the optical table in such a way that its axis becomes parallel to an imaginary line going through the set of holes. A ‘beam height’ is placed after the mirror  $M_{r5}$ . When the retro-reflector is at the extreme left side (L) of the stage, the vertical (14.4 cm) and horizontal positions of the beam are adjusted by mirror  $M_{r3}$  with the help of screws attached to its mount as shown in Fig. 4.15(b). The beam should go through the middle of the hole in the ‘beam height’. The retro-reflector is then moved to the extreme right side (R) of the delay stage by the motion controller. The position of the beam on ‘beam height’ will be shifted from the hole as the incident beam and the axis of the delay stage may not be exactly parallel. The position of the beam is then adjusted to its previous position (hole on the ‘beam height’) with the help of mirror  $M_{r4}$ . The retro-reflector is again moved to left end of delay stage and the beam position is adjusted by mirror  $M_{r3}$ . This

procedure is continued iteratively till the beam position remains unchanged when the retro-reflector is placed at two extreme ends of the delay stage. After that the beam height is shifted to a much far away position from the retro-reflector (typically 3-4 m) and the above procedure is again performed for finer alignment of the retro-reflector. At this point, we can say that the incident beam has become precisely parallel to the motion axis of delay stage and the alignment of the retro-reflector is considered to be complete.

### ➤ **Alignment after the Retro-reflector**

After the retro-reflector the beam is sent through the path as shown in Fig. 4.10. For the alignment of the probe beam just after the retro-reflector, the mirror  $M_{r6}$  is placed on the optical table and the beam is approximately made parallel to the line of holes on the optical table. The 'beam height' is placed after the mirror  $M_{r6}$ . Two positions on the optical table are marked as 'position 1' and 'position 2' so that an imaginary line joining the two positions should be exactly parallel to the line of holes on the optical table. The 'beam height' is first placed at 'position 1'. The mirror  $M_{r5}$  is aligned, so that the beam goes through the middle of the hole in the 'beam height'. The 'beam height' is then placed at 'position 2' and the incident point of the beam on the 'beam height' is adjusted to the hole by using  $M_{r6}$ . The 'beam height' is again moved back to 'position 1' and the beam is aligned by mirror  $M_{r5}$ . A number of iteration is performed until the beam is fully aligned at the two positions of the 'beam height'. After that two convex lenses ( $L_1$  and  $L_2$ ) are placed in a telescopic arrangement in the beam path for collimating the beam and for magnifying the beam diameter (as  $f_2 > f_1$ ). The beam should be passed through the centre of the lenses at normal incidence to avoid spatial chirping. First a white screen is placed at the beam path slightly far away from where the second lens would be placed and the position of the beam is marked. The first lens ( $L_1$ ) is now brought in to its position and by adjusting its horizontal and vertical positions and tilt it is made sure that the position of the beam on the screen is not affected and only the beam diameter gets expanded due to the divergence from its focus, which is well before the screen position. The second lens is then placed precisely at a distance of  $f_1 + f_2$  from the first lens following the same method as for the first lens so that the beam position on the screen remains unaffected. The screen is now moved to at least three positions far away from the telescopic arrangement and the beam diameter is measured to ensure the proper collimation of the beam.

The beam is then passed through the centre of a Glan-Thompson polarizer in such a way that the spatial profile (shape and intensity) of the transmitted beam should be symmetric on both sides of the centre. The optical axis of the polarizer is set parallel to the polarization axis of the beam so that the transmitted intensity from the polarizer becomes maximum. The beam is then guided through the path as shown in Fig. 4.10 with the help of the mirror  $M_{r7}$  and the beam combiner  $B_2$  (50:50 beam splitter). The dielectric coating of  $B_2$  should face the probe beam. The reflected beam from the beam combiner  $B_2$  should be exactly parallel to the array of holes on the optical table and the height is adjusted to 14.4 cm. The corresponding alignment procedure is shown schematically in Fig. 4.15(d). The alignment procedure is similar to the alignment of beam after mirror  $M_{r6}$ . In this case the ‘beam height’ is first placed in ‘position 1’. The beam position is adjusted to the hole on the ‘beam height’ by mirror  $M_{r7}$ . The ‘beam height’ is then placed at ‘position 2’ and the beam position is again placed back to the hole on the ‘beam height’ by beam combiner  $B_2$ . The method is repeated till the beam is incident exactly at the same point (on the hole) on the ‘beam height’ when placed at ‘position 1’ and ‘position 2’.

#### ➤ **Alignment of the Pump Beam**

The SHG output is used as the pump beam. The beam is guided through the path as shown in Fig. 4.10 with the help of three mirrors,  $M_{b1}$ ,  $M_{b2}$  and  $M_{b3}$ . We know that at zero delay the optical path lengths of pump and probe beams should be equal. The zero delay should be obtained when the retro-reflector is positioned close to the left end of delay stage so that we can have a maximum utilization of the length of delay stage as the time delay between the pump and probe beams. Before alignment of the pump beam, we calculated the optical path length of pump beam and probe beams starting from the beam splitter  $B_1$  and ending at the beam combiner  $B_2$ . For calculating the optical path of the pump beam the optical path inside SHG should also be taken into account accurately. The optical path inside the SHG is shown in Fig. 4.9. The optical path of probe was calculated by keeping the retro-reflector close to the left end of the delay stage. In order to get a negative delay (probe beam reaches the sample before the pump) between pump and probe beams, the path length of pump beam should be kept slightly longer (10-15 mm) than the path length of the probe beam when the retro-reflector is at the extreme left side on delay stage. After calculation, the difference between path lengths of pump and probe were adjusted by re-positioning the mirrors  $M_{b1}$ ,  $M_{b2}$  and  $M_{b3}$ . During the initial development, we also placed the pump and

probe beams on a fast photodiode and the signals were monitored by using an oscilloscope to get a rough idea about the differences between their optical paths.

The alignment of pump beam was started after fixing the positions of the mirrors  $M_{b1}$ ,  $M_{b2}$  and  $M_{b3}$ . After passing through the beam combiner  $B_2$ , the pump beam should be exactly collinear with the probe beam. Therefore, the pump beam is aligned with the help of the 'beam height' and mirrors  $M_{b1}$  &  $M_{b3}$ . During the alignment of the pump, the positions of the 'beam height' are kept same as the positions (position 1 & position 2) used for the alignment of the probe beam after the polarizer. When the 'beam height' is placed at 'position 1', mirror  $M_{b1}$  is adjusted whereas for 'position 2', mirror  $M_{b3}$  is adjusted.

### ➤ Alignment of the Microscope Objective (MO)

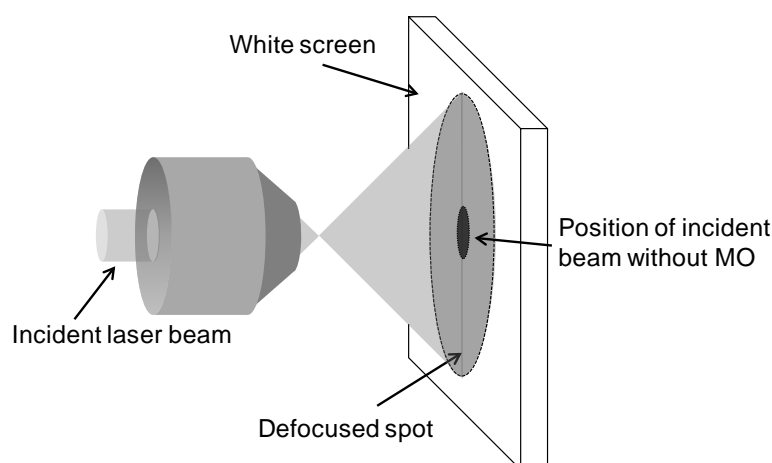


Fig. 4.16: A schematic diagram showing the alignment procedure of the microscope objective.

The alignment of the MO is a very crucial step for obtaining a good spatial overlap of the pump and the probe beams. First, a white screen is placed perpendicular to the beam path (Fig. 4.16). The incident position of aligned probe beam is marked on the screen. Then the MO is placed in such a way that the beam is incident on the centre of the back aperture of the MO and almost filling the aperture as shown in Fig. 4.16. The output beam from MO now falls on the white screen in a defocused condition. If the beam is incident exactly on the centre of the back aperture and passes through the axis of the MO, then the defocused beam on the white screen should be exactly circular and the marked position of incident beam without the MO should be at the centre of the defocused beam. If marked spot is shifted vertically or horizontally from the centre of incident defocused beam, then the incident beam on MO is not exactly centered. In that case the MO is moved either horizontally (for adjusting horizontal shift) or vertically (for adjusting vertical shift) to correct this error. After

that the intensity profile of the defocused spot is checked. If the intensity profile is uniform throughout the circular spot and symmetrically distributed on all sides of centre then further alignment is not needed. If there is an asymmetry present in the intensity profile, then the tilt of the axis of the MO is adjusted with the screws attached to the MO mount till a symmetric intensity profile is achieved.

#### ➤ **Alignment of the Optical Bridge Detector (OBD)**

Before placing the optical bridge detector, the probe beam is made parallel to the array of hole on the optical table with the help of mirror  $M_{r8}$ . The OBD is then placed in such a way that the beam is incident on the centre of the front aperture of the OBD. The beam then falls on the two photodiodes and gets reflected from the two and comes out of the OBD. If the incident beam and the axis of the detector are collinear, then the back-reflected beams will also be collinear to the incident beam. An aperture is placed on the incident beam path just before the OBD and the OBD is rotated around its horizontal and vertical axes to bring the back-reflected beams back to the aperture. The output voltages A, B, A + B and A – B are also monitored for finer alignment of the detector.

### **4.3.5 Some Routine Alignments**

The alignment procedures mentioned above were performed during the construction of the TRMOKE microscope. In general, all the alignments mentioned above are not required to be performed in everyday's experiment. The above procedures (except the alignment of optical table) are only required if there is a significant walking of the output beam from Tsunami due to the fluctuation in the environment temperature and humidity. However, performances of the lasers generally degrade after few months (4-6 months) due the change in the environment. Therefore, a routine alignment of the laser cavity is required at a regular interval of 4-6 months depending upon their conditions. The internal optical components of the lasers are re-aligned to optimize the laser performance. A significant amount of walking of the output beam from Tsunami is observed after the cavity alignment. Therefore, the above alignment procedures (except the alignment of optical table) of the set up are repeated. Normally, the following steps are performed before starting the daily experiment.

- At first, the output power and spectra of Tsunami is checked. The output power is maximized after adjusting the central wavelength ( $\lambda_0 = 800$  nm) and FWHM ( $\sim 10$  nm

or more) with the help of external micrometer controllers of Tsunami (Fig. 4.14(a) & (b)).

- The alignment of the retro-reflector is checked by placing the ‘beam height’ in the path of probe beam after the retro-reflector and by moving the retro-reflector from the left end to the right end of the delay stage. If there is a movement of the probe beam while moving the retro-reflector then the alignment procedure explained in section 4.3.4 is performed.
- The collinearity of the pump and probe beams is checked by placing the ‘beam height’ after the beam combiner ( $B_2$ ). Both beams should go through the hole on the beam height. Then the overlap between the pump and the probe is checked by observing their images in CCD camera. If they are not spatially overlapped on the sample then the overlapping is adjusted with the help of mirrors  $M_{b1}$ ,  $M_{b3}$  and  $M_{r6}$ ,  $M_{r7}$ .
- Now, we check whether the pump-probe is co-axial with the MO or not. For that the MO is moved back and forth with the help of micrometer screw attached to it. The probe and pump beam is focused and defocused, which can be seen in the TV screen attached to the CCD camera. If the pump and the probe beams are exactly co-axial with MO, then they will be focused-defocused keeping their centres fixed at a particular position. If there is a movement of the centre either along the horizontal direction or the vertical direction, then the pump and probe are not collinear with the MO. The pump and probe are made collinear with the help of the mirrors  $M_{b1}$ ,  $M_{b3}$  and  $M_{r6}$ ,  $M_{r7}$ .
- Finally, the alignment of the OBD is checked. If misalignment of detector is found then it is aligned by the method mentioned in the section 4.3.4.

The routine alignment helps to get a basic alignment of the set up. A fine tuning is required before starting the measurement. This is usually done with a standard sample (a small piece of Si(100) wafer). The Si wafer is mounted on the sample holder with its polished surface facing the pump and probe beams. The pump and probe fluences are chosen to be about  $10 \text{ mJ/cm}^2$  and  $2 \text{ mJ/cm}^2$  (with the help of attenuators  $A_1$  and  $A_2$ ). The dc value of the total reflectivity ( $A + B$ ) signal in the OBD is checked by a multimeter. For a reasonably good alignment of the set up, the dc reflectivity signal is more than 500 mV. If the measured voltage is lower than that, then the alignments of the MO and the OBD are improved. After that the total reflectivity just after the zero delay (by moving the stage to the position just after the zero delay) is checked. For a reasonably good alignment, this value should be

between 500  $\mu\text{V}$  or more in our set up. If the A + B signal in the lock-in amplifier is found to be lower than the above value, the overlapping of pump-probe on the sample surface is improved by adjusting the mirrors  $M_{b1}$ ,  $M_{b3}$  and  $M_{r6}$ ,  $M_{r7}$ . After that the time-resolved reflectivity data from the Si wafer is measured over about  $\sim 2000$  ps. The cross-correlation of pump and probe can be obtained by fitting a Gaussian function to the reflectivity signal at the zero delay, which is usually  $\sim 100$  fs.

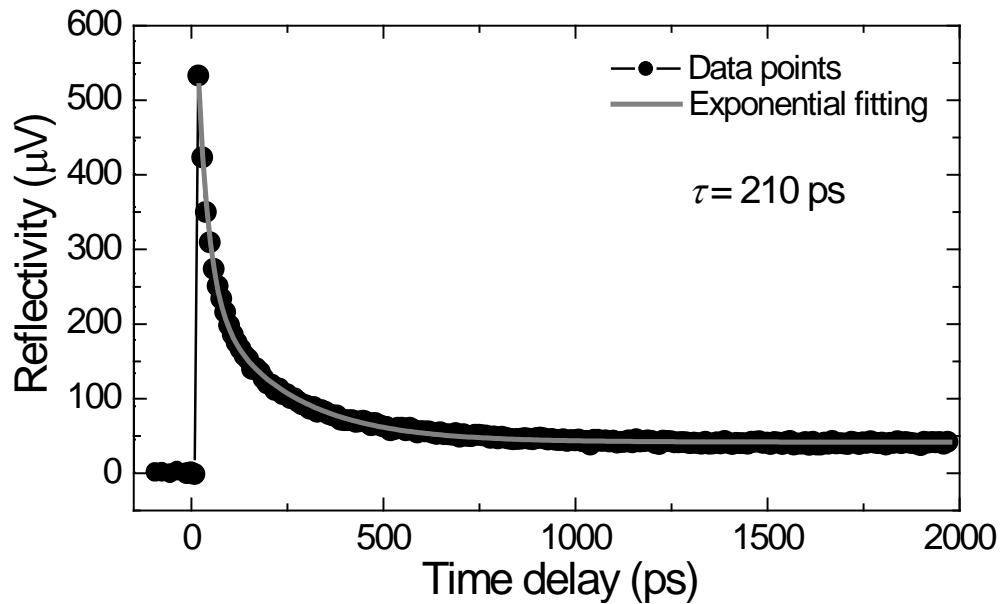


Fig. 4.17: The reflectivity signal (A + B) from a Si(100) wafer as function of the time delay between the pump and the probe beams. The decay of the reflectivity signal after the zero delay has been fitted with a double exponential decay function. The time constant of the longer decay is 210 ps.

A typical reflectivity signal is shown as a function of the time delay between the pump and the probe in Fig. 4.17. This shows that the reflectivity sharply goes to a maximum value right after the zero delay position and then decays exponentially as the time delay increases. For a good alignment of the retro-reflector and the pump and probe beams, the reflectivity for the standard Si sample should decay with a time constant of  $\sim 210$  ps. We take this as the standard data for a good alignment of our set up. A faster decay of the reflectivity often indicates that the spatial overlap between the pump and probe beams is lost with the movement of the delay stage. In this case the delay stage is aligned by optimizing the total reflectivity signal at later time delays instead of optimizing it right after the zero delay. Let us say the retro-reflector is placed at the position of 25 ps in time delay. The reflectivity signal is then improved by re-aligning the pump and the probe beams. The delay stage is then placed say, at 40 ps in time delay. The reflectivity signal is again improved by re-aligning pump-

probe. After optimizing the reflectivity signal at 3-4 time delays, the full time-resolved reflectivity signal is measured again. If now the decay time is found to be close to or same as the standard value (210 ps), then the alignment is complete, else the above procedure is repeated until the desired decay time is obtained. Once the whole alignment is finished, the set up is said to be ready for measurement.

#### **4.4 Static Magneto-optical Kerr Effect (SMOKE) Microscope**

The static magneto-optical Kerr effect (SMOKE) microscope was used to measure the magnetic hysteresis loops from some arrays of magnetic dots. The schematic diagram of the set up is shown in Fig. 4.18. A CW laser of wavelength ( $\lambda$ ) = 632 nm was used for this measurement. The laser beam goes through a variable attenuator. The intensity of the transmitted light is controlled by moving the attenuator perpendicular to the beam with the help of a moving stage. The beam is then passed through a Glan-Thompson polarizer with s-polarization. The linearly polarized beam is then chopped at 1-2 kHz frequency by a chopper controlled by a controller unit. The chopped beam is incident on an extra long working distance (25 mm) microscope objective (MO) with N. A. = 0.55 and magnification =  $\times 40$ . The incident point of the beam on back aperture of the MO is away from the centre as shown in Fig. 4.18. In that case the beam will be incident on the sample at an oblique angle less than  $90^\circ$  with the sample surface. The reflected beam from the sample gets collected by the front lens assembly of the MO and comes out of the back aperture of the MO through a point diametrically opposite to the point of incidence. The magnetic field is applied in the plane of the sample. In this geometry the longitudinal Kerr rotation is measured by sending the back-reflected beam to an optical bridge detector (OBD) as described in section 4.3.3. First the balanced condition is obtained in absence of any magnetic field by rotating the axis of the polarized beam splitter (PBS) slightly away from  $45^\circ$ . A calibration of the OBD is done by rotating the PBS by  $1^\circ$  on both sides of the balanced condition and by recording the dc output of the detector. When the magnetic field is applied, the detector will no longer be in the balanced condition (*i.e.*,  $A \neq B$ ). The difference signal ( $A - B$ ) is measured at a function of the bias magnetic field and is converted to Kerr rotation by multiplying it with the calibration factor. The output signal is measured in a phase sensitive manner by using a lock-in amplifier with a reference signal from the chopper. For the measurement of the hysteresis loops from an array of nanodots, the laser spot is carefully placed at a desired position on the nanodots by using a scanning  $x$ - $y$ - $z$  stage. Sometimes a quarter wave plate is placed before optical

bridge detector (OBD) to convert Kerr ellipticity into Kerr rotation. This is generally done for Ni, as this material has larger Kerr ellipticity than Kerr rotation.

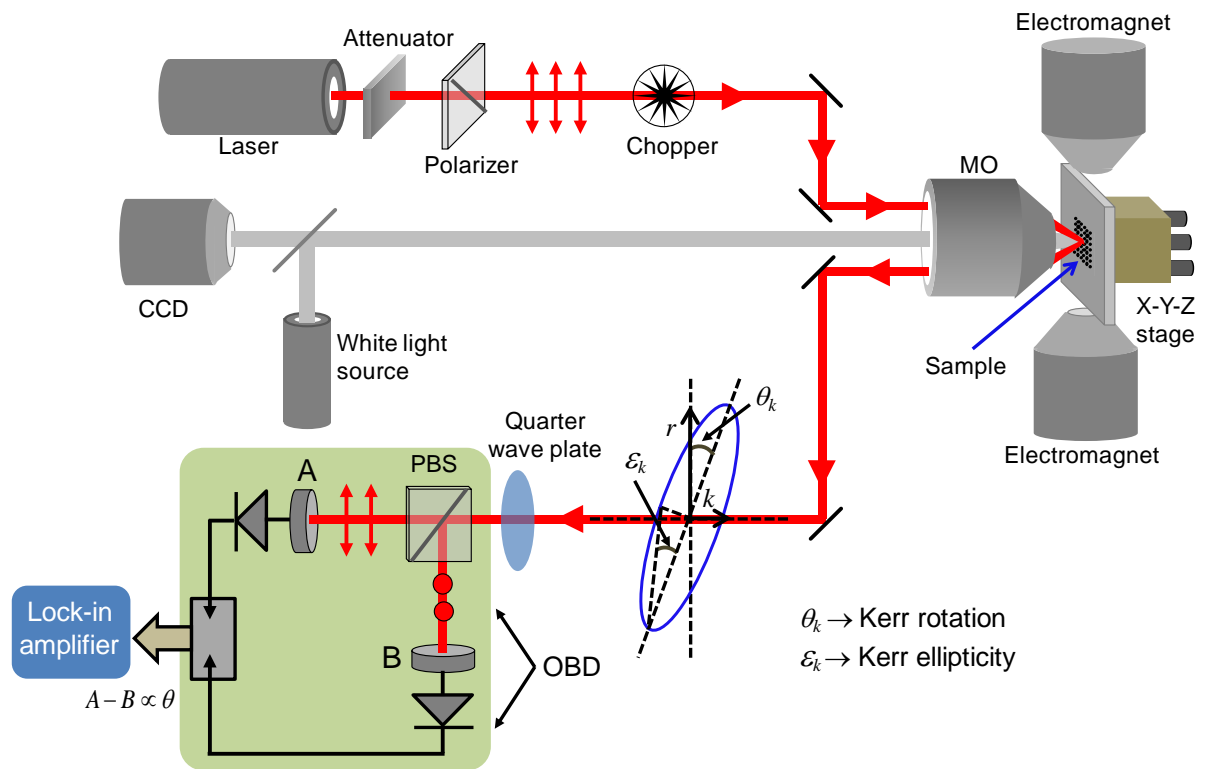


Fig. 4.18: A schematic diagram of static magneto-optical Kerr effect (SMOKE) microscope.

## Bibliography

1. J. Kerr, *Philos. Mag. Series 5* **3**, 321 (1877).
2. A. Hubert and R. Schafer, "Magnetic Domains: The Analysis of Magnetic Microstructure," *Springer*, (Berlin, 1998).
3. M. R. Freeman and W. K. Hiebert, "Spin Dynamics in Confined Magnetic Structures I," *Springer*, edited by B. Hillebrands and K. Ounadjela ( Berlin, Heidelberg, 2002).
4. M. R. Freeman, R. R. Ruf, and R. J. Gambino, *IEEE Trans. Magn.* **27**, 4840 (1991).
5. W. K. Hiebert, A. Stankiewicz, and M. R. Freeman, *Phys. Rev. Lett.* **79**, 1134 (1997).
6. E. Beaurepaire, J. C. Merle, A. Daunois, and J.-Y. Bigot, *Phys. Rev. Lett.* **76**, 4250 (1996).
7. M. van Kampen, C. Jozsa, J. T. Kohlhepp, P. LeClair, L. Lagae, W. J. M. de Jonge, and B. Koopmans, *Phys. Rev. Lett.* **88**, 227201 (2002).
8. A. Barman, V. V. Kruglyak, R. J. Hicken, C. H. Marrows, M. Ali, A. T. Hindmarch, and B. J. Hickey, *Appl. Phys. Lett.* **81**, 1468 (2002).
9. P. S. Keatley, V. V. Kruglyak, A. Barman, S. Ladak, R. J. Hicken, J. Scott, and M. Rahman, *J. Appl. Phys.* **97**, 10R304 (2005).
10. A. Barman, S. Wang, J. D. Maas, A. R. Hawkins, S. Kwon, A. Liddle, J. Bokor, and H. Schmidt, *Nano Lett.* **6**, 2939 (2006).
11. M. Bauer, R. Lopusnik, J. Fassbender, and B. Hillebrands, *Appl. Phys. Lett.* **76**, 2758 (2000).
12. A. Barman, T. Kimura, Y. Otani, Y. Fukuma, K. Akahane, and S. Meguro, *Rev. Sci. Instrum.* **79**, 123905 (2008).
13. A. Hubert and R. Schäfer, "Magnetic Domains: The Analysis of Magnetic Microstructures," *Springer*, NewYork (1998).
14. W. K. Hiebert, "Experimental Micromagnetic Dynamics: Ultrafast Magnetization Reversal Using Time Resolved Scanning Kerr Effect Microscopy," Ph.D Thesis, Department of Physics, University of Alberta, (2001).
15. Z. Q. Qiu and S. D. Bader, *Rev. Sci. Instrum.* **71**, 1243 (2000).
16. W. T. Silfvast, "Laser Fundamentals," 2nd edition, *Cambridge University Press*, Cambridge, UK (1996).
17. O. Svelto, "Principles of Lasers," 5th Edition, *Springer*, New York, USA (2009).

18. User's Manual, "Millenia Pro s-Series: Diode-Pumped, CW Visible Laser System", *Spectra-Physics*, California, USA (2007).
19. User's Manual, "Tsunami: Mode-locked Ti:sapphire Laser", *Spectra-Physics*, California, USA (2002).
20. User's Manual, "Model 3980: Frequency Doubler and Pulse Selector", *Spectra-Physics*, California, USA (2002).

## CHAPTER 5

---

# Micromagnetic Simulations

---

### 5.1 Introduction

In sections 2.6.5 and 2.7.4, we discussed about the Kittel formula and magnetostatic spin waves in magnetic medium. In those cases the magnetization was considered to be uniform throughout the sample. Magnetization dynamics was calculated by solving the nonlinear ordinary differential equation *i.e.*, the Landau-Lifshitz-Gilbert (LLG) equation (Eq. 2.6.11) by linearizing it under small angle approximation. The assumption of uniform magnetization is true for infinitely extended bulk magnetic materials or two dimensional magnetic thin films under certain conditions (such as the sample magnetization should be above saturation). However, in confined magnetic structures (except perfect ellipsoid) like nanostripes, nanodots, nanoparticles, nanowires, antidots, the above assumption is not true because the magnetization inside them becomes nonuniform even above the saturation field due to the nonuniform nature of the demagnetizing field. Though discrete spin models (energy is described by either Ising or Hisenberg Hamiltonian) can take into account of the nonuniformity of magnetization inside small nanostructures, but it becomes very difficult to calculate the internal spin configurations of micron or sub-micron size magnetic structures and arrays due to the limitation of computational resources. The micromagnetic continuum theory has been developed by scientists to overcome the gap between macrospin formalism and discrete spin model. In micromagnetic simulations, the samples are divided or discretized into a large number of cells and each cell is assigned with a single spin (equivalent to the average magnetization of the cell). The dynamics of these spins in the cells are calculated numerically by solving the LLG equation (Eq. 2.6.11).

## 5.2 Free Energies of a Ferromagnetic Element in Micromagnetics

We discussed in section 2.2 that the total free energy of a ferromagnetic material in presence of an external magnetic field can be written as sum of different free energies *i.e.*

$$E_{total} = E_Z + E_d + E_e + E_K, \quad (5.2.1)$$

where  $E_Z$  is interaction energy of the magnetization with the external magnetic field. It is also called the Zeeman energy.  $E_d$  is the magnetostatic self-energy of ferromagnetic material,  $E_e$  is the exchange energy and  $E_K$  is the magnetocrystalline anisotropy energy. In micromagnetism, the above free energy can be written as [1]

$$E_{total} = \int_V \left[ -\mathbf{M} \cdot \mathbf{H}_Z - \frac{1}{2} \mathbf{M} \cdot \mathbf{H}_d + A \left( (\nabla u_x)^2 + (\nabla u_y)^2 + (\nabla u_z)^2 \right) + K_1 (1 - (\mathbf{a} \cdot \mathbf{u})) \right] dv, \quad (5.2.2)$$

where  $H_Z$  is the Zeeman field,  $H_d$  is the demagnetizing field,  $A$  is the exchange stiffness constant,  $K_1$  is the first order magnetocrystalline anisotropy constant,  $\mathbf{a}$  is the unit vector parallel to the easy axis and  $\mathbf{u}$  is the space and time dependent unit vector of magnetization. The space and time dependent magnetization term can be written as [2]

$$\mathbf{M}(x, t) = M_s(x) \cdot \mathbf{u}(x, t), \quad |\mathbf{u}| = 1. \quad (5.2.3)$$

In equilibrium, total energy ( $E_{total}$ ) will be minimum and variation of  $E_{total}$  with  $\mathbf{u}$  vanishes. Therefore,

$$\frac{\delta E_{total}}{\delta \mathbf{u}} = 0. \quad (5.2.4)$$

This gives Brown's equation [3]

$$\mathbf{u} \times (M_s \mathbf{H}_Z + M_s \mathbf{H}_d + 2A \Delta \mathbf{u} + 2K_1 \mathbf{a}(\mathbf{u} \cdot \mathbf{a})) = 0. \quad (5.2.5)$$

This means, in equilibrium  $\mathbf{M}$  is parallel to an effective field ( $\mathbf{H}_{eff}$ ), which is given by

$$\mathbf{H}_{eff} = \frac{2A}{M_s} \Delta \mathbf{u} + \frac{2K_1}{M_s} \mathbf{a}(\mathbf{u} \cdot \mathbf{a}) + \mathbf{H}_Z + \mathbf{H}_d. \quad (5.2.6)$$

In equilibrium, the torque produced by  $\mathbf{H}_{eff}$  on  $\mathbf{M}$  also vanishes *i.e.*,

$$\mathbf{M} \times \mathbf{H}_{eff} = 0. \quad (5.2.7)$$

The minimization of Eq. 5.2.2 may give equilibrium magnetization distribution of nanomagnets. However, in a micromagnetic system, the energy landscape is usually very complicated and contains many local maxima, minima and saddle points. Therefore, a more appropriate approach to reach an equilibrium condition of a system in a local minimum could be provided by a dynamic description of magnetization through an energy landscape. The motion of a magnetic moment is governed by the LLG equation of motion where time rate of change in magnetization ( $\mathbf{M}$ ) is described as a combination of torque produced by effective magnetic field ( $\mathbf{H}_{eff}$ ) and a phenomenological damping term

$$\frac{d\mathbf{M}}{dt} = -\gamma(\mathbf{M} \times \mathbf{H}_{eff}) + \frac{\alpha}{M_s} \left( \mathbf{M} \times \frac{d\mathbf{M}}{dt} \right). \quad (5.2.8)$$

In micromagnetics, the system is discretized into a number of cells. Therefore, the contributions to the total energy should also be discretized. The discrete approximation of spatially varying magnetization can be written as [2]

$$\mathbf{M}(x) \approx M_s(x) \sum_i \mathbf{u}_i \eta_i \approx \sum_i M_{s,i} \mathbf{u}_i \eta_i = \sum_i \mathbf{M}_i, \quad (5.2.9)$$

where  $\eta_i$  denotes the basis function of the  $i^{\text{th}}$  cell. The effective magnetic field in the  $i^{\text{th}}$  cell would be [2]

$$\mathbf{H}_{i,eff} = - \left( \frac{\delta E_{tot}}{\delta \mathbf{M}} \right)_i \approx - \frac{1}{V_i} \frac{\partial E_{tot}}{\partial \mathbf{M}_i} = - \frac{1}{V_i M_{s,i}} \frac{\partial E_{tot}}{\partial \mathbf{u}_i}. \quad (5.2.10)$$

The Zeeman energy can be expressed as [2]

$$E_Z = \int_V (-\mathbf{M} \cdot \mathbf{H}_Z) dv = \int_V \sum_j M_{s,j} \sum_k^{x,y,z} u_{j,k} \eta_j H_{Z,k} dv. \quad (5.2.11)$$

Uniaxial magnetocrystalline anisotropy energy can be written as [2]

$$E_K = \int_V \sum_j K_1 \left( 1 - (\mathbf{a} \cdot \mathbf{u}_j \eta_j)^2 \right) dv. \quad (5.2.12)$$

The exchange energy can be expressed as [2]

$$E_e = \int_V \sum_j A (\nabla u_j \eta_j)^2 dv. \quad (5.2.13)$$

The magnetostatic self-energy can be expressed as [2]

$$E_d = \int_V \nabla \cdot \mathbf{M} dv = \int_V \sum_j \sum_k^{\{x,y,z\}} \nabla_k u_{j,k} \eta_j = \int_V \sum_j \sum_k^{\{x,y,z\}} u_{j,k} \nabla_k \eta_j. \quad (5.2.14)$$

## 5.3 Micromagnetic Simulation Methods and Solvers

### 5.3.1 Introduction: Different LLG Solvers

To calculate magnetization dynamics in nanomagnets we need to solve nonlinear Landau-Lifshitz-Gilbert (LLG) equation (Eq. 5.2.8). Obtaining exact solutions of LLG equation faces many technical difficulties like acquisition of the boundary and initial conditions. An alternative route to this solution is numerical calculation. There are two common approaches to solve LLG equation numerically: (i) finite-difference method (FDM) and (ii) finite-element method (FEM). In both approaches, the samples are divided or discretized into a large number of cells and each cell is assigned with a single spin (equivalent to the average magnetization of the cell). The size of each cell is generally kept smaller than the exchange length ( $l_{ex}$ ) of the material under consideration to take into account of the exchange interactions among the spins in addition to the magnetostatic interactions among them. In this way, both methods lead to a set of simultaneous linear equations [4]. The dynamics of the spins in the cells are then numerically calculated by integrating LLG equation over time by using available micromagnetic solvers. Below, we have listed different micromagnetic simulation codes and also calculation methods used in those codes (taken from Ref. [4]).

**Table: 5.1**

	Name of Simulation Code	Developer	Calculation Method	Source Websites
Free Software	Object Oriented Micromagnetic	M. Donahue and D. Porter	FDM	<a href="http://math.nist.gov/oommf/">http://math.nist.gov/oommf/</a>

Packages	Frameworks (OOMMF)			
	NMAG	H. Fangohr and T. Fischbacher	FEM	<a href="http://nmag.soton.ac.uk">http://nmag.soton.ac.uk</a>
	MAGPAR	Werner Scholtz	FEM	<a href="http://magnet.atp.tuwie.n.ac.at/scholz/magpar">http://magnet.atp.tuwie.n.ac.at/scholz/magpar</a>
Commercial Software Packages	LLG Simulator	M. R. Scheinfein	FDM	<a href="http://llgmicro.home.mindspring.com/">http://llgmicro.home.mindspring.com/</a>
	MicroMagus	D.V. Berkov and N. L. Gorn	FDM	<a href="http://www.micromagus.de/">http://www.micromagus.de/</a>

Appropriate modeling strategies and use of these codes are always required for a system of interest in order to obtain reliable numerical simulation results. In section 2.6.2, we discussed about the time scale of different magnetization dynamics starting from 1 fs to hundreds of ns. All the numerical simulation codes utilize the LLG equation according to continuum micromagnetics. Therefore, numerical calculation results are valid for time scales longer than 1 ps and dimensions greater 1 than nm. In this thesis, quasistatic magnetization reversal dynamics has been numerically simulated by OOMMF [5] and NMAG [6]. The ultrafast precessional magnetization dynamics has been simulated by OOMMF and LLG micromagnetic simulator. The magnetostatic stray field profiles have been calculated by LLG micromagnetic simulator [7]. In the sections below, we will describe about OOMMF, NMAG and LLG micromagnetic simulator.

### 5.3.2 Object Oriented Micromagnetic Framework (OOMMF)

In OOMMF, the LLG equations are solved by FDM in micromagnetic framework. It was developed at the National Institute of Standards and Technology, Gaithersburg, MD by Mike Donahue and Don Porter in 1999. OOMMF software is written in C++ and Tcl. In OOMMF, the sample or space is discretized into small cuboidal cells as shown by a schematic diagram in Fig. 5.1(a). These cells are often called ‘finite differences’. All the cells are same in size. All the required parameters like bulk saturation magnetization, exchange

stiffness constant, magnetocrystalline anisotropy, Zeeman field, sample structure and dimensions and the magnetic field geometry are provided at the beginning of the simulation through a file called ‘MIF’ file, written in Tcl/Tk script. In addition to that an initial state of magnetization is also provided at the starting point of simulation. When the simulation is started, the evolvers update the magnetization configuration from one step to the next. There are mainly two types of evolvers: (i) time evolvers, which track Landau-Lifshitz-Gilbert dynamics and (ii) minimization evolvers, which locate the local minima in the energy surface through direct minimization techniques [5]. Time evolver implements a simple first order forward Euler method with step size control on the LLG ODE. Evolvers are controlled by drivers. The evolvers must be compatible with the drivers, such as time evolvers must be paired with time drivers, and minimization evolvers must be paired with minimization drivers. In our case we have used time driver and time evolver. The drivers hand a magnetization configuration to the evolvers with a request to advance the configuration by one step (also called an iteration). It is the role of the drivers, not the evolvers, to determine when a simulation stage or run is complete. Driver detects when stages and runs are finished, using criteria specified in the MIF problem description, and can enforce constraints, such as making sure stage boundaries respect time stopping criteria.

The convergence criterion in the simulation is created by setting the stopping value of  $d\mathbf{m}/dt$  or time. The time or value of  $d\mathbf{m}/dt$  is set in such a way that the maximum torque,  $\mathbf{m} \times \mathbf{H}$  (where  $\mathbf{m} = \mathbf{M}/M_S$ ) goes well below  $10^{-6}$  A/m. At the stopping time the maximum value of  $d\mathbf{m}/dt$  across all spins drops below the set value. One advantage of this method is that the demagnetizing field can be computed very efficiently (via fast Fourier transformation techniques).

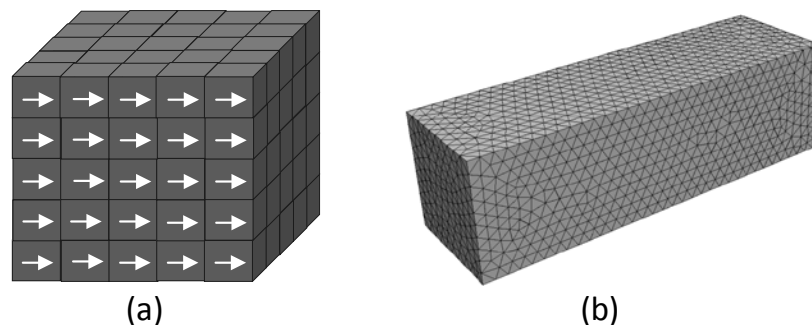


Fig. 5.1: The schematic diagrams show the discretization of a rectangular sample into a number of (a) cuboidal cells with equal size and (b) tetrahedral cells with varying size. The second figure is reproduced from Ref. [8].

### 5.3.3 NMAG

In NMAG, the LLG equations are solved by finite element method (FEM) in micromagnetic framework. In NMAG, the sample or space is discretized into small tetrahedral cells as shown in Fig. 5.1(b) [8]. The tetrahedra are sometimes referred to as the (finite element) mesh elements. Typically, the geometry of these tetrahedral cells does vary throughout the simulated region. Before starting a simulation, the mesh is generated by using a software called ‘Python’. Figure 5.1(b) actually shows the generated mesh for a rectangular element. In FEM, the demagnetizing field is calculated by Fredkin and Koehler hybrid finite element/boundary element method. The advantage of this method (over OOMMF’s approach) is that curved and spherical geometries can be spatially resolved much more accurately. However, this method of calculating the demagnetization field is less efficient than OOMMF’s approach for thin films. In particular, memory requirements for the boundary element method grow as the square of the number of surface points.

The finite difference simulations are best when the geometry of nanomagnet is of rectangular shape. Let us assume that we need to simulate a sphere. Figure 5.2(a) shows the discretization of sphere with cuboidal cells. It shows that the edges are very rough and the sphere is not well resolved by cubes. Though, in actual simulation we can resolve the geometry better by decreasing cell size, but still exact shape is not reproduced very well. In contrast, the FEM subdivides the sample or space into many small tetrahedra. Typically, the geometry of these tetrahedral cells does vary throughout the simulated region. This allows to combine the tetrahedra to approximate complicated geometries. In Fig. 5.2(b), the same sphere is subdivided by cells with tetrahedral structure. It is clear that the spherical shape is quite well reproduced by tetrahedral cells.

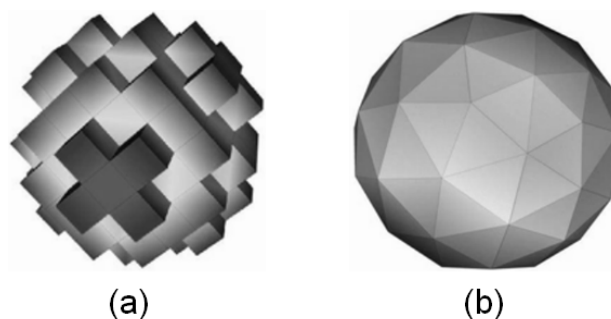


Fig. 5.2: The diagrams show the discretization of a spherical nanoelement with (a) cuboidal cells and (b) tetrahedral cells. The figures are reproduced from Ref. [8].

Another important difference between OOMMF and NMAG is that the magnetization degrees of freedom in OOMMF are associated with the centers of the cells, while in NMAG, they are associated with the corners.

➤ **Useful Tools:**

In NMAG simulation, we have also used two visualization tools for visualizing magnetization configuration of magnetic nanoelements at different magnetic field: (i) Visualisation ToolKit (vtk); <http://www.vtk.org> and (ii) MayaVi; <http://mayavi.sourceforge.net/>. VTK provides an open source, freely available software system for 3D computer graphics, image processing, and visualization. ‘MayaVi’ is a free, easy to use scientific data visualizer. It is written in Python and uses the Visualization Toolkit (VTK) for graphical rendering [8].

### **5.3.4 LLG Micromagnetic Simulator**

In LLG micromagnetic simulator, the LLG equation is solved by FDM like in OOMMF [7]. However, some extra features are found in LLG micromagnetic simulator, which are not found in OOMMF. In OOMMF simulation, the effect of temperature can not be incorporated. Therefore, the simulations are generally performed at  $T = 0$  K. Whereas in LLG micromagnetic simulator, the temperature effect can be introduced by providing an equivalent random magnetic field. The quasistatic magnetic properties are strongly affected by temperature. Therefore, the temperature effect may be introduced during the study of quasistatic magnetization reversal dynamics in magnetic nanostructures. LLG micromagnetic simulation could be ideal for this kind of study. Again in LLG micromagnetic simulator, magnetization dynamics can be triggered by spin polarized current, which is an essential requirement for studying magnetization dynamics in spin valve like structures. Another important feature is that the magnetostatic interaction among magnetic nanoelements can be visualized by coloured contour plots, which can not be done by using OOMMF. We have used this particular feature to calculate magnetostatic stray field profiles for array of magnetic dots [9-10]. Finally, it is easier in LLG Micromagnetic Simulator to control the input magnetic parameters for each layer in a multilayered nanostructure than in OOMMF where the script is quite complicated.

## 5.4 Methods of Calculating Power and Phase Profiles of Resonant Modes

In this thesis, the power and phase profiles of the resonant modes have been numerically calculated by using Dotmag software developed by our group [11-12]. To understand the procedure better we present an example and the whole procedure is summarized in Fig. 5.3. Figure 5.3(a) shows the simulated spatially averaged magnetization ( $M_z$ ) vs time graph for a 20 nm thick and 200 nm wide single permalloy square shaped dot with a bias field of 1.25 kOe applied along the horizontal edge ( $x$ -axis) of the dot (shown in the inset of Fig. 5.3(a)). The simulation is done by OOMMF. The OOMMF simulation produces a single file (called .omf files) for each point of simulated time domain magnetization (black solid circles). That file contains the information about the magnetization of the sample as a function of space ( $x, y, z$ ). The spatial profiles of the  $z$ -component of magnetization correspond to two different points 'a' and 'b' (marked by solid red circles) are shown in Fig. 5.3(b). The spatial distributions of the dynamical magnetization at the points 'a' and 'b' (Fig. 5.3(b)) show a subtle difference. However, those dynamical images correspond to a number of modes superposed with appropriate powers and phases and it is not straightforward to extract the spatial information of the individual resonant modes from OOMMF simulation. We extract the power and phase profiles of the individual resonant modes by a method described as below [11-12]. Mathematically the space-time variation of magnetization may be expressed as

$$\mathbf{M}(t, r) = \mathbf{M}(t, x, y, z). \quad (5.4.1)$$

The fast Fourier transform (FFT) of the time-resolved spatially averaged magnetization curve gives the frequency spectrum as shown in Fig. 5.3(c). The FFT spectrum shows three well resolved resonant modes. The spatial profile of the power and phase information for various resonant modes are obtained by fixing one of the spatial co-ordinates of the time dependent magnetization and then by performing a discrete Fourier transform with respect to time in the Dotmag software. The output files produced by the Dotmag software plot space dependent power and phase at discrete frequencies, where frequency resolution depends upon the total simulation time. The spatial resolution of calculated power and phase depends upon the discretization of sample during micromagnetic simulation.

During the FFT, the  $z$ -coordinate is fixed (say at  $z = z_m$ ) to get in-plane ( $x$ - $y$ ) distribution of power and phase. The FFT of magnetization at  $z = z_m$  gives

$$\tilde{M}^{z_m}(f, x, y) = FFT(M^{z_m}(t, x, y)). \quad (5.4.2)$$

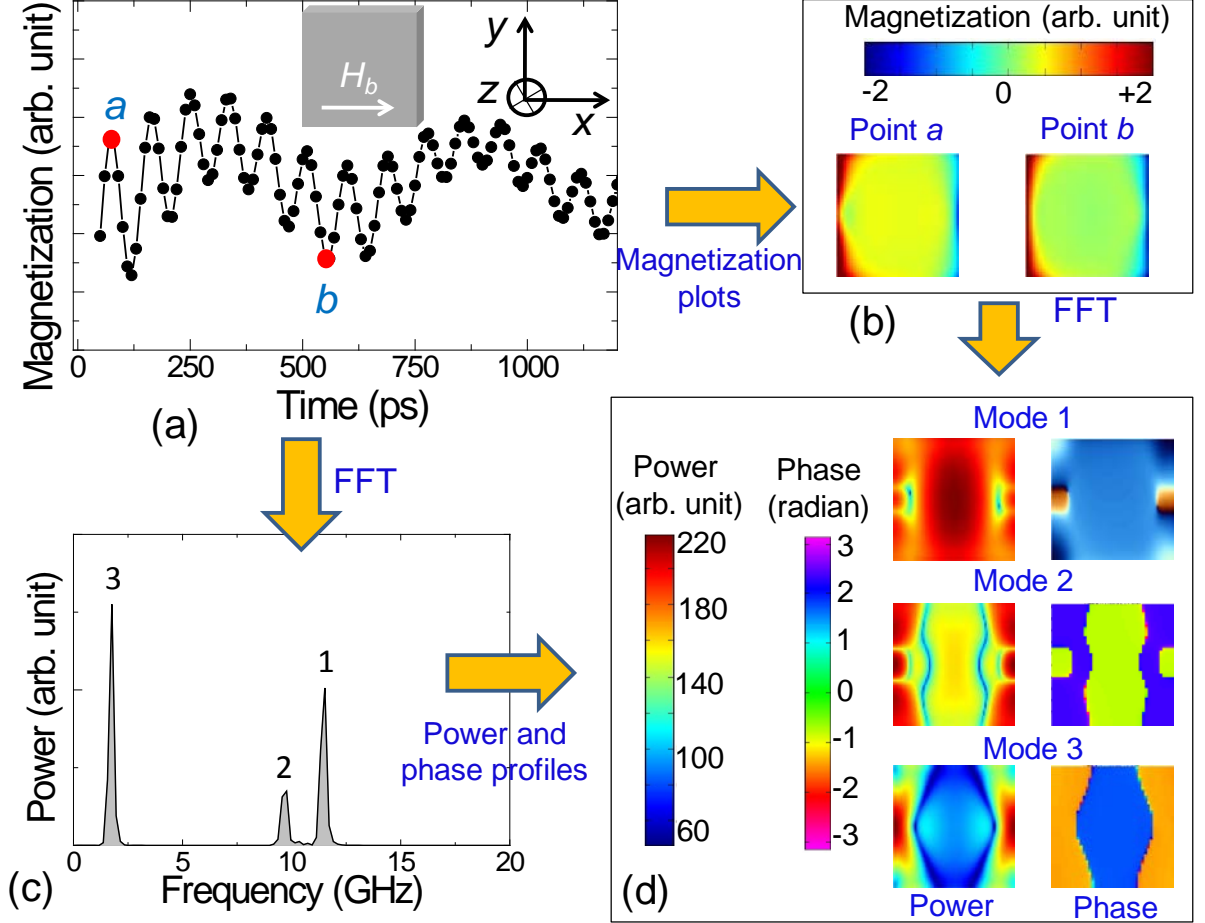


Fig. 5.3: (a) Simulated spatially averaged magnetization ( $M_z$ ) vs time is shown for a 20 nm thick and 200 nm wide single permalloy square shaped dot with a bias field ( $H_b$ ) of 1.25 kOe applied along the horizontal edge ( $x$ -axis) of the dot. (b) The spatial distribution of the  $z$ -component of magnetization is shown for two different times ('a' and 'b') marked by red solid dots on the curve. The colour scale is shown on top of the figure. (c) The fast Fourier transform (FFT) of simulated time-resolved magnetization curve is shown. It shows three well resolved resonant peaks. (d) The calculated power and phase distributions corresponding to three resonant modes are shown. The corresponding colour scales are shown inside the box.

The power and phase profiles of the resonant modes as a function of  $x$ ,  $y$  at  $f = f_n$  are expressed as:

$$\text{Power: } P^{z_m, f_n}(x, y) = 20 \log_{10} \left| \tilde{M}^{z_m}(f_n, x, y) \right| \quad (5.4.3)$$

$$\text{Phase: } \Phi^{z_m, f_n}(x, y) = \tan^{-1} \left( \frac{\text{Im}(\tilde{M}^{z_m}(f_n, x, y))}{\text{Re}(\tilde{M}^{z_m}(f_n, x, y))} \right). \quad (5.4.4)$$

The obtained power and phase profiles of the resonant modes are shown in Fig. 5.3(d). It now clearly resolves three different modes, namely the centre mode (mode 1), edge mode (mode 3) and a mixture of the edge mode and the Damon Eshbach mode (mode 2).

## Bibliography

1. T. Schrefl, W. Scholz, D. Süß, and J. Fidler, *J. Magn. Magn. Mater.* **226–230, Part 2**, 1213 (2001).
2. W. Scholz, J. Fidler, T. Schrefl, D. Suess, R. Dittrich, H. Forster, and V. Tsiantos, *Comp. Mater. Sci.* **28**, 366 (2003).
3. W. Scholz, T. Schrefl, and J. Fidler, *J. Magn. Magn. Mater.* **233**, 296 (2001).
4. S.-K. Kim, *J. Phys. D: Appl. Phys.* **43**, 264004 (2010).
5. M. Donahue and D. G. Porter, “OOMMF User’s guide, Version 1.0,” *NIST Interagency Report No. 6376, National Institute of Standard and Technology, Gaithersburg, MD, URL: <http://math.nist.gov/oommf>*, (1999).
6. T. Fischbacher, M. Franchin, G. Bordignon, and H. Fangohr, *IEEE Trans. Magn.* **43**, 2896 (2007).
7. M. R. Scheinfein, “LLG Micromagnetic Simulator,” <http://llgmicro.home.mindspring.com/>, (1997).
8. H. Fangohr, T. Fischbacher, M. Franchin, G. Bordignon, J. Generowicz, A. Knittel, M. Walter, and M. Albert, “NMAG User Manual Documentation, Release 0.2.1,” (2012).
9. B. Rana, D. Kumar, S. Barman, S. Pal, Y. Fukuma, Y. Otani, and A. Barman, *ACS Nano* **5**, 9559 (2011).
10. B. Rana and A. Barman, *SPIN* **3**, 1330001 (2013).
11. D. Kumar, O. Dmytriiev, S. Ponraj, and A. Barman, *J. Phys. D: Appl. Phys.* **45**, 015001 (2012).
12. G. Venkat, D. Kumar, M. Franchin, O. Dmytriiev, M. Mruczkiewicz, H. Fangohr, A. Barman, M. Krawczyk, and A. Prabhakar, *IEEE Trans. Magn.* **49**, 524 (2013).

## CHAPTER 6

---

# Collective Magnetization Dynamics of Arrays of Square $\text{Ni}_{80}\text{Fe}_{20}$ Dots With Varying Areal Density

---

### 6.1 Background

Ordered arrays of nanomagnets have inspired technological progress within information storage [1], memory [2], spin logic [3], spin torque nano-oscillators (STNOs) [4] and magnonic crystals [5-7]. Magnetostatically coupled nanomagnets in an ordered array may show long wavelength collective dynamics [8-10], where the dynamics of the constituent nanomagnets maintain constant amplitude and phase relationships similar to the acoustic and optical modes of phonons. Such long wavelength collective modes pose obstacles to the applications of nanomagnet arrays in storage, memory devices and magnetic field sensors, where the individual characters of the nanomagnets (bits) must be retained. On the other hand, to achieve a more useful power level, a microwave emitter should consist of arrays of phase coherent nano-oscillators. The long wavelength collective dynamics in the form of Bloch waves, defined in the first Brillouin zone (BZ) of an artificial lattice, can also be manipulated by tailoring the lattice to form two-dimensional magnonic crystals [11-12], the magnetic analog of photonic or phononic crystals.

Magnetization dynamics in planar arrays of nanomagnets and single nanomagnets have been experimentally studied by time-domain [8, 10-11, 13-14], frequency-domain [15] and wave-vector-domain techniques [9, 12, 16] and by analytical methods [17-18] and micromagnetic simulations [19]. To this end the frequency, damping and spatial patterns of collective modes and dispersion relations of frequency with the wave vector of magnon

propagation have been studied. However, very few attempts have been made to understand the systematic variation of collective magnetization dynamics in ordered arrays of nanomagnets with varying areal density. This is even more important when the constituent elements possess nonuniform magnetic ground state configurations and consequently, the interaction between the elements in the arrays and its effects on various nonuniform modes become quite complicated.

The collective magnetization dynamics of ferromagnetic nanodot arrays have been studied by a variety of techniques in the frequency-, time- and wave-vector-domains. All the techniques have their own advantages and limitations. In 2002, S. Jung *et al.* [20] reported collective magnetization dynamics of square arrays of circular permalloy dots with varying sizes and separations in the sub-micron range by using conventional ferromagnetic resonance. Two additional resonant peaks were observed on both sides of the main resonant peak corresponding to the uniform mode. The Brillouin Light Scattering study on the collective spin wave dynamics of arrays of cylindrical dots with fixed diameter and with varying interelement separations shows the existence of four fundamental modes namely, the edge mode, backward volume like mode, Damon Eshbach mode and mixed modes [21]. The existence of the normal modes within each isolated element in the array and the splitting of the fundamental mode into three collective modes were shown experimentally as well as with the aid of micromagnetic simulations. In 2008, an extensive study of collective magnetization dynamics of square ferromagnetic nanoelements for a range of bias fields was reported [22]. It was shown that the dynamic behaviour strongly depends upon the magnetic ground states of the nanodots. The co-existence of two branches of modes (centre mode and edge mode) above a crossover field and vanishing of the higher frequency branch below the crossover field were observed. Micromagnetic simulations showed the spatial nature of the excited modes and the magnetic ground states. The collective behaviour of the edge mode of stadium shaped magnetic dots were reported by time-resolved scanning Kerr microscopy [10]. It was shown that as the bias field is decreased, the broad single peak splits into three narrower peaks at a crossover field. Micromagnetic simulations showed that the natures of the modes are backward volume like mode, uniform mode and Damon Eshbach mode. In 2009, a systematic micromagnetic study on the static and dynamic behaviours of thin circular and square magnetic elements were reported [19]. The precessional frequency and damping were studied as a function of the width to separation ratio in arrays of square and circular magnetic elements and a comparison of those with the single nanomagnet dynamics. A significant

variation in the resonant frequency and damping of the arrays with the variation of interelement separation was observed due to the variation in the dipolar magnetic field in the array. Generally, resonant frequency and damping increases with the decrease in the interelement separation and single resonant mode splits into multiple modes due to the collective effect when the width to separation ratio becomes greater than one. The damping increases due to the mutual dynamic dephasing.

In this chapter, we demonstrate the excitation and detection of collective ultrafast magnetization dynamics in arrays of square  $\text{Ni}_{80}\text{Fe}_{20}$  (permalloy) elements with 200 nm width and with varying interelement separation by an all optical time-resolved magneto-optical Kerr effect (TRMOKE) microscope. Our technique enabled us to avoid any complicated sample fabrication process and also to obtain a much better temporal resolution (100 fs) than the previously reported non-optical excitation techniques of the collective magnetization dynamics. We will start with the investigation of quasistatic magnetization reversal of blanket permalloy thin film and arrays of permalloy nanodots. Then, we will present the ultrafast magnetization dynamics of a blanket  $10 \times 10 \mu\text{m}^2$  permalloy thin film with 20 nm thickness ( $t$ ). Subsequently, we will present the ultrafast magnetization dynamics of arrays of square shaped nanodots with 200 nm width ( $W$ ), 20 nm thickness ( $t$ ) and with varying edge-to-edge separation ( $S$ ) between 50 nm and 400 nm. We will also present the dependence of collective magnetization dynamics on the external bias magnetic field ( $H_b$ ). Our study shows that the magnetization dynamics of nanodot arrays undergo a systematic transition from a strongly collective regime to a completely isolated regime through various weakly collective regimes as the areal density of the array is decreased systematically at a fixed bias magnetic field. In addition, for a fixed and high value of the areal density the uniform collective dynamics again undergoes a transition to nonuniform collective dynamics or weakly collective dynamics as the bias magnetic field magnitude is reduced from saturation to lower values. We have also investigated the effective damping behaviour of the collective magnetization dynamics as a function of areal density and magnitude of the bias field. The experimental works are reproduced by micromagnetic simulations and simulated magnetic ground states, magnetostatic field distributions and power and phase profiles of the various collective modes were used to establish an extensive understanding of the observed magnetization dynamics.

## 6.2 Sample Fabrication, Characterization and Experimental Techniques

$10 \times 10 \mu\text{m}^2$  square arrays of permalloy elements with 200 nm width ( $W$ ), 20 nm thickness ( $t$ ) and interelement (edge-to-edge) separation ( $S$ ) varying from 50 to 400 nm were prepared by a combination of electron beam evaporation and electron beam lithography. A bilayer PMMA/MMA (polymethyl methacrylate/methyl methacrylate) resist pattern was first prepared on thermally oxidized Si(100) substrate by using electron beam lithography with a dose current of 100 pA and dose time of 0.9  $\mu\text{s}$ . A 20 nm thick permalloy was then deposited on the resist pattern by electron beam evaporation at a base pressure of about  $2 \times 10^{-8}$  Torr. A 10 nm thick  $\text{SiO}_2$  capping layer was deposited on top of permalloy to protect the dots from degradation when exposed to the optical pump-probe experiments in air. This is followed by the lifting-off of the sacrificial material and oxygen plasma cleaning of the residual resists that remained even after the lift-off process. A square permalloy blanket film with 10  $\mu\text{m}$  width and 20 nm thickness was also prepared by UV photolithography at the same deposition condition as the dot arrays.

In Fig. 6.1(a), a typical scanning electron micrograph (SEM) of a  $10 \times 10 \mu\text{m}^2$  blanket permalloy thin film is shown. The corresponding atomic force microscope (AFM) image (Fig. 6.1(b)) shows that the blanket film is of good quality except for a small amount of edge roughness and rounded corners. However, it does not affect the magnetization dynamics significantly, as the laser beam is focused at the middle of the blanket film and no significant effect from the boundary is expected. The profile of the height as measured by AFM (not shown in the figure) shows that the overall thickness of the film and protective layer of  $\text{SiO}_2$  is about 30 nm (film thickness = 20 nm and thickness of  $\text{SiO}_2$  layer = 10 nm). The sample surface is in  $x$ - $y$  plane and the magnetic field ( $H$ ) was applied parallel to the edge of the film (along  $x$ -axis) as shown on top of Fig. 6.1(a).

Figure 6.1(c) shows SEM images of  $10 \times 10 \mu\text{m}^2$  square arrays of permalloy dots. A representative AFM image of dot array with  $S = 100$  nm is also shown in Fig. 6.1(d). The three-dimensional view of the AFM image clearly shows a smooth film surface as well as the depth profile. The SEM and the AFM images show that the arrays were well fabricated with a slightly rounded corner and with small ( $< 5\%$ ) deviation of the dots from their nominal dimensions.

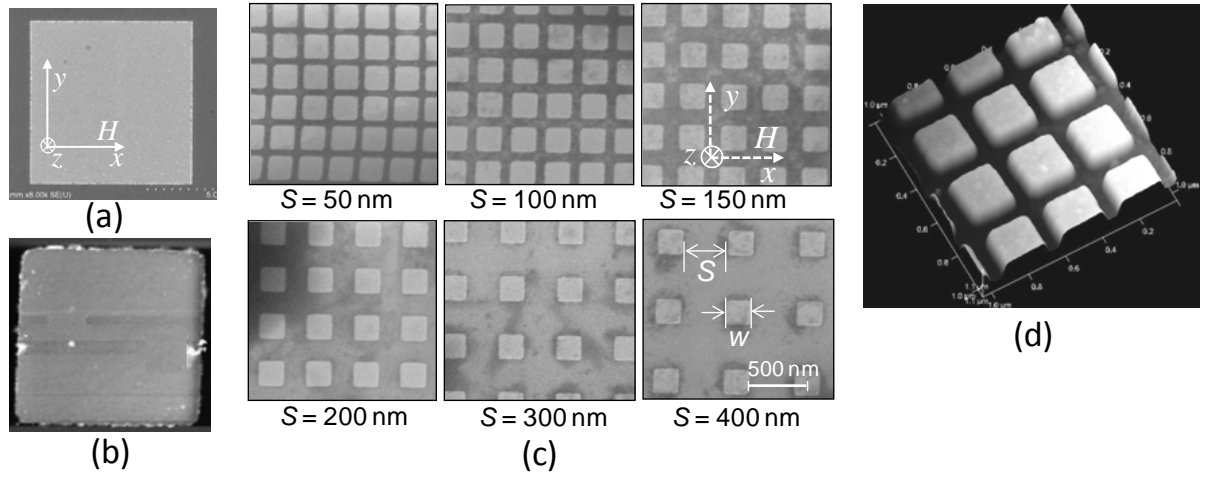


Fig. 6.1: (a) A typical scanning electron micrograph (SEM) and (b) atomic force microscope (AFM) image of  $10 \times 10 \mu\text{m}^2$  blanket permalloy thin film is shown. The sample surface is in  $x$ - $y$  plane. The geometry of magnetic field is shown on top of the SEM image. (c) Scanning electron micrographs of arrays of square permalloy dots with width ( $W$ ) = 200 nm, thickness ( $t$ ) = 20 nm and with varying edge-to-edge interelement separations ( $S$ ) from 50 nm to 400 nm. (d) AFM image of array of 200 nm square dots with  $S = 100$  nm.

The static magneto-optical Kerr effect (SMOKE) microscope was used to measure magnetic hysteresis loops (Kerr rotation as a function of the magnetic field ( $H$ )) for  $10 \times 10 \mu\text{m}^2$  blanket permalloy thin film and arrays of 200 nm permalloy dots. A linearly polarized CW laser beam of wavelength ( $\lambda$ ) = 632 nm was used for this measurement. The linearly polarized beam, chopped at 1-2 kHz frequency by a chopper, is incident on an extra long working distance (25 mm) microscope objective (MO) with N. A. = 0.55 and magnification =  $\times 40$ . The incident point of the beam on back aperture of the MO is kept away from the centre, so that the beam is incident on the sample at an oblique angle less than  $90^\circ$  with the sample surface. The reflected beam from the sample gets collected by the front lens assembly of the MO and comes out of the back aperture of the MO through a point diametrically opposite to the point of incidence. The magnetic field is applied in the plane of the sample. In this geometry, the longitudinal Kerr rotation is measured by sending the back-reflected beam to an optical bridge detector (OBD). The Kerr rotation was measured in a phase sensitive manner by using a lock-in amplifier with a reference signal from the chopper.

The ultrafast magnetization dynamics of the blanket thin film and the dot arrays were measured by using our home-built time-resolved magneto-optical Kerr effect microscope based upon a two-colour collinear pump-probe setup. The second harmonic ( $\lambda = 400$  nm,

pulse width  $\approx 100$  fs) of a Ti-sapphire laser (Tsunami, Spectra Physics, pulse width  $\approx 70$  fs) was used to pump the samples, while the time delayed fundamental ( $\lambda = 800$  nm) laser beam was used to probe the dynamics by measuring the polar Kerr rotation by means of the optical bridge detector, which completely isolates the Kerr rotation and the total reflectivity signals. The pump power used in these measurements is about  $15 \text{ mJ/cm}^2$ , while the probe power is much weaker and is about  $3 \text{ mJ/cm}^2$ . The probe beam is focused to a spot size of  $800$  nm and placed at the centre of each array by a microscope objective with numerical aperture N. A. =  $0.65$  and a closed loop piezoelectric scanning  $x$ - $y$ - $z$  stage. The pump beam is spatially overlapped with the probe beam after passing through the same microscope objective in a collinear geometry. Consequently, the pump spot is slightly defocused (spot size  $\approx 1 \mu\text{m}$ ) on the sample plane, which is also the focal plane of the probe spot. The probe spot is placed at the centre of the pump spot. A large magnetic field is first applied at a small angle ( $\sim 15^\circ$ ) to the sample plane to saturate its magnetization. The magnetic field strength is then reduced to the bias field value ( $H_b$  = component of bias field along  $x$ -direction), which ensures that the magnetization remains saturated along the bias field direction. The bias field was tilted  $15^\circ$  out of the plane of the sample to have a finite demagnetizing field along the direction of the pump pulse, which is eventually modified by the pump pulse to induce precessional magnetization dynamics within the dots. The pump beam was chopped at  $2 \text{ kHz}$  frequency and a phase sensitive detection of the Kerr rotation was used.

### 6.3 Quasistatic Magnetization Dynamics of $10 \times 10 \mu\text{m}^2$

#### Permalloy Blanket Thin Film and Arrays of $200 \text{ nm}$ Square Permalloy Dots

In Fig. 6.2(a), experimentally measured magnetic hysteresis loops (Kerr rotation as a function of the magnetic field ( $H$ )) for a  $10 \times 10 \mu\text{m}^2$  blanket permalloy thin film and arrays of  $200 \text{ nm}$  permalloy dots with  $S = 50 \text{ nm}$ , are shown. A focused laser spot of about  $2 \mu\text{m}$  width was placed at the centre of the blanket film (array) to acquire the loops. The figure shows a square hysteresis loop for the permalloy blanket film with  $11 \text{ Oe}$  of coercive field ( $H_C$ ) and about  $100\%$  remanence ( $M_r$ ). The square hysteresis loop indicates that the magnetization reversal occurs through the coherent rotation of the spins of the blanket film within the focused laser spot. The hysteresis loop for arrays of  $200 \text{ nm}$  permalloy dots with  $S = 50$  is visibly deviated from square shape as observed for the blanket film. As the interdot

separation ( $S$ ) increases, the shapes of the hysteresis loops change further and they deviate more from the square shape (Fig. 6.2(b)). Though the Kerr signals become very noisy, but the general features can be extracted from the measured hysteresis loops.

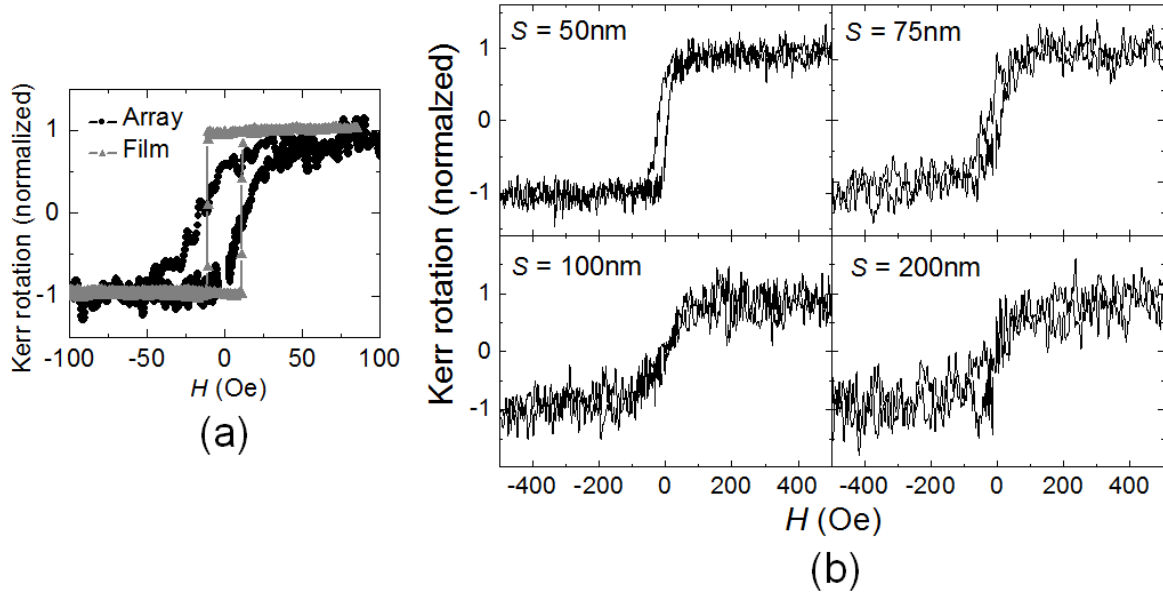


Fig. 6.2: (a) Normalized static MOKE loops for a  $10 \times 10 \mu\text{m}^2$  blanket permalloy thin film and array of 200 nm wide permalloy square shaped dots with  $S = 50$  nm are shown. (b) Normalized static MOKE loops for arrays of 200 nm wide permalloy square shaped dots are shown for four different interdot separations  $S = 50$  nm, 75 nm, 100 nm and 200 nm.

For  $S = 400$  nm (not shown), the nanodots are magnetostatically isolated and they reverse independent of the neighbours according to their intrinsic switching fields. The switching fields of all the dots are not the same due to small size and shape distributions. Therefore, a gradual reversal of magnetization is observed as the field is changed from  $H_{\text{max}}$  to  $-H_{\text{max}}$  and in this case the hysteresis loop is deviated by maximum amount from the square shaped loop. For the array with  $S < 400$  nm ( $S = 200$  nm), the nanodots start to interact with each other (magnetostatic interaction among the nanodots with separation will be shown later in this chapter). Therefore, reversal of each dot is influenced by the magnetostatic stray fields from the neighbouring dots. Due to the introduction of a weakly collective behaviour, the saturation field ( $H_S \sim 400$  Oe) for this case decreases as compared to that for the array with  $S = 400$  nm ( $> 400$  Oe). As the separation is further decreased below 200 nm ( $S = 100$  nm), the collective behaviour increases and the magnetic flux may start to flow through a number of nanodots leading towards the formation of local closure domain structures [23]. Therefore, the saturation field decreases further (150 Oe) while the remanence increases to  $\sim$

10%. With further decrease of  $S$  below 100 nm, the dots become very strongly coupled with each other by magnetostatic interactions. At  $S = 50$  nm, the saturation field is only  $\sim 70$  Oe, while the remanence has increased to about 65%. The coercive field is also  $\sim 13$  Oe, as compared to 11 Oe for the blanket permalloy thin film. We believe that the intrinsic magnetization reversal of the individual nanodots in the array is suppressed significantly in this case and a strong collective reversal is observed. However, there is still a deviation in the hysteresis loop for the array with  $S = 50$  nm than that of the blanket film. The deviation is attributed to the defects and edge roughness in the dots introduced during nanofabrication. The edge roughness and defects introduces local anisotropy (pinning) fields, which are aligned along random directions. Therefore, the spins in those regions do not follow the collective magnetization reversal as opposed to the other parts of the array. The signal-to-noise ratio of the MOKE loops also increases gradually with the decrease in  $S$  due to increase in the collective magnetization reversal process.

## 6.4 Ultrafast Magnetization Dynamics of $10 \times 10 \mu\text{m}^2$ Permalloy Blanket Thin Film

Before measuring the dynamics of the dot arrays, we measured the dynamics of the  $10 \times 10 \mu\text{m}^2$  blanket permalloy thin film. This measurement helped us to extract the magnetic parameters of the material used for the nanodot arrays. In Fig. 6.3(a), the geometry of the bias magnetic field ( $H_b$ ) and the schematic of the pump and probe spots are shown on top of the AFM image of  $10 \times 10 \mu\text{m}^2$  blanket permalloy thin film. The sample surface is in the  $x$ - $y$  plane and the bias magnetic field is applied at about  $15^\circ$  out from the plane of the sample. The in-plane component of the bias field ( $H_b$ ) is parallel to the edge of the film along  $x$ -axis as shown on the top of Fig. 6.3(a). Figures 6.3(b) and (c) show the reflectivity and Kerr rotation data as a function of the time delay between pump and the probe beams measured from the blanket permalloy film at a bias field of 1.4 kOe (well above the saturation field). The reflectivity signal (Fig. 6.3(b)) shows a sharp increase at zero delay followed by a bi-exponential decay. The sharp increase in the reflectivity is due to the creation of hot electrons (charge degree of freedom) above the Fermi level [24]. The bi-exponential decay originates from the relaxation of the hot electrons to its ground state through electrons-phonons relaxation and heat diffusion to the environment or substrate [24]. Our main focus is not to study of reflectivity (electron or phonon dynamics) but to study the magnetic signal. The Kerr

rotation was recorded for up to 1500 ps time delay. To find out the ultrafast demagnetization and fast relaxation times precisely, we recorded the data points at a time step of 100 fs for an initial time window of up to 25 ps, while the rest part of the dynamics was recorded at a time step of 5 ps to extract the slow relaxation time, precession and damping of magnetization.

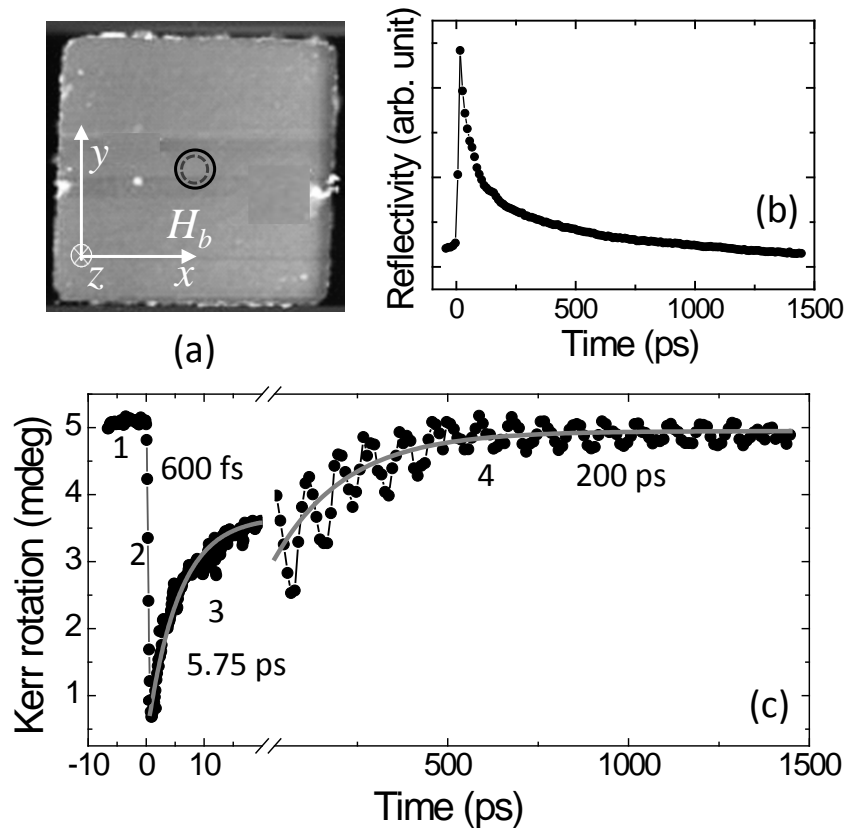


Fig. 6.3: (a) The geometry of bias magnetic field and schematics of the pump and the probe beams are shown on the top of an AFM image of  $10 \times 10 \mu\text{m}^2$  blanket permalloy thin film. (b) A typical time-resolved reflectivity data is plotted as a function of the time delay between the pump and the probe. (c) A typical Kerr rotation data from the blanket thin film with a bias field magnitude ( $H_b$ ) of 1.4 kOe, applied along the positive  $x$ -axis. The time-resolved Kerr rotation shows four distinct regions, marked by numbers (1, 2, 3 and 4). The corresponding time scale is also written on top of the graph. The solid grey line in regions 3 and 4 are the bi-exponential fitting to the data, which gives the relaxation times  $\tau_1 = 5.75$  ps and  $\tau_2 = 200$  ps.

The time-resolved Kerr rotation shows four distinct regions marked as 1, 2, 3 and 4 in Fig. 6.3(c). In region 1 (–ve delay), the probe reaches the sample before the pump beam *i.e.*, before any excitation of the sample, and hence no variation in magnetization (Kerr rotation) is observed with time. This gives the saturated magnetization state at the applied bias field. In region 2, the probe beam reaches at the same time (zero delay) or just after the pump beam.

The magnetization (Kerr rotation) drops sharply to a minimum value within about 600 fs. This corresponds to the ultrafast demagnetization of the sample [25]. This demagnetization is occurred due to the thermalized population of spins above the Fermi level (discussed in section 2.6.3) [26-27]. In region 3, magnetization is recovered very sharply with a time constant ( $\tau_1$ ) of 5.75 ps due to the relaxation of spins by spin-lattice interaction. After that, the slow recovery of magnetization is observed with a time constant of about 200 ps along with the precession of magnetization, which is marked as region 4. This slow relaxation occurs due to the diffusion of electron and lattice heat to the surroundings (in this case the Si substrate) [24, 28].

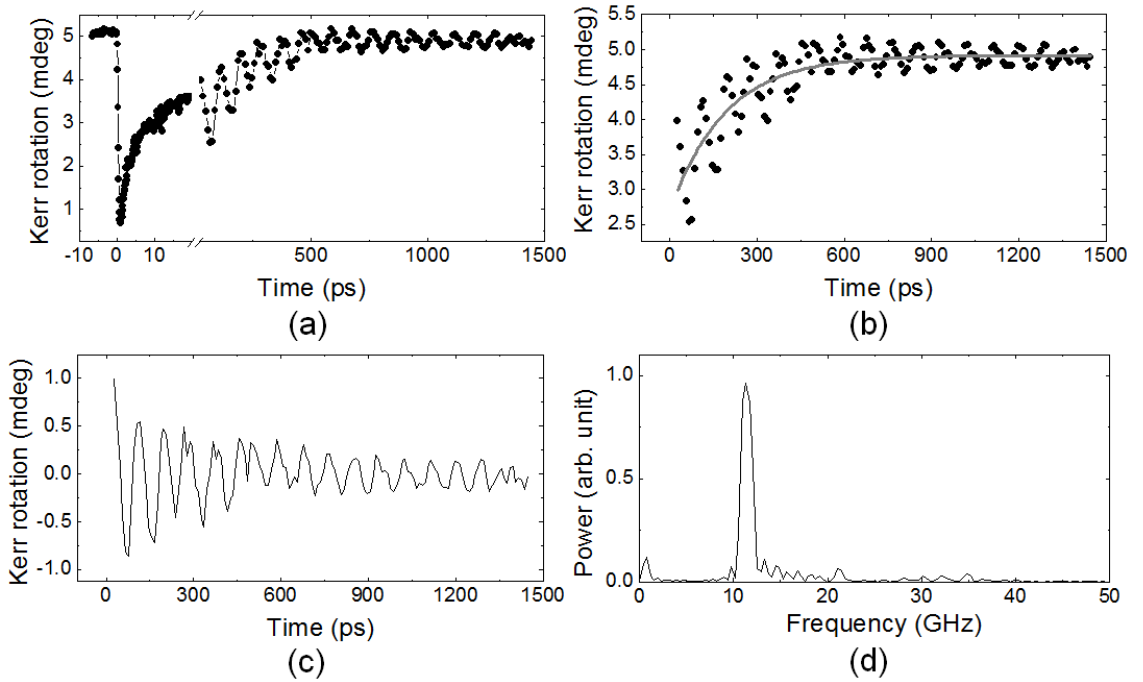


Fig. 6.4: (a) The time-resolved Kerr rotation from the blanket permalloy thin film with a bias magnetic field  $H_b = 1.4$  kOe, applied along the positive  $x$ -axis. The solid line is only a guide to the eyes. (b) The oscillatory part of the time-resolved Kerr rotation (symbol) with a bi-exponential fit (solid line). (c) The background subtracted time-resolved Kerr rotation data and (d) the corresponding FFT power spectra showing the resonant mode.

The relaxation times ( $\tau_1 = 5.75$  ps,  $\tau_2 = 200$  ps) of magnetization were extracted by fitting the post demagnetization time-resolved Kerr rotation data with a bi-exponential function as shown by the solid grey line in Fig. 6.3(c). The bi-exponential function is given by

$$M(t) = M(0) + Ae^{-t/\tau_1} + Be^{-t/\tau_2}, \quad (6.4.1)$$

where  $M(0)$  is the initial magnetization,  $A$ ,  $B$  are the relaxation constants and  $\tau_1$  and  $\tau_2$  are the fast and slow relaxation time, respectively.

To investigate the precession frequency and damping, the oscillatory part of the time-resolved Kerr rotation (marked as 4) is separated out and the bi-exponential background is fitted as shown in Fig. 6.4(b). The bi-exponential background is then subtracted from the oscillatory part and fast Fourier transform (FFT) on the background subtracted data (Fig. 6.4(c)) is then performed. Figure 6.4(d) shows the frequency spectra as obtained from the precessional signal measured from the blanket permalloy film at  $H_b = 1.4$  kOe, applied along positive  $x$ -axis. The frequency resolution of the FFT spectra depends upon the total measurement time.

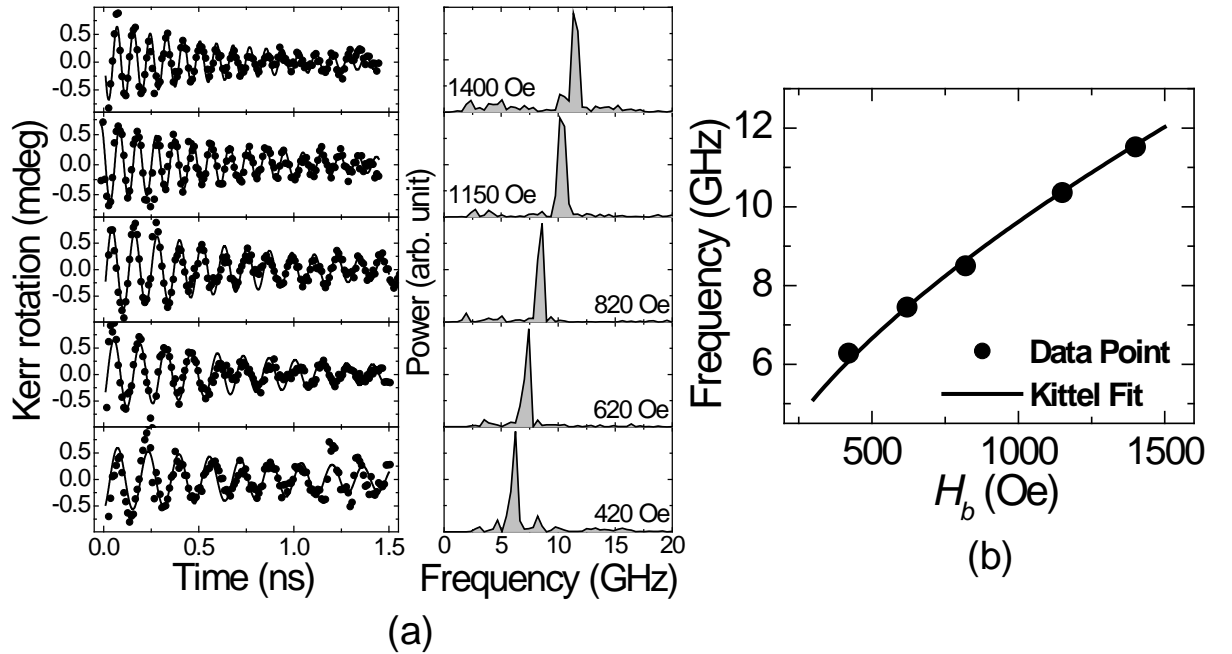


Fig. 6.5: (a) Left panel (solid circles) shows the background subtracted time-resolved Kerr rotation signals measured from a  $10 \times 10 \mu\text{m}^2$  blanket permalloy film as function of the bias magnetic field applied along  $x$ -axis. Solid black lines are fits with Eq. 6.4.3. Right panel shows the FFT power spectra of the time-resolved data. (b) Frequencies of the uniform precessional mode as a function of the bias magnetic field (solid circles) and the fit with the Kittel formula (solid line) are shown.

The left column of Fig. 6.5(a) shows the background subtracted time-resolved Kerr rotations (solid circles) measured from the blanket permalloy thin film at different bias magnetic field magnitudes. The right column shows corresponding FFT power spectra. Single precessional mode corresponding to the uniform precession of magnetization is observed for all values of the bias magnetic field. Frequencies of uniform precessional modes

are plotted as a function of the bias magnetic field (solid circles) and are fitted with the Kittel formula (Eq. 6.4.2) [29] (solid line) for uniform precession of magnetization (Fig. 6.5(b)). The Kittel formula is given by

$$f = \frac{\gamma}{2\pi} \sqrt{(H_b + H_k)(H_b + H_k + 4\pi M_s)}, \quad (6.4.2)$$

where  $\gamma$  is the gyromagnetic ratio,  $H_b$  is the bias field,  $H_k$  is the magnetocrystalline anisotropy and  $M_s$  is the saturation magnetization for permalloy. From the fitting, the magnetic parameters were obtained as  $\gamma = 18.5$  MHz/Oe,  $H_k \approx 0$  and  $M_s = 860$  emu/cm<sup>3</sup>.

To extract the damping coefficient, the time-resolved background subtracted Kerr rotation data at different bias magnetic fields are fitted with a damped sine curve given by

$$M(t) = M(0)e^{-\frac{t}{\tau}} \sin(2\pi ft - \phi). \quad (6.4.3)$$

The relaxation time  $\tau$  is related to the damping coefficient  $\alpha$  by the relation  $\tau = 1/(2\pi f\alpha)$ , where  $f$  is the frequency of the uniform mode and  $\phi$  is the initial phase of the oscillation [30]. The fitted data are shown by solid black lines in Fig. 6.5(a). The extracted values of  $\alpha$  for the permalloy film is found out to be  $0.017 \pm 0.001$  for all values of the bias field.

## 6.5 Ultrafast Magnetization Dynamics of Arrays of 200 nm Square Permalloy Dots as a Function of Areal Density

### 6.5.1 Ultrafast Demagnetization and Remagnetization

In this section, we will investigate the effect of areal density of nanodots on the ultrafast demagnetization and fast remagnetization times. The samples are already shown in Fig. 6.1. In Fig. 6.6, we show the time-resolved Kerr rotation for the arrays of nanodots with  $S = 50$  nm, 100 nm and 200 nm, for the first 25 ps with a time resolution of 100 fs to illustrate the ultrafast demagnetization and the fast remagnetization. For all values of  $S$ , the demagnetization time is found to be between 500 and 600 fs, which means that the demagnetization time is independent of the geometry of the array. This is because the thermalization time, which is responsible for demagnetization is an intrinsic property of the material and is independent of extrinsic parameters like sample geometry.

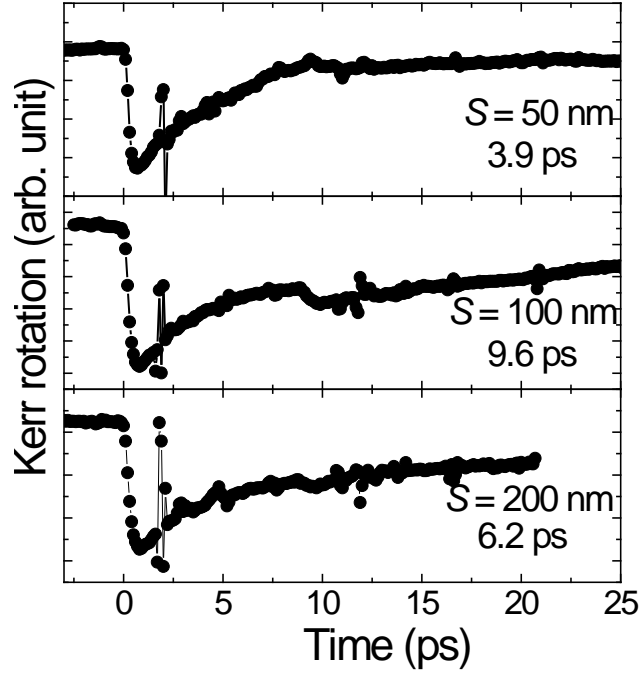


Fig. 6.6: Time-resolved Kerr rotation for the first 25 ps is shown for arrays of 200 nm square shaped permalloy dots with interdot separation  $S = 50$  nm, 100 nm and 200 nm. The ultrafast demagnetization time is between 500 and 600 fs, while the fast relaxation time  $\tau_l$  is shown next to each time-resolved trace.

To find out the fast relaxation times ( $\tau_l$ ), the relevant part of the time-resolved data is separated out and is fitted with a single exponentially decaying function:

$$M(t) = M(0) + Ae^{-t/\tau_l}. \quad (6.5.1)$$

The fast relaxation ( $\tau_l$ ) time, which is also known as the fast remagnetization time is found to vary non-monotonically between 3.9 and 9.6 ps for different arrays. The literatures say that the faster relaxation ( $\tau_l$ ) of magnetization occurs after the ultrafast demagnetization because spins exchange thermal energy and angular momentum with the lattice through spin-lattice or spin-orbit interaction.  $\tau_l$  may vary from sub-ps to several ps depending upon the strength of the spin-orbit coupling and the specific heats of the spins and phonons [24, 28, 31]. The relaxation time also depends on the density of laser excitation [24, 28] and magneto-crystalline anisotropy. In this case all the above parameters remained unchanged except for the strength of the spin-orbit interaction. In ferromagnetic solids, the spin-orbit interaction is determined not only by the intrinsic atomic spin-orbit coupling, but also by the local lattice structure and symmetry [32-33]. In nanomagnets, percentage of surface spins is larger than the bulk materials. Therefore, in nanomagnets there are many surface spins which experience

different ligand fields from those of the interior spins due to the structural discontinuity at the surface. Hence, the rate of energy and momentum transfer from spin to lattice in nanomagnets is significantly influenced by the surface spins [33]. This signifies that the magnetization relaxation time for surface spins is faster than the interior spins [34]. In our case, there is a small size and shape distribution in the nanodots and the average size of the nanodots may be different for different arrays. The ratio of the number of surface to volume spins of smaller particles is larger than the same for the larger particles. Therefore, the relaxation time ( $\tau_1$ ) of smaller particles should be faster than the larger particles. This is probably the reason for obtaining a variation in  $\tau_1$  for different arrays. In addition, the presence of sample roughness and defects may also play an important role in the variation of  $\tau_1$  to some extent. However, since the non-idealities and defects in the samples do not vary systematically with the variation in the interdot separation, no systematic variation in  $\tau_1$  with the same is observed.

The slow relaxation ( $\tau_2$ ) time, which is also known as the slow remagnetization time, also varies randomly between 150 and 200 ps for arrays with different separations. The second or longer relaxation time ( $\tau_2$ ) corresponds to the diffusion of electron and lattice heat to the surroundings (in this case the Si substrate) [24, 28]. Diffusion rate depends upon the type of substrate as well as the physical contacts between the nanodots with the substrate and the environments of the nanodots itself. The variation in the slower relaxation time ( $\tau_2$ ) may be attributed to the variation in the configurations of the nanodots in different arrays and their physical contacts with the Si substrates.

## 6.5.2 Time-resolved Precessional Dynamics: Experimental Results

Figures 6.7(a) and (b) show the background subtracted time-resolved Kerr rotation data and the corresponding FFT spectra from the arrays of permalloy dots with  $W = 200$  nm and with varying  $S$  between 50 nm and 400 nm at a fixed bias magnetic field value  $H_b = 1.25$  kOe. The geometry of the bias field is shown on top of Fig. 6.1(c). The FFT spectra show a clear variation in the precession frequencies with the increase in  $S$  [35]. A single resonant mode is observed for  $S = 50$  nm and 75 nm, but the amplitude of precession for  $S = 75$  nm decays faster than that for  $S = 50$  nm due to the inhomogeneous line broadening. For  $S = 100$  nm, a lower frequency mode is appeared along with the partial splitting of the intense resonant mode. For  $S = 150$  nm, three distinct modes are observed and the situation remains

same till  $S < 400$  nm, although the splitting amplitude increases with the increase in  $S$ . For  $S = 400$  nm, another drastic change occurs and only two distinct well separated modes are observed.

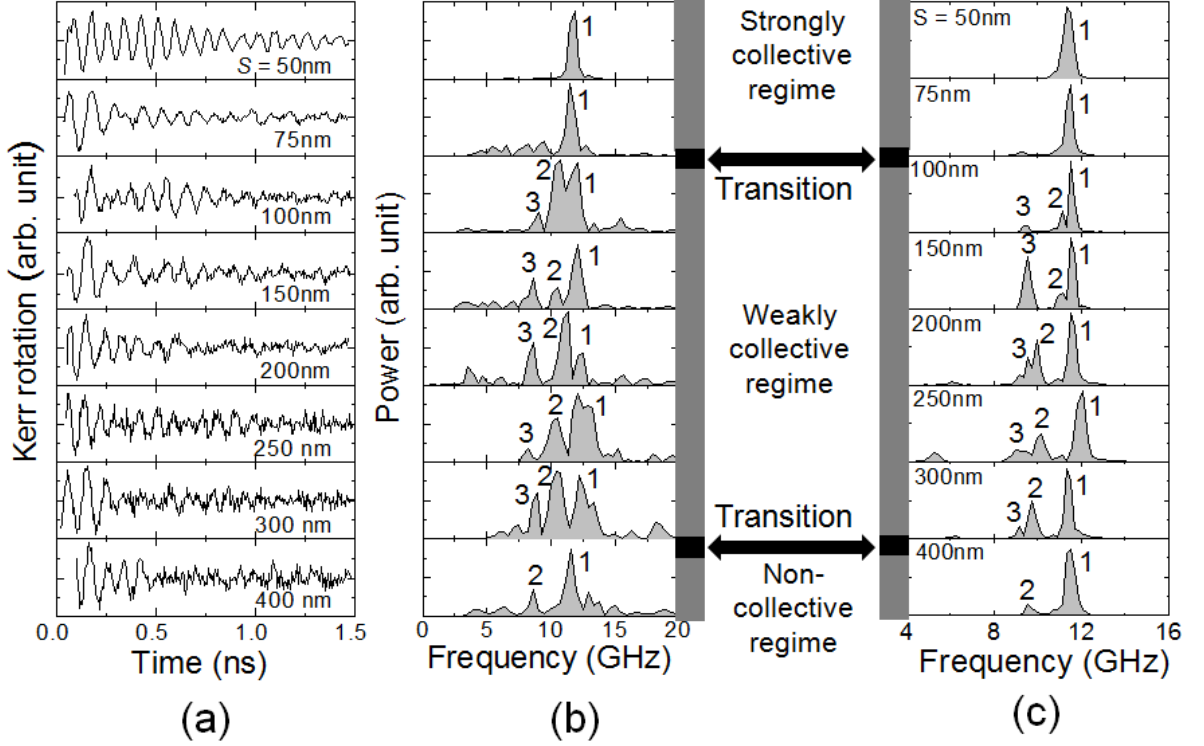


Fig. 6.7: (a) Experimental time-resolved Kerr rotations and (b) corresponding FFT spectra are shown for arrays of permalloy square dots with width ( $W$ ) = 200 nm, thickness ( $t$ ) = 20 nm, and varying interdot separations ( $S$ ) at  $H_b = 1.25$  kOe. (c) FFT spectra of simulated time-domain magnetization for  $7 \times 7$  array of dots with same specifications as in the experiment.

### 6.5.3 Micromagnetic Simulations

We have performed finite difference method based micromagnetic simulations by using OOMMF software [36] to understand the details of the observed modes. For the simulation,  $7 \times 7$  square arrays of permalloy dots with  $W = 200$  nm,  $t = 20$  nm and varying  $S$  from 50 nm to 400 nm were considered. It was found that a minimum  $7 \times 7$  array of dots is required to take into account of the effect of the long range magnetostatic interaction correctly [37]. The observed deviations in the dot size and the interdot separation from the nominal dimensions from the SEM images are incorporated in the sample geometry although the precise profile of the edge roughness and deformation could not be incorporated in the finite difference method based micromagnetic simulations used here. The extracted materials parameters ( $\gamma$ ,  $H_k$  and  $M_S$ ) from the dynamics of  $10 \times 10 \mu\text{m}^2$  blanket permalloy film were

used in the micromagnetic simulations for the arrays. The exchange stiffness constant  $A$  was obtained from literature [38]. The samples were discretized into a number of cuboidal cells of size  $5 \times 5 \times 20 \text{ nm}^3$ . The lateral dimensions of the cells were set lower than the exchange length for permalloy ( $\sim 5.3 \text{ nm}$ ) to incorporate the role of exchange interaction on the dynamics. The thickness of the cells was set same as the sample thickness, which is much larger than the exchange length. This is because we were not interested in studying the perpendicular standing spin wave (PSSW) modes. Instead of that we are interested to study the collective in-plane modes. Further test simulations with reduced cell sizes do not show any significant changes in the static and dynamic behaviours and also in the mode profiles.

The ground states of magnetization were carefully prepared in the same way as was done in the experiment. First, a large magnetic field (5 kOe) was applied parallel to the edge of the array ( $10\text{-}15^\circ$  tilted from the sample plane) (Fig. 4.11(a)) and then the magnitude of the magnetic field was reduced to the bias field value with sufficient time for relaxation so that the maximum torque,  $\mathbf{m} \times \mathbf{H}$ , where  $\mathbf{m} = \mathbf{M}/M_S$ , goes well below  $10^{-6} \text{ A/m}$ . This is very important because the ground state strongly depends upon the history of the applied magnetic field. In this case, a high value of damping constant ( $\alpha = 0.9$ ) is used so that magnetization can reach the equilibrium state quickly. To trigger the precession, a pulsed magnetic field of peak amplitude = 30 Oe and rise time = 40 ps was applied perpendicular to the sample plane assuming the magnetic ground state as the initial magnetization state. During the dynamical calculation  $\alpha$  is set at 0.008, the typical value for permalloy [39]. The dynamic simulations were run for time duration of 4 ns at time steps of 5 ps. The convergence criterion for the dynamic simulation is set on the simulation time steps. The experimentally observed modes and the key features are qualitatively reproduced by the micromagnetic simulations as shown in Fig. 6.7(c). In the simulation, appearance of a single resonance mode at  $S = 50$ , presence of a low amplitude lower frequency mode at  $S = 75 \text{ nm}$ , broadening and splitting of the resonant mode at  $S = 100 \text{ nm}$ , occurrence of three distinct modes between 150 & 300 nm, and the appearance of two well defined modes for  $S = 400 \text{ nm}$  are observed. The dynamic behaviour can be divided into three distinct regimes: a uniform (strongly) collective regime ( $S \leq 75 \text{ nm}$ ), a nonuniform (weakly) collective regime ( $100 \text{ nm} \leq S \leq 300 \text{ nm}$ ) and a non-collective (isolated) regime ( $S > 300 \text{ nm}$ ). A systematic transition from one regime to another is observed with the variation in the areal density from both experimental and simulated results.

## 6.5.4 Numerical Calculation of Magnetostatic Field Distribution

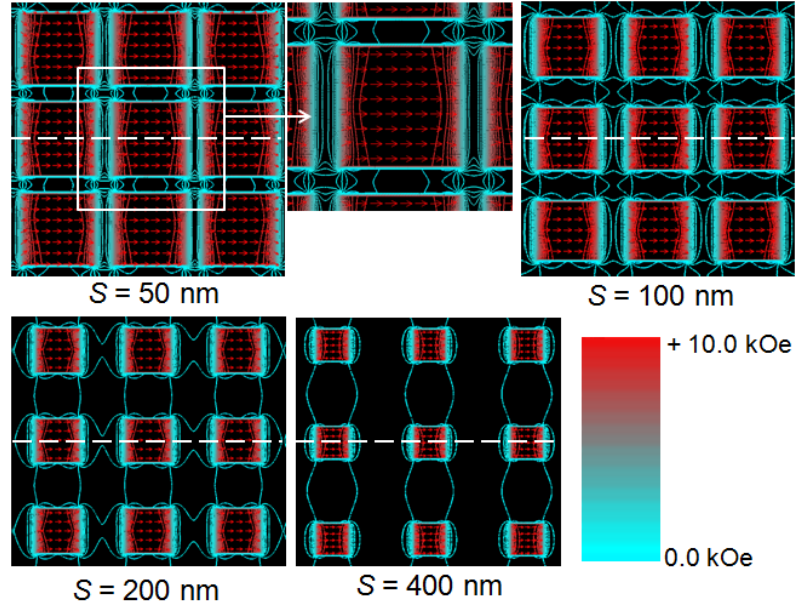


Fig. 6.8: Profiles of the simulated magnetostatic field distribution ( $x$ -component) for  $3 \times 3$  arrays of permalloy dots with  $W = 200$  nm and with varying  $S$  values are shown for  $H_b = 1.25$  kOe. The magnetostatic fields were calculated for array of  $7 \times 7$  elements, out of which  $3 \times 3$  elements from the centre have been shown. The arrows inside the dots represent the magnetization states of the dots. The strength of the stray magnetic field is presented by a contour map with a colour bar as shown at the bottom right corner of the figure.

In the above study, we varied the areal density of the array, which effectively varied the magnetostatic interaction among the dots. In order to get an idea of how this interaction changes as a function of the areal density, we have simulated magnetostatic field distributions for  $7 \times 7$  arrays of dots with different interdot separation ( $S$ ). The simulations were done by LLG micromagnetic simulator [40]. Figure 6.8 shows contour maps of the simulated magnetostatic fields for  $3 \times 3$  dots taken from the centre of larger ( $7 \times 7$ ) arrays. The magnetostatic field profiles have been shown for four different separations ( $S = 50, 100, 200$  and  $400$  nm). For larger separation ( $S \geq 400$  nm), the interaction among the dots is negligible and they are magnetostatically isolated. As the separation decreases, the interactions among the dots increase, which modify the magnetic ground states and the corresponding dynamics. For  $S \leq 75$  nm, the dots are strongly coupled to each other, giving rise to a strongly collective dynamics both in quasistatic magnetization reversal and in precessional magnetization dynamics.

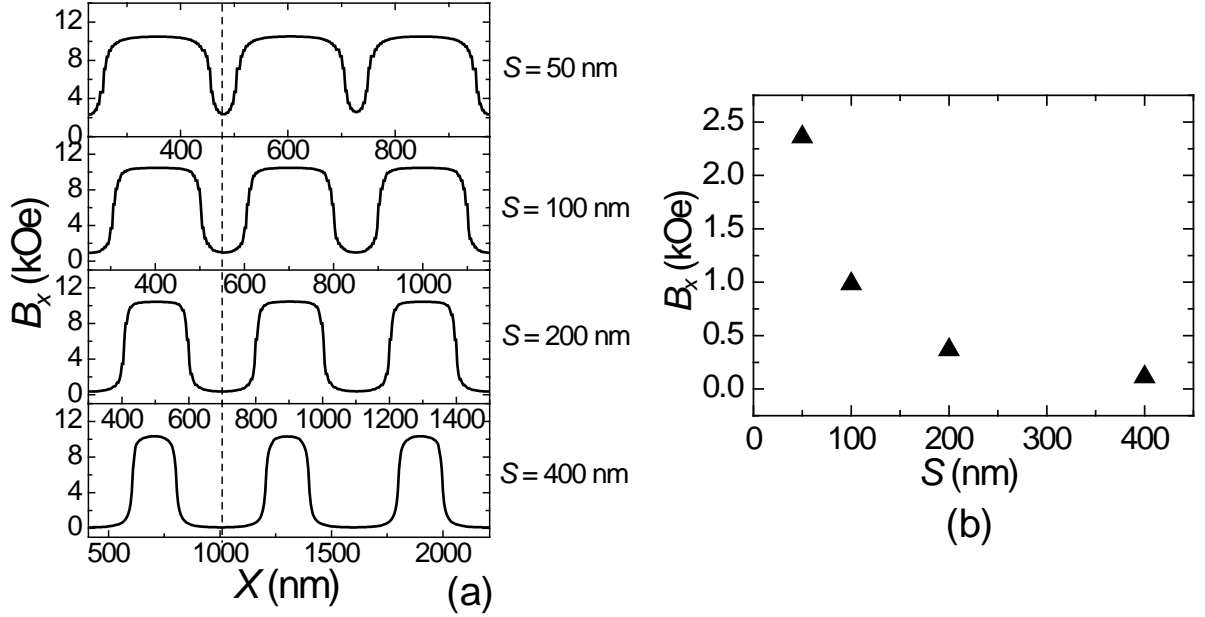


Fig. 6.9: (a) Lineplots of the magnetostatic fields from arrays of 200 nm square permalloy dots with  $S = 50$  nm, 100 nm, 200 nm and 400 nm are shown. The lineplots were taken along the dotted lines (parallel to  $x$ -axis) as shown in Fig. 6.8. (b) The magnitudes of the  $x$ -component of the stray magnetic field at the centre of the gap between two consecutive dots are plotted as a function of  $S$ . The values of  $B_x$  were taken along the dotted line as shown in (a).

To get the quantitative values of the stray magnetic fields, we have also calculated the lineplots of the magnetostatic fields along the dotted lines as shown in Fig. 6.8. The lineplots are presented in Fig. 6.9(a). In Fig. 6.9(b) the magnitudes of the  $x$ -component of the stray magnetic field ( $B_x$ ) at the centre of the gap between two consecutive dots are plotted as a function of  $S$ . The plot shows that  $B_x$  is quite high ( $\sim 2.25$  kOe) for  $S = 50$  nm and decreases steeply with the increase in  $S$  and becomes  $\sim 110$  Oe for  $S = 400$  nm.

### 6.5.5 Power and Phase Profiles of Resonant Modes

To understand the natures of the observed collective modes, we have further simulated the spatial profiles of the powers and phases corresponding to each resonant mode [41]. The mode profiles are calculated by the method as described in section 5.4. At first, we simulated the mode profiles for a single nanodot with  $W = 200$  nm and for the  $10 \times 10 \mu\text{m}^2$  blanket film. The simulated mode spectra for these two samples are shown in Fig. 6.10 (1st column) along with their static magnetization states (2nd column). The mode profiles (power) are shown in the 3rd, 4th and 5th columns for  $H_b = 1.25$  kOe applied parallel to the horizontal edge of the elements. The blanket film shows a single mode, whereas the 200 nm dot shows

three modes. The magnetic ground state for the blanket film is almost uniform with negligible edge demagnetized regions, which leads to the uniform precession of the majority spins and hence a single uniform mode. However, for the 200 nm dot the magnetic ground state becomes nonuniform with a prominent demagnetized region near the edges, which leads to three distinct modes. Figure 6.10 shows that mode 1 is the centre mode (CM) and mode 3 is the edge mode (EM), while mode 2 is a mixture of edge mode and a Damon Eshbach (EM-DE) mode.

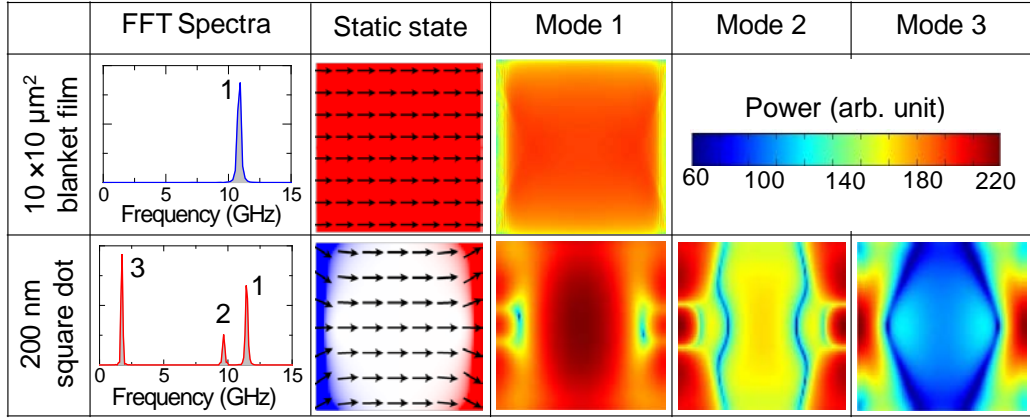


Fig. 6.10: Simulated mode spectra for a  $10 \times 10 \mu\text{m}^2$  permalloy blanket film and a single permalloy dot with  $W = 200 \text{ nm}$  are shown (1st column) along with their static magnetization states (2nd column) and mode profiles (3rd, 4th and 5th column) for  $H_b = 1.25 \text{ kOe}$  applied parallel to the horizontal edge of the elements. The colour scale for power profile is shown in the first row.

Power and phase profiles of the resonant modes for arrays of 200 nm dots with varying interdot separation ( $S$ ) are shown in Fig. 6.11 for  $3 \times 3$  elements extracted from the centres of the larger ( $7 \times 7$ ) arrays. For  $S = 50 \text{ nm}$ , a uniform collective precession (in-phase) of all the dots are observed due to the strong magnetostatic interaction among the dots. This mode is completely different from the CM observed in the single 200 nm dot as the mode occupies a major volume of the dots including regions originally occupied by the EM for a single dot. For  $S = 100 \text{ nm}$ , the highest frequency mode (mode 1) corresponds to the collective precession of the dots, where the mode profiles of constituent dots look similar to the CM of a single dot. In mode 3, the power profiles of constituent dots look identical to the mixed EM-DE mode of single 200 nm dot. Mode 2 is a backward volume magnetostatic (BWVMS) like mode. The mode profiles for arrays with  $S = 200 \text{ nm}$  and  $S = 300 \text{ nm}$  (not shown) look identical to the modes observed for the array with  $S = 100 \text{ nm}$ , with slight modifications due to the change in the strength of magnetostatic stray fields. For  $S = 400 \text{ nm}$ ,

the mode profiles of constituent dots look similar to the modes observed for a single 200 nm dot. For this separation, the dots are magnetostatically isolated and collective behaviour is absent.

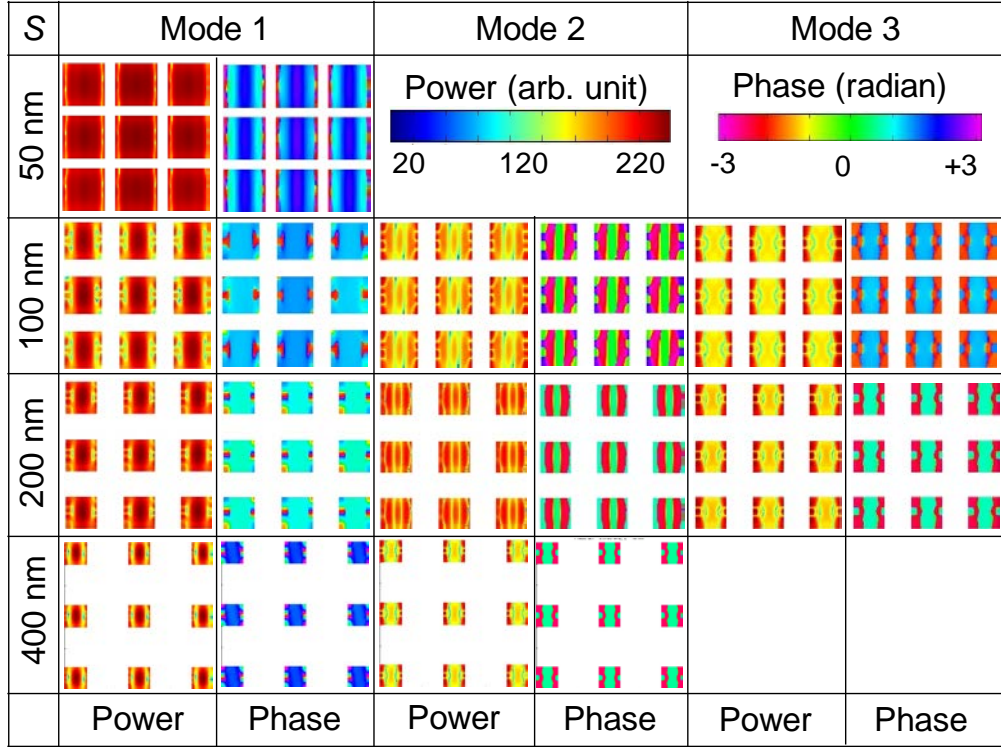


Fig. 6.11: Power and phase distributions of the simulated modes for arrays of 200 nm dots with varying interdot separation  $S$  at  $H_b = 1.25$  kOe. The colour scales for power and phase are shown in the top row.

In the above, we have described the collective behaviours of the higher frequency modes, as observed in the experiment. The lower frequency EM was not taken into account. In Fig. 6.12(a), the EM's from the arrays are shown along with their spatial profiles, which look identical to the EM of the individual 200 nm element. Surprisingly, this mode remains unaffected in the array both in the frequency spectra and in the mode profile. This EM was not consistently observed in the experimental data. This is probably because the defects and edge roughness of the lithographically fabricated nanodots strongly affect this mode leading towards very small power in this mode. Further, inhomogeneous line broadening and smaller experimental time window in the TRMOKE measurements make it difficult to resolve this mode for the 200 nm dots [22]. In Fig. 6.12(b), we show simulated results for several  $S$  values between 50 and 100 nm to resolve the value of  $S$  at which the mode splitting occurs.

Simulation shows that a shoulder of the main peak appears at  $S = 75$  nm, which splits completely at  $S = 90$  nm.

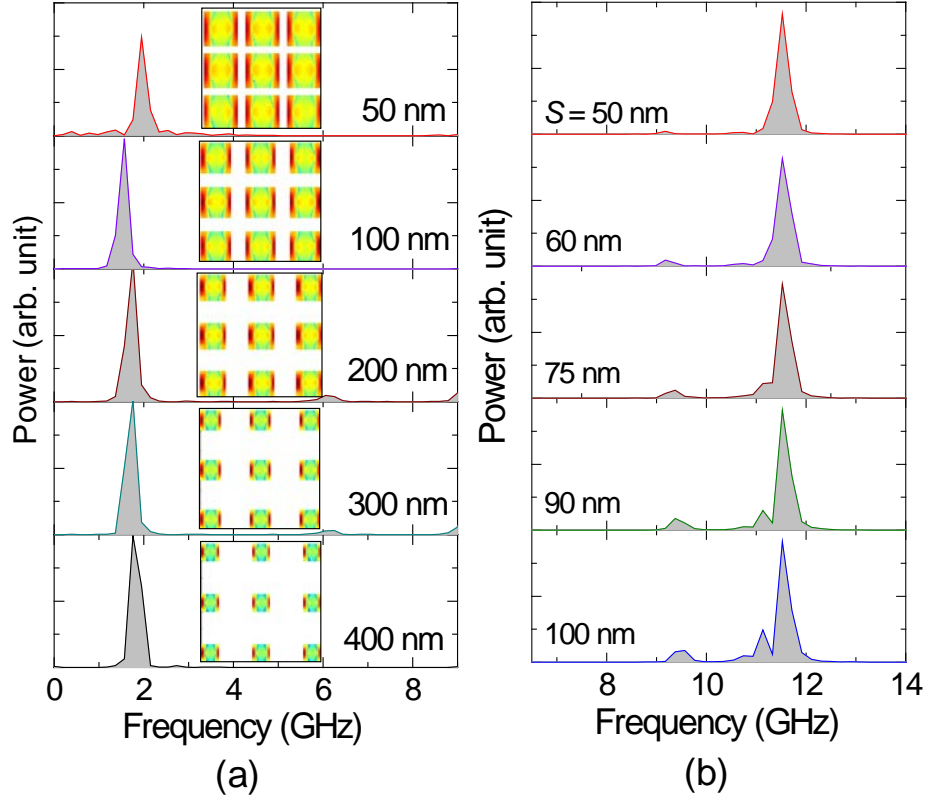


Fig. 6.12: (a) Simulated power spectra for arrays of 200 nm permalloy dots with varying interdot separation  $S$ , illustrating the effect of the array on the edge mode of the single 200 nm permalloy dot. The corresponding mode (power) profiles are shown next to each spectrum. (b) Simulated power spectra from arrays of 200 nm permalloy dots for  $50 \text{ nm} \leq S \leq 100 \text{ nm}$  are shown with smaller steps of  $S$  to reveal the precise value of  $S$ , at which the mode splitting occurs.

## 6.6 Damping as a Function of Areal Density

We have calculated the effective damping coefficient ( $\alpha_{eff}$ ) of the collective precession of the arrays as a function of the interdot separation ( $S$ ).  $\alpha_{eff}$  is also known as the apparent damping and is different from the intrinsic Gilbert damping  $\alpha$ . The experimental time-resolved Kerr rotation data were fitted with a damped sinusoidal curve using Eq. 6.4.3, where the frequency  $f$  is the average frequency of the observed modes [42]. The values of  $\alpha_{eff}$  were extracted by the method as described in section 6.4 and are plotted along with the error bars as a function of  $S$  (Fig. 6.13). The plot shows that  $\alpha_{eff} \approx 0.017$  for array with  $S = 50$  nm, identical to that obtained for the  $10 \times 10 \mu\text{m}^2$  blanket thin film of same thickness. The  $\alpha_{eff}$

increases sharply with the increase in  $S$  and saturates at about 0.025 at  $S = 100$  nm. For  $S = 50$  nm, the coherent precession of all the dots in the array and suppression of the edge modes observed in an isolated dot leads to a lower  $\alpha_{eff}$  same as that of the blanket thin film. As  $S$  increases, the interdot coupling decreases and the coherence of the precession also decreases. For  $S > 100$  nm, occurrence of mode splitting and appearance of a third mode lead to the mutual dephasing among the modes and causing a higher  $\alpha_{eff}$  value of about 0.025.

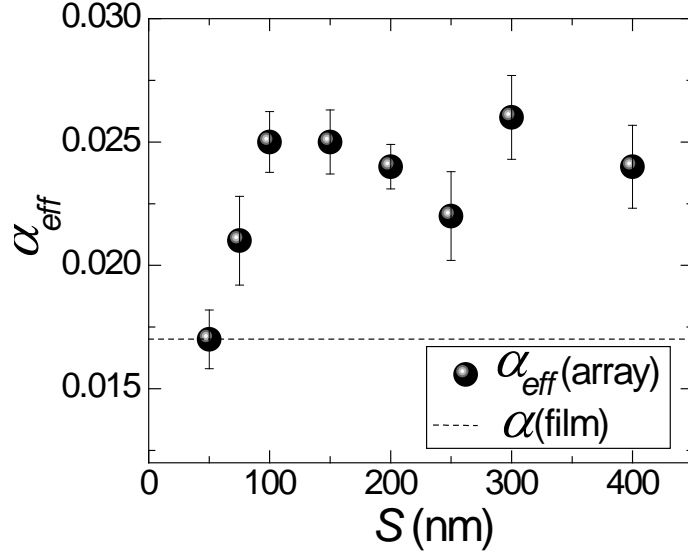


Fig. 6.13: Variation of the effective damping coefficient  $\alpha_{eff}$  for arrays of 200 nm permalloy dots at  $H_b = 1.25$  kOe is plotted as a function of the interdot separation  $S$ . The dotted horizontal line shows the damping coefficient of the uniform mode of a  $10 \times 10 \mu\text{m}^2$  blanket permalloy thin film at  $H_b = 1.25$  kOe.

## 6.7 Collective Magnetization Dynamics as a Function of Bias Field

### 6.7.1 Magnetic Ground State as a Function of Bias Field

The bias magnetic field strongly affects the static magnetic configurations of an individual nanodot as well as that of an array. The internal fields within the individual dots become more nonuniform with the decrease in the bias field resulting in a strong variation in the interdot magnetostatic interaction. Consequently, the dynamic behaviours of the dot array also changes significantly with the bias field magnitude ( $H_b$ ). Figure 6.14 shows the static magnetic configurations at different  $H_b$  values for a single 200 nm permalloy dot and an array

of permalloy dots with  $W = 200$  nm and  $S = 50$  nm. The magnetic ground state of the single dot remains in a flower ('F') state as the bias field decreases from 1.25 kOe to 0. However, the volume of the demagnetized region is increased. At  $H_b = 1.25$  kOe, the static magnetic configurations of all the dots in the array are in flower ('F') states. However, as  $H_b$  is reduced to 0.6 kOe a distribution of 'C' states and 'S' states are observed. The geometries of the 'C' states and 'S' states are slightly modified with the reduction of the magnitude of the bias field, but the overall distribution looks similar below 0.6 kOe.

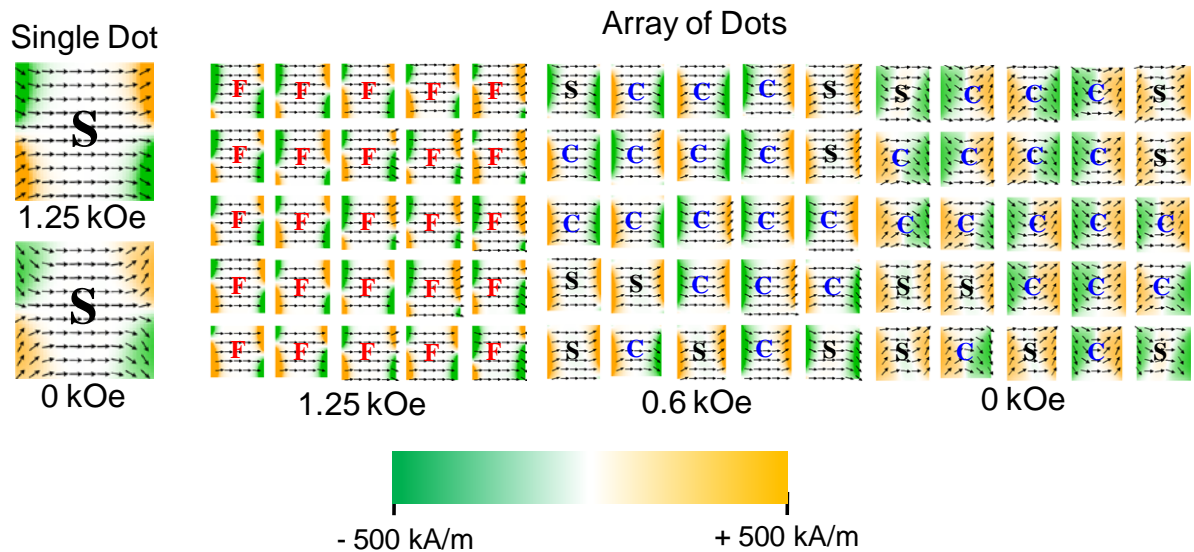


Fig. 6.14: Simulated static magnetization states for a single 200 nm square permalloy dot and an array of 200 nm square permalloy dots with  $S = 50$  nm are shown at different values of  $H_b$ . The colour scale (orange-white-green) which indicates the  $y$ -component of magnetization, is shown at the bottom of figure. 'F', 'S' and 'C' denote flower-like, S-like and C-like states.

### 6.7.2 Precessional Dynamics as a Function of Bias Field

Left column of Fig. 6.15(a) shows the time-resolved Kerr rotation data at various  $H_b$  values, while the right column shows the corresponding FFT spectra. For  $H_b = 1.25$  kOe, a single uniform collective mode is observed as discussed before. The mode is broadened at  $H_b = 0.8$  kOe due to the inhomogeneous line broadening and a splitting occur for  $H_b \leq 0.6$  kOe. Consequently, the strongly collective dynamics of the array becomes weakly collective. The frequencies of the modes also decrease monotonically with the decrease in  $H_b$ . The experimental and simulated resonant modes are plotted in Fig. 6.15(b). From the experimental data two branches of modes are observed, both of which vary systematically with the bias magnetic field. On the other hand, the simulation shows three branches. The

highest frequency branch obtained from the simulation agree with the experimental data and this mode fits well with the Kittel formula with similar parameters obtained from the  $10 \times 10 \mu\text{m}^2$  blanket permalloy thin film. This clearly shows that this mode corresponds to the strongly collective precession of all elements in the array and the elements lose their individual characters in this mode. In the case of simulated results, two additional modes appear for  $H_b < 0.6$  kOe. Out of those the higher frequency mode has a frequency very close to the Kittel mode. The two closely spaced higher frequency modes were not resolved in the experiment, probably due to the lack of required spectral resolution and we observed a single mode there. The lowest frequency mode obtained in the simulation varies systematically with  $H_b$  and agree qualitatively with the lowest frequency branch observed from experiment. The lack of quantitative agreement may be attributed to the physical differences between the experimental and the simulated samples, in particular the edge roughness and deformation during the lift-off process.

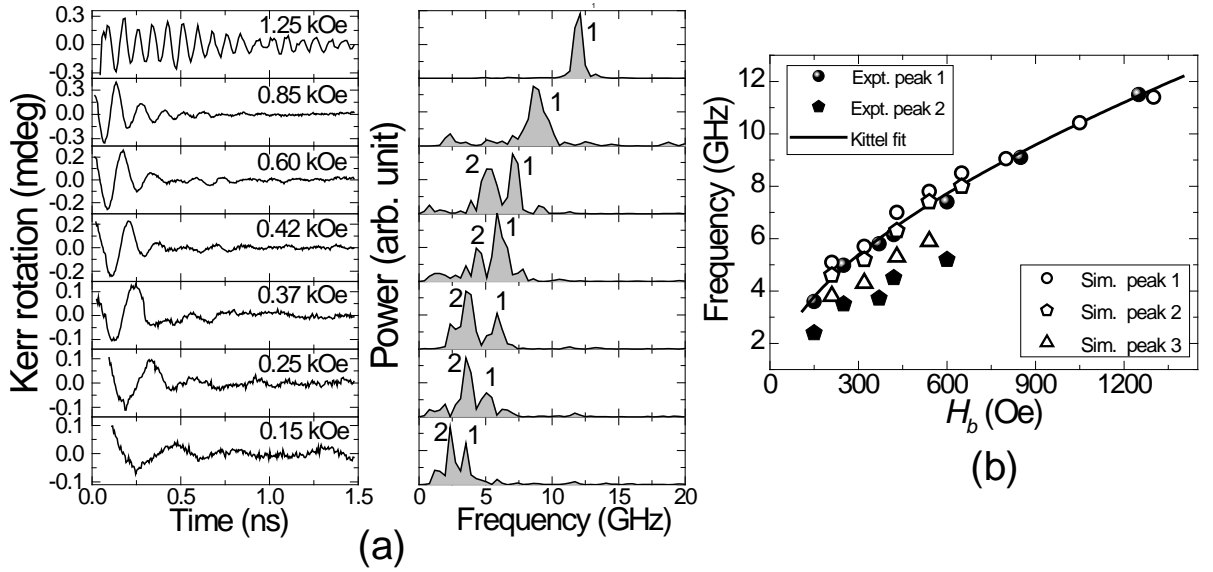


Fig. 6.15: (a) Experimental time-resolved Kerr rotations at different bias fields (left panel) and the corresponding FFT spectra (right panel) are shown for the array of 200 nm dots with  $S = 50$  nm. (b) Plot of the frequencies of the experimentally observed resonant peaks and simulated resonant peaks for different bias field magnitudes. The plotted modes are fitted with the Kittel mode with similar parameters obtained from the  $10 \times 10 \mu\text{m}^2$  blanket permalloy film.

## 6.8 Damping as a Function of Bias Field

The effective damping coefficient ( $\alpha_{eff}$ ) also depends upon the bias field. We have calculated  $\alpha_{eff}$  of the collective precession of the array with  $S = 50$  nm as a function of the

bias field using the method as described in section 6.4 and plotted it as a function of the bias field ( $H_b$ ) (Fig. 6.16). The plot shows that  $\alpha_{eff} \approx 0.017$  at  $H_b = 1.25$  kOe, but it increases drastically to a large value (0.063) as  $H_b$  decreases to 0.85 kOe. For  $H_b < 0.85$  kOe,  $\alpha_{eff}$  increases gradually and eventually saturates at about 0.07 for  $H_b < 0.5$  kOe. We have already discussed that, for  $S = 50$  nm, the collective precession of all the dots in the array and suppression of the edge modes of the individual nanodots lead to a lower value of  $\alpha_{eff}$  same as that of the blanket thin film. As  $H_b$  decreases to 0.85 kOe, the uniform collective mode is significantly broadened due to an inhomogeneous line broadening, leading towards a much higher damping than that for  $H_b = 1.25$  kOe. As  $H_b$  is further decreased below 0.85 kOe, the magnetic ground state of the array is changed and mode splitting occurs, leading towards further increase in damping. For  $H_b < 0.5$  kOe, no further significant change in the mode spectra are observed and hence  $\alpha_{eff}$  saturates at about 0.07.

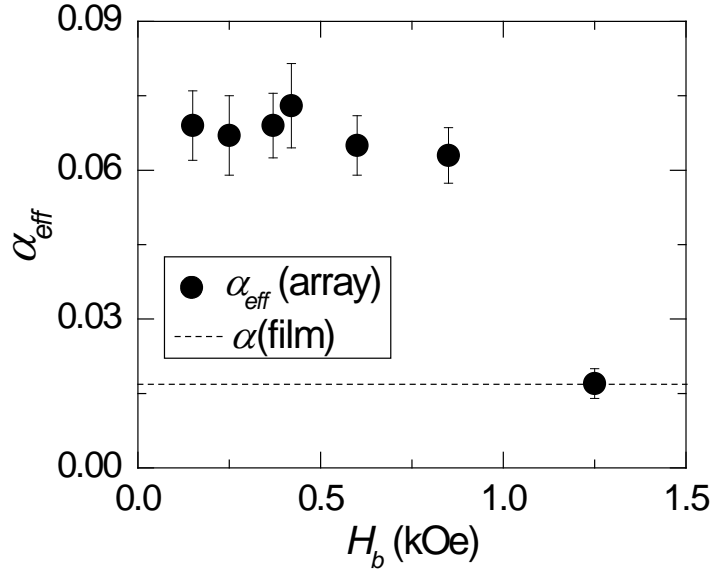


Fig. 6.16: Variation of the effective damping coefficient  $\alpha_{eff}$  as a function of the bias magnetic field ( $H_b$ ) for an array of 200 nm square permalloy dots with interdot separation  $S = 50$  nm. The dotted horizontal line shows the damping of the uniform mode of a  $10 \times 10 \mu\text{m}^2$  blanket permalloy thin film.

## 6.9 Summary

In summary, we have investigated the quasistatic and ultrafast collective magnetization dynamics in  $10 \times 10 \mu\text{m}^2$  arrays of 200 nm wide square permalloy dots with varying areal density. A significant variation in the quasistatic magnetization reversal dynamics is observed with the reduction of the edge-to-edge separation ( $S$ ) between the dots

and the hysteresis loops of the arrays change significantly. The saturation magnetic field reduces and the remanence increases with the decrease in the interdot separation and attain values very close to a  $10 \times 10 \text{ }\mu\text{m}^2$  blanket permalloy thin film with similar thickness when  $S$  becomes minimum (50 nm). The coercive field also becomes very close to that for the blanket thin film, indicating a transformation to a strongly collective reversal mechanism. In the ultrafast magnetization dynamics, the demagnetization time remains unaffected by the areal density of the array. In contrast, the fast relaxation time shows a significant but random variation with the areal density, which is attributed due to the random size distribution and defects in the dots of different arrays. In the precessional dynamics, a systematic transition from the uniform (strongly) collective dynamics to non-collective (isolated) dynamics is observed through a nonuniform (weakly) collective dynamical regime with the increase in the interdot separation. Remarkably, in the uniform collective regime, the edge modes of the constituent dots are suppressed. A lower effective damping ( $a_{eff}$ ), which is identical to that for a blanket permalloy thin film is observed in the uniform collective regime. However, the value of  $a_{eff}$  increases with the increase in  $S$  due to the increment of the incoherence of precession between the nanodots as a result of the reduced interdot coupling and the corresponding mode splitting. The transition from the uniform collective regime to non-collective regime with the increase in the interdot separation is attributed to a systematic decrease in the magnetostatic coupling among the dots. Further, the strongly collective dynamics undergoes a transition to a weakly collective regime with the decrease in the bias field magnitude. The reason behind this is the increase in the nonuniformity in the magnetic ground states of the nanodots with the decrease in the bias field. Consequently, the effective damping also shows a concurrent increase with the decrease in the bias field.

## Bibliography

1. O. Hellwig, A. Berger, T. Thomson, E. Dobisz, Z. Z. Bandic, H. Yang, D. S. Kercher, and E. E. Fullerton, *Appl. Phys. Lett.* **90**, 162516 (2007).
2. S. Tehrani, E. Chen, M. Durlam, M. DeHerrera, J. M. Slaughter, J. Shi, and G. Kerszykowski, *J. Appl. Phys.* **85**, 5822 (1999).
3. A. Imre, G. Csaba, L. Ji, A. Orlov, G. H. Bernstein, and W. Porod, *Science* **311**, 205 (2006).
4. S. Kaka, M. R. Pufall, W. H. Rippard, T. J. Silva, S. E. Russek, and J. A. Katine, *Nature* **437**, 389 (2005).
5. V. V. Kruglyak, S. O. Demokritov, and D. Grundler, *J. Phys. D: Appl. Phys.* **43**, 264001 (2010).
6. S. Neusser and D. Grundler, *Adv. Mater.* **21**, 2927 (2009).
7. B. Lenk, H. Ulrichs, F. Garbs, and M. Münzenberg, *Phys. Rep.* **507**, 107 (2011).
8. V. V. Kruglyak, A. Barman, R. J. Hicken, J. R. Childress, and J. A. Katine, *Phys. Rev. B* **71**, 220409(R) (2005).
9. Z. K. Wang, H. S. Lim, V. L. Zhang, J. L. Goh, S. C. Ng, M. H. Kuok, H. L. Su, and S. L. Tang, *Nano Lett.* **6**, 1083 (2006).
10. V. V. Kruglyak, P. S. Keatley, A. Neudert, R. J. Hicken, J. R. Childress, and J. A. Katine, *Phys. Rev. Lett.* **104**, 027201 (2010).
11. N. I. Polushkin, S. A. Michalski, L. Yue, and R. D. Kirby, *Phys. Rev. Lett.* **97**, 256401 (2006).
12. G. Gubbiotti, S. Tacchi, G. Carlotti, N. Singh, S. Goolaup, A. O. Adeyeye, and M. Kostylev, *Appl. Phys. Lett.* **90**, 092503 (2007).
13. A. Barman, S. Wang, J. D. Maas, A. R. Hawkins, S. Kwon, A. Liddle, J. Bokor, and H. Schmidt, *Nano Lett.* **6**, 2939 (2006).
14. Z. Liu, R. Brandt, Y. Yahagi, B. Hansen, B. Harteneck, J. Bokor, A. R. Hawkins, and H. Schmidt, *Appl. Phys. Lett.* **98**, 052502 (2011).
15. G. N. Kakazei, Y. G. Pogorelov, M. D. Costa, T. Mewes, P. E. Wigen, P. C. Hammel, V. O. Golub, T. Okuno, and V. Novosad, *Phys. Rev. B* **74**, 060406(R) (2006).
16. S. Tacchi, M. Madami, G. Gubbiotti, G. Carlotti, H. Tanigawa, T. Ono, and M. P. Kostylev, *Phys. Rev. B* **82**, 024401 (2010).

17. L. Giovannini, F. Montoncello, and F. Nizzoli, *Phys. Rev. B* **75**, 024416 (2007).
18. P. V. Bondarenko, A. Y. Galkin, B. A. Ivanov, and C. E. Zaspel, *Phys. Rev. B* **81**, 224415 (2010).
19. A. Barman and S. Barman, *Phys. Rev. B* **79**, 144415 (2009).
20. S. Jung, B. Watkins, L. DeLong, J. B. Ketterson, and V. Chandrasekhar, *Phys. Rev. B* **66**, 132401 (2002).
21. G. Gubbiotti, M. Madami, S. Tacchi, G. Carlotti, and T. Okuno, *J. Appl. Phys.* **99**, 08C701 (2006).
22. P. S. Keatley, V. V. Kruglyak, A. Neudert, E. A. Galaktionov, R. J. Hicken, J. R. Childress, and J. A. Katine, *Phys. Rev. B* **78**, 214412 (2008).
23. L. J. Heyderman, H. H. Solak, C. David, D. Atkinson, R. P. Cowburn, and F. Nolting, *Appl. Phys. Lett.* **85**, 4989 (2004).
24. A. Laraoui, V. Halté, M. Vomir, J. Vénuat, M. Albrecht, E. Beaurepaire, and J.-Y. Bigot, *Eur. Phys. J. D* **43**, 251 (2007).
25. E. Beaurepaire, J. C. Merle, A. Daunois, and J.-Y. Bigot, *Phys. Rev. Lett.* **76**, 4250 (1996).
26. L. Guidoni, E. Beaurepaire, and J.-Y. Bigot, *Phys. Rev. Lett.* **89**, 017401 (2002).
27. J.-Y. Bigot, M. Vomir, and E. Beaurepaire, *Nat. Phys.* **5**, 515 (2009).
28. A. Laraoui, J. Venuat, V. Halte, M. Albrecht, E. Beaurepaire, and J.-Y. Bigot, *J. Appl. Phys.* **101**, 09C105 (2007).
29. C. Kittel, *Phys. Rev.* **73**, 155 (1948).
30. A. Barman, S. Wang, J. Maas, A. R. Hawkins, S. Kwon, J. Bokor, A. Liddle, and H. Schmidt, *Appl. Phys. Lett.* **90**, 202504 (2007).
31. J.-Y. Bigot, M. Vomir, L. H. F. Andrade, and E. Beaurepaire, *Chem. Phys.* **318**, 137 (2005).
32. W. Hübner and K. H. Bennemann, *Phys. Rev. B* **53**, 3422 (1996).
33. C.-H. Hsia, T.-Y. Chen, and D. H. Son, *J. Am. Chem. Soc.* **131**, 9146 (2009).
34. C.-H. Hsia, T.-Y. Chen, and D. H. Son, *Nano Lett.* **8**, 571 (2008).
35. B. Rana, S. Pal, S. Barman, Y. Fukuma, Y. Otani, and A. Barman, *Appl. Phys. Express* **4**, 113003 (2011).
36. M. Donahue and D. G. Porter, "OOMMF User's guide, Version 1.0," *NIST Interagency Report No. 6376*, National Institute of Standard and Technology, Gaithersburg, MD, URL: <http://math.nist.gov/oommf>, (1999).

37. K. Y. Guslienko, V. Novosad, Y. Otani, H. Shima, and K. Fukamichi, *Phys. Rev. B* **65**, 024414 (2001).
38. K. H. J. Buschow, “Handbook of Magnetic Materials,” Volume 18, *Elsevier*, North Holland: Amsterdam, The Netherlands (2009).
39. M. Oogane, T. Wakitani, S. Yakata, R. Yilgin, Y. Ando, A. Sakuma, and T. Miyazaki, *Jpn. J. Appl. Phys.* **45**, 3889 (2006).
40. M. R. Scheinfein, “LLG Micromagnetic Simulator,” <http://llgmicro.home.mindspring.com/>, (1997).
41. D. Kumar, O. Dmytriiev, S. Ponraj, and A. Barman, *J. Phys. D: Appl. Phys.* **45**, 015001 (2012).
42. B. Rana and A. Barman, *SPIN* **3**, 1330001 (2013).

## CHAPTER 7

---

# Magnetization Dynamics of Arrays of 50 nm $\text{Ni}_{80}\text{Fe}_{20}$ Dots Down to the Single Nanodot Regime

---

### 7.1 Background

The quest to measure the ultrafast magnetization dynamics of nanomagnets continues to be an important problem in nanoscience and nanotechnology [1-9]. Picosecond magnetization dynamics of nanoscale magnetic structures is important for many present and future technologies including magnetic data storage [10-11], logic devices [12-14], spintronics [15] and magnetic resonance imaging [16]. Emerging technologies such as spin torque nano-oscillators [17] and magnonic crystals [18-19] rely heavily upon the fast and coherent spin wave dynamics of nanomagnets and the generation and manipulation of spin waves in spatially modulated magnetic nanostructures. Novel techniques for fabrication of nanomagnets arrays [20] and applications toward biomedicine [21] show exciting new promises. Overall, the detection and understanding of nanomagnet dynamics down to the single nanomagnet regime have become increasingly important. Investigation of picosecond dynamics of arrays of nanoscale magnetic dots has inferred that, for dot sizes less than 200 nm, the response of the magnetization to a pulsed magnetic field is spatially nonuniform and is dominated by localized spin wave modes [22]. This nonuniformity may result in a degradation of the signal-to-noise ratio in future nanomagnetic devices. However, the measurements were done in densely packed arrays where the intrinsic dynamics of the individual dots are strongly influenced by the magnetostatic stray fields of the neighbouring dots. Magnetostatically coupled nanomagnets in a dense array may show collective behaviours both in the quasistatic magnetization reversal [23] and in the precessional

dynamics [22, 24-28]. In the quasistatic regime, the strong interdot magnetostatic interactions result in collective rotation of magnetic spins and formation of flux closure through a number of dots during the reversal. On the other hand, in the collective precessional dynamics the constituent nanomagnets maintain definite amplitude and phase relationships. Magnetization dynamics in dense arrays of nanomagnets have been studied both experimentally by time-domain [22, 24], frequency-domain [25-26], and wave-vector-domain [27-28] techniques; and theoretically by analytical [29-30] and micromagnetic [31] methods. To this end the frequency, damping and spatial patterns of spin waves and dispersion relations of frequency with wave vector of spin wave propagation have been studied. On the other hand, magnetization dynamics of isolated nanomagnets well beyond the diffraction limit have been reported by time-resolved magneto-optical techniques [3, 5-6, 8-9].

The intrinsic magnetization dynamics including the precession frequency and damping of single cylindrical Ni dots of varying dot diameters (aspect ratios) down to 125 nm were reported [2, 4]. The measurements were done by a cavity enhanced all optical TRMOKE setup. To enhance the Kerr signal from the nanodots, with dimensions well below the diffraction limited probe laser spot, they were coated with SiN layer (Fabry-Pérot cavity) along with an anti-reflection coating on the Si substrate to minimize the nonmagnetic background. In another study, the magnetization dynamics of 160 nm magnetic disks were studied by TRSKM [5]. The transition between vortex and quasi-uniform magnetization state was demonstrated by sweeping the bias magnetic field and the frequencies of the fundamental modes of the nano-disk show a hysteresis behaviour as a function of the applied bias field. The main outcome of this study was to demonstrate that by changing the shape of the disk the annihilation field of the vortex can be controlled over a wide range keeping the nucleation field almost unchanged. Z. Liu *et al.* in 2011 [9] reported the measurement of magnetization dynamics of a smaller magnetic dot (150 nm in diameter) in the environment of a larger magnetic dot with known resonant frequency by all optical TRMOKE and the effect of the magnetostatic interaction on the dynamics of the smaller dot. Another recent TRSKM study on single nanomagnet [8] showed the suppression of edge mode in the nanomagnet by large amplitude magnetization dynamics. The results were supported by micromagnetic simulation. This observation is useful for application of single nanomagnets as spin transfer torque oscillator where a large amplitude magnetic excitation is required.

Despite the above progress, picosecond magnetization dynamics including the damping behaviour of isolated nanomagnets in the sub-100 nm lateral dimension has never

been reported. In this chapter, we present an all optical far field measurement of the picosecond magnetization dynamics of arrays of square  $\text{Ni}_{80}\text{Fe}_{20}$  (permalloy) dots of 50 nm width and with varying edge-to-edge separation ( $S$ ) between 200 and 50 nm [32]. When the dots are separated by large distance ( $S \geq 150$  nm), they reveal the dynamics of the isolated nanomagnet. The isolated nanomagnets revealed a single resonant mode, whose damping is slightly higher than the unpatterned thin film value. With the decrease in interdot separation the effects of dipolar and quadrupolar interactions become important, and we observe an increase in precession frequency and damping. At the highest areal density a sudden jump in the apparent damping is observed due to the mutual dephasing of two closely spaced eigenmodes of the array.

## 7.2 Sample Fabrication, Characterization and Measurement Technique

The general descriptions of the sample fabrication, structural and topographical characterization and measurement technique to study the time-resolved magnetization dynamics can be found in chapters 3 and 4. Here we describe the specific details of the experimental techniques. The samples were prepared by a combination of electron beam evaporation and electron beam lithography. A bilayer PMMA/MMA (polymethyl methacrylate/methyl methacrylate) resist pattern was first prepared on thermally oxidized Si(100) substrate by using electron beam lithography and 20 nm thick permalloy layer was deposited on the resist pattern by electron beam evaporation at a base pressure of about  $2 \times 10^{-8}$  Torr. A 10 nm thick  $\text{SiO}_2$  capping layer was deposited on top of permalloy to protect the dots from degradation when exposed to the optical pump-probe experiments in air. This is followed by the lifting-off of the sacrificial material and oxygen plasma cleaning of the residual resists that remained even after the lift-off process.

This leaves  $10 \times 10 \mu\text{m}^2$  arrays of square permalloy dots with nominal dimensions as width ( $W$ ) = 50 nm, thickness ( $t$ ) = 20 nm and edge-to-edge separation ( $S$ ) varying from 50 to 200 nm. The scanning electron micrographs of dot arrays are shown in Fig. 7.1(a). The SEM images show some deviations in the dimensions and shapes of the dots from their nominal dimensions. The corners are rounded due to the limitations of electron beam lithography. A representative atomic force microscope (AFM) image of an array of 50 nm dots with  $S = 100$  nm is also shown in Fig. 7.1(b). In AFM image, the width to separation ratio is apparently

deviated from the actual values due to the finite tip radius ( $\sim 10$  nm) of AFM. In spite of these deviations, the general features are maintained. A square permalloy blanket film with  $10\ \mu\text{m}$  width and  $20$  nm thickness was also prepared at the same deposition conditions as the dot arrays to obtain the magnetic parameters of the material used in the dot arrays.

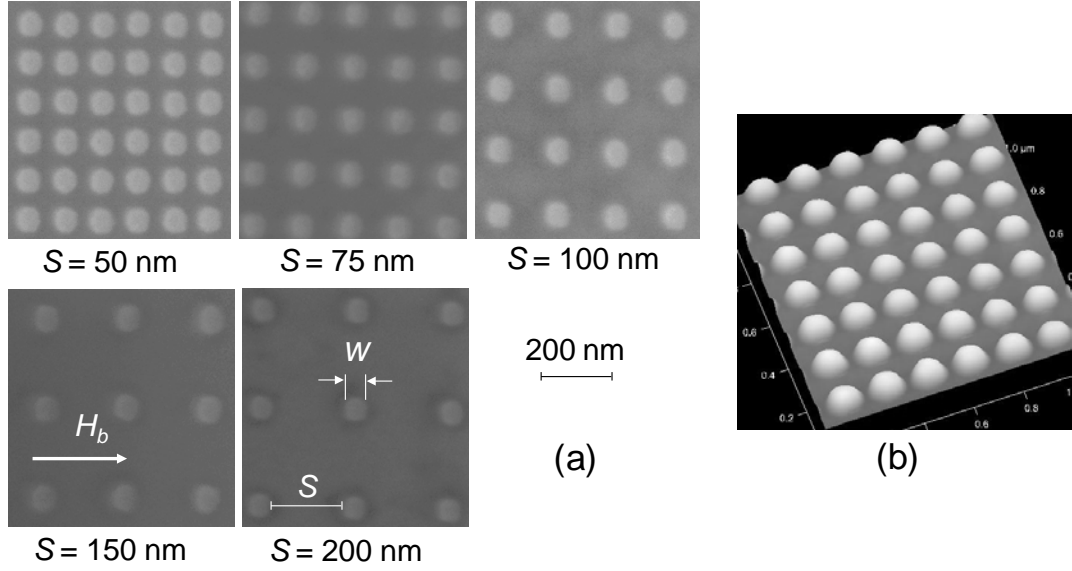


Fig. 7.1: (a) Scanning electron micrographs of  $50$  nm permalloy dots with edge-to-edge separations ( $S$ ) varying from  $50$  to  $200$  nm are shown. The direction of the applied bias field is also shown on top of the image for  $S = 150$  nm. (b) Atomic force microscope (AFM) image of an array of  $50$  nm permalloy dots with  $S = 100$  nm is shown.

The ultrafast magnetization dynamics was measured by using a time-resolved magneto-optical Kerr effect microscope based upon a two-colour collinear pump-probe setup. The two-colour collinear arrangement enabled us to achieve a very good spatial resolution and sensitivity even in an all optical excitation and detection scheme of the precessional dynamics. The second harmonic ( $\lambda = 400$  nm, pulse width  $\approx 100$  fs) of a Ti-sapphire laser (Tsunami, Spectra Physics, pulse width  $\approx 70$  fs) was used to pump the samples, while the time delayed fundamental ( $\lambda = 800$  nm) laser beam was used to probe the dynamics by measuring the polar Kerr rotation by means of a balanced photodiode detector, which completely isolates the Kerr rotation and the total reflectivity signals. The pump power used in these measurements is about  $15\ \text{mJ}/\text{cm}^2$ , while the probe power is much weaker and is about  $3\ \text{mJ}/\text{cm}^2$ . The probe beam is focused to a spot size of  $800$  nm and placed at the centre of each array by a microscope objective with numerical aperture  $N. A. = 0.65$  and a closed loop piezoelectric scanning  $x$ - $y$ - $z$  stage. The pump beam is spatially overlapped with the probe beam after passing through the same microscope objective in a collinear geometry.

Consequently, the pump spot is slightly defocused (spot size  $\approx 1 \mu\text{m}$ ) on the sample plane, which is also the focal plane of the probe spot. The probe spot is placed at the centre of the pump spot. A large magnetic field is first applied at a small angle ( $\sim 15^\circ$ ) to the sample plane to saturate its magnetization. The magnetic field strength is then reduced to the bias field value ( $H_b =$  component of bias field along  $x$ -direction), which ensures that the magnetization remains saturated along the bias field direction. The bias field was tilted  $15^\circ$  out of the plane of the sample to have a finite demagnetizing field along the direction of the pump pulse, which is eventually modified by the pump pulse to induce precessional magnetization dynamics within the dots. The pump beam was chopped at 2 kHz frequency and a phase sensitive detection of the Kerr rotation was used. Before starting the measurement of magnetization dynamics by all optical pump-probe set up, extreme care was taken to increase the sensitivity of the measurements. The Kerr rotation signals from a thin film and a larger permalloy dot were enhanced to the maximum possible values by optimizing the optical alignments as discussed in sections 4.3.4 and 4.3.5 in chapter 4. The time-resolved data was recorded for a maximum duration of 1 ns, and this was found to be sufficient to record all important features of the dynamics including the spectral resolution of the double peaks for the sample with  $S = 50 \text{ nm}$  and measurement of the damping coefficient.

## 7.3 Results and Discussions

### 7.3.1 Variation of Precession Frequency with Areal Density of the Arrays

Figure 7.2(a) and (b) show the time-resolved reflectivity and Kerr rotation data, respectively from the array of 50 nm dots with separation  $S = 50 \text{ nm}$  at a bias field  $H_b = 2.5 \text{ kOe}$ . Figure 7.2(c) shows only the demagnetization and the fast relaxation explicitly. The reflectivity shows a sharp rise followed by a bi-exponential decay. On the other hand, the time-resolved Kerr rotation data shows a fast demagnetization within 500 fs and a bi-exponential decay with decay constants of about 8 and 116 ps (with  $\pm 10\%$  deviation in both). The demagnetization and decay times are found to be independent of the areal density of the arrays. The precessional dynamics appears as an oscillatory signal above the decaying part of the time-resolved Kerr rotation data. The bi-exponential background is subtracted from the time-resolved Kerr signal before performing the fast Fourier transform (FFT) to find out the corresponding power spectra.

Figure 7.3(a) shows the time-resolved Kerr rotation data from the permalloy dot arrays with  $S$  varying between 50 and 200 nm at  $H_b = 2.5$  kOe [32]. The data is presented after removing the ultrafast demagnetization part and subtracting a bi-exponential background from the raw data to illustrate the precessional dynamics. Clear precession is observed for  $S$  up to 200 nm, where the dots are expected to be magnetostatically isolated and hence exhibit single dot like behaviour. The corresponding FFT spectrum (Fig. 7.3(b)) shows a dominant single peak at 9.04 GHz. As  $S$  decreases the precession continues to have a single resonant mode but the peak frequency generally increases with the decrease in  $S$ . For  $S = 150$  nm, the peak frequency decreases slightly although the error bars are large enough to maintain the general trend of increase in the frequency with the decrease in  $S$  as stated above. At  $S = 50$  nm, the single resonant mode splits into two closely spaced modes with the appearance of a lower frequency peak.

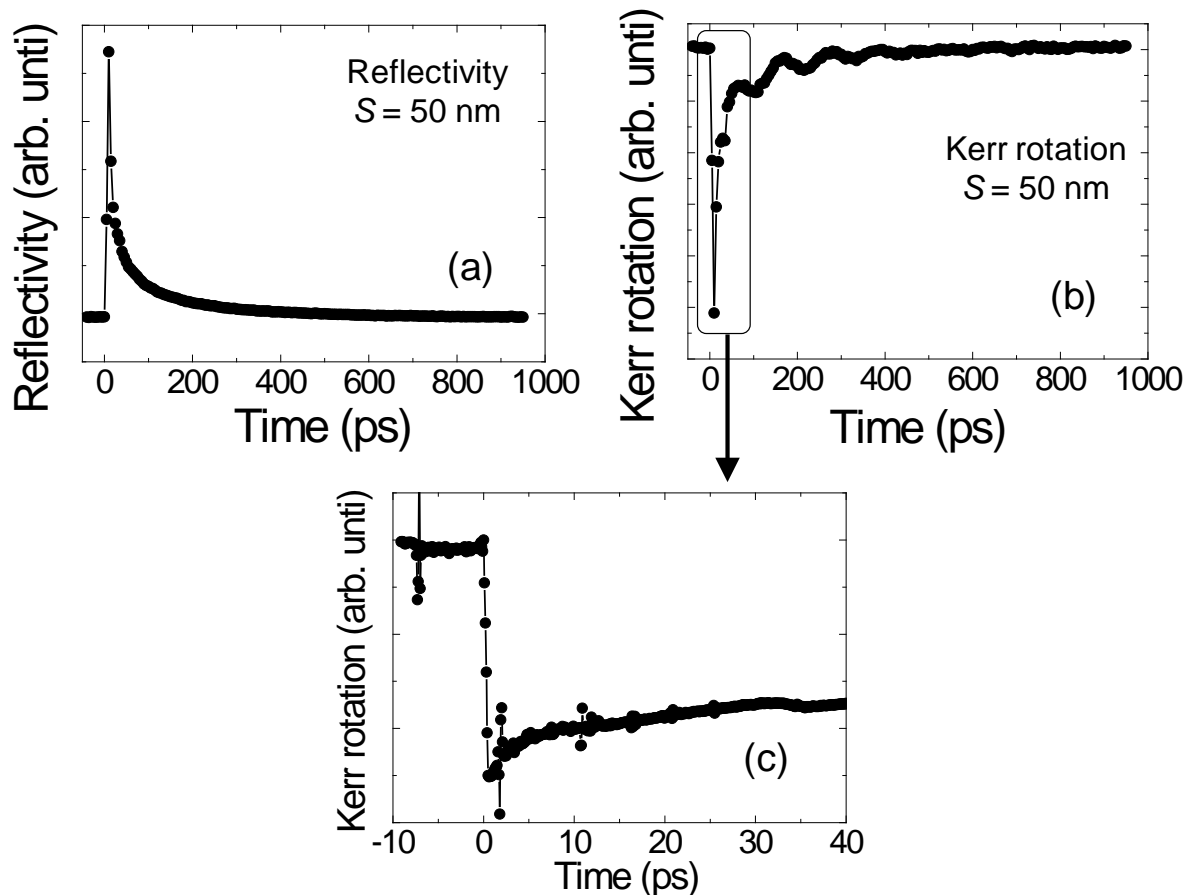


Fig. 7.2: (a) Time-resolved reflectivity and (b) Kerr rotation data for an array of 50 nm permalloy dots with interdot separation  $S = 50$  nm at  $H_b = 2.5$  kOe. (c) The initial part of the dynamics is shown with a greater time resolution to illustrate the ultrafast demagnetization and the fast relaxation.

In Fig. 7.3(c), we show the FFT spectra of the time-resolved magnetization obtained from micromagnetic simulations of arrays of  $7 \times 7$  dots using the OOMMF software [33]. In general, the deviation in the shape and dimensions as observed in the experimental samples are included in the simulated samples, but the precise edge roughness profiles and deformations are not always possible to include in the finite difference method based micromagnetic simulations used here, where samples are divided into rectangular prism-like cells. In the simulation, the arrays were divided into cells of  $2.5 \times 2.5 \times 20 \text{ nm}^3$  dimensions and the material's parameters for permalloy were used as  $\gamma = 18.5 \text{ MHz/Oe}$ ,  $H_K = 0$ ,  $M_S = 860 \text{ emu/cc}$  and  $A = 1.3 \times 10^{-6} \text{ erg/cm}$ . The material's parameters for permalloy were obtained by measuring the precession frequency of the  $10 \times 10 \text{ }\mu\text{m}^2$  blanket thin film as a function of the in-plane bias field and by fitting the bias field variation of frequency with Kittel formula [34]. The exchange stiffness constant  $A$  was obtained from literature [35]. The lateral cell size is well below the exchange length  $l_{ex} = (2A/(\mu_0 M_S^2))^{1/2}$  of permalloy (5.3 nm), and further reduction of the cell size does not change the magnetic energies appreciably. Test simulations with discretization along the thickness of the samples do not show any variation in the resonant modes, which is expected as this will only affect the perpendicular standing spin waves, whereas in the present study we have concentrated on the spin waves with an in-plane component of wave-vector. The equilibrium states are obtained by allowing the system to relax under the bias field for sufficient time so that the maximum torque ( $\mathbf{m} \times \mathbf{H}$ ,  $\mathbf{m} = \mathbf{M}/M_S$ ) goes well below  $10^{-6} \text{ A/m}$ . The dynamic simulations were obtained for a total duration of 4 ns at time steps of 5 ps. Consequently, the simulated linewidths of the resonant modes are narrower, which enabled us to clearly resolve the mode splitting in the simulation. The simulation reproduces the important features as observed in the experiment, namely the observation of a single resonant mode for the arrays with  $S$  varying between 200 and 75 nm, a systematic increase in the resonant mode frequency with the decrease in  $S$ , and finally a mode splitting at  $S = 50 \text{ nm}$ . However, the increase in the resonant frequency with a decrease in  $S$  is less steep as compared to the experimental result. The deviation is larger for smaller values of  $S$  possibly due to the increased nonidealities in the physical structures of the samples in this range, as discussed earlier. Furthermore, the relative intensities of the two modes observed for the array with  $S = 50 \text{ nm}$  are not reproduced by the simulation. This is possibly because the lower frequency mode is a propagating mode and the finite boundary of the simulated array of  $7 \times 7$  elements may cause much faster decay of the propagating mode as opposed to that in the much larger array of  $100 \times 100$  elements studied experimentally.

In Fig. 7.4(a), we plot the precession frequency as a function of the ratio of width ( $W$ ) to centre-to-centre separation ( $a$ ), where  $a = W + S$ . For  $W/a \leq 0.25$  ( $S \geq 150$  nm) the frequency is almost constant but for  $W/a > 0.25$  ( $S < 150$  nm) the frequency increases sharply both for the experimental and simulated data. We fit both data with Eq. 7.3.1 including both dipolar and quadrupolar interaction terms [36]:

$$f = f_0 - A\left(\frac{W}{a}\right)^3 + B\left(\frac{W}{a}\right)^5, \quad (7.3.1)$$

where  $A$  and  $B$  are the strengths of the dipolar and quadrupolar interactions and  $f_0$  is the intrinsic resonant mode frequency of magnetostatically isolated dots.

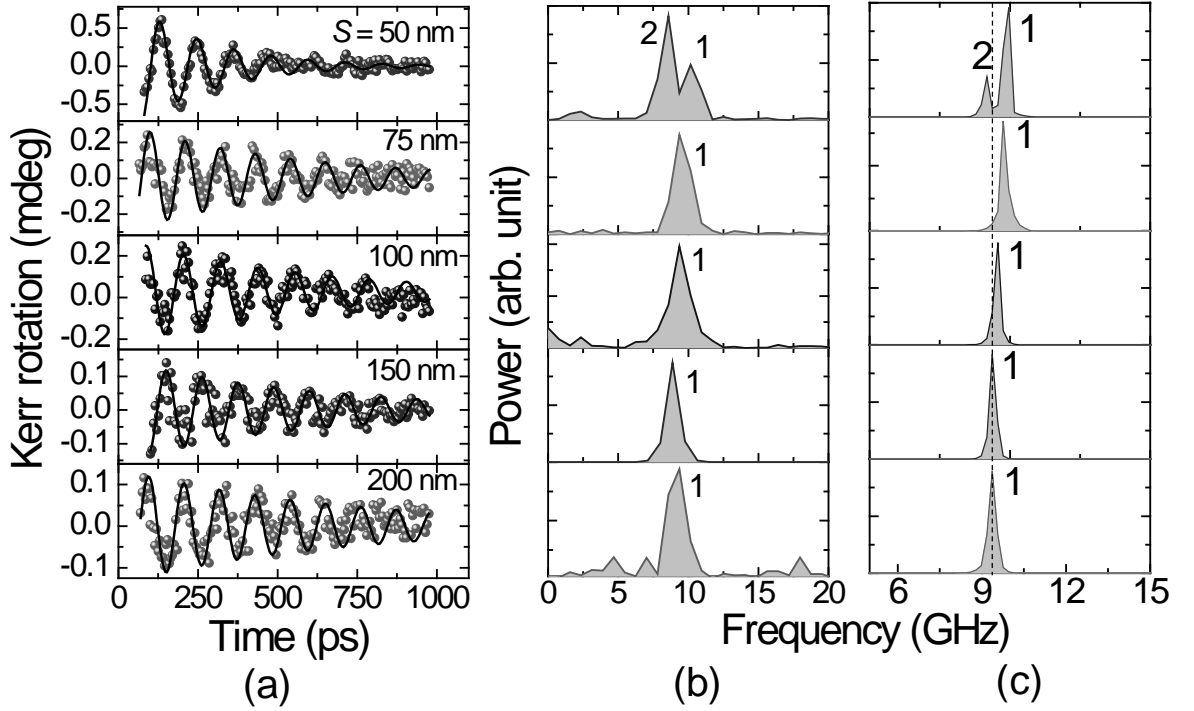


Fig. 7.3: (a) Experimental time-resolved Kerr rotations and (b) the corresponding FFT spectra are shown for arrays of permalloy dots with width = 50 nm, thickness = 20 nm and with varying interdot separation  $S$  at  $H_b = 2.5$  kOe. (c) The FFT spectra of the simulated time-resolved magnetization are shown. The peak numbers are assigned to the FFT spectra. The dotted line in panel ‘c’ shows the simulated precession frequency of a single permalloy dot with width = 50 nm, thickness = 20 nm.

The fitted data are shown by solid lines in Fig. 7.4(a). The simulated data fits well with Eq. 7.3.1, while the fit is reasonable for the experimental data, primarily due to the large deviation in data points for the arrays with  $S = 75$  nm and 150 nm. However, the theoretical curve passes through the error bars for those data points. The quadrupolar contribution is

dominant over the dipolar contribution as is also evident from the sharp increase in the frequency for  $W/a > 0.25$ . The dipolar contributions extracted from the curve fitting are almost identical for both experimental and simulated results, whereas for the experimental data the quadrupolar contribution is about 30% greater than that for the simulated data.

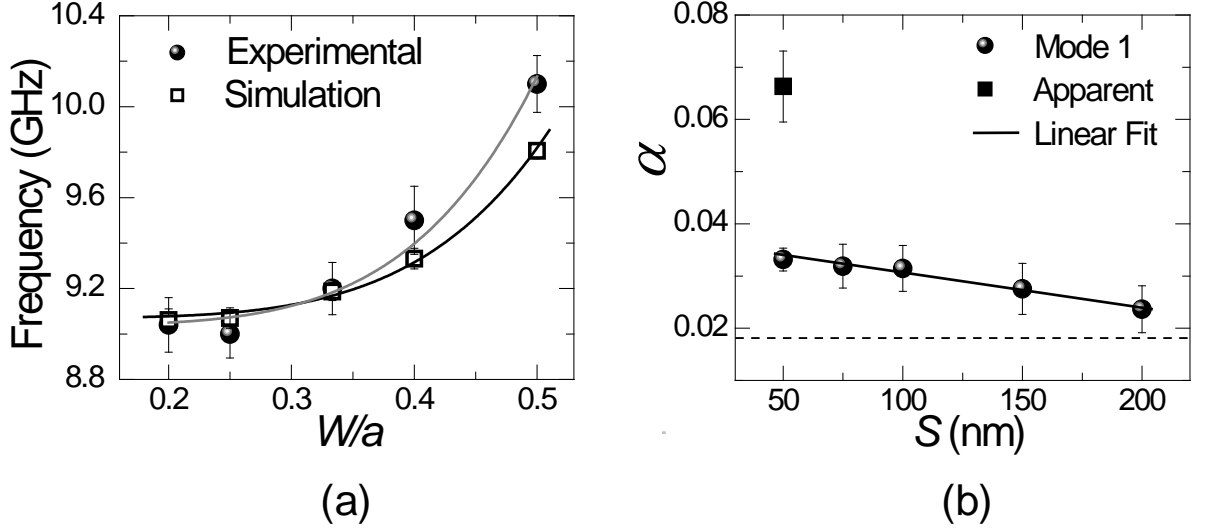


Fig. 7.4: (a) The precession frequency is plotted as a function of  $W/a$ . The circular and square symbols correspond to the experimental and simulated results, respectively, while the solid curves correspond to the fit to Eq. 7.3.1. (b) The damping coefficient  $\alpha$  is plotted as a function of  $S$ . The symbols correspond to the experimental data, while the solid line corresponds to a linear fit. The dashed line corresponds to the measured value of  $\alpha$  for a continuous permalloy film grown under identical conditions.

### 7.3.2 Variation of Damping of Precession with Areal Density of the Arrays

We have further investigated the damping behaviour of the nanomagnets in the array. The time domain data was fitted with a damped sine curve:

$$M(t) = M(0)e^{-t/\tau} \sin(2\pi ft - \phi) \quad (7.3.2)$$

where the relaxation time  $\tau$  is related to the Gilbert damping coefficient  $\alpha$  by the relation  $\tau = 1/(2\pi f\alpha)$ ,  $f$  is the experimentally obtained precession frequency and  $\phi$  is the initial phase of the oscillation. The fitted data is shown by solid lines in Fig. 7.3(a). The damping coefficient  $\alpha$ , as extracted from the above fitting, is plotted as a function of the interdot separation  $S$  along with the error bars in Fig. 7.4(b). The sample with  $S = 200$  nm shows the lowest  $\alpha$  of about 0.023. This value of  $\alpha$  is slightly higher than the damping coefficient (0.017) measured for a permalloy film of 20 nm thickness grown under identical conditions to those for the arrays of

permalloy dots. Since the dots are magnetostatically isolated, the increase in damping due to the mutual dynamic dephasing of the permalloy dots is unlikely for  $S = 200$  nm. Another possibility is the dephasing of more than one mode within the individual dots [37], which is also ruled out due to the appearance of a dominant single mode in the individual dots. Hence, we believe this increase in damping is possibly due to the defects [38] produced in these dots during nanofabrication, which is quite likely due to the small size of these dots. As  $S$  decreases, the magnetostatic interaction between the dots becomes more prominent and hence the mutual dephasing of slightly out-of-phase magnetization precession of the dots in the array becomes more prominent [31], and consequently  $\alpha$  increases systematically with the decrease in  $S$  down to 75 nm. At  $S = 50$  nm, a different situation arises, where the single resonant mode splits into two closely spaced modes and the apparent damping (square symbol in Fig. 7.4(b)) of the time-domain oscillatory signal jumps suddenly from 0.032 to 0.066. Clearly, this is due to the out-of-phase superposition of two closely spaced modes within the array, as shown later in this article. To understand the correct damping behaviour of the uniform resonant mode, we have isolated the time-domain signal for the mode 1 from the lower lying mode (mode 2) by using fast Fourier filtering. The extracted damping of the filtered time-domain signal for the sample with  $S = 50$  nm is about 0.033, which is consistent with the systematic increase in the damping coefficient of the arrays with decreasing  $S$ , as shown by the circular symbols in Fig. 7.4(b).

### 7.3.3 Micromagnetic Analysis of the Observed Precessional Dynamics

To gain more insight into the dynamics, we have calculated the magnetostatic field distribution of the simulated arrays, and the contour plot of the magnetostatic fields from the  $3 \times 3$  dots at the centre of the array is shown in Fig. 7.5. At larger separations, the stray fields from the dots remain confined close to their boundaries and the interactions among the dots is negligible. As the interdot separation decreases, the stray fields of the neighbouring dots start to overlap causing an increase in the effective field acting on the dots and consequently the corresponding precession frequency. At  $S = 50$  nm, the stray field is large enough to cause a strong magnetostatic coupling between the dots and hence the collective precession modes of the dots in the array [31].

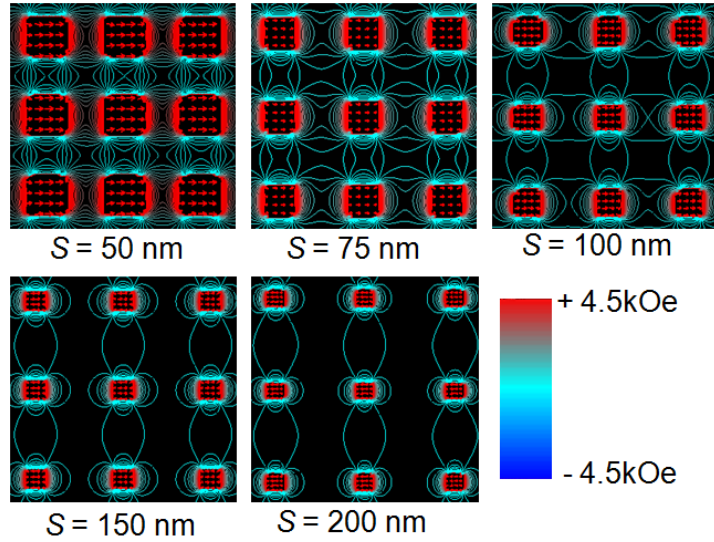


Fig. 7.5: Simulated magnetostatic field distributions ( $x$ -component) are shown for arrays of permalloy dots with  $S = 50, 75, 100, 150$  and  $200$  nm at  $H_b = 2.5$  kOe. The arrows inside the dots represent the magnetization states of the dots, while the strengths of the stray magnetic fields are represented by the colour bar at the bottom right corner of the figure.

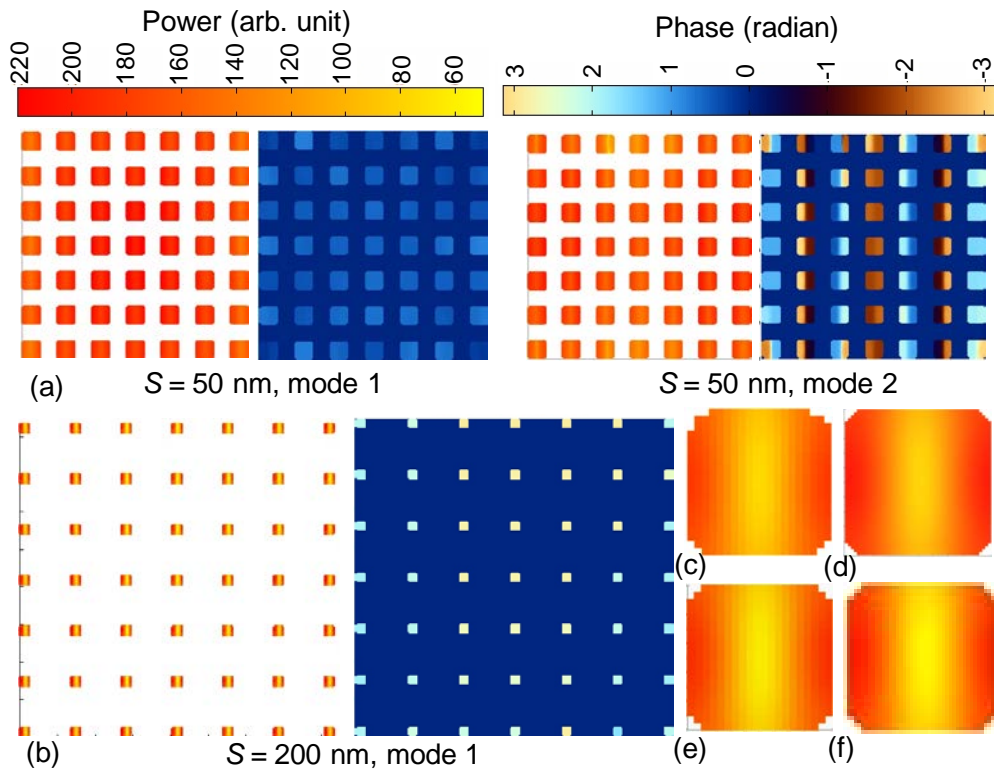


Fig. 7.6: The power and phase maps corresponding to different resonant frequencies are shown for the arrays with (a)  $S = 50$  nm and (b)  $S = 200$  nm. We have also simulated the power maps for a single 50 nm dot with 20 nm thickness with different cell sizes as (c)  $2.5 \times 2.5 \times 20$  nm<sup>3</sup>, (d)  $1 \times 1 \times 20$  nm<sup>3</sup>, and (e)  $2.5 \times 2.5 \times 5$  nm<sup>3</sup> and compared it with (f) the central dot from the  $7 \times 7$  array with  $S = 200$  nm. The colour bars at the top of the images represent the power and phase values within the images.

The spatial natures of the modes were investigated by numerically calculating the spatial distributions of power and phases corresponding to the resonant modes of the samples. The power and phase maps of the resonant modes for the arrays with  $S = 50$  and  $200$  nm are shown in Fig. 7.6(a) and (b). For  $S = 50$  nm, the main resonant mode (mode 1) corresponds to the in-phase precession of majority of the dots in the array apart from the dots near the edges. The intensities of the dots increase from the edge to the centre of the array. The lower frequency mode (mode 2), on the other hand, shows that the dots in the consecutive columns precess out-of-phase, while the dots in the alternative columns precess in-phase. The intensity again shows small variation from the edge to the centre of the array. The spatial variation of the phase of precession of the dots is similar to the backward volume magnetostatic modes (BWVMS) with the wave vector parallel to the bias magnetic field ( $H_b$ ) and both lie within the plane of the sample. For  $S = 200$  nm, the single resonant mode (mode 1) corresponds to the precession of the individual dots and hence all of them have identical power and phase. For comparison we have calculated the power and phase maps of the only resonant mode of a single  $50$  nm wide dot (Fig. 7.6(c)-(e)) with different cell size ((c)  $2.5 \times 2.5 \times 20$  nm<sup>3</sup>, (d)  $1 \times 1 \times 20$  nm<sup>3</sup> and (e)  $2.5 \times 2.5 \times 5$  nm<sup>3</sup>), which is found to be the edge mode [22, 36, 39] that occupies the major fraction of the volume of the dot. It is important to note that the mode structure remains independent of the chosen cell size. A closer view to the central dot of the array with  $S = 200$  nm shows (Fig. 7.6(f)) an identical mode structure to that of the single dot, ensuring that in this array the dynamics is dominated by that of the single dot.

## 7.4 Summary

In summary, we have detected the picosecond precessional dynamics in arrays of  $50$  nm permalloy dots down to the single nanodot regime by an all optical time-resolved magneto-optical Kerr effect microscope. The interdot separation ( $S$ ) varies from  $200$  nm down to  $50$  nm and the numerical calculation of magnetostatic fields show a transition from a magnetostatically isolated regime to a coupled regime as  $S$  decreases. Consequently, we observe a single precessional mode for  $S$  down to  $75$  nm, whose frequency increases with the decrease in  $S$ . This has been analytically modelled by introducing the dipolar and quadrupolar contributions to the precession frequency. At the smallest separation  $S = 50$  nm, we observe a splitting of the resonant mode, and a lower frequency mode appears in addition to the existing mode. Analyses of power and phase maps of the resonant modes reveal that the dynamics of a single dot with  $50$  nm width is dominated by the edge mode. In sparsely packed arrays ( $S \geq$

150 nm) we primarily observe the isolated dynamics of the constituent dots, all in phase. For  $S = 50$  nm, the observed modes correspond to the uniform collective precession of the array (higher frequency mode) and an out-of-phase precession of the consecutive columns of the array parallel to the bias field (lower frequency mode). The damping also shows significant variation with the areal density. For  $S = 200$  nm, that is, in the single nanodot regime, the damping is minimum at about 0.023, which is slightly higher than the damping coefficient (0.017) of a permalloy thin film of the same thickness. We understand this slight increase in damping is a result of the defects introduced in the dots during nanofabrication. However, the damping increases further with the decrease in  $S$  as a result of the dynamic dephasing of the precession of the weakly interacting dots. At  $S = 50$  nm, the dephasing due to the superposition of two resonant modes results in a sudden increase in the apparent damping of the precession. The ability of all optical detection of the picosecond dynamics of 50 nm dots down to the single nanomagnet regime and understanding of the effects of magnetostatic interaction on those dots when placed in a dense array will be important from a fundamental scientific viewpoint as well as for their future applications in various nanomagnetic devices.

## Bibliography

1. I. N. Krivorotov, N. C. Emley, J. C. Sankey, S. I. Kiselev, D. C. Ralph, and R. A. Buhrman, *Science* **307**, 228 (2005).
2. A. Barman, S. Wang, J. D. Maas, A. R. Hawkins, S. Kwon, A. Liddle, J. Bokor, and H. Schmidt, *Nano Lett.* **6**, 2939 (2006).
3. Y. Acremann, J. P. Strachan, V. Chembrolu, S. D. Andrews, T. Tyliczszak, J. A. Katine, M. J. Carey, B. M. Clemens, H. C. Siegmann, and J. Stöhr, *Phys. Rev. Lett.* **96**, 217202 (2006).
4. A. Barman, S. Wang, J. Maas, A. R. Hawkins, S. Kwon, J. Bokor, A. Liddle, and H. Schmidt, *Appl. Phys. Lett.* **90**, 202504 (2007).
5. Z. Liu, R. D. Sydora, and M. R. Freeman, *Phys. Rev. B* **77**, 174410 (2008).
6. J. M. Shaw, T. J. Silva, M. L. Schneider, and R. D. McMichael, *Phys. Rev. B* **79**, 184404 (2009).
7. J. Jersch, V. E. Demidov, H. Fuchs, K. Rott, P. Krzysteczko, J. Munchenberger, G. Reiss, and S. O. Demokritov, *Appl. Phys. Lett.* **97**, 152502 (2010).
8. P. S. Keatley, P. Gangmei, M. Dvornik, R. J. Hicken, J. R. Childress, and J. A. Katine, *Appl. Phys. Lett.* **98**, 082506 (2011).
9. Z. Liu, R. Brandt, Y. Yahagi, B. Hansen, B. Harteneck, J. Bokor, A. R. Hawkins, and H. Schmidt, *Appl. Phys. Lett.* **98**, 052502 (2011).
10. T. Thomson, G. Hu, and B. D. Terris, *Phys. Rev. Lett.* **96**, 257204 (2006).
11. O. Hellwig, A. Berger, T. Thomson, E. Dobisz, Z. Z. Bandic, H. Yang, D. S. Kercher, and E. E. Fullerton, *Appl. Phys. Lett.* **90**, 162516 (2007).
12. D. A. Allwood, G. Xiong, C. C. Faulkner, D. Atkinson, D. Petit, and R. P. Cowburn, *Science* **309**, 1688 (2005).
13. A. Imre, G. Csaba, L. Ji, A. Orlov, G. H. Bernstein, and W. Porod, *Science* **311**, 205 (2006).
14. D. B. Carlton, N. C. Emley, E. Tuchfeld, and J. Bokor, *Nano Lett.* **8**, 4173 (2008).
15. S. Tehrani, E. Chen, M. Durlam, M. DeHerrera, J. M. Slaughter, J. Shi, and G. Kerszykowski, *J. Appl. Phys.* **85**, 5822 (1999).
16. S. H. Chung, A. Hoffmann, S. D. Bader, C. Liu, B. Kay, L. Makowski, and L. Chen, *Appl. Phys. Lett.* **85**, 2971 (2004).

17. S. Kaka, M. R. Pufall, W. H. Rippard, T. J. Silva, S. E. Russek, and J. A. Katine, *Nature* **437**, 389 (2005).
18. S. Neusser and D. Grundler, *Adv. Mater.* **21**, 2927 (2009).
19. A. V. Chumak, V. S. Tiberkevich, A. D. Karenowska, A. A. Serga, J. F. Gregg, A. N. Slavin, and B. Hillebrands, *Nat. Commun.* **1**, 141 (2010).
20. J. K. W. Yang, Y. S. Jung, J.-B. Chang, R. A. Mickiewicz, A. Alexander Katz, C. A. Ross, and K. K. Berggren, *Nat. Nano.* **5**, 256 (2010).
21. D.-H. Kim, E. A. Rozhkova, I. V. Ulasov, S. D. Bader, T. Rajh, M. S. Lesniak, and V. Novosad, *Nat. Mater.* **9**, 165 (2010).
22. V. V. Kruglyak, A. Barman, R. J. Hicken, J. R. Childress, and J. A. Katine, *Phys. Rev. B* **71**, 220409(R) (2005).
23. L. J. Heyderman, H. H. Solak, C. David, D. Atkinson, R. P. Cowburn, and F. Nolting, *Appl. Phys. Lett.* **85**, 4989 (2004).
24. V. V. Kruglyak, P. S. Keatley, A. Neudert, R. J. Hicken, J. R. Childress, and J. A. Katine, *Phys. Rev. Lett.* **104**, 027201 (2010).
25. S. Jung, B. Watkins, L. DeLong, J. B. Ketterson, and V. Chandrasekhar, *Phys. Rev. B* **66**, 132401 (2002).
26. G. N. Kakazei, Y. G. Pogorelov, M. D. Costa, T. Mewes, P. E. Wigen, P. C. Hammel, V. O. Golub, T. Okuno, and V. Novosad, *Phys. Rev. B* **74**, 060406(R) (2006).
27. G. Gubbiotti, M. Madami, S. Tacchi, G. Carlotti, and T. Okuno, *J. Appl. Phys.* **99**, 08C701 (2006).
28. Z. K. Wang, H. S. Lim, V. L. Zhang, J. L. Goh, S. C. Ng, M. H. Kuok, H. L. Su, and S. L. Tang, *Nano Lett.* **6**, 1083 (2006).
29. L. Giovannini, F. Montoncello, and F. Nizzoli, *Phys. Rev. B* **75**, 024416 (2007).
30. P. V. Bondarenko, A. Y. Galkin, B. A. Ivanov, and C. E. Zaspel, *Phys. Rev. B* **81**, 224415 (2010).
31. A. Barman and S. Barman, *Phys. Rev. B* **79**, 144415 (2009).
32. B. Rana, D. Kumar, S. Barman, S. Pal, Y. Fukuma, Y. Otani, and A. Barman, *ACS Nano* **5**, 9559 (2011).
33. M. Donahue and D. G. Porter, "OOMMF User's guide, Version 1.0," *NIST Interagency Report No. 6376, National Institute of Standard and Technology, Gaithersburg, MD, URL: <http://math.nist.gov/oommf>*, (1999).
34. B. Rana and A. Barman, *SPIN* **3**, 1330001 (2013).

35. K. H. J. Buschow, "Handbook of Magnetic Materials," Volume 18, *Elsevier*, North Holland: Amsterdam, The Netherlands (2009).
36. A. A. Awad, G. R. Aranda, D. Dieleman, K. Y. Guslienko, G. N. Kakazei, B. A. Ivanov, and F. G. Aliev, *Appl. Phys. Lett.* **97**, 132501 (2010).
37. A. Barman, V. V. Kruglyak, R. J. Hicken, J. M. Rowe, A. Kundrotaite, J. Scott, and M. Rahman, *Phys. Rev. B* **69**, 174426 (2004).
38. M. Sparks, "Ferromagnetic Relaxation Theory," *McGraw-Hill*, New York (1966).
39. J. Jorzick, S. O. Demokritov, B. Hillebrands, M. Bailleul, C. Fermon, K. Y. Guslienko, A. N. Slavin, D. V. Berkov, and N. L. Gorn, *Phys. Rev. Lett.* **88**, 047204 (2002).

## CHAPTER 8

---

# Collective Magnetization Dynamics of $\text{Ni}_{80}\text{Fe}_{20}$ Nanodot Arrays with Varying Dot Size and Shape

---

### 8.1 Background

In confined ferromagnetic elements, the magnetization at the edge regions deviates from the rest of the elements even in presence of a large enough magnetic field thus creating demagnetized regions. The geometry of the demagnetized regions strongly depends upon the size and shape of the elements. These demagnetized regions play important roles in determining their magnetic ground states. Again, the profile of the stray magnetic field depends on the shapes of the boundaries of the elements as well as the internal magnetic field configuration. Therefore, the interdot magnetostatic interaction in ordered arrays of nanomagnets is strongly affected by the sizes and shapes of the elements [1-3]. The nonuniform demagnetized regions offer different potentials to the propagating spin waves. They may trap the spin waves locally or quantize them [4-11]. The intrinsic magnetization dynamics of magnetic nanodots are determined by the internal magnetic configuration of dots. On the other hand, the collective magnetization dynamics of arrays of nanodots are determined by the internal magnetization configuration of individual dots and the interplay between the static and dynamic stray fields among the dots arranged in the array. Therefore, by tuning the shape and size of magnetic dots, the intrinsic and collective magnetization dynamics of arrays of magnetic nanodots can be controlled efficiently.

A number of studies on the intrinsic and collective magnetization dynamics have been performed for varying dot size and shape. The magnetization dynamics of dots with various

shapes have been reported in different literatures [1, 11-15]. In these studies, the intrinsic and collective modes of dots with different shapes have been studied along with their spatial nature and dispersion character. In some reports, the intrinsic [16-17] or the collective magnetization dynamics [9, 13, 15, 18] have been reported for different dot size also.

In chapters 6 and 7, we have discussed about the precessional dynamics of square shaped  $\text{Ni}_{80}\text{Fe}_{20}$  (permalloy) dots of two different sizes: 200 nm and 50 nm. For 200 nm dots, the intrinsic dynamics are governed by centre mode (CM), edge mode (EM) and a mixed edge mode – Damon Eshbach (EM-DE) mode, whereas for 50 nm dots the EM dominates and the other modes are completely suppressed. Consequently, their collective dynamics also vary significantly. However, it is important to understand how this kind of variation in dynamic behaviour occurs with the dot size. In this chapter, we have studied the magnetization dynamics of arrays of dots as a function of dot size. We have also studied the collective magnetization dynamics of circular dots with varying sizes between 200 nm and 50 nm to show how magnetization dynamics are affected by the dot shape.

## 8.2 Sample Fabrication, Characterization and Measurement Technique

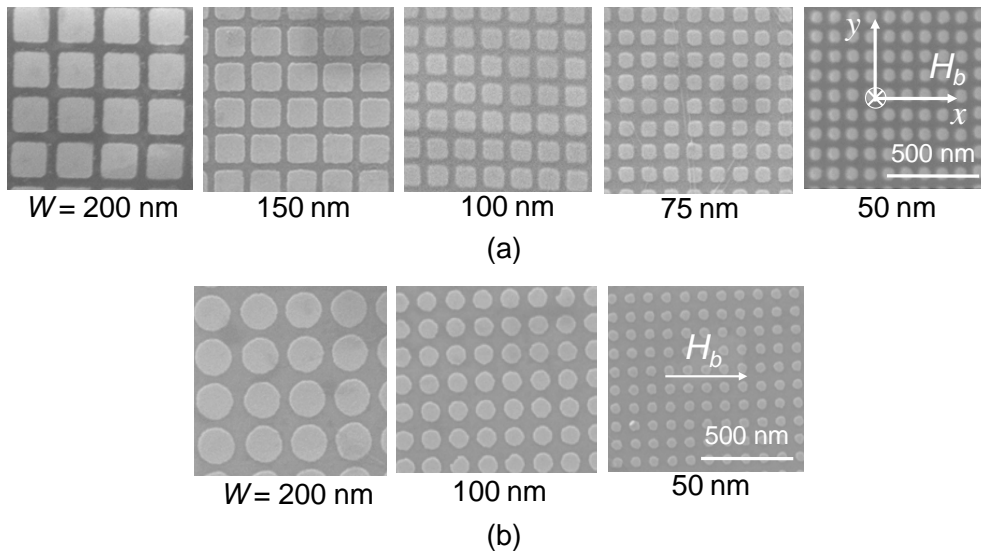


Fig. 8.1: Scanning electron micrographs for (a) arrays of square permalloy dots with fixed edge-to-edge separation ( $S$ ) of 50 nm and varying sizes ( $W$ ) from 200 nm to 50 nm and (b) arrays of circular permalloy dots with fixed edge-to-edge separation ( $S$ ) of 50 nm and varying sizes  $W = 200$  nm, 100 nm and 50 nm. The geometry of the bias field ( $H_b$ ) is shown on top of the SEM image of arrays with 50 nm dot size.

$10 \times 10 \mu\text{m}^2$  square arrays of square and circular shaped permalloy dots with interdot (edge-to-edge) separation ( $S$ ) fixed to 50 nm and width ( $W$ ) varying from 200 nm to 50 nm were prepared by a combination of electron beam lithography and electron beam evaporation. A bilayer PMMA/MMA (polymethyl methacrylate/methyl methacrylate) resist pattern was first prepared on thermally oxidized Si(100) substrate by using electron beam lithography with a dose current of about 100 pA and dose time of about 0.9  $\mu\text{s}$ , and 20 nm permalloy was then deposited on the resist pattern by electron beam evaporation at a base pressure of about  $2 \times 10^{-8}$  Torr. A 10 nm thick  $\text{SiO}_2$  capping layer was deposited on top of permalloy to protect the dots from degradation when exposed to the optical pump-probe experiments in air. This is followed by the lifting-off of the sacrificial material and oxygen plasma cleaning of the residual resists that remained even after the lift-off process.

Figure 8.1(a) shows typical scanning electron micrographs (SEM) of the square permalloy dot arrays prepared as above. The SEM images show that the arrays were well fabricated with a slightly rounded corners which increases with decreasing dot size ( $W$ ). A small ( $< 15\%$ ) deviation of the dots is also observed from their nominal dimensions. Figure 8.1(b) shows the SEM images of circular permalloy dot arrays as prepared above. Only three samples were prepared with good quality in this case as shown in Fig. 8.1(b).

The ultrafast magnetization dynamics was measured by a two-colour all optical pump-probe setup with spatial and temporal resolutions of 800 nm and 100 fs, respectively. The second harmonic ( $\lambda = 400$  nm, pulse width  $\approx 100$  fs) of a mode locked Ti-sapphire pulsed laser (pulse width  $\approx 70$  fs) is used to excite the sample. The linearly polarized fundamental laser beam ( $\lambda = 800$  nm) is used to probe the dynamics by measuring the polar Kerr rotation using an optical bridge detector (OBD). The pump power used in these measurements is about  $15 \text{ mJ/cm}^2$ , while the probe power is much weaker and is about  $3 \text{ mJ/cm}^2$ . The pump and probe beams are made collinear and focused on each array through the same microscope objective with N.A. = 0.65. The pump beam is slightly defocused at the sample surface to a larger diameter ( $\approx 1 \mu\text{m}$ ) than the probe beam, which is focused to a diffraction limited spot size of about 800 nm. The probe beam is centered on the pump beam so that slight misalignment during the course of the experiment does not affect the pump-probe signals. A large enough magnetic field is first applied at a small angle ( $\sim 15^\circ$ ) to the planes of the arrays to saturate their magnetization. The magnetic field strength is then reduced to the bias field value ( $H_b$  = component of bias field in the sample plane *i.e.* along  $x$ -axis), which ensures that the magnetization still remains saturated along the bias field direction. The pump beam was

chopped at 2 kHz frequency and a phase sensitive detection of Kerr rotations were made using lock-in amplifier.

## 8.3 Precessional Magnetization Dynamics of Square Permalloy Dot Arrays with Varying Dot Size

### 8.3.1 Static Magnetic Configurations

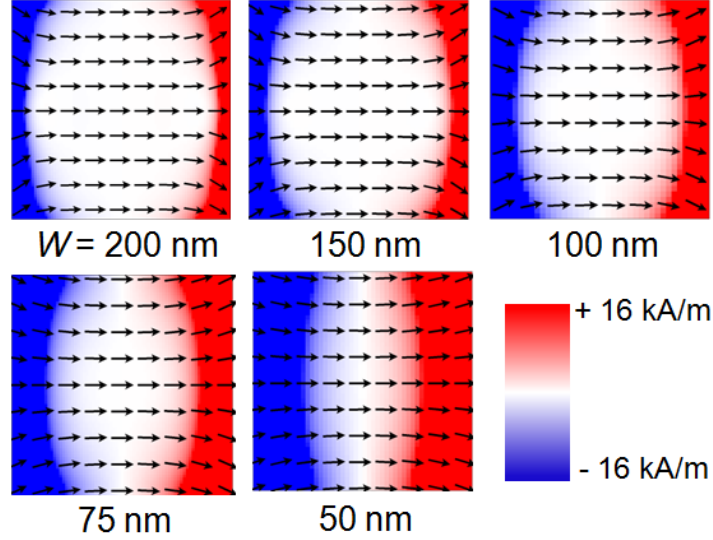


Fig. 8.2: Simulated static magnetic configurations for single square permalloy dots with varying widths ( $W$ ) at bias field  $H_b = 1.25$  kOe applied parallel to the horizontal edges of the dots. The colour map shows the  $z$ -component (out-of-plane) of the magnetization. The figures are not in the same length scale. The colour scale of magnetization is shown at right-bottom corner of the figure.

Before discussing about the experimental result, we will investigate how the magnetic ground states of single isolated nandots vary as the dot size is varied systematically from 200 nm down to 50 nm. The static magnetic configurations were simulated by OOMMF software [19] by following methods as described in chapter 6. For the simulation, single square permalloy dots with thickness ( $t$ ) = 20 nm and varying size ( $W$ ) from 200 nm to 50 nm were considered. The extracted materials parameters ( $\gamma$ ,  $H_k$  and  $M_S$ ) from the measured dynamics of a  $10 \times 10 \mu\text{m}^2$  blanket permalloy film were used in the micromagnetic simulations [2]. The dots with  $W = 200$  nm, 150 nm and 100 nm were discretized into a number of cuboidal cells of size  $5 \times 5 \times 20 \text{ nm}^3$ , whereas the dots with  $W = 75$  nm and 50 nm were discretized into a number of cuboidal cells of size  $2.5 \times 2.5 \times 20 \text{ nm}^3$ . The ‘ $x$ ’ and ‘ $y$ ’ dimensions were set lower than the exchange length for permalloy ( $\sim 5.3$  nm) to incorporate the role of exchange interaction on the dynamics. The ‘ $z$ ’ dimensions were set same as the thickness, which is

much larger than the exchange length. Further test simulations with smaller cell size did not affect the static magnetic configurations significantly. Figure 8.2 shows the simulated static magnetic configurations for the dots with the bias magnetic field  $H_b = 1.25$  kOe applied parallel to the horizontal edges of the dot [20]. The colour scale (red-white-blue) shows the  $z$ -component (out-of-plane) of magnetization. From the images it is clear that for confined magnetic nanostructures, the edge regions perpendicular to the direction of the bias field becomes demagnetized to minimize the total magnetic energy of the system. With the decrease in the size, the volume fraction of the demagnetized region becomes larger. This variation in the static magnetization state with dot size is responsible for the variation in the observed dynamic behaviour.

### 8.3.2 Intrinsic Magnetization Dynamics of Single Dots as a Function of Dot Size

Now, we will discuss about the intrinsic precessional modes of single dots. We have performed time-dependent micromagnetic simulations by using OOMMF software to understand the intrinsic dynamics of single dots as a function of dot size. The static magnetic configurations obtained as above are used as the initial states for the dynamic simulations. A bias field ( $H_b$ ) of 1.25 kOe was applied parallel to the horizontal edge of the dot and a pulse field of peak amplitude of 30 Oe with rise time of 50 ps was applied normal to the plane of the dots to trigger the precessional dynamics. The simulated resonant mode frequencies of the single dots are plotted as a function of the dot size ( $W$ ) in Fig. 8.3. The spatial distributions of the powers corresponding to all resonant modes are shown in the same figure [20]. Three different modes are observed for 200 nm dot. Mode 1 is the CM, mode 2 is the mixed EM-DE mode, while mode 3 is the EM. The resonant modes for the 150 nm dot are similar to those for the 200 nm dot with slightly modified spatial extents such as the volume occupied by the EM increases for this dot. The frequencies of the modes corresponding to each branch increase and the frequency gap between mode 1 and mode 2 decreases with the decrease in dot size. This region is marked as region 1. In region 2 ( $W = 100$  nm and 75 nm), mode 2 (EM-DE) disappears and mode 3 (EM) becomes more prominent with more extended spatial profiles as opposed to the same mode for the dots in region 1. The frequency of mode 3 increases very sharply with the decrease in  $W$  in this region. For 75 nm dot, mode 1 is the CM, occupying a smaller volume fraction of the dots as opposed to the larger dots, while mode 2 (EM) has extended significantly. In region 3 ( $W < 75$  nm), mode 1 (CM) disappears

in the frequency spectra and we observe a single mode (EM), which now occupies the major volume fraction of the dot.

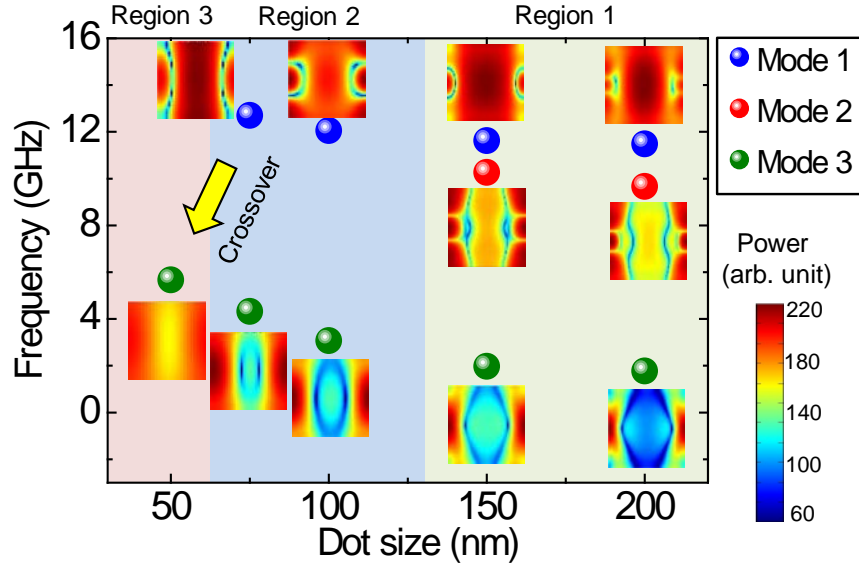


Fig. 8.3: Frequencies of the simulated resonant modes of single permalloy square dots with varying sizes ( $W = 50, 75, 100, 150$  and  $200$  nm) are plotted as a function of the dot size. The mode (power) profiles for all modes are shown. The three different background colours show three different regions of interest. Different branches of frequencies are assigned with different coloured symbols. The colour scale of power is shown at right-bottom corner of the figure.

### 8.3.3 Collective Magnetization Dynamics of Array of Dots with Varying Dot Size

To observe the collective precessional modes of dot arrays with varying dot size, we measured the time-resolved magnetization dynamics of arrays of permalloy dots with fixed edge-to-edge separation ( $S = 50$  nm, thickness ( $t = 20$  nm, and with size ( $W$ ) varying from 50 to 200 nm. At this interdot separation, the dots in all arrays are magnetostatically coupled and show collective dynamics, which is significantly different from the intrinsic dynamics of the individual dots. The time-resolved dynamics shows an ultrafast demagnetization and a bi-exponential relaxation, as discussed in previous chapters. We have eliminated the demagnetization part and subtracted the bi-exponential decay from the time-resolved data to study the precessional dynamics. Figure 8.4(a) shows the background subtracted Kerr rotation data from arrays of square permalloy dots. The time-resolved Kerr rotation data were measured for up to 1.5 ns and that was found to be sufficient for having required frequency resolution in the FFT spectra, while ensuring that the pump and probe spots do not drift

significantly *w.r.t.* the measurement position on each array during the measurement time. Figure 8.4(b) shows corresponding FFT spectra. The experimental results show primarily three branches of frequencies. The frequency of each branch increases with decreasing dot size and a crossover from higher frequency branch (branch 1) to lower frequency branches (branches 2 & 3) occurs as the dot size decreases down to 50 nm.

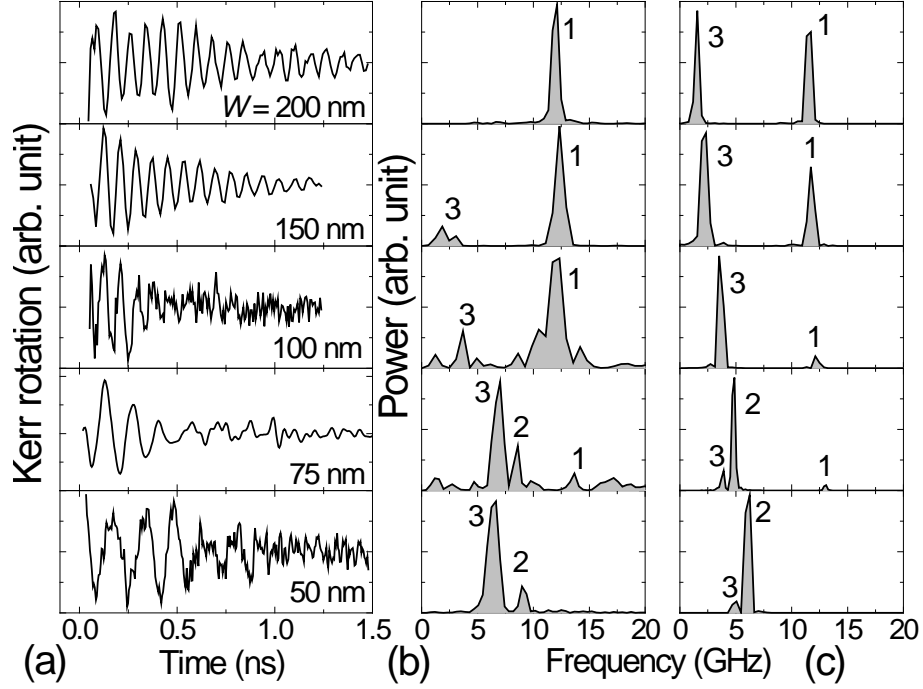


Fig. 8.4: (a) Time-resolved Kerr rotation data measured from arrays of square permalloy dots with varying dot size and with fixed interdot separation  $S = 50$  nm and (b) the corresponding FFT spectra. (c) FFT spectra of simulated magnetization dynamics for  $7 \times 7$  arrays of dots with same specifications as mentioned above.

We have performed OOMMF simulations to understand the details of the observed modes. For the simulation,  $7 \times 7$  square arrays of permalloy dots with  $S = 50$  nm,  $t = 20$  nm and varying size ( $W$ ) from 200 nm to 50 nm were considered. The arrays with  $W = 200$  nm, 150 nm and 100 nm were discretized into a number of cuboidal cells of sizes  $5 \times 5 \times 20$  nm<sup>3</sup>, whereas the arrays with  $W = 75$  nm and 50 nm were discretized into a number of cuboidal cells of sizes  $2.5 \times 2.5 \times 20$  nm<sup>3</sup>. The ‘ $z$ ’ dimensions were set same as the thickness of the dots as we are primarily interested in the confined modes within the planes of the dots. A bias field ( $H_b$ ) of 1.25 kOe was applied along the  $x$ -axis (Fig. 8.1). Figure 8.4(c) shows the FFT spectra of the simulated time-resolved magnetization data obtained from the  $7 \times 7$  arrays of dots. The simulated results qualitatively reproduce the experimental results. However, the lower branch for arrays with  $W = 200$  nm is almost invisible, and for  $W = 150$  nm and 100 nm

have much smaller power in the experiment as opposed to those observed in the simulation. We will see later in this section that for arrays of 200 nm and 150 nm dots, mode 3 is the EM of constituent dots. Therefore, the defects and edge roughness of the lithographically fabricated nanodots strongly affect this mode leading towards very small power of this mode. Further, inhomogeneous line broadening and smaller experimental time window in the TRMOKE measurements make it difficult to resolve this mode [13]. However, for array of 100 nm dots, mode 3 is observed with significant power along with the low frequency background noises.

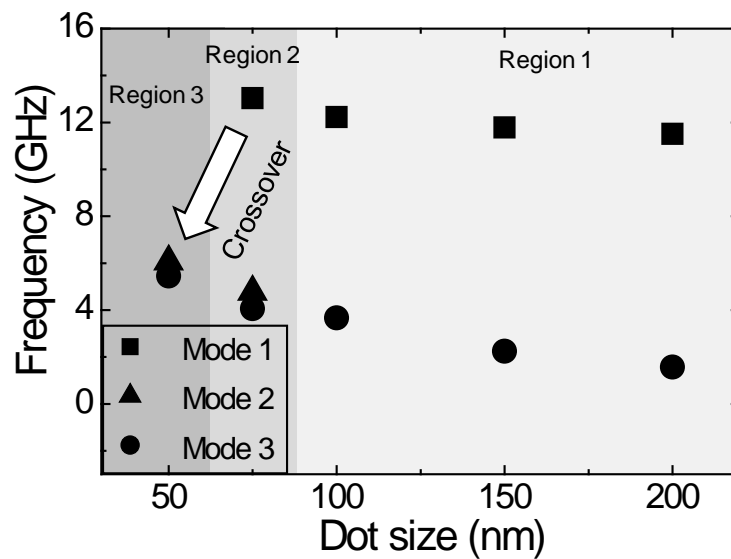


Fig. 8.5: Simulated resonant mode frequencies for arrays of square permalloy dots with  $S = 50$  nm and thickness ( $t$ ) = 20 nm are plotted as a function of dot size. The overall area of the graph has been divided into three different regions of interest by using different background colours. A crossover from the higher frequency branch to lower frequency branches is shown by an arrow.

Simulated resonant mode frequencies are plotted as a function of dot size in Fig. 8.5. We observe here three clear branches of frequencies similar to the single square dots. The overall area of the graph has been divided into three different regions of interest by using different background colours. The graph shows two clear branches of frequencies in region 1 ( $W = 200, 150$  and  $100$  nm). The frequency of each branch increases with decreasing dot size. For the array with 75 nm dots (region 2), three modes are observed as the lower frequency mode is now split into two closely spaced modes. The general trend of increasing of the frequency with the decrease in dot size is maintained. A crossover from the higher frequency branch to the lower branches occurs at the array with 50 nm dot size (region 3). The higher frequency mode completely disappears at this point, while the two closely spaced lower

frequency modes are observed like the array of 75 nm dots. The increase in frequency with the dot size is steeper for  $W < 75$  nm.

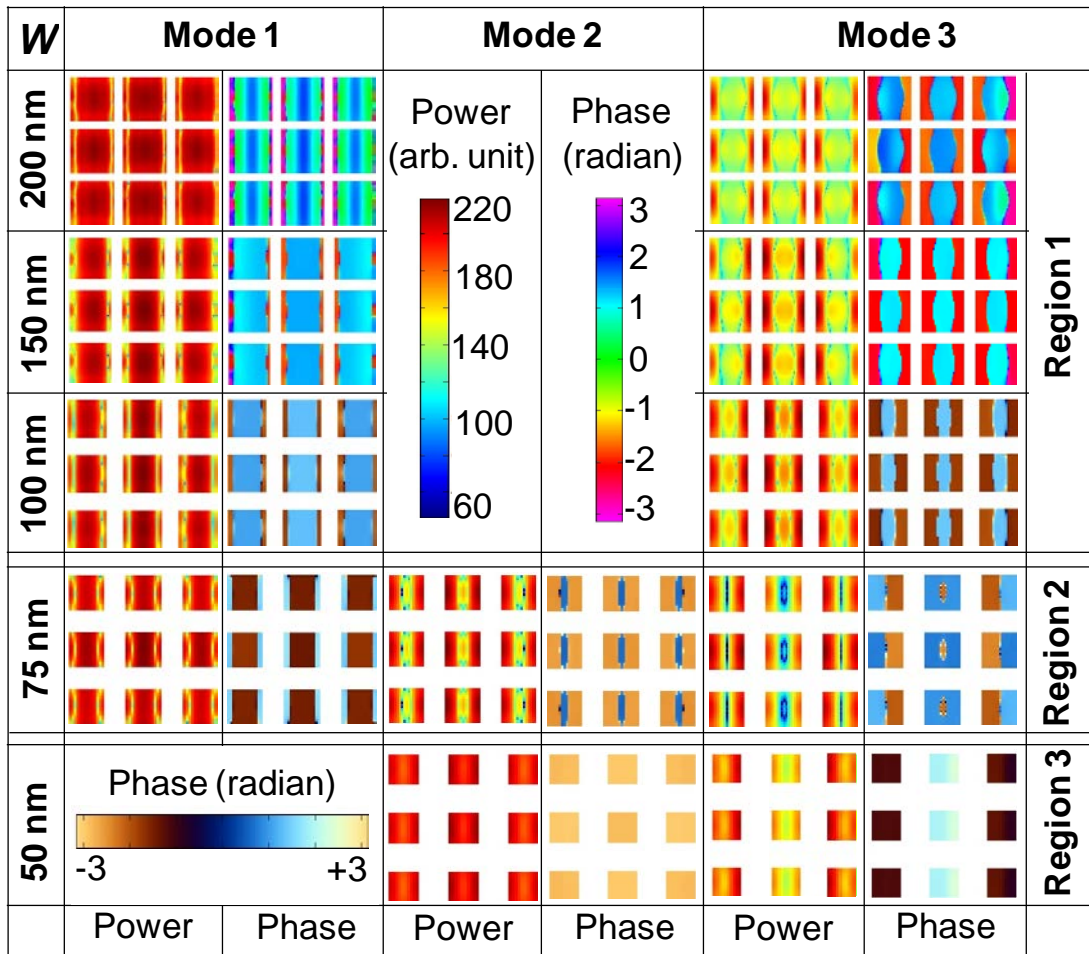


Fig. 8.6: The power and phase maps for the resonant modes for arrays of square permalloy dots with varying dot size ( $W$ ) and with  $S = 50$  nm and thickness ( $t$ ) = 20 nm are shown. The whole range is split into three regions. The colour map for power is shown in region 1. The colour map for phase for first two rows in region 1 is shown within that region, while the phase colour map for the last row in region 1, and regions 2 and 3 are shown in region 3.

The resonant mode profiles for the arrays are numerically calculated as shown in Fig. 8.6 [20]. Power and phase maps of  $3 \times 3$  dots are shown from the centre of  $7 \times 7$  arrays. The whole frequency range is split into three regions according to the dynamical behaviour. The colour map for power, as shown in region 1, is same for all regions. The colour map of phase for arrays of 150 nm and 200 nm dots are shown in region 1, while the same for arrays of 100 nm, 75 nm and 50 nm dots are shown in region 3. For the array of 200 nm dots, the higher frequency mode (mode 1) is the uniform collective mode, where the power is uniformly

distributed throughout the array and the precession of all the dots are in phase. In this case mode 2 of the single 200 nm dot is suppressed as discussed previously. Mode 3 is the coherent precession of the EM of the individual dots. For the array of 150 nm dots, mode 1 is the coherent precession of the CM of the constituent dots. This mode looks similar to the CM of a single 150 nm dot with small modification of the spatial profile due to the collective dynamical effect. Mode 3 is coherent precession of the EM of the constituent dots. Mode 2 of single 150 nm dot is suppressed similar to that of the 200 nm dot. Mode 1 for the array of 100 nm dots is the coherent precession of the modified CM of the constituent dots. Mode 2 is absent. Mode 3 is the coherent precession of the BWVMS like standing spin wave modes of the constituent dots with two nodes inside the dots. For the array of 75 nm dots, mode 1 is again the coherent precession of the modified CM of the dots. Mode 2 and 3 are very closely spaced in the frequency domain and both are coherent precession of BWVMS like standing wave modes of the constituent dots of the array. While in mode 2 there are two nodes inside the dot, for mode 3 there is a single node. The only dominant EM of a single 50 nm dot is split into two collective modes (mode 2 and mode 3). Mode 2 is the uniform mode, where the precessions of all the dots are in phase, but a small variation in the power is observed from the centre to the edges. Mode 3 is the BWVMS mode of the array, where the dots in the consecutive columns precess out-of-phase, while the dots in the alternative columns precess in-phase as discussed earlier.

## **8.4 Ultrafast Magnetization Dynamics of Circular Permalloy Dot Arrays with Varying Dot Size**

### **8.4.1 Static Magnetic Configurations**

We first investigate how the magnetic ground states of single circular nanodot vary as the dot size is varied from 200 nm to 50 nm. The static configurations of magnetization were simulated by OOMMF software by methods as described earlier. Figure 8.7(a) shows the simulated static magnetic configurations for single circular permalloy dots with varying dot size ( $W$ ) at an applied bias magnetic field ( $H_b$ ) = 2.0 kOe. The colour scale (red-white-blue) shows the  $z$ -component (out-of-plane) of magnetization. From the images it is clear that the edge regions perpendicular to the direction of the bias magnetic field becomes demagnetized like square magnetic dots to minimize the total magnetic energy of the system. However, due to the circular shape, the magnetic configurations are significantly different than that of the square dots. Unlike in the square dots, where only the edges perpendicular to the bias field

are demagnetized, here the demagnetized regions extends over the entire boundary of the circular dots. However, the demagnetized volume gradually decreases from the edge regions, which are exactly perpendicular the bias field to edges, which are parallel to the bias field. This kind of magnetic configuration is obvious to minimize the energy associated with the magnetostatic stray field and hence the total energy of the magnetic system. With the decrease in the dot size the volume fraction of the demagnetized region becomes larger and becomes dominant over the uniformly magnetized central region, where the spins are parallel to the bias magnetic field for the dot with 50 nm diameter. This variation in the static magnetization states with dot size and shape is responsible for the variation in their time-resolved magnetization dynamics.

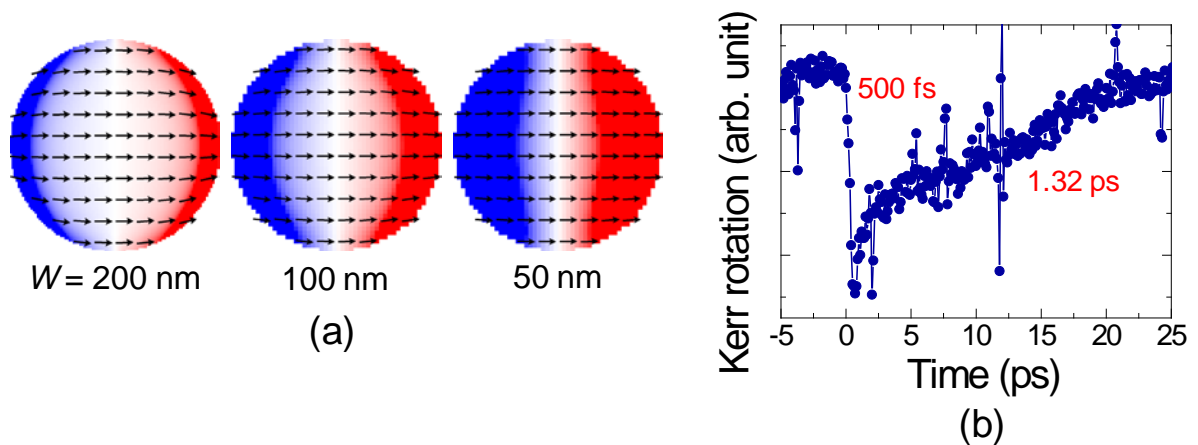


Fig. 8.7: (a) Simulated static magnetic states for single circular permalloy dots with varying size ( $W$ ) at bias field  $H_b = 2.0$  kOe. The colour map shows the  $z$ -component (out-of-plane) of magnetization. The figures are not in the same length scale. The colour scales of magnetization are same to those in Fig. 8.2. (b) The ultrafast demagnetization and fast relaxation for array of 200 nm circular dots with  $S = 50$  nm is shown.

#### 8.4.2 Intrinsic and Collective Magnetization Dynamics of Circular Permalloy Nanodots with Varying Dot Size

Figure 8.7(b) shows typical time-resolved Kerr rotation data measured from array of circular permalloy dots with  $W = 200$  nm and  $S = 50$  nm. The time-resolved data shows a demagnetization time of about 500 fs, which is identical to that observed for a permalloy  $10 \times 10 \mu\text{m}^2$  blanket thin film and also for arrays of square permalloy dots with size between 200 nm and 50 nm. The demagnetization is believed to occur due to the thermalized population of spins above the Fermi level (discussed in section 2.6.3) [21-22]. The thermalization time is an

intrinsic property of the material and is independent of extrinsic parameters like sample shape and geometry. The value of fast relaxation time constant  $\tau_f$  is found to be 1.32 ps, which varies with dot size. The value of  $\tau_f$  is also different from that observed for a permalloy  $10 \times 10 \mu\text{m}^2$  blanket thin film and also for arrays of square permalloy dots with size 200 nm. This is due to the variation of local defects and microstructures of the circular dots due to the limitation in the fabrication technique and the corresponding variation of the spin-orbit relaxation time.

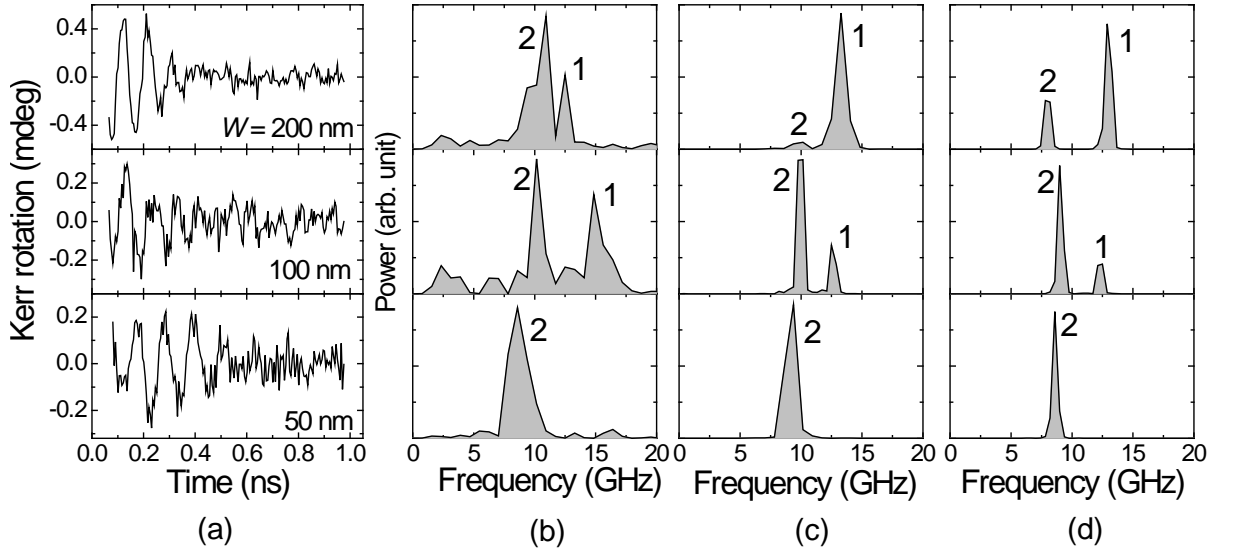


Fig. 8.8: (a) Time-resolved Kerr rotations measured from arrays of circular permalloy dots with interdot separation  $S = 50$  nm and varying dot size ( $W = 200, 100$  and  $50$  nm) and (b) the corresponding FFT power spectra. (c) The FFT power spectra of simulated time-resolved magnetization for  $7 \times 7$  arrays of circular dots with same specifications as the experimental samples. (d) The FFT power spectra of simulated time-resolved magnetization for single circular dots with dot size  $W = 200, 100$  and  $50$  nm.

The precessional magnetization dynamics for the circular dots were measured with a bias field of 2 kOe applied parallel to the symmetry axes of the arrays as shown on top of the Fig. 8.1(b). Figure 8.8(a) shows background subtracted time-resolved Kerr rotations measured from arrays of circular permalloy dots with fixed interdot separation  $S = 50$  nm and with three different dot sizes ( $W = 200, 100$  and  $50$  nm). Figure 8.8(b) shows the corresponding FFT power spectra and Fig. 8.8(c) shows the FFT power spectra of simulated time-resolved magnetization data from  $7 \times 7$  arrays of circular dots with varying size and fixed interdot separation as the experimental samples. The simulated frequency spectra for single circular dots with different size are also shown in Fig. 8.8(d).

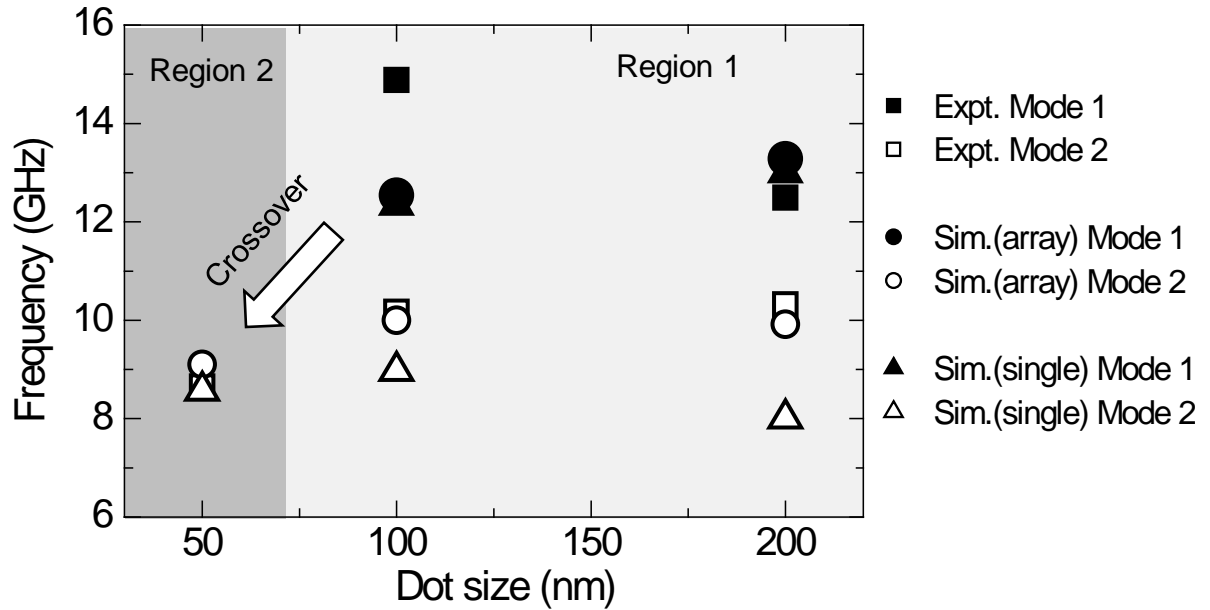


Fig. 8.9: The experimental resonant frequencies for arrays of circular permalloy dots and simulated resonant frequencies for single and arrays of circular permalloy dots are plotted as function of dot size. The overall area of the graph has been divided into two different regions of interest by using different background colours. A crossover from higher frequency branch to lower frequency branch is shown by an arrow.

For a better understanding we have plotted the variation of resonant frequencies of the circular dot arrays as a function of dot size as shown in Fig. 8.9. The overall area of the graph has been divided into two different regions of interest by using different background colours. In region 1 ( $W = 200$  nm and 100 nm), two branches of frequencies are observed for single dot as well as for arrays of dots. For single dot, the frequency of mode 1 decreases with the decrease in dot size, whereas the frequency of mode 2 increases with the decrease in dot size. The simulated results for arrays of dots show that in region 1, frequency of mode 2 remains almost unchanged with the decrease in dot size, whereas frequency of the upper branch decreases with the decrease in dot size. The experimental results show that the general behaviour of mode 2 is well reproduced by micromagnetic simulation. However, frequency of mode 1 for the array of 100 nm dots shows a discrepancy with the simulated frequency. This might be due to the defects present in the experimental sample. As the dot size decreases to 50 nm (region 2), only a single resonant mode is observed for the single dot as well as for dot array with a crossover from higher frequency branch to lower frequency branch. The experimental result also shows a single resonant mode for array of 50 nm dots. The crossover is shown by an arrow on the graph in Fig. 8.9.

### 8.4.3 Power and Phase Profiles of the Resonant Modes

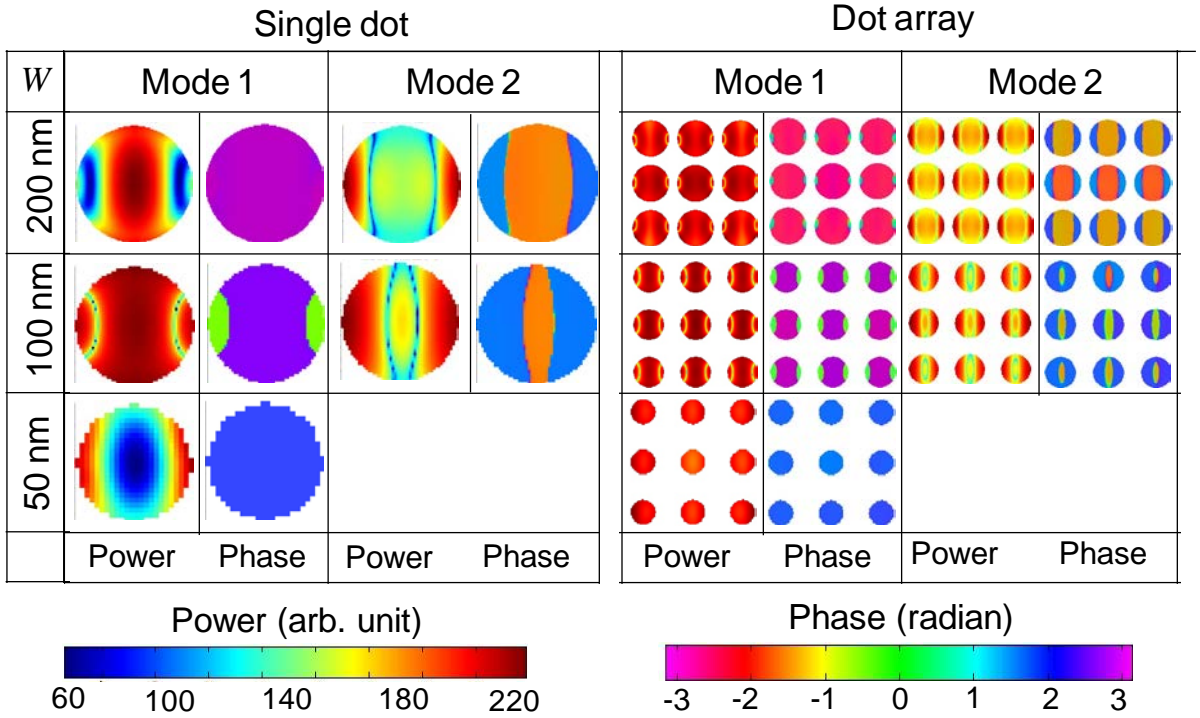


Fig. 8.10: Simulated power and phase profiles of intrinsic and collective resonant modes of circular permalloy dots with sizes  $W = 200, 100$  and  $50$  nm. For the array, the edge-to-edge separation is fixed at  $S = 50$  nm. The colour scales for power and phase are shown at the bottom of the figure.

We have numerically calculated the spatial profiles of power and phase for single and arrays of circular permalloy dots of three different size. Power and phase maps of  $3 \times 3$  dots from the centre of  $7 \times 7$  arrays are shown in Fig. 8.10 along with the power and phase maps of single dots. For a single 200 nm dot, mode 1 is the CM and mode 2 is the EM of the dot. For single 100 nm dot, mode 1 is the CM with extended profile and mode 2 is the EM of the dot. The width of the EM also increases with the decrease in dot size. For a 50 nm dot, only a single dominant EM is observed like a 50 nm square dot. For the array of 200 nm dots, mode 1 is uniform collective mode where precession of constituent dots are in phase, while the lower frequency mode is a BWVMS like mode of the constituent dots. In this case, the intrinsic CM and EM of 200 nm dots are suppressed in the observed collective modes. For array of 100 nm dots, mode 1 is the coherent precession of CM of constituent dots, whereas mode 2 is the BWVMS like mode of constituent dots. In this case the intrinsic CM is slightly modified when they are arranged in an array, whereas the intrinsic EM is modified to BWVMS like mode of constituent dots in the array. For the array of 50 nm dots, the

dominant EM of the constituent dots are suppressed by a single uniform collective mode of the array where the precession of all the dots are in the same phase.

Significant differences in the intrinsic and collective behaviours in the precessional magnetization dynamics of circular and square dots are observed. For a single 200 nm circular dot, the mixed EM-DE mode observed in the 200 nm square dot (Fig. 8.3) is absent. In arrays of 200 nm circular dots, the BWVMS like modes of constituent dots are observed instead of the edge modes of constituent dots as observed for array of 200 nm square dots. A significant difference is also observed for array of 50 nm circular dots. In this case, the lower frequency BWVMS mode of the array is not observed like the array of 50 nm square dots. The reasons behind all of these differences may be attributed to the shape of the dots, which not only changes the internal magnetic configurations of the dots but also control the profile of the magnetostatic stray fields within the array.

## 8.5 Summary

In summary, we have shown the dependence of intrinsic and collective magnetization dynamics of square and circular magnetic dots on their size varying between 200 nm and 50 nm. The intrinsic magnetization dynamics of single square magnetic dots shows mainly three different frequency branches, where the frequency of each branch increases with the decrease in dot size. For single larger dots, CM, a mixed EM-DE mode and EM are simultaneously observed. As the dot size decreases below 150 nm, EM-DE mode disappears and the EM becomes more prominent and eventually a crossover from higher frequency branch to lower frequency branch is observed as the dot size becomes lower than 75 nm. In the collective dynamics of the arrays ( $S = 50$  nm), similar behaviour such as increase in resonant frequency of each branch with decrease in dot size and a crossover from higher frequency branch to lower frequency branch below a dot size of 75 nm is observed. However, for arrays of larger dots ( $W = 200$  nm, 150 nm), the intrinsic EM-DE mode is suppressed either by the uniform collective dynamics of the array (for  $W = 200$  nm) or by the coherent precession of CMs of the constituent dot (for  $W = 150$  nm). For the arrays of dots with intermediate size ( $W = 100$  nm and 75 nm), the intrinsic EMs of single dots are modified to the BWVMS like mode of constituent dot. For smaller dot size ( $W = 50$  nm), the intrinsic dominant EM of single dot is suppressed by two closely spaced collective modes (uniform mode and BWVMS like mode) of the array.

The study of ultrafast demagnetization and fast relaxation time of arrays of 200 nm circular dots shows that the demagnetization time does not change with shape of the dots as it is an intrinsic property of the material, whereas the fast relaxation time, which depends upon spin-orbit interaction, varies with shape. The intrinsic and collective magnetization dynamics for circular dots are significantly different than those of the square dots due to the variation in the ground state of magnetization as well as the stray magnetic field profiles. Mainly two branches of frequencies are observed in intrinsic as well as in collective dynamics. A crossover from higher branch to lower branch is also observed here as the dot size decreases down to 50 nm. However, in case of circular dots, the frequency of each branch may decrease or increase with the decrease in dot size depending upon the type of the mode. For larger dots ( $W \geq 100$  nm), the intrinsic CM and EM are simultaneously observed. As the dot size decreases ( $W = 50$  nm), the EM becomes prominent and CM is suppressed and consequently, a crossover from the higher frequency branch to the lower frequency branch is observed. In the collective regime ( $S = 50$  nm), the intrinsic CMs of larger dots ( $W = 200$  nm and 100 nm) are suppressed either by uniform collective dynamics of the array (for  $W = 200$  nm) or by coherent precession of CMs of constituent dot (for  $W = 100$  nm), while the intrinsic EMs are modified to BWVMS like modes of the constituent dots. For the smallest dot ( $W = 50$  nm), the intrinsic EM is suppressed by uniform collective mode of the array.

## Bibliography

1. R. Zivieri, F. Montoncello, L. Giovannini, F. Nizzoli, S. Tacchi, M. Madami, G. Gubbiotti, G. Carlotti, and A. O. Adeyeye, *Phys. Rev. B* **83**, 054431 (2011).
2. B. Rana, S. Pal, S. Barman, Y. Fukuma, Y. Otani, and A. Barman, *Appl. Phys. Express* **4**, 113003 (2011).
3. Z. K. Wang, H. S. Lim, V. L. Zhang, J. L. Goh, S. C. Ng, M. H. Kuok, H. L. Su, and S. L. Tang, *Nano Lett.* **6**, 1083 (2006).
4. P. H. Bryant, J. F. Smyth, S. Schultz, and D. R. Fredkin, *Phys. Rev. B* **47**, 11255 (1993).
5. J. Jorzick, S. O. Demokritov, B. Hillebrands, M. Bailleul, C. Fermon, K. Y. Guslienko, A. N. Slavin, D. V. Berkov, and N. L. Gorn, *Phys. Rev. Lett.* **88**, 047204 (2002).
6. J. P. Park, P. Eames, D. M. Engebretson, J. Berezovsky, and P. A. Crowell, *Phys. Rev. Lett.* **89**, 277201 (2002).
7. G. Gubbiotti, M. Conti, G. Carlotti, P. Candeloro, E. D. Fabrizio, K. Y. Guslienko, A. Andre, C. Bayer, and A. N. Slavin, *J. Phys.: Condens. Matter* **16**, 7709 (2004).
8. V. V. Kruglyak, A. Barman, R. J. Hicken, J. R. Childress, and J. A. Katine, *J. Appl. Phys.* **97**, 10A706 (2005).
9. V. V. Kruglyak, A. Barman, R. J. Hicken, J. R. Childress, and J. A. Katine, *Phys. Rev. B* **71**, 220409(R) (2005).
10. M. Bailleul, R. Höllinger, and C. Fermon, *Phys. Rev. B* **73**, 104424 (2006).
11. G. Gubbiotti, M. Madami, S. Tacchi, G. Carlotti, and T. Okuno, *J. Appl. Phys.* **99**, 08C701 (2006).
12. G. Gubbiotti, G. Carlotti, T. Okuno, T. Shinjo, F. Nizzoli, and R. Zivieri, *Phys. Rev. B* **68**, 184409 (2003).
13. P. S. Keatley, V. V. Kruglyak, A. Neudert, E. A. Galaktionov, R. J. Hicken, J. R. Childress, and J. A. Katine, *Phys. Rev. B* **78**, 214412 (2008).
14. V. V. Kruglyak, P. S. Keatley, A. Neudert, R. J. Hicken, J. R. Childress, and J. A. Katine, *Phys. Rev. Lett.* **104**, 027201 (2010).
15. A. Barman and S. Barman, *Phys. Rev. B* **79**, 144415 (2009).

16. A. Barman, S. Wang, J. D. Maas, A. R. Hawkins, S. Kwon, A. Liddle, J. Bokor, and H. Schmidt, *Nano Lett.* **6**, 2939 (2006).
17. A. Barman, S. Wang, J. Maas, A. R. Hawkins, S. Kwon, J. Bokor, A. Liddle, and H. Schmidt, *Appl. Phys. Lett.* **90**, 202504 (2007).
18. J. M. Shaw, T. J. Silva, M. L. Schneider, and R. D. McMichael, *Phys. Rev. B* **79**, 184404 (2009).
19. M. Donahue and D. G. Porter, “OOMMF User’s guide, Version 1.0,” *NIST Interagency Report No. 6376, National Institute of Standard and Technology, Gaithersburg, MD, URL: <http://math.nist.gov/oommf>*, (1999).
20. B. Rana and A. Barman, *SPIN* **3**, 1330001 (2013).
21. L. Guidoni, E. Beaurepaire, and J.-Y. Bigot, *Phys. Rev. Lett.* **89**, 017401 (2002).
22. J.-Y. Bigot, M. Vomir, and E. Beaurepaire, *Nat. Phys.* **5**, 515 (2009).

## CHAPTER 9

---

# Role of Configurational Magnetic Anisotropy in Collective Magnetization Dynamics of $\text{Ni}_{80}\text{Fe}_{20}$ Nanodot Arrays

---

### 9.1 Background

In chapters 6-8, we have mainly addressed the collective magnetization dynamics as a function of the strength of the bias magnetic field, areal density of the array and sizes and shapes of the nanodots. A number of experimental and theoretical studies of magnetization precession in ordered arrays of nanomagnets have revealed various interesting observations including the size dependent precession frequency and damping, collective modes, anisotropic spin wave propagation, dynamic configurational anisotropy and observations of rich spin wave mode structures [1-8]. The collective magnetization dynamics of magnetic nanodot arrays is determined by the interplay between the static and dynamic internal and stray magnetic fields and with the variation of the relative orientation of the bias magnetic field *w.r.t.* the nanodot arrays both the internal fields within the individual elements and the stray fields in an array are expected to vary and result in the variation in the intrinsic and collective spin wave mode structures.

Few reports are found on the effects of the shape and configurational anisotropies upon FMR modes of individual elements [9-10]. However, very few attempts have been made to study the dependence of collective spin wave modes on the relative orientation of the applied bias field and the symmetry of the array [1, 5, 11-12]. It has been shown that the configurational magnetic anisotropy originates from the anisotropic dipole–dipole interaction between magnetically unsaturated parts of the dots. It plays a very important role on the

collective magnetization dynamics of micron or sub-micron size magnetic dots. In Ref. [5] the dominant role of dynamic configurational anisotropy on the collective magnetization dynamics of very thin magnetic dots has been reported.

In this chapter, we present the precessional dynamics of square arrays of square magnetic dots, where the individual dots possess nonuniform magnetic ground states and consequently, a number of resonant modes are observed as the bias field direction is varied from the edge to the diagonal of the dots [13-14]. We investigate how the anisotropy in the spin wave manifold is affected by the strength of the magnetostatic coupling as the arrays undergo transition from a single uniform collective mode to a number of nonuniform collective modes.

## 9.2 Sample Fabrication, Characterization and Measurement Technique

The samples were fabricated by a combination of electron beam evaporation and electron beam lithography. A bilayer PMMA/MMA (polymethyl methacrylate/methyl methacrylate) resist pattern was first prepared on thermally oxidized Si(100) substrate by using electron beam lithography, and the permalloy was deposited on the resist pattern by electron beam evaporation at a base pressure of about  $2 \times 10^{-8}$  Torr. A 10 nm thick SiO<sub>2</sub> capping layer was deposited on top of the permalloy layer to protect the dots from degradation when exposed to the optical pump-probe experiments in air. This is followed by the lifting-off of the sacrificial material and oxygen plasma cleaning of the residual resists that remained even after the lift-off process.

We investigated  $10 \times 10 \mu\text{m}^2$  arrays of square permalloy dots of 200 nm width ( $W$ ), 20 nm thickness ( $t$ ) and with edge-to-edge interelement separation ( $S$ ) of 50 nm and 100 nm. The scanning electron micrographs (Fig. 9.1(a)) show that the dots are of good quality with slightly rounded corners. However, the general nominal features are maintained. The ultrafast magnetization dynamics of the arrays were studied by an all optical time-resolved magneto-optical Kerr effect microscope [14-17]. The samples were pumped by 400 nm laser pulses (pulse width = 100 fs) of about  $15 \text{ mJ/cm}^2$  fluence and the ensuing magnetization dynamics were probed by 800 nm laser pulses (pulse width = 70 fs) of about  $3 \text{ mJ/cm}^2$  fluence. The bias field was tilted at  $15^\circ$  angle from the plane of the sample. The azimuthal angle ( $\phi$ ) of the in-plane component of bias field ( $H_b$ ) is varied and the time-resolved Kerr rotations and

reflectivity were measured at each  $\phi$  value. The geometry of applied bias field is shown on top of the SEM image of the array with  $S = 100$  nm in Fig. 9.1(a). The precessional dynamics appears as an oscillatory signal above the slowly decaying part of the time-resolved Kerr rotation signal after a fast demagnetization within 500 fs, and a fast remagnetization within 10 ps.

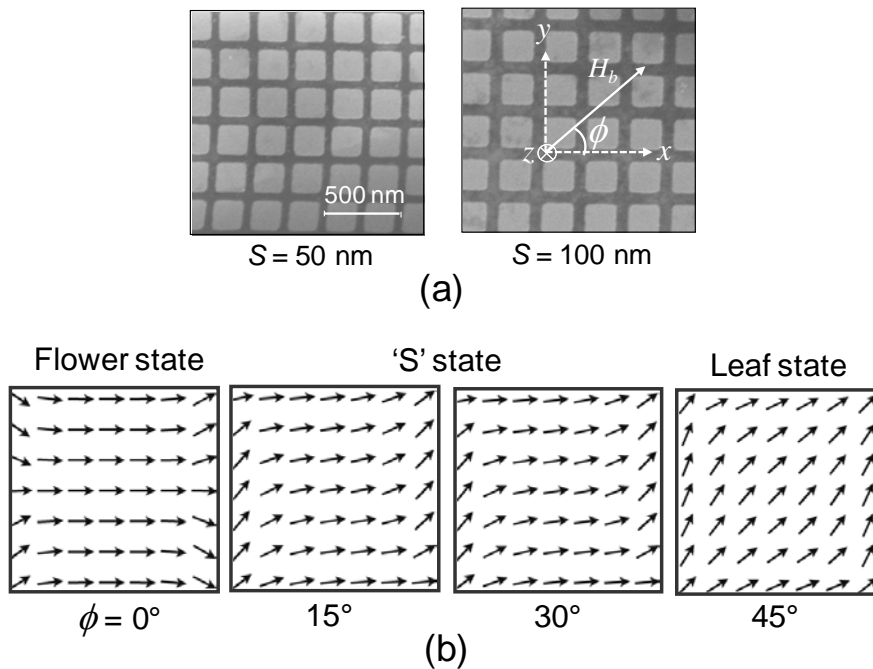


Fig. 9.1: (a) Scanning electron micrographs for arrays of square permalloy dots with size ( $W$ ) = 200 nm and separation ( $S$ ) = 50 nm and 100 nm. The geometry of the applied bias field is shown on top of the SEM image of the array with  $S = 100$  nm. (b) Simulated static magnetization states are shown for a single 200 nm square dot of thickness ( $t$ ) = 20 nm at a bias field ( $H_b$ ) of 1.15 kOe applied at different azimuthal angles ( $\phi$ ).

### 9.3 Static Magnetization Configuration and Magnetostatic Field Profiles as a Function of the Azimuthal Angle of the Bias Magnetic Field

To get an idea on how the internal magnetization states of the individual dots and the magnetostatic stray fields of the arrays vary with the azimuthal angle ( $\phi$ ) of the bias magnetic field, we simulated the static magnetic configurations at different values of the azimuthal angle ( $\phi$ ) of the bias field for a single 200 nm dot and also for arrays of 200 nm dots. The

static magnetic configurations have been calculated by OOMMF software [18] by dividing the samples into cuboidal cells of  $5 \times 5 \times 20 \text{ nm}^3$  volume.

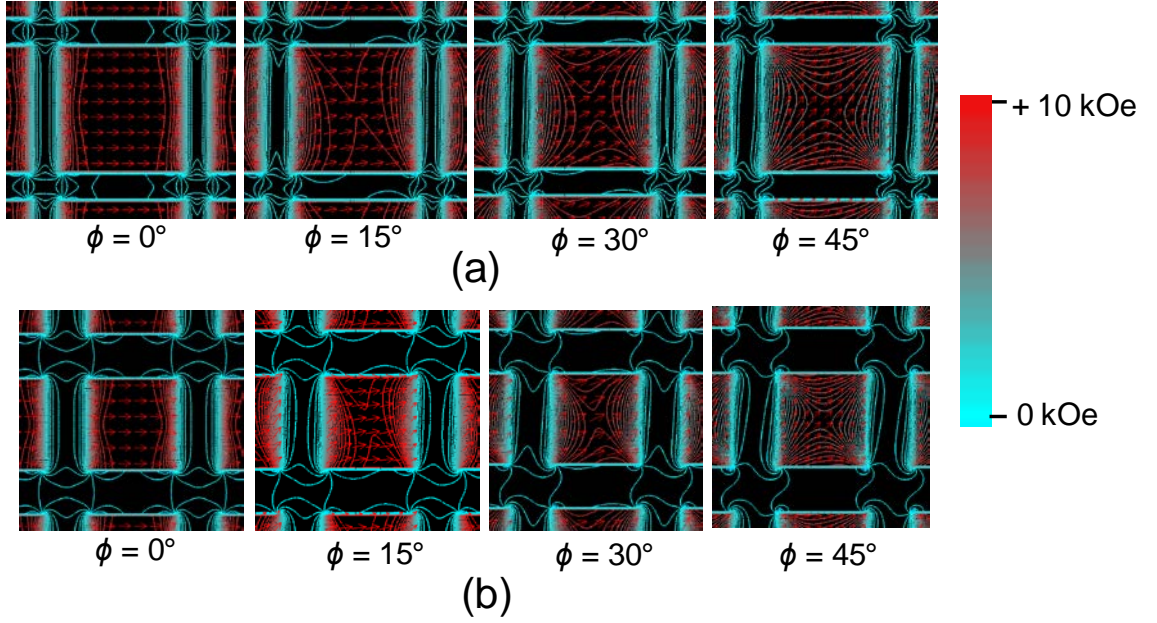


Fig. 9.2: Contour plots of magnetostatic fields at different azimuthal angles ( $\phi$ ) of the in-plane bias field of magnitude  $H_b = 1.15 \text{ kOe}$  for arrays of  $200 \text{ nm}$  square shaped permalloy dots with interdot separations ( $S$ ) of (a)  $50 \text{ nm}$  and (b)  $100 \text{ nm}$ . The arrows inside the dots show the magnetization states of the dots and the colour map as shown in the extreme right side of figure represents the  $x$ -component of the magnetostatic field.

Figure 9.1(b) shows that the static magnetic configuration for a  $200 \text{ nm}$  dot changes from a ‘flower’ state to a ‘leaf’ state via ‘S’ states as the bias field ( $H_b$ ) of magnitude  $1.15 \text{ kOe}$  is rotated from  $\phi = 0^\circ$  to  $45^\circ$ . Magnetostatic field distributions at a bias field value of  $1.15 \text{ kOe}$  were also calculated for  $5 \times 5$  arrays of dots by using LLG micromagnetic simulator [19]. The simulated stray field distributions around the central dot at various values of  $\phi$  are shown in Figs. 9.2(a) and (b). It is observed that the stray field and the internal field profiles change significantly with  $\phi$ . A four-fold anisotropy may be expected to be observed with the variation of  $\phi$  in the dot arrays as a reflection of the combined effects of the four-fold symmetry of the shapes of individual dots and the lattice symmetry of the array.

## 9.4 Results and Discussions

Figures 9.3(a) and (b) show the bi-exponential background subtracted time-resolved Kerr rotations and the corresponding fast Fourier transform (FFT) power spectra from the

array with  $S = 50$  nm at  $H_b = 1.15$  kOe applied at different values of  $\phi$  ( $0^\circ \leq \phi \leq 180^\circ$ , at steps of  $15^\circ$ ). For  $\phi = 0^\circ, 90^\circ$  and  $180^\circ$ , we observe a single uniform collective mode of the array but at the intermediate values of  $\phi$ , we observe a splitting of the single mode into two modes. The frequencies of the modes also vary significantly with  $\phi$ .

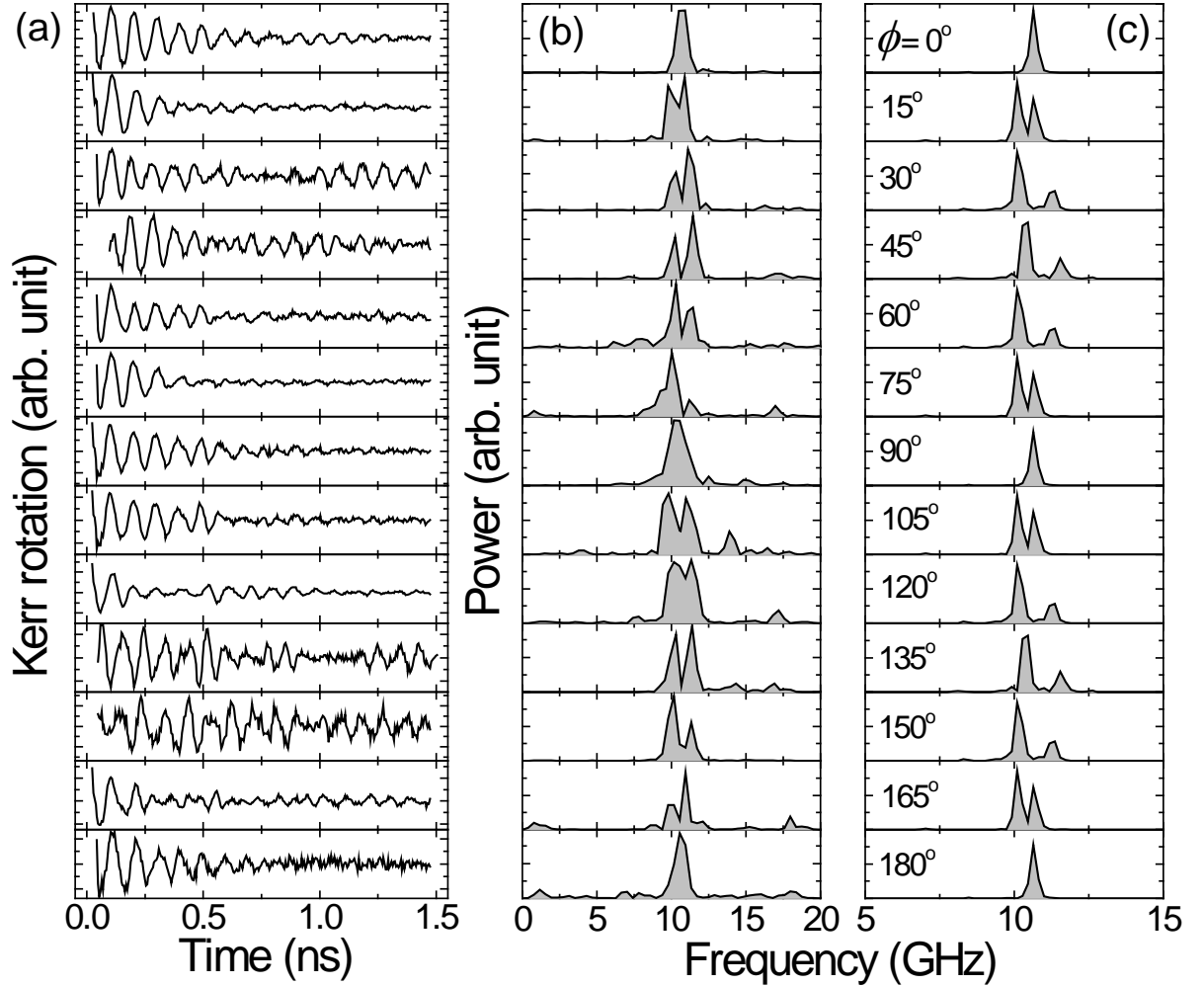


Fig. 9.3: (a) Experimentally measured time-resolved Kerr rotations at  $H_b = 1.15$  kOe applied at different azimuthal angles ( $\phi$ ) and (b) the corresponding FFT power spectra are shown. (c) FFT spectra of the simulated time-domain magnetization obtained from a  $7 \times 7$  array of 200 nm magnetic dots with 50 nm edge-to-edge separation are shown for different values of  $\phi$ .

In Fig. 9.4(a), we have plotted the central frequency of each resonance peak as a function of  $\phi$ . Two well separated branches are visible, where the upper branch is observed for all values of  $\phi$ , whereas the lower branch is missing along the three symmetry axes ( $\phi = 0^\circ, 90^\circ$  and  $180^\circ$ ). A clear four-fold anisotropy is observed in the angular variation of the frequency for both branches with the easy axes at  $\phi = 45^\circ$  and  $135^\circ$  and hard axes at  $\phi = 0^\circ$ ,

90° and 180°. The angular variation of frequency is fitted with Kittel formula after introducing a four-fold anisotropy constant  $K_4$  and assuming zero magnetocrystalline anisotropy ( $K_2$ ) for permalloy [20] (following equation 2.6.34 in chapter 2).

$$f = \frac{\gamma}{2\pi} \left( \left[ H_b - \frac{4K_4}{M} \cos 4\phi \right] \times \left[ H_b + 4\pi M - \frac{K_4}{M} (3 + \cos 4\phi) \right] \right)^{1/2}, \quad (9.4.1)$$

where  $\gamma$  is the gyromagnetic ratio and  $M$  is the effective value of magnetization within the regions where the modes are localized. The upper and lower branches show four-fold anisotropy fields ( $K_4/M$ ) of about 22 Oe and 14 Oe, respectively.

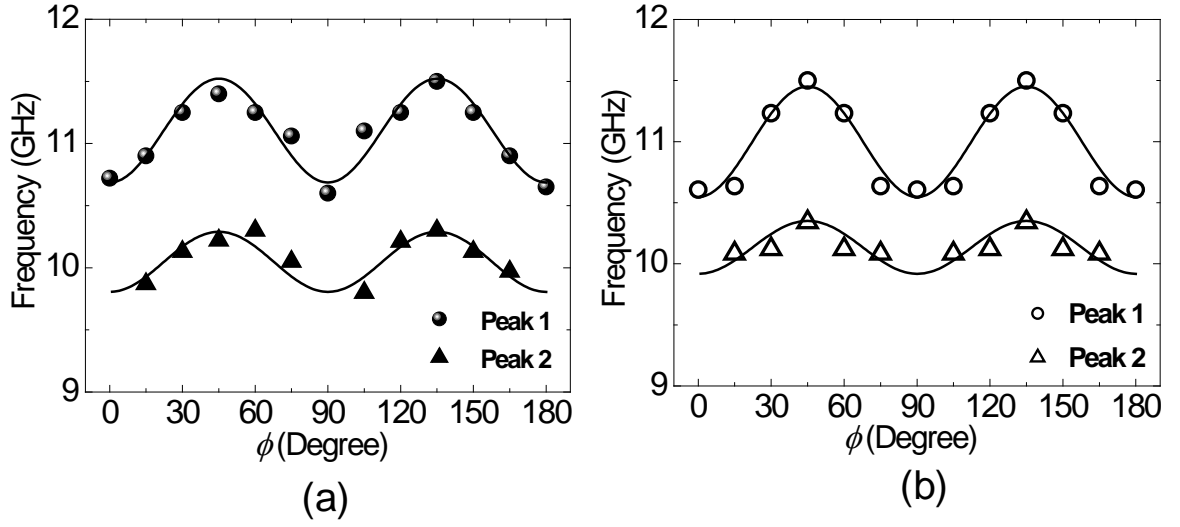


Fig. 9.4: (a) The experimental and (b) simulated resonant mode frequencies for array of 200 nm magnetic dots with  $S = 50$  nm are plotted as a function of the azimuthal angle ( $\phi$ ) of the applied bias field. The solid lines correspond to fit to Eq. 9.4.1.

We have performed micromagnetic simulations by using OOMMF software [18] on arrays of  $7 \times 7$  square permalloy dots with similar dimensions as the experimental samples and by dividing the samples into cuboidal cells of  $5 \times 5 \times 20$  nm<sup>3</sup> volume. The bias field was applied in experimental configurations and a pulsed excitation was given along the  $z$ -direction for the dynamic simulations [21]. In Fig. 9.3(c), FFT power spectra of simulated time-domain magnetization obtained from a  $7 \times 7$  array of 200 nm permalloy dots with  $S = 50$  nm are shown. The simulated spectra reproduce the experimental results qualitatively along with all the key features as described above. The simulated mode frequencies are plotted as a function of  $\phi$  in Fig. 9.4(b), which reproduces the key experimental observations

with the four-fold anisotropy fields ( $K_4/M$ ) of 25 Oe and 13 Oe for the upper and lower branches, respectively.

We have also simulated the angular variation of the magnetization dynamics of a single  $200 \times 200 \text{ nm}^2$  permalloy dot. Figure 9.5(a) shows the plot of its mode frequencies as a function of  $\phi$ . Four distinct branches are observed, out of which branches 2 and 4 show four-fold anisotropy with anisotropy fields ( $K_4/M$ ) of 16 Oe and 8 Oe, respectively, while the other two branches show no clear symmetry. At  $\phi = 0^\circ, 90^\circ$  and  $180^\circ$  two well separated modes are observed, out of which the lower frequency mode is clearly suppressed in the array with  $S = 50 \text{ nm}$ . At  $45^\circ$  and  $135^\circ$ , two modes are again observed. At intermediate values of  $\phi$ , we observe four modes for the single dots but in the arrays two of those modes disappear, while two other modes are modified.

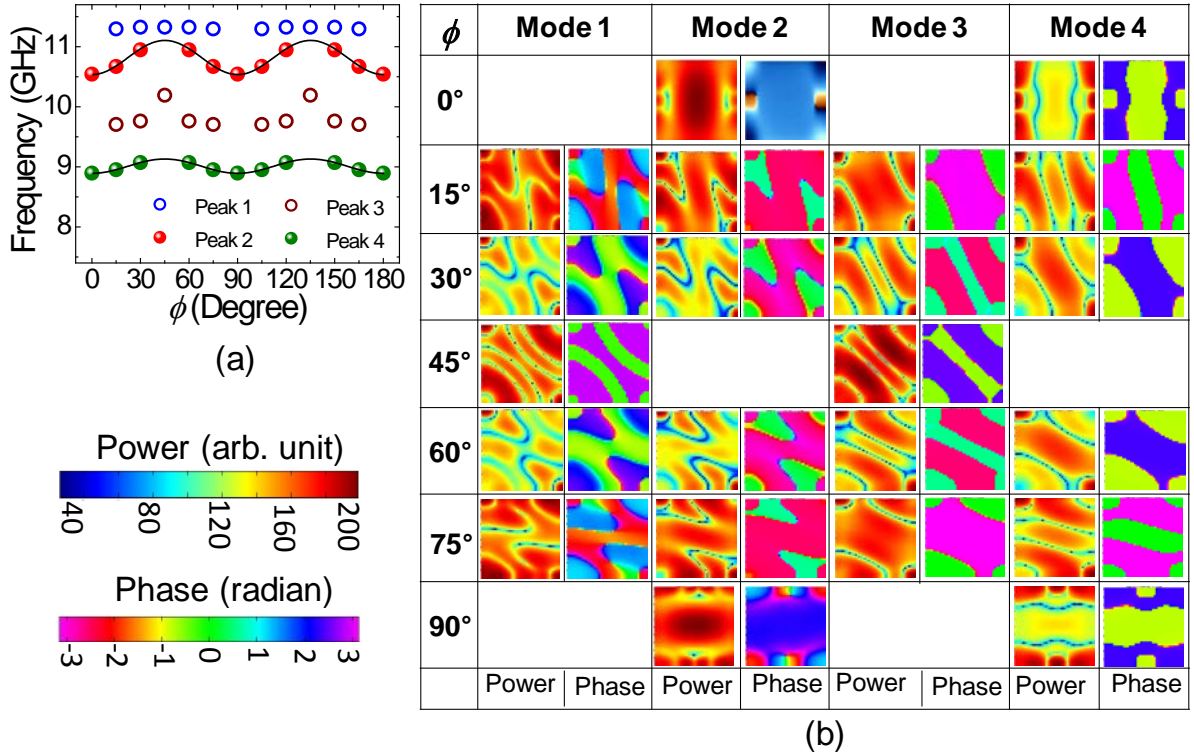


Fig. 9.5: (a) Simulated precession frequencies as a function of the azimuthal angle ( $\phi$ ) of the applied bias field and fit to Eq. 9.4.1 (solid lines) are shown for a single square permalloy dot with width = 200 nm and thickness = 20 nm. (b) The simulated power and phase profiles of the resonant modes are shown. The azimuthal angle  $\phi$  is shown in the first column.

We have further simulated the power and phase maps of each resonant mode for both the single 200 nm dot (Fig. 9.5(b)) and for the array with  $S = 50 \text{ nm}$  (Fig. 9.6). We

concentrated on the  $3 \times 3$  dots at the centre of the array, which experience almost uniform magnetostatic environment. At  $\phi = 0^\circ$ , the two modes are the centre mode (CM) and mixed edge mode – Damon Eshbach (EM-DE) mode of the single dot and clearly the EM-DE mode is suppressed in this array due to the strong magnetostatic fields from the neighbouring elements. When the bias field is applied along directions between two edges of the elements, a mixture of backward volume magnetostatic (BWVMS) and DE modes with different mode numbers (mixed modes) are observed. At the intermediate angles ( $15^\circ$  and  $30^\circ$ ), modes 1 and 4 are completely suppressed, while modes 2 and 3 are modified due to the interelement interaction in the array. However, for  $\phi = 45^\circ$ , both the modes remain intact with slight modification in their frequencies. Hence, the collective dynamics is almost non-existent for  $\phi = 45^\circ$  although it appears with varying extents for  $0^\circ \leq \phi < 45^\circ$  in arrays with  $S = 50$  nm.

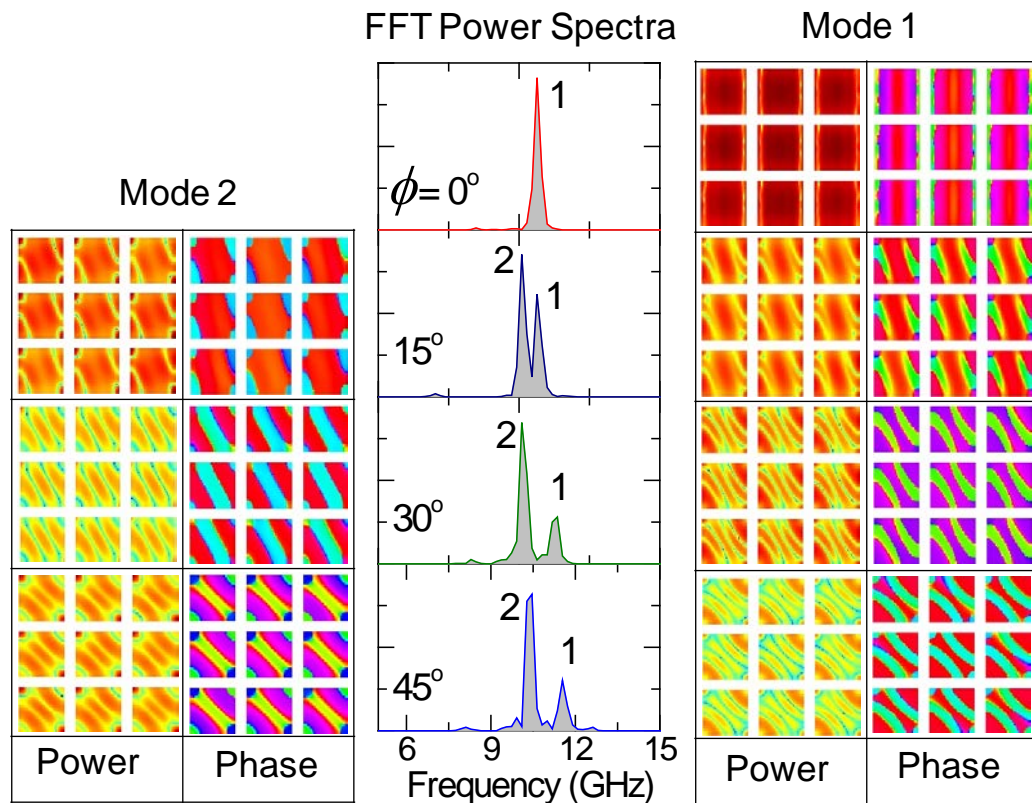


Fig. 9.6: Power and phase distributions of the resonant modes for an array of 200 nm square permalloy dots with 50 nm interdot separation are shown (extreme left and extreme right columns) along with the FFT power spectra (middle column) for four different values of  $\phi$ . The scales of the colour maps are same as in Fig. 9.5.

We have also simulated the angular variation of the resonant modes for array with  $S = 100$  nm. Figure 9.7(a) shows the plot of resonant mode frequencies as a function of  $\phi$ . Two

branches of frequencies showing clear four-fold anisotropy are again observed. Few other modes are also observed in between the two branches but those modes do not show any clear four-fold symmetry. We have fitted branches 1 and 2 with Eq. 9.4.1. From the fittings, the four-fold anisotropy field ( $K_4/M$ ) values come out to be 22 Oe and 25 Oe for branch 1 and 2, respectively. Figure 9.7(b) shows the power and phase profiles of the simulated modes. At  $\phi = 0^\circ$ , three modes are observed. Mode 1 is the CM, mode 2 is the BWVMS-like mode and mode 3 is the mixed mode (EM-DE) of individual dots. However, at  $\phi = 15^\circ$  two mixed modes are observed. The power profiles of mode 1 and mode 2 of the array looks identical to the power profiles of mode 2 and mode 4 of the single dot. For  $\phi = 30^\circ$ , three mixed modes are observed, while for  $\phi = 45^\circ$ , again two mixed modes are observed where the mode profiles of constituent dots look identical to those of the single dot. The EM is absent for  $\phi = 15^\circ, 30^\circ$  and  $45^\circ$ . Although, there is a common observation of non-collective dynamics for  $\phi = 45^\circ$  for both  $S = 50$  nm and 100 nm, in the former case the transition from strongly collective regime ( $\phi = 0^\circ$ ) to non-collective regime ( $\phi = 45^\circ$ ) occurs gradually, while in the latter case no clear trend is observed.

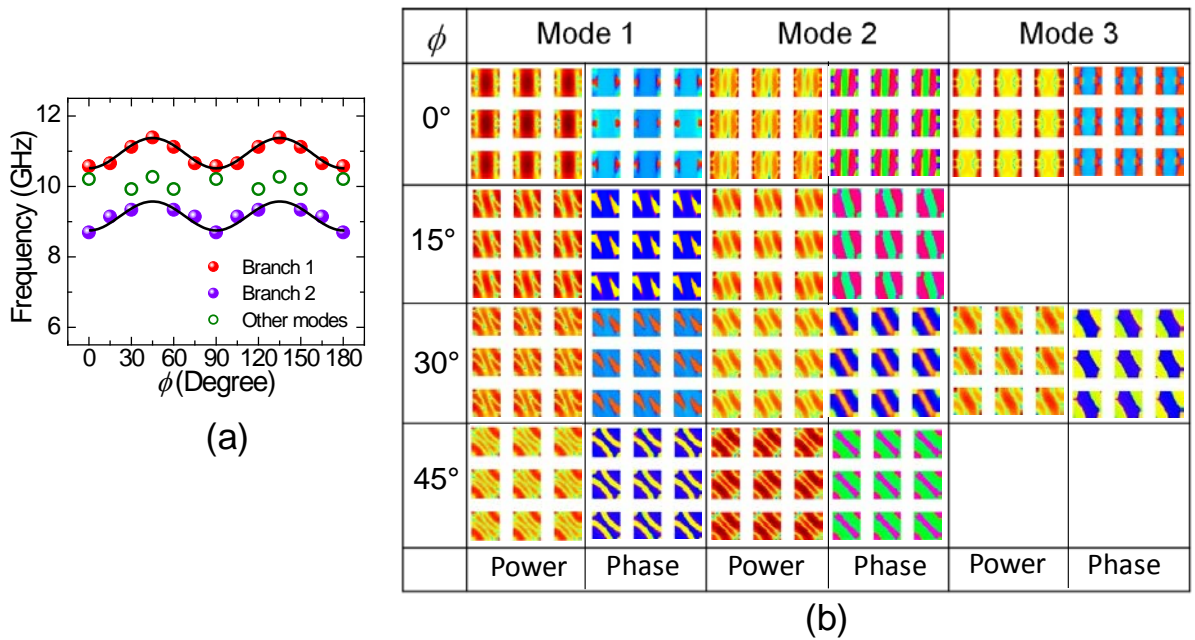


Fig. 9.7: (a) Simulated resonant mode frequencies for array of 200 nm square dots with 100 nm interdot separation are plotted as a function of the azimuthal angle ( $\phi$ ) of the bias field. (b) Power and phase distributions of the simulated modes are shown for four different values of  $\phi$ . The scales of the colour maps are same to those in Fig. 9.5.

## 9.5 Summary

In summary, we have studied the dependence of the collective modes on the azimuthal angle ( $\phi$ ) of the bias magnetic field in arrays of permalloy dots with 200 nm dot width, 20 nm thickness and with interelement separations ( $S$ ) of 50 nm and 100 nm. Experimental measurements and simulations show a uniform collective mode for  $S = 50$  nm and transition to a nonuniform collective regime at  $S = 100$  nm with the splitting of the main resonant mode. For  $S = 50$  nm, a gradual transition from uniform collective regime to a non-collective regime occurs as  $\phi$  changes from  $0^\circ$  to  $45^\circ$ . Consequently, two different branches of resonant frequencies are observed. Each frequency branch shows a four-fold configurational anisotropy coming from the shape anisotropy of constituent dots of array and the four-fold anisotropy in the lattice arrangement of array. In the weakly collective regime ( $S = 100$  nm), although the dynamics at  $\phi = 45^\circ$  is non-collective similar to that for  $S = 50$  nm, transition from  $0^\circ$  to  $45^\circ$  does not follow a clear pattern. The observed variation in the intrinsic and collective dynamics with the azimuthal angle is attributed due to the variation of internal magnetic configuration of individual dot as well as the variation of the stray field profiles among the dots with the azimuthal angle.

## Bibliography

1. S. Jung, B. Watkins, L. DeLong, J. B. Ketterson, and V. Chandrasekhar, *Phys. Rev. B* **66**, 132401 (2002).
2. V. V. Kruglyak, A. Barman, R. J. Hicken, J. R. Childress, and J. A. Katine, *Phys. Rev. B* **71**, 220409(R) (2005).
3. G. Gubbiotti, M. Madami, S. Tacchi, G. Carlotti, and T. Okuno, *J. Appl. Phys.* **99**, 08C701 (2006).
4. Z. K. Wang, H. S. Lim, V. L. Zhang, J. L. Goh, S. C. Ng, M. H. Kuok, H. L. Su, and S. L. Tang, *Nano Lett.* **6**, 1083 (2006).
5. V. V. Kruglyak, P. S. Keatley, R. J. Hicken, J. R. Childress, and J. A. Katine, *Phys. Rev. B* **75**, 024407 (2007).
6. A. Barman and S. Barman, *Phys. Rev. B* **79**, 144415 (2009).
7. V. V. Kruglyak, P. S. Keatley, A. Neudert, R. J. Hicken, J. R. Childress, and J. A. Katine, *Phys. Rev. Lett.* **104**, 027201 (2010).
8. S. Tacchi, M. Madami, G. Gubbiotti, G. Carlotti, H. Tanigawa, T. Ono, and M. P. Kostylev, *Phys. Rev. B* **82**, 024401 (2010).
9. Y. Zhai, J. Shi, X. Y. Zhang, L. Shi, Y. X. Xu, H. B. Huang, Z. H. Lu, and H. R. Zhai, *J. Phys.: Condens. Matter* **14**, 7865 (2002).
10. M. Pardavi-Horvath, C. A. Ross, and R. D. McMichael, *IEEE Trans. Magn.* **41**, 3601 (2005).
11. C. Mathieu, C. Hartmann, M. Bauer, O. Buettner, S. Riedling, B. Roos, S. O. Demokritov, B. Hillebrands, B. Bartenlian, C. Chappert, D. Decanini, F. Rousseaux, E. Cambril, A. Muller, B. Hoffmann, and U. Hartmann, *Appl. Phys. Lett.* **70**, 2912 (1997).
12. G. N. Kakazei, P. E. Wigen, K. Y. Guslienko, R. W. Chantrell, N. A. Lesnik, V. Metlushko, H. Shima, K. Fukamichi, Y. Otani, and V. Novosad, *J. Appl. Phys.* **93**, 8418 (2003).
13. B. Rana, D. Kumar, S. Barman, S. Pal, R. Mandal, Y. Fukuma, Y. Otani, S. Sugimoto, and A. Barman, *J. Appl. Phys.* **111**, 07D503 (2012).
14. B. Rana and A. Barman, *SPIN* **3**, 1330001 (2013).

15. S. Pal, B. Rana, O. Hellwig, T. Thomson, and A. Barman, *Appl. Phys. Lett.* **98**, 082501 (2011).
16. B. Rana, D. Kumar, S. Barman, S. Pal, Y. Fukuma, Y. Otani, and A. Barman, *ACS Nano* **5**, 9559 (2011).
17. S. Saha, R. Mandal, S. Barman, D. Kumar, B. Rana, Y. Fukuma, S. Sugimoto, Y. Otani, and A. Barman, *Adv. Funct. Mater.* **23**, 2378 (2013).
18. M. Donahue and D. G. Porter, "OOMMF User's guide, Version 1.0," *NIST Interagency Report No. 6376, National Institute of Standard and Technology, Gaithersburg, MD, URL: <http://math.nist.gov/oommf>*, (1999).
19. M. R. Scheinfein, "LLG Micromagnetic Simulator," <http://llgmicro.home.mindspring.com/>, (1997).
20. A. Barman, V. V. Kruglyak, R. J. Hicken, A. Kundrotaite, and M. Rahman, *Appl. Phys. Lett.* **82**, 3065 (2003).
21. A. Barman and R. C. Sharma, *J. Appl. Phys.* **102**, 053912 (2007).

## CHAPTER 10

---

# Quasistatic Magnetization Reversal Dynamics of Ni Nanoparticles

---

### 10.1 Background

The magnetic nanoparticles have profound importance like other magnetic nanostructures due to their potential applications in magnetic data storage [1], biomedicine and biotechnology [2-3], magnetic resonance imaging [4], catalysis [5] and magnetic fluids [6]. Ordered arrays of single domain magnetic nanoparticles assembled on a substrate would be ideal for most of the device applications so that the magnetization states of the individual elements in the array could be addressed [7]. However, nanoparticles tend to form agglomerates to reduce their surface to volume ratio and the associated free energies [8]. For magnetic nanoparticles, minimization of magnetic energy is an additional parameter, which helps the formation of chains and clusters of nanoparticles coupled by exchange and dipolar interactions [9-10]. The geometry of the coupled nanoparticles may be manipulated to various two-dimensional and three-dimensional patterns by using magnetic interactions or by an external magnetic field [11-13].

The knowledge of magnetization reversal processes of magnetic nanoparticles is important for their applications in devices. To this end some efforts have been made on the theoretical and experimental understanding of the quasistatic and the ultrafast magnetization reversal of isolated magnetic nanoparticles and their ensembles [14-19]. In the quasistatic regime, recent reports have shown the magnetization reversal through the internal spin waves in relatively large nanoparticles [14], an angular dependence of switching field due to higher order anisotropy [15], effect of exchange biasing in magnetization reversal and thermal stability in magnetic nanoparticles [16], coherent magnetization reversal of magnetic

nanoparticles with magnetocrystalline and shape anisotropies [20] and the influence of surface anisotropy on the magnetization reversal with ellipsoidal shape [21]. In the ultrafast regime, the intrinsic magnetization reversal and dynamics of single magnetic nanoparticles have been demonstrated by an rf field driven nonlinear resonance [17] or by direct optical pumping [18]. Further theoretical work [19] predicts ballistic magnetization reversal by ultrashort magnetic field pulse. Further, magnetization reversal mechanisms of single hexagonal shaped magnetic platelets [22-23] and assemble of platelets [24] have been reported.

Most of the experimental studies of magnetization reversal of magnetic nanoparticles measure an ensemble of clusters and chains of nanoparticles. Ensembles of particles interacting by exchange energy are known as interaction domains [25] and collective magnetization reversal of such interacting nanomagnets has been a topic of interest [26]. In addition, magnetic logic operations have been demonstrated in exchange-coupled patterned nanomagnets [27]. Experimental results from Co and Fe nanoclusters with sub-10 nm individual particles [28-29] have shown the formation of a correlated superspin glass resulting from the frustration between the interparticle exchange interaction and the randomly oriented intraparticle anisotropy. In densely packed ensembles of magnetically interacting nanoparticles, which would have been individually superparamagnetic, the interactions may lead to an ordered magnetic phase, the so-called superferromagnetic state. This has recently been demonstrated experimentally by X-ray photoemission electron microscopy and magneto-optical Kerr microscopy [30].

However, the detailed magnetization reversal mechanisms of magnetic nanoclusters and nanochains of various geometries have not been studied in detail before. The complicated geometries of such systems offer greater challenge to the interpretation of the experimental data. In this chapter, we present the experimental and micromagnetic simulation studies of magnetization reversal of chains and clusters of single domain Ni nanoparticles of various geometries. We investigate the role of various local magnetic configurations taken by the above systems during the reversal in obtaining the shapes of the magnetic hysteresis loops.

## 10.2 Magnetization Reversal in Clusters of Ni Nanoparticles

### 10.2.1 Sample Preparation and Characterization

Ni nanoparticles were prepared by the reduction of nickel chloride ( $\text{NiCl}_2 \cdot 6\text{H}_2\text{O}$ ) by hydrazine hydrate ( $\text{N}_2\text{H}_5\text{OH}$ ) in presence of sodium hydroxide ( $\text{NaOH}$ ).  $\text{NiCl}_2$  solutions in ethylene glycol of three different molar concentrations (A = 30 mM, B = 45 mM, and C = 60 mM) were mixed with equal volumes of  $\text{N}_2\text{H}_5\text{OH}$  (80%) solution at a fixed molar concentration ratio of 20 of  $\text{N}_2\text{H}_5\text{OH}$  with  $\text{NiCl}_2$ . Then 0.1 M  $\text{NaOH}$  was added to the solution at 70–80  $\mu\text{l/ml}$  and the solution was stirred at about  $80^\circ\text{C}$  temperature. The  $\text{pH}$  of the final solution was always maintained at about 10.0, and after 1 h of stirring the solution turns gray black due to the formation of Ni nanoparticles. The solution was then cooled, washed with ethanol and distilled water for several times, and dried at room temperature to collect the nanoparticles in the powder form.

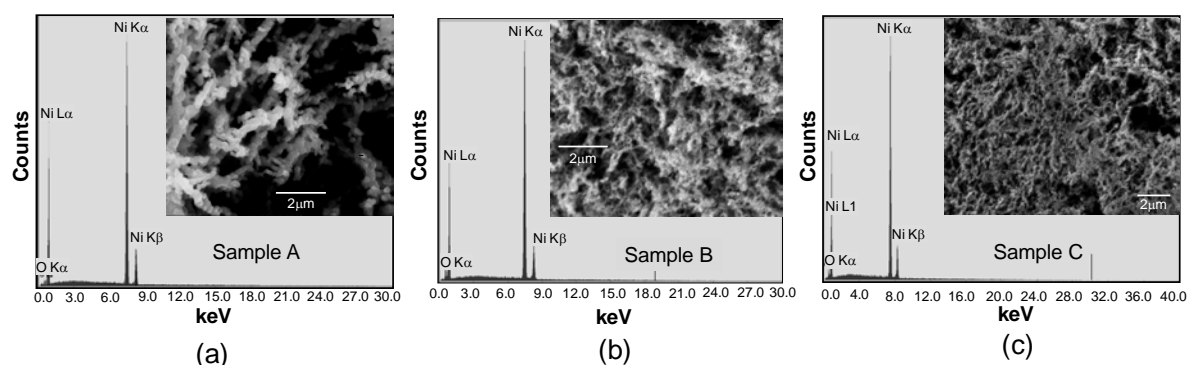


Fig. 10.1: The EDX spectra obtained from Ni nanoparticles samples [(a) sample A, (b) sample B and (c) sample C] are shown. The corresponding scanning electron micrographs are shown in the inset.

The microstructure and composition of the nanoparticles were investigated by using scanning electron microscope (SEM), X-ray diffraction (XRD) and energy dispersive X-ray (EDX) spectrometer. Figures 10.1(a), (b) and (c) show the EDX spectra of samples A, B and C and their corresponding scanning electron micrographs at the inset. The EDX spectra show a little trace of oxygen apart from the Ni peaks, which confirms the elemental purity of Ni with a slight oxidation of the surface layer. The scanning electron micrographs show that the nanoparticles form clusters and chains with branching in arbitrary directions in all three samples. The constituent nanoparticles in the clusters have somewhat spherical shape with diameter between 40 and 50 nm for samples B and C and about 200 nm in sample A. In addition, sample A is less agglomerated and has a better spherical structure. Such variation in

size and clustering is related to the slight variation in the preparation condition and the formation of Ni-hydrazine complex for sample A [31]. Figure 10.2(a) shows the XRD patterns from all three samples. The XRD pattern of the Ni nanoparticles with  $\text{CuK}_\alpha$  radiation ( $\lambda = 0.154 \text{ nm}$ ) shows the characteristic peaks for Ni at the  $2\theta$  values of  $44.5^\circ$ ,  $51.8^\circ$  and  $76.4^\circ$  correspond to (111), (200) and (220) crystal planes. It reveals that the synthesized Ni has face centered cubic (*fcc*) structure with a lattice parameter of 0.352 nm. By using the Debye–Scherrer formula, we obtained the crystallite size of about 15 – 20 nm for all three samples.

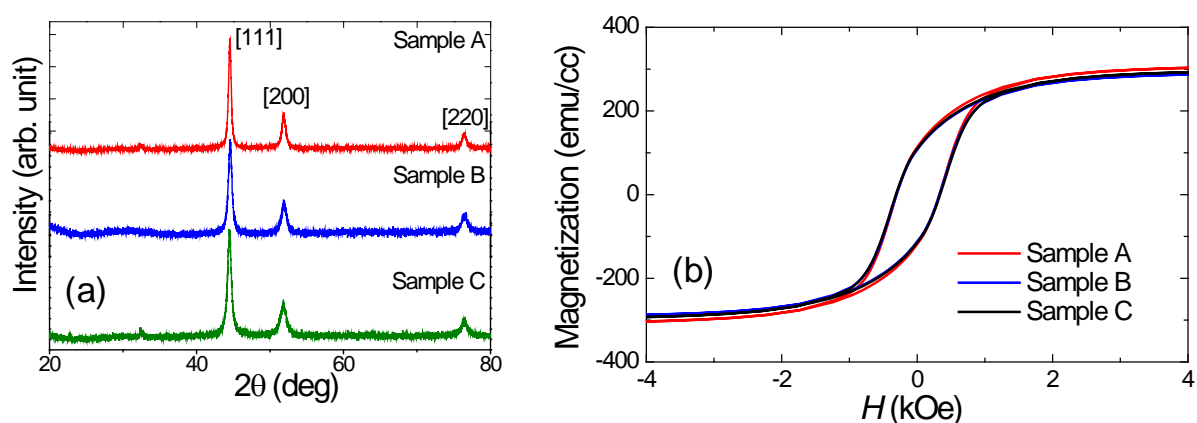


Fig. 10.2: (a) The XRD patterns from all three samples are shown. (b) The experimental results of magnetization ( $M$ ) vs applied magnetic field ( $H$ ) data are shown for all three samples.

## 10.2.2 Results and Discussions

The magnetization ( $M$ ) vs the applied magnetic field ( $H$ ) was measured at room temperature (300 K) by using vibrating sample magnetometer (VSM). The experimental  $M$ - $H$  data obtained from three samples are very similar with slight variation in the saturation magnetization ( $M_S$ ) and the coercive field ( $H_C$ ) values (Fig. 10.2(b)) [32]. The observed  $M_S$  is about 300 emu/cc as compared to the bulk value of 484 emu/cc and  $H_C$  is about 320 Oe as compared to the bulk value of  $< 1$  Oe. The reduction in  $M_S$  is probably due to the surface oxidation and random surface spins, while the increase in  $H_C$  is primarily due to the shape anisotropy of the nanoparticles associated with the demagnetizing field. Since sample A has much larger particle size as compared to samples B and C, a discernible difference in magnetization reversal behaviour is expected. However, the observed similarity suggests that the reversal behaviour of the cluster as a whole is more dominant than that of the constituent particles.

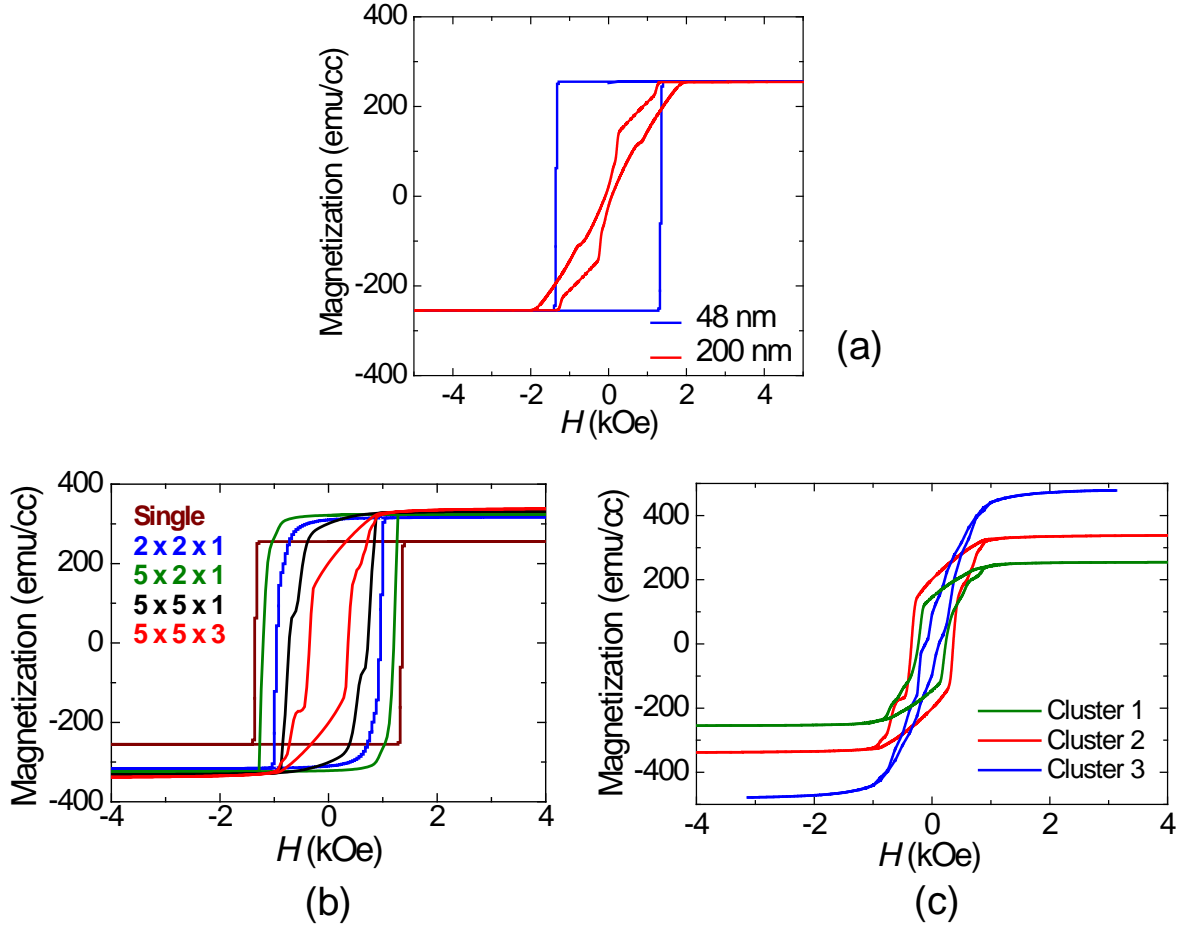


Fig. 10.3: (a) The simulated  $M$ - $H$  curves are shown for single Ni nanoparticles of 48 nm and 200 nm diameters. (b) The simulated  $M$ - $H$  loops with increasing number of overlapped (10%) particles in cluster. (c) The simulated  $M$ - $H$  loops for three different clusters (cluster 1, cluster 2 and cluster 3) composed of  $5 \times 5 \times 3$  particles.

In order to understand the reversal mechanism for the clusters of nanoparticles, we have performed micromagnetic simulations using both finite difference and finite element analyses using public domain softwares OOMMF [33] and NMAG [34]. We tested both OOMMF and NMAG for standard problems and obtained similar results but the application of NMAG is essential for random clusters of nanoparticles. We have simulated single spherical nanoparticles of 48 and 200 nm diameters and also clusters of various geometry formed of above particles. The periodic clusters of non-overlapped (cluster 1) and overlapped (10% of the radii) (cluster 2) particles were studied. In addition, clusters of randomly oriented nanoparticles with variable overlap between 0% and 80% of the radii (cluster 3) were also studied by using NMAG. The samples were divided into cuboidal cells with size down to  $2 \times 2 \times 2 \text{ nm}^3$  for OOMMF simulations and tetrahedral cells with dimensions  $< 2 \text{ nm}$  for NMAG simulations. The  $M$ - $H$  data were computed by first slowly increasing the field from zero to +

5 kOe (above saturation) and then by varying the field between + 5 and - 5 kOe in steps of 40 Oe to complete a full cycle. The  $M$ - $H$  data averaged over the whole sample and spatial magnetization images at different field values were computed. For a single particle with 48 nm diameter, a square hysteresis loop is observed with  $H_C > 1.3$  kOe and  $M_S \sim 250$  emu/ cc, but for the 200 nm particle the shape of the  $M$ - $H$  loop is different with the signature of vortex formation and annihilation, although  $M_S$  is still  $\sim 250$  emu/cc (Fig. 10.3(a)). The simulated  $M$ - $H$  curves for single nanoparticles are largely different from the experimental observations. Simulations of periodic clusters of nanoparticles show a gradual decrease in  $H_C$  with the increase in the number of nanoparticles (Fig. 10.3(b)), and for a cluster of minimum  $5 \times 5 \times 3$  particles, the loop shape is similar to the experimental observation. For cluster 1,  $M_S$  is about 250 emu/cc and is much below the experimental value (300 emu/cc), while for cluster 2,  $M_S$  (330 emu/cc) is little higher than the experimental value (Fig. 10.3(c)). Comparison of experimental and simulation results show that there must be a finite overlap between the nanoparticles, and hence the nanoparticles in the experimental samples are both exchange and magnetostatically coupled.

The simulated magnetization images during the reversal for the single particles and clusters are shown in Fig. 10.4. The 48 nm single particle (Fig. 10.4(a)) reverses by a coherent rotation of magnetization at  $H_C = 1.3$  kOe. The 200 nm single particle (Fig. 10.4(b)) reverses through the formation of a vortex like state. The vortex core and the spins at the equator of the sphere remain parallel to the earlier field direction but the rest of the spins helically rotate from north- to south-pole of the sphere towards the reversed field. This is followed by the reversal of the equator spins and finally the core spins and we observe a fully reversed magnetization state. Figure 10.4(c) shows the reversal mechanism for cluster 2 with  $5 \times 5 \times 3$  particles. As the applied field is reduced from positive saturation, the collective magnetization of the cluster first shows the formation of a C-like state followed by a multi domain state. After this, a vortex-like state appears at one end of the cluster and slowly moves toward the other end with further reduction in field and finally moves out of the cluster and an inverted C-like state appears. This is followed by a flower-like state and, finally, saturated magnetic states for all particles in the cluster.

Although cluster 2 reproduces the experimental  $M$ - $H$  curves quite well, we have also simulated a cluster of randomly arranged nanoparticles to mimic the SEM image. We allowed arbitrary amount of overlap from 0% to 80% but having identical individual dimensions and total number of the particles for this geometry (cluster 3). The simulated hysteresis loop for

cluster 3, as shown in Fig. 10.3(c), has  $H_C \sim 100$  Oe and  $M_S \sim 470$  emu/cc. These values are much different from the experimental results and are closer to values for bulk Ni. The reversal mechanism for cluster 3 is incoherent but shows the indication of formation and annihilation of vortices in the cluster. However, the various other well defined domain states observed for cluster 2 are not observed in this case. The observation of nearly bulk like  $M_S$  and small  $H_C$  values suggests that the assumptions of totally random arrangements and arbitrary amount of overlap of nanoparticles in agglomerated clusters are not correct. Instead, the particles may be partially overlapped, which gives rise to finite amount of exchange coupling between the nanoparticles and consequently larger  $M_S$  than single and non-overlapped ensembles of nanoparticles. In addition, the experimentally obtained  $H_C$  is closer to cluster 2 than cluster 3, which suggests that the clusters in the experimental samples have finite amount of ordering.

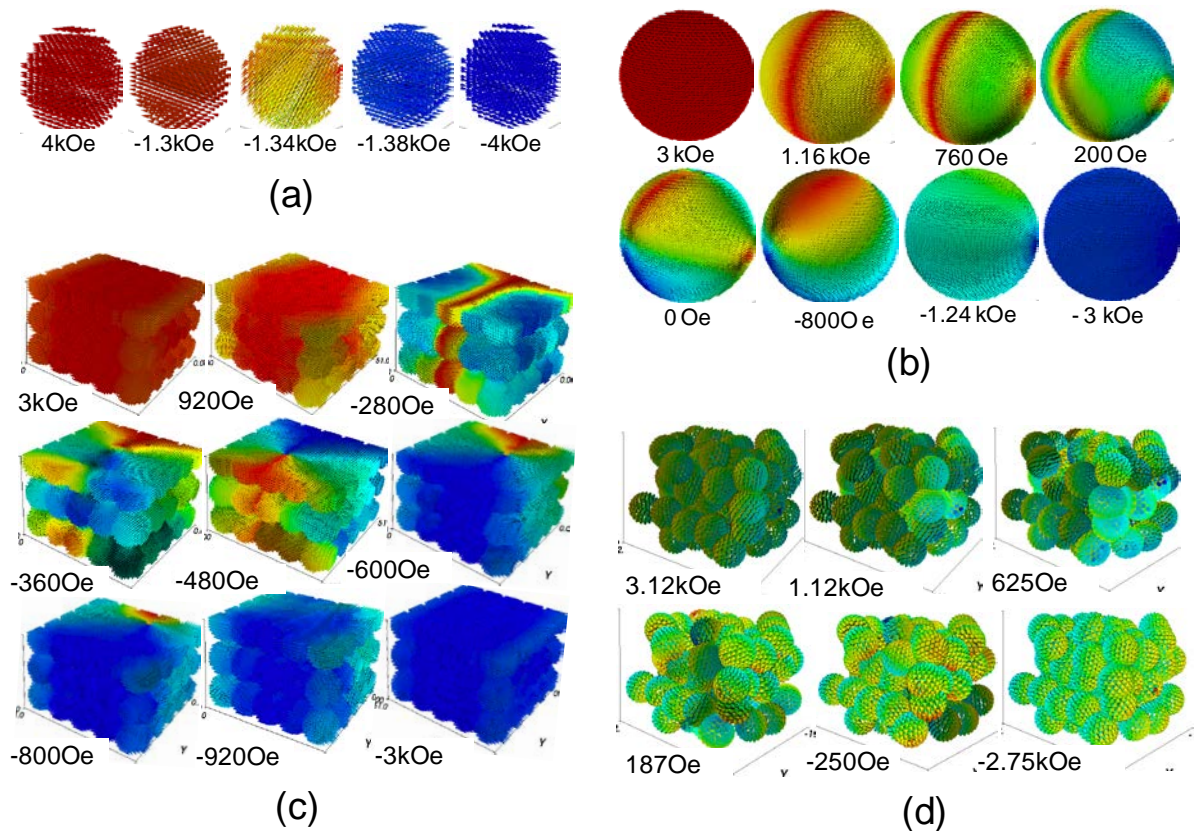


Fig. 10.4: Simulated magnetization images at various applied magnetic field ( $H$ ) values for (a) 48 nm single spherical particle, (b) 200 nm single spherical particle, (c) periodic cluster of  $5 \times 5 \times 3$  particles (cluster 2) and (d) random cluster of 75 particles (cluster 3). The constituent particles are spherical with 48 nm in diameter.

## 10.3 Magnetization Reversal of Ni Nanoparticles Assembled in Different Geometries

### 10.3.1 Sample Preparation and Characterization

Ni nanoparticles coated with polyethylenimine (PEI) ( $S_1$ ,  $S_2$  and  $S_3$ ) and in uncoated form ( $S_4$ ) were prepared by the chemical reduction of nickel chloride ( $\text{NiCl}_2 \cdot 6\text{H}_2\text{O}$ ) by hydrazine hydrate ( $\text{N}_2\text{H}_5\text{OH}$ ) in the presence of sodium hydroxide ( $\text{NaOH}$ ), which acts as a catalyst [35].  $\text{NiCl}_2$  solutions of various molar concentrations ( $S_1$  and  $S_2$ : 5 mM;  $S_3$ : 64 mM; and  $S_4$ : 45 mM) in ethylene glycol were mixed with equal volumes of  $\text{N}_2\text{H}_5\text{OH}$  (80%) solution after keeping the molar concentration ratio of  $\text{N}_2\text{H}_5\text{OH}$  to  $\text{NiCl}_2$  at 20. After that 0.1 M  $\text{NaOH}$  was added to the solution at 70-80  $\mu\text{L}/\text{mL}$ , and the solution was stirred at about 80°C. The  $\text{pH}$  of the final solution was maintained at about 10.0 and after 45 to 60 min of stirring the solution turns gray black due to the formation of Ni nanoparticles. The solution was then cooled to room temperature, washed with ethanol and distilled water for several times and dried to collect the uncoated nanoparticles in the powder form. To prepare nanoparticles coated with PEI, when the solution turns gray black, it was immediately cooled in an ice bath at 0°C, and PEI (0.4 wt% for  $S_1$ ; 1 wt% for  $S_2$ ; and 4.5 wt% for  $S_3$ ) was added to the solution. The solution was thermostated in an ultrasonic bath at 25°C and was finally magnetically recovered after 0.5 h. A magnetic field of about 250 Oe was applied during the synthesis to assist the magnetic interactions between the particles during growth.

The microstructure and composition of the nanoparticles were investigated by using SEM, XRD and EDX spectrometer. Figure 10.5(a) shows the typical scanning electron micrographs from four different samples ( $S_1$ ,  $S_2$ ,  $S_3$  and  $S_4$ ) showing the formation of chains and clusters of different configurations.  $S_1$  shows long chains with a single particle along the width of the chain with negligible branching, while  $S_2$  shows broad chains formed of a number of particles along the width.  $S_3$  shows shorter chains with plenty of ‘X’- and ‘Y’-like branching and  $S_4$  shows largely random arrangement of the particles with no preferred shape. However, the average size of the constituent particles is about 50 nm in all four samples.

Figure 10.5(b) shows the EDX spectra from  $S_1$ , demonstrating the chemical purity of the Ni nanoparticles with very little (< 1%) oxidation. Figure 10.5(c) shows the XRD data from  $S_1$ , which shows the characteristic peaks from *fcc* Ni crystals. By using the Debye–Scherrer formula we obtain the crystallite size of about 10–15 nm, which shows the

polycrystalline nature of the Ni nanoparticles. Similar results from EDX and XRD were obtained for the other three samples (not shown).

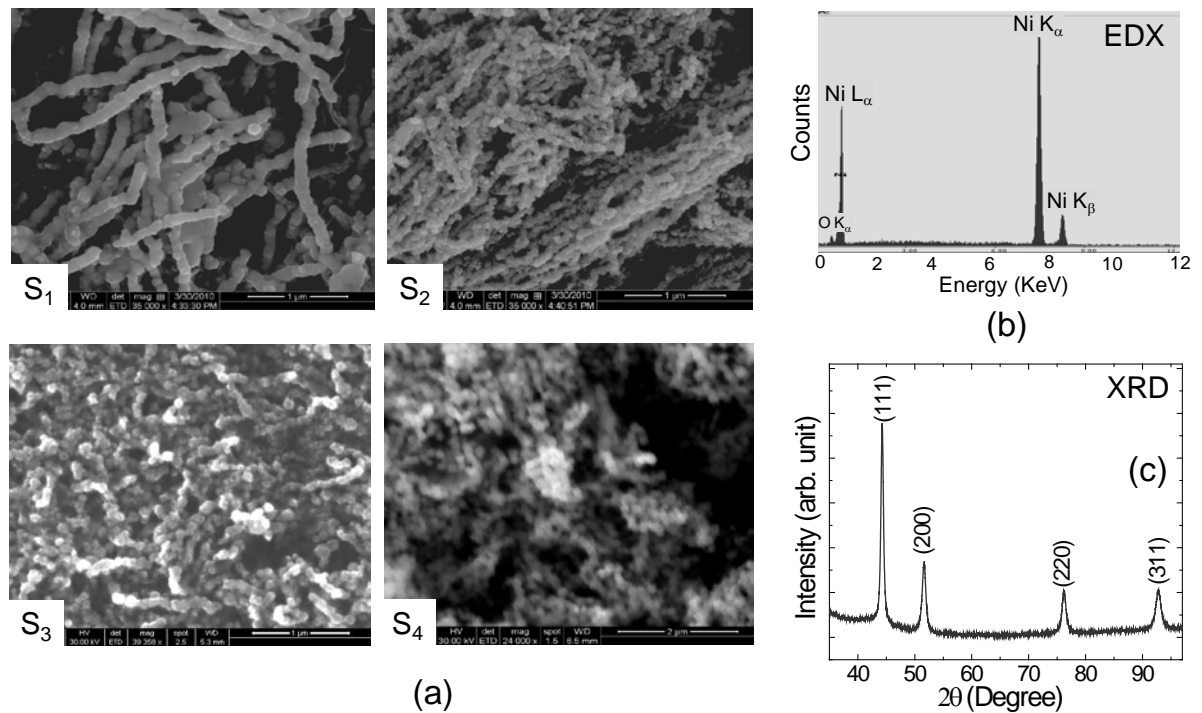


Fig. 10.5: (a) The scanning electron micrographs from four different samples ( $S_1$ ,  $S_2$ ,  $S_3$  and  $S_4$ ) are shown. The (b) EDX spectrum and the (c) XRD pattern from sample  $S_1$  are shown.

### 10.3.2 Results and Discussions

The magnetization ( $M$ ) vs the applied magnetic field ( $H$ ) at room temperature was measured by VSM. Figure 10.6(a) shows the experimental hysteresis loops from all four samples ( $S_1$ ,  $S_2$ ,  $S_3$  and  $S_4$ ) at room temperature [36]. No clear evidence of exchange bias due to surface oxidation is observed. The magnetic parameters including the remanence ( $M_r/M_S$ ), the coercive field ( $H_C$ ) and the saturation field ( $H_S$ ) change significantly from  $S_1$  to  $S_4$  due to the different microstructures.  $S_1$  shows the largest remanence of about 50% and  $H_C$  of 260 Oe, while for  $S_2$ , remanence is 44% and  $H_C = 320$  Oe.  $S_3$  has a remanence of 38% and  $H_C = 330$  Oe, and finally  $S_4$  has much smaller remanence of 14% and  $H_C = 150$  Oe. The saturation field is at a minimum in  $S_1$ , which increases gradually to reach a maximum for  $S_4$ . The saturation magnetization ( $M_S$ ) is also at a minimum in  $S_1$  ( $\sim 200$  emu/cm<sup>3</sup>) and it increases to reach the maximum in  $S_4$  ( $\sim 400$  emu/cm<sup>3</sup>), but remains lower than that of bulk Ni (484 emu/cc).

To understand the underlying mechanisms of the observed magnetization reversal, we have performed micromagnetic simulations using NMAG [34]. In NMAG, the samples are discretized into tetrahedral meshes with average dimension of about 4 nm to fill the sample volumes and surfaces smoothly and typical examples are shown in Fig. 10.6(b). The meshes are very carefully designed and are refined several times before simulations due to the complicated geometry of the simulated microstructures. This ensured the elimination of any spurious effects arising from the surface artifacts of the simulated samples. Four different sample geometries are simulated as shown in the insets of panels of Fig. 10.6(c), which closely resemble the local microstructures of the experimental samples. The geometries are based upon spheres with 48 nm radii arranged with random coordinates and are generated by a homebuilt code written in C<sup>++</sup>. S<sub>1</sub> is a chain with a single sphere along the width, while S<sub>2</sub> is a broad chain with a number of spheres along the width and has an aspect ratio of about 5. S<sub>3</sub> is a chain with ‘X’- and ‘Y’-like branching and S<sub>4</sub> is a randomly arranged cluster of nanoparticles.

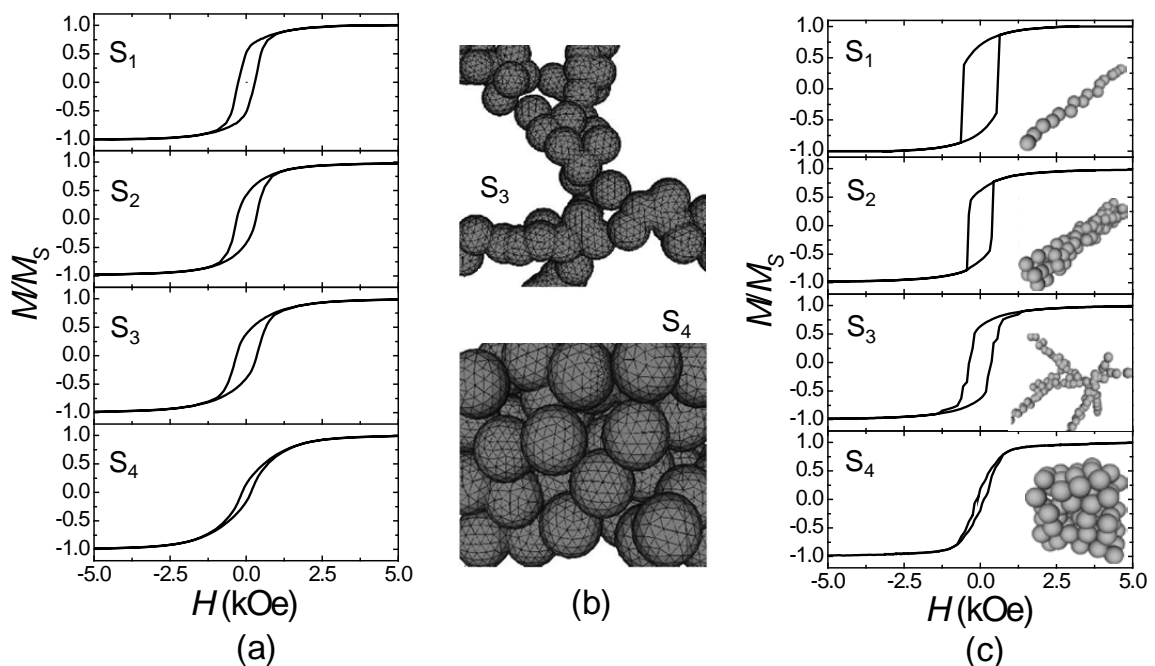


Fig. 10.6: (a) The experimental data of normalized magnetization ( $M/M_S$ ) as a function of the applied magnetic field ( $H$ ) are shown for samples S<sub>1</sub>, S<sub>2</sub>, S<sub>3</sub> and S<sub>4</sub>. (b) Typical discretizations of the simulated samples used in the finite element method based micromagnetic simulations are shown. Due to clarity, enlarged views from the specific regions of simulated microstructures S<sub>3</sub> and S<sub>4</sub> are shown. (c) Simulated normalized magnetization ( $M/M_S$ ) is plotted as a function of the applied magnetic field ( $H$ ) for four samples. The insets show the geometries of the simulated microstructures. The dimensions of the unit spheres in the microstructures are not in scale.

The hysteresis loops were simulated by first saturating the magnetization in the positive field direction and then by cycling the field between positive and negative saturation fields. To take into account the randomness of microstructures in the experimental samples with the direction of the applied magnetic field in the global measurements, we have applied the field at  $45^\circ$  to the simulated microstructures, which, in effect, randomizes the field direction. This is even more important for  $S_1$  and  $S_2$  as compared to  $S_3$  and  $S_4$  due to distinct shape anisotropy in these microstructures. Four panels of Fig. 10.6(c) show the simulated hysteresis loops, which qualitatively reproduce the features observed in the experiment. The lack of precise quantitative agreements between the experimental and simulation results is attributed to the global averaging of the magnetic parameters due to the random arrangements of the local microstructures, and the absence of finite temperature effects in the simulation. Nevertheless, we can extract the qualitative information about the magnetization reversal processes from the simulation results.

All four samples are formed of physically overlapped and exchange-coupled particles, and the magnetization reversal depends primarily on the overall cluster geometry rather than the constituent particles. The reversal, in general, occurs through the formation and melting of local domain structures and typical examples are shown in Fig. 10.7. Formation of vortex-like structures, helical spin configuration (fanning-like) and curling-like modes of magnetization are typical features of the reversal of the chains and clusters, although the constituent particles in a cluster reverse by the quasi-coherent rotation of magnetization. However, reversals of the constituent particles at different magnetic fields (incoherence) cause the formation of the domain structures in the clusters. Experiment and simulation both show the largest remanence for  $S_1$ , which has the highest shape anisotropy and this gradually decreases to  $S_3$  as the anisotropy decreases. The microstructure for  $S_4$  is random and consequently the remanence is minimal. Due to the higher spatial ordering of the microstructure in  $S_1$ , we observe the formation of less stable domains in this sample. Consequently, the reversal occurs by fanning- and curling-like modes of magnetization and the saturation field is minimum in  $S_1$ , which agrees with experiment. Simulation shows the highest coercive field in  $S_1$  as the majority of the spins coherently cross the shape anisotropy barrier. The quantitative disagreement with experiment in this sample is mainly due to the absence of finite temperature effect in the simulation.

The simulation is performed at  $T = 0$  K and hence the simulated  $H_C$  value is larger, as expected. In  $S_2$  and  $S_3$ , the spatial ordering of the microstructure is lower and we observe the

formation of some highly stable local magnetic domains such as complete or partial vortices in addition to the fanning-like mode of magnetization. Consequently, the magnetization reversal occurs gradually by the local ordering of magnetization with the external field, and hence the saturation field is higher but the coercive field is lower than those in  $S_1$ . The agreement of  $H_C$  values between experiment and simulation is slightly better than  $S_1$ , since the structural disorder starts to compete with the temperature effect in  $S_2$  and  $S_3$ . In  $S_4$ , the reversal occurs primarily through the formation of a number of complete and incomplete vortices, which are energetically highly stable structures and they significantly reduce the net magnetization at  $H = 0$  Oe due to the flux closure inside the sample. Consequently, the saturation field is very high, the coercive field is very low, and the remanent magnetization is at a minimum in this case. In  $S_4$ , the structural disorder is dominant over the temperature effect and hence the agreement between the experiment and simulation is best among all four samples. Due to the largest overlap between the particles, the interparticle exchange energy is highest and the saturation magnetization is closest to the bulk value in  $S_4$ . In contrast, due to the smallest possible inter-particle overlap in  $S_1$ , the exchange interaction and hence the saturation magnetization is smallest in  $S_1$ .

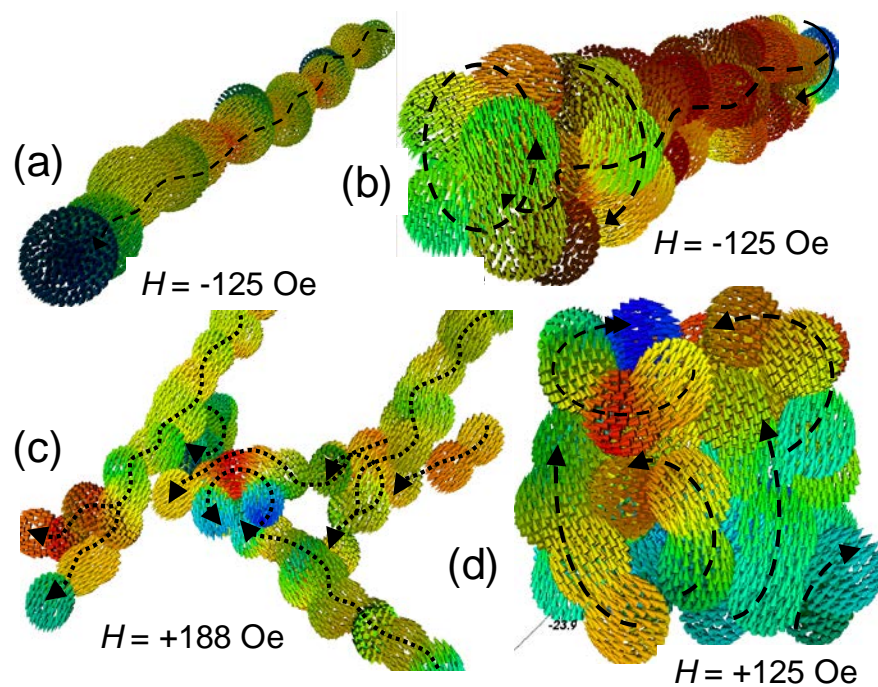


Fig. 10.7: The spatial maps of the simulated magnetization (arrows) and the energy due to the external field (colour map) for samples (a)  $S_1$ , (b)  $S_2$ , (c)  $S_3$  and (d)  $S_4$  at specific values of the external magnetic fields are shown. The dashed arrows are given as a guide to the eye to follow the spatial variation of magnetization.

## 10.4 Magnetic Shape Anisotropy in Chains of Ni Nanoparticles

### 10.4.1 Sample Preparation and Characterization

To prepare Ni nanoparticles, 45 mM Ni chloride ( $\text{NiCl}_2$ ) was dissolved in ethylene glycol. Then, 0.9 M hydrazine hydrate ( $\text{N}_2\text{H}_5\text{OH}$ ) and 0.1 M NaOH was added to that solution. The molar ratio of  $\text{N}_2\text{H}_5\text{OH}$  and  $\text{NiCl}_2$  was kept around 20 and  $p\text{H}$  value of the final solution was maintained around 10. After adding NaOH, the solution was continuously stirred in a beaker using magnetic stirrer at 70–80°C temperature. After 45 to 60 minutes when the colour of the solution turned to grey black indicating the formation of nanoparticles, the reaction was immediately stopped and the beaker was cooled at 0°C using ice to avoid agglomeration of the nanoparticles. Then the uncoated nanoparticles were cleaned for several times using distilled water and ethanol. To coat the nanoparticles with polyethylenimine (PEI), the cleaned nanoparticles were dispersed in distilled water and 1 wt% of PEI was added to the dispersed nanoparticles. The solution was then thermostated for 30–45 minutes at 25°C using ultrasonic bath. The coated nanoparticles were magnetically recovered and dried at room temperature.

For the preparation of Ni nanochain, the polymer coated nanoparticles were redispersed in ethanol and centrifuged to select monodispersed single domain nanoparticles. Then a drop of very dilute colloidal solution of monodispersed nanoparticles was placed on a cleaned Si substrate and a large magnetic field ( $> 6$  kOe) was applied in the plane of the Si substrate by electromagnets. When the nanoparticles were in colloidal form, they were easily aligned along the magnetic lines of force to form one-dimensional chain like structures. When the solution was dried, the chain like structures were retained due to the magnetostatic forces between the constituent nanoparticles. The size, shape, crystal structure and chemical purity of the nanochains were investigated by using SEM, XRD and EDX spectrometer, respectively. The magnetization ( $M$ ) vs the applied magnetic field ( $H$ ) was measured at room temperature by using VSM.

Figures 10.8(a) and (b) show the typical scanning electron micrographs of Ni nanochains. In Fig. 10.8(a), only a single chain of Ni has been shown and in Fig. 10.8(b) we have shown a larger area of the sample with a number of parallel chains. The particles are almost spherical in shape and monodisperse, though a small amount of agglomeration is there. The individual particle size is about 50 nm, which assures that they are single domain.

Some of the chains are isolated, while the others are arranged parallel to each other with varying separations from less than 10 nm to several microns. The EDX spectrum of the nanoparticles, as shown in Fig. 10.8(c), confirms the chemical purity of the nanoparticles with a little amount of oxidization. The XRD pattern of the Ni nanoparticles with CuK $\alpha$  radiation ( $\lambda = 0.154$  nm) is shown in Fig. 10.8(d). The observed XRD peaks at the  $2\theta$  values of  $44.5^\circ$ ,  $51.8^\circ$ ,  $76.4^\circ$  and  $92.9^\circ$  correspond to (111), (200), (220) and (311) crystal planes of Ni, respectively. It reveals that the synthesized Ni has face centered cubic (*fcc*) structure with a lattice parameter of 0.352 nm.

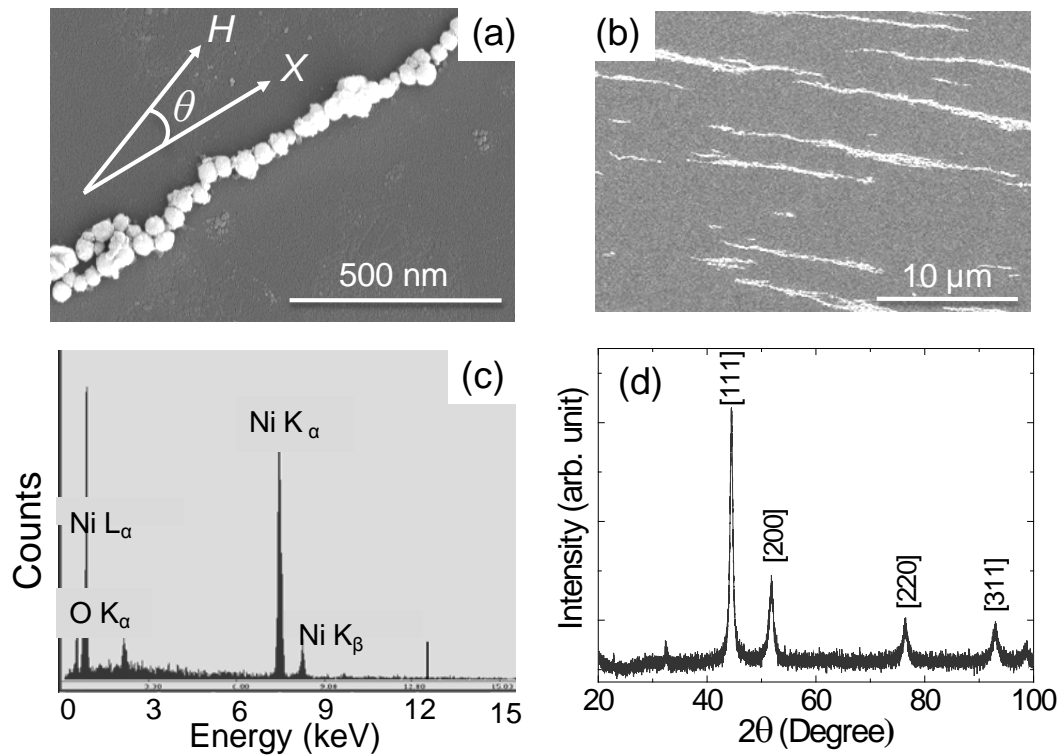


Fig. 10.8: Scanning electron micrograph of (a) single Ni chain and (b) a number of parallel chains of Ni nanoparticles are shown. The geometry of applied field is shown on top of Fig. (a). (c) EDX spectrum and (d) XRD pattern are shown for same sample.

## 10.4.2 Results and Discussions

To investigate how the magnetization reversal depends upon the direction of the applied magnetic field, we measured  $M$ - $H$  curves at different angles ( $\theta$ ) of the magnetic field *w.r.t.* the axes of the chains [37]. The geometry of the applied magnetic field ( $H$ ) for measuring  $M$ - $H$  curve is shown on top of Fig. 10.8(a). The experimental  $M$ - $H$  curves, measured by VSM at room temperature for three different angles of the magnetic field (Fig.

10.9(a)), show that the coercive field ( $H_C$ ) and remanence ( $M_r$ ) are maximum (140 Oe & 34%, respectively) when the magnetic field is applied along the axis of the chain ( $\theta = 0^\circ$ ) and minimum (52 Oe & 15%, respectively) when the field is applied perpendicular to the axis of the chain ( $\theta = 90^\circ$ ). On the other hand, the saturation field ( $H_S$ ) is minimum (about 3 kOe) for the first case and maximum (about 6 kOe) for the second case. Since the magnetocrystalline anisotropy of Ni is very small ( $K_u = -5.7 \times 10^3 \text{ J/m}^3$ ), the shape anisotropy of the chains dominates and the long-axis of the chain behaves as the magnetic easy-axis while the short-axis behaves as the magnetic hard-axis.

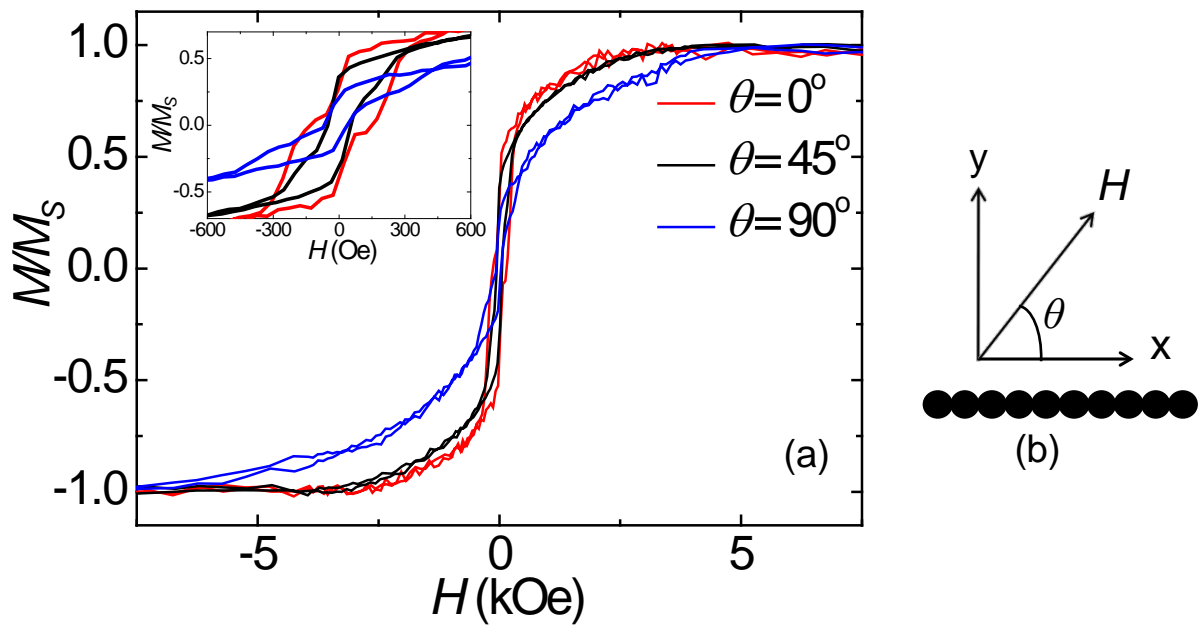


Fig. 10.9. (a) The VSM results of Ni chains are shown with different angles ( $\theta$ ) of the applied magnetic field with the axes of the chains. Inset shows the expanded view of the  $M$ - $H$  curves. (b) The geometry of the applied magnetic field for simulation is shown schematically.

To understand the details of the magnetization reversal process, we have performed micromagnetic simulations by OOMMF [33]. We have simulated two different sample geometries, a single chain made of 20 spherical Ni nanoparticles of 50 nm diameter and arrays of three such Ni chains. The inter-particle distance (edge-to-edge) in a chain is equal to zero, while the inter-chain distances ( $S$ ) in the arrays are 5 nm, 10 nm and 50 nm. Typical material parameters for Ni  $4\pi M_S = 6.15 \text{ kOe}$ ,  $A = 9 \times 10^{-12} \text{ J/m}$ ,  $K_u = -5.7 \times 10^3 \text{ J/m}^3$  and  $\gamma = 17.6 \text{ MHz/Oe}$  are assumed in the simulation, where  $M_S$  is the saturation magnetization,  $A$  is the exchange constant,  $K_u$  is the magnetocrystalline anisotropy constant and  $\gamma$  is the gyromagnetic ratio. For the simulations, the samples were divided into cuboidal cells of size  $5 \times 5 \times 5 \text{ nm}^3$ . The simulated hysteresis loops were calculated by first increasing the field up

to + 10 kOe and then varying it between + 10 kOe & – 10 kOe in steps of 50 Oe. In the simulations, the magnetic field was applied at three different angles ( $\theta$ ) *w.r.t.* the length of the chains. The geometry of applied field for simulation is schematically shown in Fig. 10.9(b). To understand the reversal processes, the spatial maps of magnetization were taken at different values of the applied magnetic field.

In Fig. 10.10(a), the simulated hysteresis loops are shown for a single chain. We have already shown that for a single domain spherical Ni nanoparticle the magnetization reversal occurs through the coherent rotation of magnetization associated with a square hysteresis loop. However, for a chain composed of a number of single domain spherical Ni nanoparticles (Fig. 10.10(b)) the magnetization reversal was modified to curling and fanning-like modes due to the exchange and magnetostatic interactions between the particles. Here, we also observe that the shape of the chain controls the reversal behaviour for magnetic fields applied at different directions *w.r.t.* the length of the chains. For applied field at  $\theta = 0^\circ$ , almost square like hysteresis loop is observed with nearly 100% remanence and  $H_C = 1.76$  kOe. Figure 10.10(c) presents the spatial maps of magnetization for  $\theta = 0^\circ$ , which shows that the reversal starts from the two ends of all spheres in the chain as the field is increased towards the negative value but the central regions of the spheres remain magnetized in the original direction. At  $H = -1.80$  kOe, the central region along the chain-axis takes curling like configuration and at  $H = -1.84$  kOe that region collectively reverses towards the applied field direction. For  $\theta = 45^\circ$ , both the remanence and coercive field go down and ultimately become zero for  $\theta = 90^\circ$ . For  $\theta = 45^\circ$  (Fig. 10.10(d)), the magnetization of the spheres do not reverse collectively. The magnetization of individual spheres reverses one after another starting from two ends and progresses towards the centre with increased negative field. The reversal is completely different for  $\theta = 90^\circ$  (Fig. 10.10(e)). In this case, majority of the spins reverse slowly and collectively through the formation of curling like modes. Though there is a reasonable qualitative agreement between the experimental and the simulated hysteresis loops for single chain, no quantitative agreement is observed. In the experimental samples, a number of chains lie nearly parallel to each other on the substrate at random separations. Therefore, the hysteresis loops are significantly modified due to the long-range magnetostatic interactions.

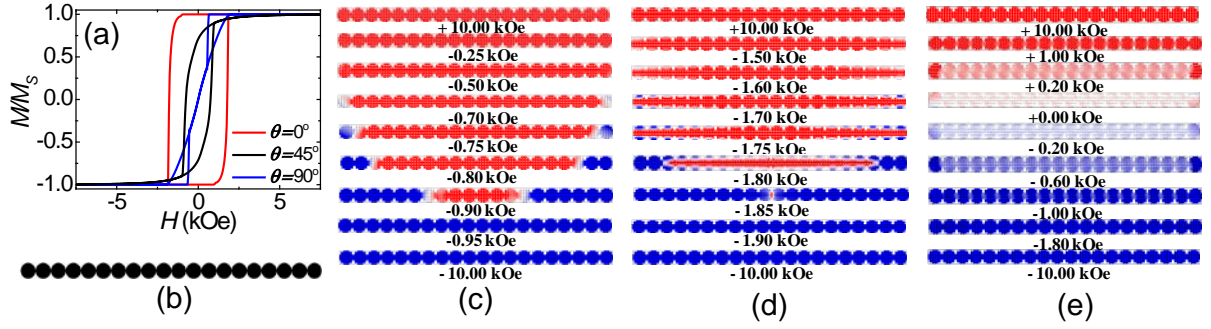


Fig. 10.10: (a) The simulated  $M$  vs  $H$  curves of single Ni chain for three different angles ( $\theta$ ) of the applied magnetic field *w.r.t.* the length of the chain. (b) The schematic of a single chain for simulation is shown. Spatial maps of magnetization at different magnetic field values for (c)  $\theta = 0^\circ$ , (d)  $\theta = 45^\circ$ , (e)  $\theta = 90^\circ$ . The colour map (red-white-blue) indicates the projection of vector magnetization on the image plane.

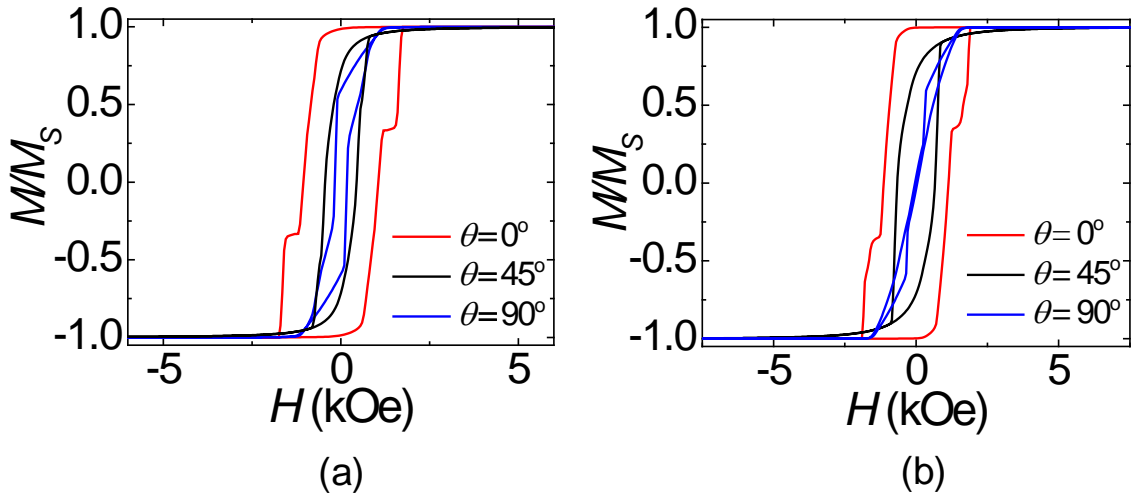


Fig. 10.11: Hysteresis loops of three parallel Ni nanochains with separation (a)  $S = 5$  nm and (b)  $S = 50$  nm for three different angles ( $\theta$ ) of the applied magnetic field *w.r.t.* the length of the chains.

To mimic the experimental sample geometry better, we have further simulated the hysteresis loops for three parallel Ni chains with separations  $S = 5$  nm,  $S = 10$  nm and  $S = 50$  nm. Figure 10.11(a) and (b) shows the hysteresis loops for  $S = 5$  nm and 50 nm, which look similar to those for the single chain for  $\theta = 0^\circ$  and  $\theta = 45^\circ$  and also the magnetic parameters are nearly identical. However, for  $\theta = 90^\circ$ , the loops are different than that of a single chain. For  $S = 5$  nm, the chains are strongly dipolar coupled. For  $\theta = 0^\circ$ , the magnetization reversal starts from the end regions of 1<sup>st</sup> and 3<sup>rd</sup> rows but the central region remains unchanged. Consequently, an antiferromagnetic like spin structure between the consecutive rows starts to form, which becomes complete at  $H = -1.75$  kOe. Beyond that the central part of the middle

row reverses through the fanning mode and finally reversal occurs at  $H = -1.8$  kOe. At  $\theta = 45^\circ$ , the magnetization reversal starts from the central part of all the chains, which is followed by the reversal of the spheres at the ends of the chains. For  $\theta = 90^\circ$ , the magnetization reversal starts from the ends of all the chains collectively. Following that a local flux closure structure is formed and this is followed by the reversal of the magnetization of the central part of the chains.

Figure 10.12(a) shows the hysteresis loop for  $S = 10$  nm (Fig. 10.12(b)). In this case, the chains are less strongly dipolar coupled. For  $\theta = 0^\circ$  (Fig. 10.12(c)), the magnetization reversal starts from the two ends of the alternative rows, which slowly propagates towards the centre and at  $H = -1.90$  kOe the 1<sup>st</sup> and 3<sup>rd</sup> rows reverse completely. This is followed by the magnetization reversal of the middle row. Overall, the magnetization reversal goes through the formation of nonuniform modes. For  $\theta = 45^\circ$ , the reversal occurs through a complicated pattern formation (Fig. 10.12(d)). For  $\theta = 90^\circ$ , the magnetization reversal starts from the two ends of all the chains (Fig. 10.12(e)). This is followed by the formation of local flux closure like structure and curling-like mode

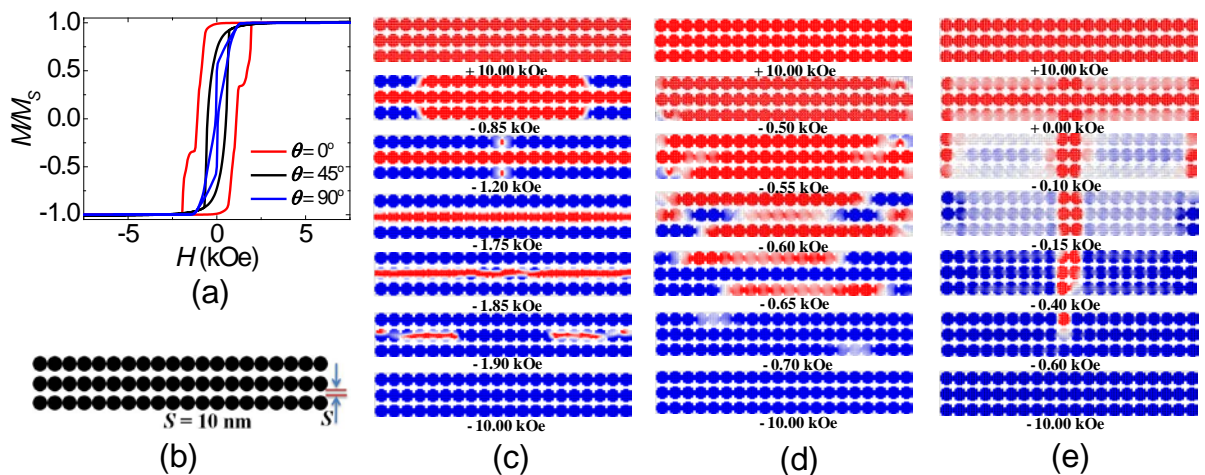


Fig. 10.12: (a) Simulated hysteresis loops of three parallel chains with separation  $S = 10$  nm. (b) The schematic of the array of chains for simulation. The spatial maps of magnetization at different values of  $H$  for (c)  $\theta = 0^\circ$ , (d)  $\theta = 45^\circ$ , (e)  $\theta = 90^\circ$ .

For  $S = 50$  nm, the chains are weakly dipolar coupled. For  $\theta = 0^\circ$ , the magnetization reversal mechanism of the chain at the centre of the array is similar to that of a single chain (not shown). However, the reversal of the 1<sup>st</sup> and the 3<sup>rd</sup> rows starts from the edges of the chains and is followed by the reversal of the centre of the chain. For  $\theta = 45^\circ$  and  $90^\circ$ , the magnetization reversal starts from the edges of the chains.

The simulated results for three parallel chains give the better qualitative agreement with the experimental results than those from a single chain. However, the lack of precise quantitative agreement between the experimental and simulation results stems from the fact that the simulations are performed at  $T = 0$  K and the imperfection of the real samples as opposed to those assumed in the simulation.

## 10.5 Summary

In summary, we have reported the magnetization reversal of chains and clusters of chemically synthesized single domain dipolar and exchange coupled Ni nanoparticles of various geometries by experiment and micromagnetic simulations. Considering the local microstructures of the samples in micromagnetic simulations, we are able to reproduce the experimental observations, qualitatively. In case of clusters formed by randomly arranged Ni nanoparticles, the experimental  $M-H$  data were better reproduced by a periodic arrangement of partially overlapped nanoparticles as opposed to single nanoparticles and cluster of randomly arranged nanoparticles. As opposed to a coherent rotation of magnetization expected for single domain nanoparticles, the magnetization reversal of the whole cluster occurs through the appearance of various domain states including C-state, vortex-like state and flower-like state, although the individual particles in the cluster maintain primarily single domain state. Various domain structures occur in the cluster due to the incoherence of the magnetization reversal between the constituent particles in the cluster.

We have compared the reversal behaviour of chains and clusters of Ni nanoparticles with four distinct geometries. The magnetization reversal of the clusters and chains is dominated by the interparticle exchange and the shape anisotropy of the overall clusters and occurs through the formation of various local magnetic configurations. In chain-like structures, the fanning- and curling-like modes of magnetization reversal cause the smallest saturation field, and the largest coercive field and remanence. However, in more entangled structures such as branched chains and random clusters, formation of more stable magnetic configurations such as vortices causes a larger saturation field, but a smaller coercive field and remanence.

In case of parallel chains, the overall geometry controls the reversal mechanism, and the magnetic hysteresis loops with magnetic field applied along the long-axis and short-axis of the chains show magnetic easy-axis and hard-axis like behaviours. Micromagnetic

simulations on a single Ni nanochain do not give good qualitative agreement with the experimental result. However, simulations with three parallel chains give better qualitative agreement with the experimental results. The reversal mechanism is modified due to the magnetostatic interaction between the chains and formation of local flux closure like structures are observed during the magnetization reversal, which causes low remanence, smaller coercive field and larger saturation field for the loops with the magnetic field applied perpendicular to the length of the Ni nanochains.

Chains of nanomagnets are potential candidates for propagation of magnons and may be used as future building blocks for magnonic crystals. Hence understanding the magnetic ground state and magnetization processes at various times and length scales are important. Despite the lack of precise quantitative agreements between the experimental and simulation results, a qualitative agreement is observed and a combination of both results would possibly lead to more precise experiments and better understanding of the magnetization processes in chains and clusters of magnetic nanoparticles.

## Bibliography

1. B. D. Terris and T. Thomson, *J. Phys. D: Appl. Phys.* **38**, R199 (2005).
2. M. Arruebo, R. Fernández-Pacheco, M. R. Ibarra, and J. Santamaría, *Nano Today* **2**, 22 (2007).
3. A. K. Gupta and M. Gupta, *Biomaterials* **26**, 3995 (2005).
4. S. H. Chung, A. Hoffmann, S. D. Bader, C. Liu, B. Kay, L. Makowski, and L. Chen, *Appl. Phys. Lett.* **85**, 2971 (2004).
5. A.-H. Lu, W. Schmidt, N. Matoussevitch, H. Bönemann, B. Spliethoff, B. Tesche, E. Bill, W. Kiefer, and F. Schüth, *Angew. Chem.* **116**, 4403 (2004).
6. V. E. Fertman, “Magnetic Fluids Guidebook: Properties and Applications,” *Hemisphere Publishing Co.*, New York (1990).
7. S. Sun, C. B. Murray, D. Weller, L. Folks, and A. Moser, *Science* **287**, 1989 (2000).
8. J. Park, J. Joo, S. G. Kwon, Y. Jang, and T. Hyeon, *Angew. Chem. Int. Ed.* **46**, 4630 (2007).
9. W. Zhou, L. He, R. Cheng, L. Guo, C. Chen, and J. Wang, *J. Phys. Chem. C* **113**, 17355 (2009).
10. Y. Zhang, L. Sun, Y. Fu, Z. C. Huang, X. J. Bai, Y. Zhai, J. Du, and H. R. Zhai, *J. Phys. Chem. C* **113**, 8152 (2009).
11. B. A. Grzybowski, H. A. Stone, and G. M. Whitesides, *Nature* **405**, 1033 (2000).
12. J. C. Love, A. R. Urbach, M. G. Prentiss, and G. M. Whitesides, *J. Am. Chem. Soc.* **125**, 12696 (2003).
13. G. Cheng, D. Romero, G. T. Fraser, and A. R. Hight Walker, *Langmuir* **21**, 12055 (2005).
14. D. A. Garanin and H. Kachkachi, *Phys. Rev. B* **80**, 014420 (2009).
15. E. Bonet, W. Wernsdorfer, B. Barbara, A. Benoît, D. Mailly, and A. Thiaville, *Phys. Rev. Lett.* **83**, 4188 (1999).
16. D. Givord, V. Skumryev, and J. Nogués, *J. Magn. Magn. Mater.* **294**, 111 (2005).
17. C. Thirion, W. Wernsdorfer, and D. Mailly, *Nat. Mater.* **2**, 524 (2003).
18. A. Barman, S. Wang, J. D. Maas, A. R. Hawkins, S. Kwon, A. Liddle, J. Bokor, and H. Schmidt, *Nano Lett.* **6**, 2939 (2006).
19. A. Sukhov and J. Berakdar, *Phys. Rev. Lett.* **102**, 057204 (2009).

20. H. Schmidt and R. J. Ram, *J. Appl. Phys.* **89**, 507 (2001).
21. Ò. Iglesias and A. Labarta, *Phys. Stat. Solid. C* **1**, 3481 (2004).
22. Y. Nakatani, Y. Uesaka, and N. Hayashi, *J. Appl. Phys.* **67**, 5143 (1990).
23. Y. Uesaka, Y. Nakatani, and N. Hayashi, *Jpn. J. Appl. Phys.* **30**, 2489 (1991).
24. B. K. Mahato, A. Ganguly, B. Rana, and A. Barman, *J. Phys. Chem. C* **116**, 22057 (2012).
25. D. J. Craik and E. D. Isaac, *Proc. Phys. Soc., London* **76**, 160 (1960).
26. R. Skomski, *J. Phys.: Condens. Matter* **15**, R841 (2003).
27. K. D. Sorge, A. Kashyap, R. Skomski, L. Yue, L. Gao, R. D. Kirby, S. H. Liou, and D. J. Sellmyer, *J. Appl. Phys.* **95**, 7414 (2004).
28. C. Binns, M. J. Maher, Q. A. Pankhurst, D. Kechrakos, and K. N. Trohidou, *Phys. Rev. B* **66**, 184413 (2002).
29. S. A. Koch, G. Palasantzas, T. Vystavel, J. T. M. De Hosson, C. Binns, and S. Louch, *Phys. Rev. B* **71**, 085410 (2005).
30. S. Bedanta, T. Eimüller, W. Kleemann, J. Rhensius, F. Stromberg, E. Amaladass, S. Cardoso, and P. P. Freitas, *Phys. Rev. Lett.* **98**, 176601 (2007).
31. G.-y. Huang, S.-m. Xu, G. Xu, L.-y. Li, and L.-f. Zhang, *T. Nonferr. Metal. Soc.* **19**, 389 (2009).
32. B. Rana, M. Agrawal, S. Pal, and A. Barman, *J. Appl. Phys.* **107**, 09B513 (2010).
33. M. Donahue and D. G. Porter, "OOMMF User's guide, Version 1.0," *NIST Interagency Report No. 6376, National Institute of Standard and Technology, Gaithersburg, MD, URL: <http://math.nist.gov/oommf>*, (1999).
34. T. Fischbacher, M. Franchin, G. Bordignon, and H. Fangohr, *IEEE Trans. Magn.* **43**, 2896 (2007).
35. S.-H. Wu and D.-H. Chen, *J. Colloid Interface Sci.* **259**, 282 (2003).
36. M. Agrawal, B. Rana, and A. Barman, *J. Phys. Chem. C* **114**, 11115 (2010).
37. B. Rana, A. Ganguly, and A. Barman, *IEEE Trans. Magn.* **47**, 2859 (2011).

## CHAPTER 11

---

# Ultrafast Magnetization Dynamics of Ni Nanoparticles

---

### 11.1 Background

Magnetic data storage is a very important application of nanomagnets among multidisciplinary applications as discussed in the previous chapters. One of the fundamental issues in magnetic data storage is to achieve a fast magnetization switching (reversal) of the data bits. Current data storage technology relies upon domain wall motion, which limits the operational speed in the nanosecond regime. New strategies are required to overcome the current limitations of magnetization reversal processes. Consequently, new topics like magnetization switching through precessional dynamics [1-2], ultrashort laser pulse assisted switching [3], switching by spin polarized current [4] and rf magnetic field assisted ultrafast switching [5] are becoming subjects of intense research. Control of ultrafast magnetization dynamics in magnetic nanostructures is very important in applications like spintronics and magnetic data storage devices [6-7].

Unlike lithographically patterned ordered nanomagnets and their arrays, only few studies are found on the ultrafast magnetization dynamics of magnetic nanoparticles. In Ref. [5], the magnetization reversal of nanoparticles was reported at a dc magnetic field well below the switching field. To trigger the switching, a rf magnetic field was applied in parallel to the dc magnetic field. The study of ultrafast magnetization dynamics of exchange decoupled Fe nanoparticles with diameters down to 25 nm was reported by Buchanan *et al.* [8-9]. In both studies, the Fe nanocrystals were prepared by implantation of 80 keV Fe<sup>+</sup> ions to a fluence of  $1.5 \times 10^{17}$  ions/cm<sup>2</sup> in optical-quality fused quartz wafers. In Ref. [8], the dynamic response was triggered by a current pulse propagating through a lithographically

patterned wire and was probed by using time-resolved Kerr microscope. The in-plane and out-of-plane switching dynamics are quite different and independent of the magnitude of the in-plane bias magnetic field. Nanoparticles arrays exhibit a very strong and fast out-of-plane magnetization response due to strong dipole interactions between the particles and very little dependence on the particular structure and arrangement of the particles is observed in simulations at these time scales. Reference [9] reveals few unique properties offered by the nanocomposites, which includes the high resonance frequency, strong effective damping and electrically insulating character. These are very favorable for applications in sensors. The study of ultrafast magnetization of superparamagnetic Co nanoparticles, embedded in a dielectric matrix shows a strongly damped precessional motion [10]. It was reported that magnetization precession is damped faster in the superparamagnetic particles than in Co films or when the particle size decreases, suggesting that the damping is enhanced at the metal dielectric interface. In this particular study, the magnetization trajectory was observed after bypassing the thermal fluctuation of superparamagnetic Co nanoparticles. The dependence of ultrafast magnetization dynamics on the size of nanocrystals and pump fluence were reported in 2008 [11]. It was shown that the percentage of demagnetization increases with the increase in the pump fluence, and the amplitude of the slower recovery component increases with the size of the nanocrystals, which suggests the size-dependent ferrimagnetic ordering throughout the volume of the nanocrystal. A further study on  $\text{Fe}_3\text{O}_4$  nanoparticles reveals the role of surface spins of the nanoparticles on the spin-lattice relaxation [12]. It was shown how the relaxation time varies with the nanoparticles size due to the variation of the volume percentage of surface spins *w.r.t.* the internal spins. This proposes a possibility of controlling the spin-lattice relaxation time by modifying the surface of nanomaterials. Another theoretical study showed the local control of magnetization trajectory to a predefined path by applying a sequence of two perpendicular magnetic pulses, each with a duration less than the precessional period [13]. In this case, the magnetization tilt angle is increased monotonically to achieve a predefined state within tens of picoseconds. The method can be used for fast field-assisted thermal switching.

Magnetic nanoparticles often agglomerate and form chains and clusters [14-15] in order to minimize the surface energy associated with high surface to volume ratio and magnetostatic energy. Therefore, understanding the ultrafast magnetization dynamics of magnetic nanoparticles in form of clusters and chains is very important for their implementations in future technologies. However, no attempts have been made till now to

study the ultrafast magnetization dynamics of magnetic nanoparticles in the form of clusters and chains. In this chapter, we investigate ultrafast magnetization dynamics in Ni nanoparticles with different assembling geometries. We will explicitly study how the ultrafast magnetization dynamics in different time scales are influenced by the assembling geometry of the nanoparticles.

## 11.2 Sample Preparation, Characterization and Experimental Technique

To study the ultrafast magnetization dynamics, Ni nanoparticles with four different geometries ( $S_1$ ,  $S_2$ ,  $S_3$  and  $S_4$ ) as shown in the previous chapter (chapter 10) in Fig. 10.5(a) were prepared by the chemical reduction of nickel chloride ( $\text{NiCl}_2 \cdot 6\text{H}_2\text{O}$ ) by hydrazine hydrate ( $\text{N}_2\text{H}_5\text{OH}$ ) in the presence of sodium hydroxide ( $\text{NaOH}$ ) [16]. The samples were dispersed on bare Si(100) substrates by dropcasting from a colloidal solution. The typical scanning electron micrographs (Fig. 10.5(a)) from four different samples ( $S_1$ ,  $S_2$ ,  $S_3$  and  $S_4$ ) show the formation of chains and clusters of different configurations.  $S_1$  shows long chains with a single particle along the width of the chain with negligible branching, while  $S_2$  shows broad chains formed of a number of particles along the width.  $S_3$  shows shorter chains with plenty of ‘X’- and ‘Y’-like branching and  $S_4$  shows largely random arrangement of the particles with no preferred shape. However, the average size of the constituent particles is about 50 nm in all four samples. The observed microstructures are randomly arranged throughout the sample dispersed on the Si substrate. The EDX spectrum in Fig. 10.5(b) confirms the chemical purity of nanoparticles except for a little trace of oxygen, while the XRD pattern in Fig. 10.5(c) confirms the *fcc* lattice structure of Ni.

The ultrafast magnetization dynamics was measured by using time-resolved magneto-optical Kerr effect (TRMOKE) microscope based upon a two-colour collinear pump-probe setup (section 4.3.3). The second harmonic ( $\lambda = 400$  nm, pulse width  $\approx 100$  fs) of a Ti-sapphire oscillator output (Tsunami, Spectra Physics, pulse width  $\approx 70$  fs) was used to pump the samples, while the time delayed fundamental ( $\lambda = 800$  nm) laser beam was used to probe the dynamics by measuring the polar Kerr rotation by means of a balanced photodiode detector, which completely isolates the Kerr rotation and the total reflectivity signals. The pump power used in these measurements is about  $15 \text{ mJ/cm}^2$ , while the probe power is much weaker and is about  $2 \text{ mJ/cm}^2$ .

Since our setup is based on magneto-optical Kerr effect measurement *i.e.*, in the back-reflected geometry, we need to take some precautions for this measurement. The dispersed nanoparticles on the Si substrate offers more scattering than specular reflection for the pump and probe beams. This degrades the reflectivity and Kerr signal in different ways. First, only a small fraction of the scattered probe beam can be efficiently collected and sent to the detector, which makes the total intensity of the light on the photodiodes very small. Second, possible depolarization effect of the scattered light can reduce the effective Kerr signal. Third, and most damaging effect is the possibility of reaching of some scattered pump light in the detector. Since the pump beam is modulated by the chopper at 1-2 kHz frequency, which is also the reference frequency to the lock-in amplifier, even small amount of pump light reaching the detector can saturate the lock-in signal and disable the measurement of Kerr effect of the reflected probe beam. To overcome this problem, a 10 nm thick nonmagnetic capping layer of SiO<sub>2</sub> was deposited on the Ni nanoparticles samples by rf magnetron sputtering at a base pressure of  $3 \times 10^{-8}$  Torr and at an Ar pressure of 10 mTorr. The SiO<sub>2</sub> capping layer is optically transparent at the wavelengths of pump and probe beams. It also reduces the background signal significantly by smoothing out the sample surface. Furthermore, these SiO<sub>2</sub> layers protect the samples from oxidation due to heating of the samples during the pump-probe measurement.

The bias magnetic field ( $H_b$  = component of bias field along sample plane), was tilted 15° out of the plane of the sample to have a finite demagnetizing field along the direction of the pump pulse, which is eventually modified by the pump pulse to induce precessional magnetization dynamics within the nanoparticles. The pump beam was chopped at 2 kHz frequency and a phase sensitive detection of the polar Kerr effect of the plane polarized probe beam was made by using a lock-in amplifier. It is well known that for Ni Kerr rotation is smaller than the Kerr ellipticity and hence for the TRMOKE measurements of the Ni nanoparticles, we have preferred to measure the Kerr ellipticity. From Eq. 2.8.29 we know that the complex Kerr rotation is expressed as  $\frac{2}{1-\epsilon}[-(k_- - k_+) + i(n_- - n_+)]$ , where the real part is the Kerr rotation and the imaginary part corresponds to the Kerr ellipticity. If we introduce a quarter wave plate in front of the optical bridge detector it will produce a  $\pi/2$  phase difference between the ‘s’ and ‘p’ components so that the analyzing polarizer will see the complex Kerr rotation as  $-\frac{2}{1-\epsilon}[(n_- - n_+) + i(k_- - k_+)]$  *i.e.*, the Kerr rotation and

ellipticity is interchanged [17]. By measuring the (A – B) signal from the optical bridge detector as a function of the time delay between the pump and the probe beams, we then effectively measure the time-resolved Kerr ellipticity, which enhances the signal-to-noise ratio of the time-domain data as compared to the time-resolved Kerr rotation data from the same Ni nanoparticles.

### 11.3 Demagnetization and Relaxation of Ni Nanoparticles

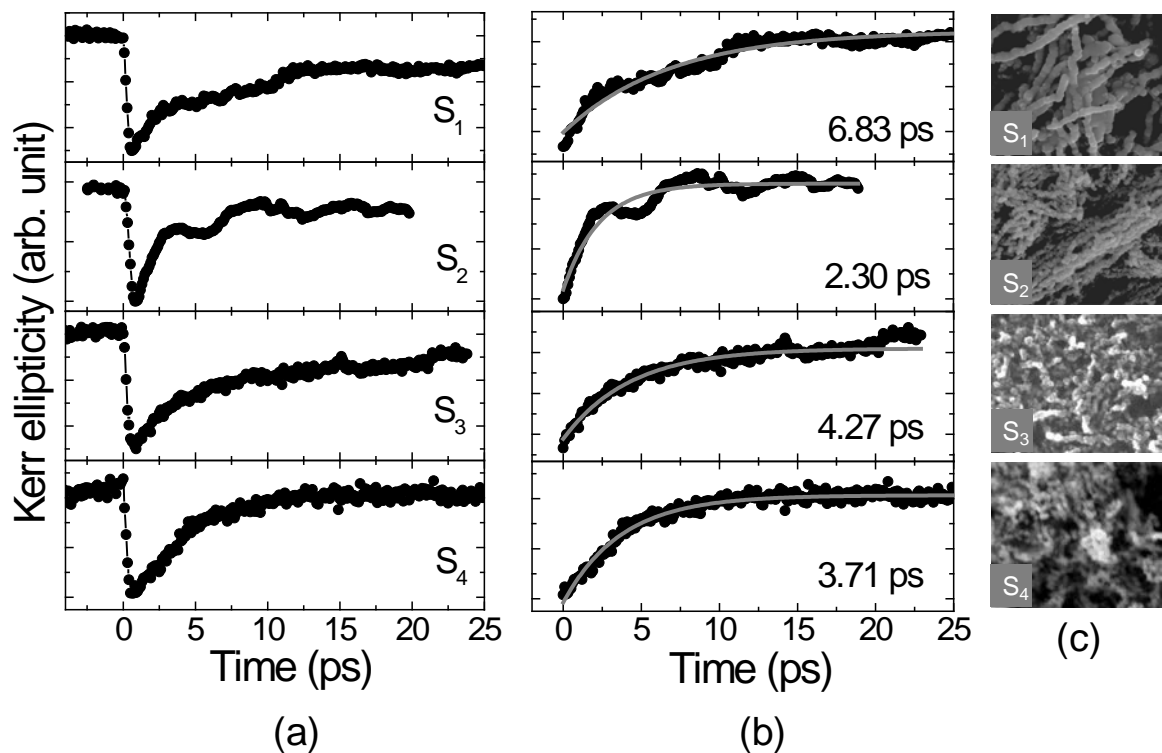


Fig. 11.1: (a) Ultrafast demagnetization and fast relaxation of samples S<sub>1</sub>, S<sub>2</sub>, S<sub>3</sub> and S<sub>4</sub>. (b) Only the relaxation parts of the Kerr ellipticities are shown. The grey solid lines are the fittings with a single exponential decay function (Eq. 11.1). (c) Typical scanning electron micrographs of the samples are shown.

Figure 11.1(a) (first column) shows the ultrafast demagnetization and the fast relaxation thereafter measured from samples S<sub>1</sub>, S<sub>2</sub>, S<sub>3</sub> and S<sub>4</sub>. The Kerr ellipticity was measured as function of the time delay between the pump and the probe beams. For measuring the demagnetization and the fast relaxation times, we recorded Kerr ellipticity up to a time delay of 25 ps at a time step of 100 fs. The typical sample geometries, which are same as in Fig. 10.5(a) are again shown in Fig. 11.1(c) for convenience. Figure 11.1(a) shows very clear Kerr ellipticity signals for all the samples. The graphs show that the Ni

nanoparticles are demagnetized within about 500-600 fs and the sample geometry does not affect the demagnetization time significantly. The demagnetization is believed to occur due to the thermalized population of spins above the Fermi level (discussed in section 2.6.3) [18-19]. The thermalization time is an intrinsic property of the material and is independent of extrinsic parameters like sample geometry. The measured time constants corresponding to different dynamical regimes for the four samples studied here are listed in table 11.1.

**Table 11.1**

<b>Sample geometry</b>	<b>Demagnetization time (fs)</b>	<b>Fast relaxation time <math>\tau_1</math> (ps)</b>	<b>Slow relaxation time <math>\tau_2</math> (ps)</b>
S <sub>1</sub>	500	6.83	286
S <sub>2</sub>	600	2.30	Could not measure
S <sub>3</sub>	500	4.27	900
S <sub>4</sub>	500	3.71	140

To find out the fast relaxation times ( $\tau_1$ ), the relaxation parts are separated out and are fitted with a single exponential function as shown in Fig. 11.1(b). The single exponential decay function can be expressed as

$$M(t) = M(0) + Ae^{-t/\tau_1}, \quad (11.1)$$

where  $M(0)$  is the initial magnetization,  $A$  is the relaxation coefficient and  $\tau_1$  is the fast relaxation time. Table 11.1 shows that the values of  $\tau_1$  vary from 2.30 to 6.83 ps for four different sample geometries. It is believed that the faster relaxation ( $\tau_1$ ) of magnetization occurs after the ultrafast demagnetization because spins exchange energy and angular momentum with the lattice through spin-lattice or spin-orbit interaction.  $\tau_1$  may vary from sub-ps to several ps depending upon the strength of the spin-orbit coupling and the specific heats of the spins and phonons [20-22]. The relaxation time also depends on the density of laser excitation [20-21] and magnetocrystalline anisotropy. Here, all of these parameters

remain unchanged except the strength of the spin-orbit interaction. In ferromagnetic solids, this spin-orbit interactions are not only determined by the intrinsic atomic spin-orbit coupling, but also by the local lattice structure and symmetry [12, 23]. In nanomagnets, percentage of surface spins is larger than the bulk materials. Therefore, in nanomagnets there are many surface spins under different ligand fields from those of the interior spins due to the structural discontinuity at the surface. Hence, the rate of energy and momentum transfer from spin to lattice in nanomagnets is significantly influenced by the surface spins [12]. This signifies that the magnetization relaxation time for surface spins is faster than the interior spins [11]. In our case, there is a small size and shape distribution in the nanoparticles and there is a small size distribution within the nanoparticles for each sample, which also varies from one sample to another. The ratio of the number of surface to volume spins of smaller particles is larger than the ratio of the number of surface to volume spins of larger particles. Therefore, the fast relaxation time ( $\tau_f$ ) of smaller particles should be faster than the larger particles. This is probably the reason for obtaining a variation in  $\tau_f$  for different samples. The presence of sample roughness and defects may also play an important role in the variation of  $\tau_f$  to some extent. In addition, different environment of the nanoparticles in different samples due to different clustering geometry also contributes to the variation in  $\tau_f$ . However, it is difficult to isolate the above effects systematically due to the complicated morphology of the samples.

To find out the longer relaxation times, the Kerr ellipticity data for the samples were measured up to 1500 ps time delay at a time step of 5 ps. Unfortunately, we could not measure the slow relaxation from sample S<sub>2</sub> due to the presence of very large background coming during the longer measurement time. The Kerr ellipticity data for S<sub>1</sub>, S<sub>3</sub> and S<sub>4</sub> are shown in Fig. 11.2(a). To find out the long relaxation times, the Kerr signals are fitted with a bi-exponential decay function given by

$$M(t) = M(0) + Ae^{-t/\tau_1} + Be^{-t/\tau_2}, \quad (11.2)$$

where  $M(0)$  is the initial magnetization,  $A$ ,  $B$  are the relaxation coefficients and  $\tau_1$  and  $\tau_2$  are the fast and slow relaxation times, respectively. The fitted curves are shown by grey solid lines in Fig. 11.2(b). We observed a significant variation (between 140 and 900 ps) in the longer relaxation time ( $\tau_2$ ) for three different samples. The second or longer relaxation time ( $\tau_2$ ) corresponds to the diffusion of electron and lattice heat to the surroundings (in this case

the Si substrate) [20-21]. Diffusion rate depends upon the type of substrate as well as the physical contact between the nanoparticles with the substrate and the environments of the nanoparticles itself. The variation in the slower relaxation time ( $\tau_2$ ) may be attributed to the variation in the configurations of the nanoparticles in different samples and their physical contacts with the Si substrates. The later factor could not be controlled well during the dropcasting of the nanoparticles on the Si substrate.

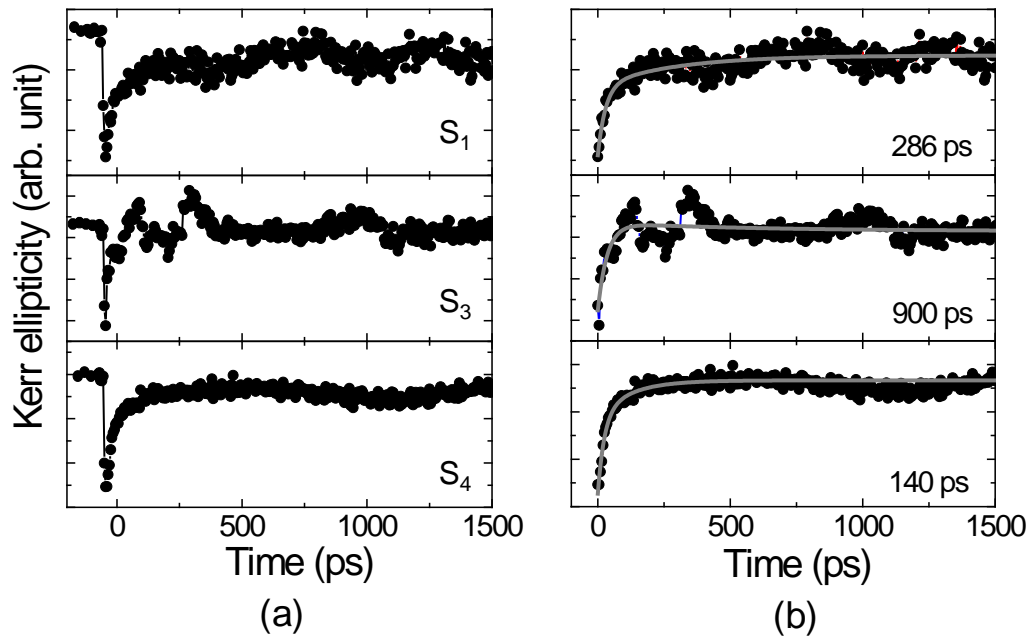


Fig. 11.2: (a) The time-resolved Kerr ellipticity data for samples S<sub>1</sub>, S<sub>3</sub> and S<sub>4</sub> are shown for a longer time scale (up to 1500 ps). (b) The data are fitted with the bi-exponential decay function (grey solid lines) and the extracted long relaxation times ( $\tau_2$ ) are shown in the graphs.

## 11.4 Precessional Magnetization Dynamics of Ni Nanoparticles

### 11.4.1 Precessional Dynamics as a Function of Bias Field

First, we study how the precessional dynamics varies with the bias field magnitude ( $H_b$ ). Figure 11.3(a) shows a scanning electron micrograph of sample S<sub>1</sub>. The geometry of the bias magnetic field and schematics of the pump and the probe beams are shown on top of the figure. The bias field ( $H_b$ ) of different magnitudes was applied while keeping its direction unchanged. The hysteresis loop ( $M-H$ ) of the sample is shown in Fig. 11.3(b). Solid circular points on top of the hysteresis loop denote the magnetization of the sample at different bias field values, for which the precessional magnetization dynamics were measured. The

hysteresis loop shows that as the magnetic field decreases from 1000 Oe to 520 Oe (*i.e.*, the range of the bias field values used in the experiment) the magnetization ( $M$ ) changes from 162 emu/cc to 144 emu/cc (*i.e.*, from 81% to 72% of  $M_S$ ). The saturation field ( $H_S$ ) for this sample is about 3-4 kOe. Therefore, the dynamics was probed with  $H_b$  values below the saturation field ( $H_S$ ).

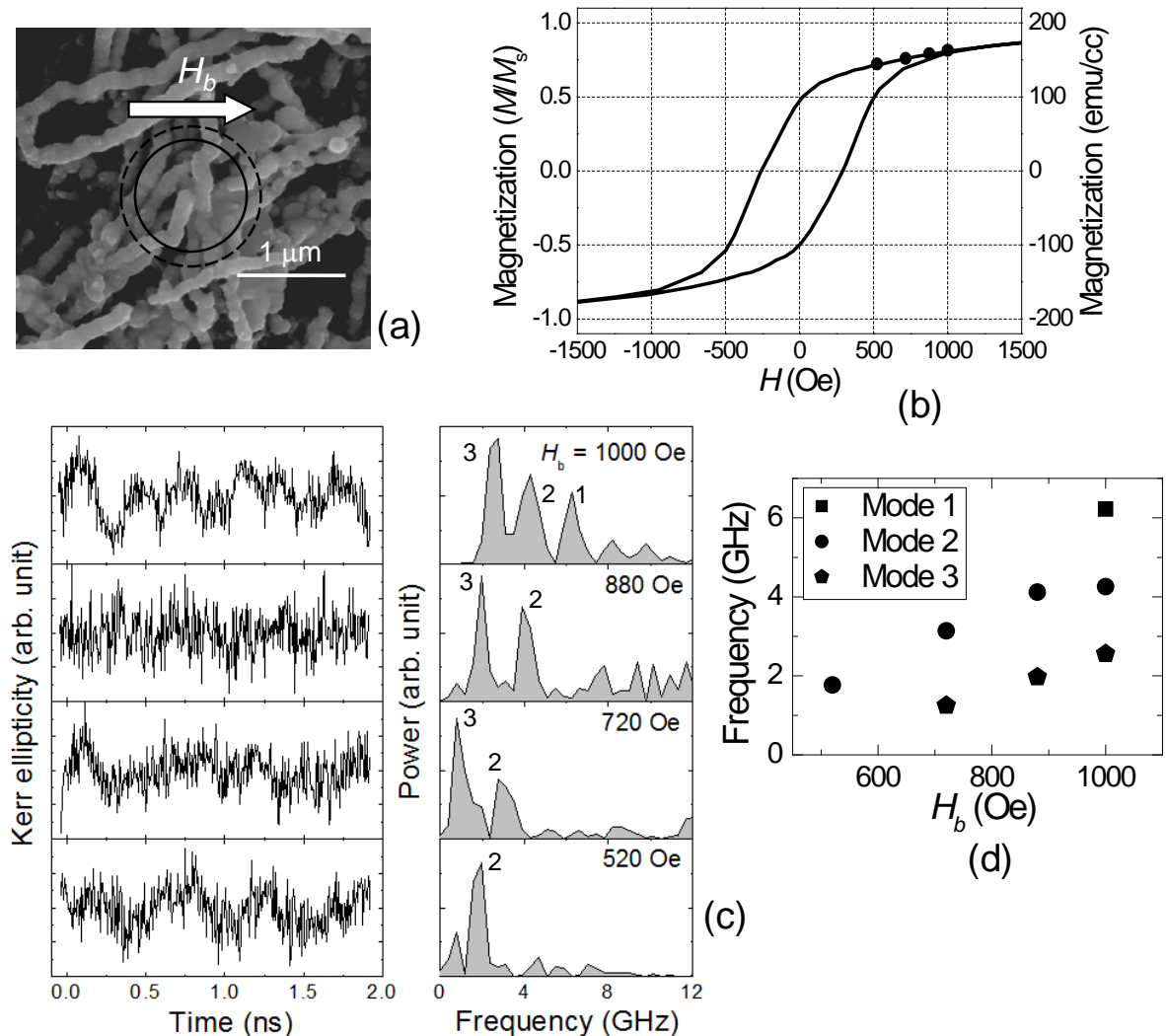


Fig. 11.3: (a) Scanning electron micrograph of sample  $S_1$ . The geometry of the bias field and the pump and the probe spots are shown schematically on top of the figure. (b) Hysteresis loop ( $M-H$ ) of the sample is shown. Solid circular points on top of the hysteresis loop denote the static magnetization values of the sample at different bias field values, for which the precessional dynamics were measured. (c) In left column, background subtracted Kerr ellipticity signals are shown for the same sample as a function of  $H_b$ . The right column shows corresponding FFT power spectra. The peak numbers are assigned to the FFT power spectra. (d) The frequencies of the observed resonant modes are plotted as a function of  $H_b$ .

Precessional magnetization dynamics was measured by recording the time-resolved Kerr ellipticity for time delay up to 2000 ps at time steps of 5 ps. The background subtracted Kerr ellipticity data are shown in the left column of Fig. 11.3(c). Though the Kerr signals look noisy, the general features of the dynamics can be extracted. The right column shows corresponding FFT power spectra. The peak numbers are assigned to the FFT power spectra. The FFT power spectra show a number of well resolved collective precessional modes at all values of bias fields. The frequencies of the resonant modes are plotted as a function of the bias fields ( $H_b$ ) and are shown in Fig. 11.3(d). The graph shows different branches of frequencies. The frequency of each branch decreases monotonically with the decrease in bias field. The resonant frequencies depend upon the total effective field ( $H_{eff}$ ) of the sample at the positions where the dynamics are probed. The total effective field is composed of the applied bias field ( $H_b$ ), demagnetizing field ( $H_d$ ) due to the sample shape and magnetization, the stray magnetic field from the neighbouring particles ( $H_s$ ), magnetocrystalline anisotropy field ( $H_a$ ) and the exchange field ( $H_e$ ). In our measured samples,  $H_a$  and  $H_e$  are not expected to vary significantly, but  $H_b$  and  $H_d$  and  $H_s$  varies. The observed frequency branches do not fit with the analytical Kittel formula for the uniform resonant mode. In Kittel formula, the magnetization of the samples is assumed to be uniform and also constant with the change in the bias field magnitude *i.e.*, the bias field should be above saturation. However, in the present measurement the magnetization varies with the bias magnetic field. In addition, very complicated domain configurations occur at varying magnetic fields for all these samples as shown in chapter 10. These complicated magnetic ground states lead towards a number of nonuniform resonant modes depending upon the local spin configuration. However, a quantitative modeling of the observed resonant modes is found to be difficult due to the lack of the computational resources during the course of this thesis.

#### 11.4.2 Precessional Dynamics as a Function of Sample Geometry

We have further measured the precessional dynamics of Ni nanoparticles arranged in different geometries. We could measure the precessional dynamics from samples  $S_1$ ,  $S_3$  and  $S_4$ . However, the measurement of precessional dynamics from sample  $S_2$  was not possible due to smaller signal-to-noise ratio. Figure 11.4 shows the FFT power spectra of background subtracted Kerr ellipticity data for three samples ( $S_1$ ,  $S_3$  and  $S_4$ ) at a fixed value of  $H_b = 1$  kOe applied in the plane of the samples. The FFT spectra again reveal a number of modes and the mode frequencies vary significantly with the sample geometry. A general trend is observed

that the frequencies of the modes decrease from  $S_1$  to  $S_4$ . The reason behind that is probably the variation in magnetic ground state configurations with the change in sample geometry. As the sample is changed from  $S_1$  to  $S_4$ , more closure domain configurations (Fig. 10.7) tend to occur, which may lead to the lower value of local magnetization and hence the corresponding mode frequencies.

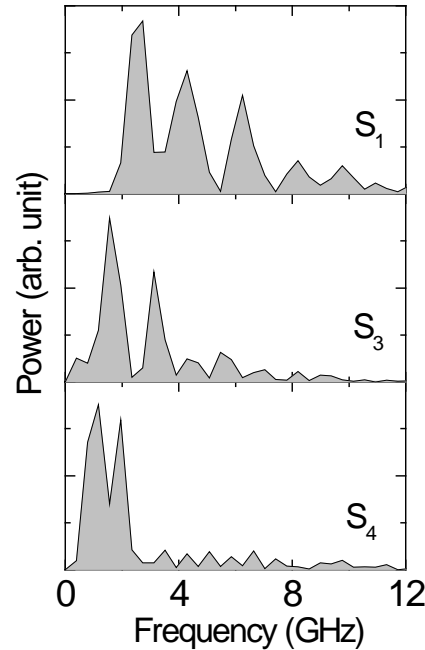


Fig. 11.4: The FFT spectra of background subtracted time-resolved Kerr ellipticity data are shown for three samples ( $S_1$ ,  $S_3$  and  $S_4$ ) at a fixed value of  $H_b = 1$  kOe applied in plane of the samples.

As explained for the case of bias field dependence of precessional mode frequencies, the quantitative reproduction of the modes and their variation with the cluster and chain geometry requires detailed time-dependent three-dimensional micromagnetic simulations. However, due to the limitation of computational resources it was not possible during the course of this thesis and will be a subject of future research. However, we obtained a qualitative understanding about the precessional modes from the magnetic ground state configurations.

## 11.5 Summary

We have studied the ultrafast magnetization dynamics of single domain Ni nanoparticles with distinctly different local microstructural arrangements. The magnetization dynamics were measured for four such microstructures, where the constituent nanoparticles

are arranged in long chain-like, bundle-like, dendrite-like and random agglomerate arrangements. The ultrafast magnetization dynamics were measured by an all optical TRMOKE set up. The experimental results show that the ultrafast demagnetization time does not depend on the sample geometry as it is an intrinsic property of material. However, a variation in the fast relaxation time ( $\tau_1$ ) is observed due to the finite size and shape distribution of the nanoparticles and also variation in the surface properties. A significant variation in the slow relaxation time ( $\tau_2$ ) is also observed, which is mainly attributed due to the variation of interface properties between the nanoparticles and the Si substrate. We have also measured the picosecond precessional dynamics for those samples. The precessional frequency spectra for long chains with single particle along the width show a systematic decrease in the resonance frequency with the decrease in the bias field magnitude, where mainly three resonant frequency branches are observed. The decrease in the frequency of each branch is steeper than as expected from Kittel formula for uniform magnetization. This is because the bias field values were below the saturation field value and the magnetization also decreases with the decrease in bias field. The precessional frequency spectra for samples with different geometries also show a significant variation. In general, the resonant frequency decreases as we go from parallel chains ( $S_1$ ) to random agglomerate of nanoparticles ( $S_4$ ). This is qualitatively attributed to the decrease of local magnetization value due to formation of more closure domain structures as the sample is varied from  $S_1$  to  $S_4$ . The observed resonant modes are basically nonuniform collective modes of the ensembles of nanoparticles. Quantitative reproduction and understanding of the precessional modes would require detailed time-dependent three-dimensional micromagnetic simulations with finite-element method, which is computationally very demanding and was not possible during the course of this thesis. However, we obtained a qualitative understanding about the variation of the resonant modes with the bias field values as well as the geometry of the microstructural arrangements by considering their magnetic ground states.

## Bibliography

1. H. W. Schumacher, C. Chappert, P. Crozat, R. C. Sousa, P. P. Freitas, J. Miltat, J. Fassbender, and B. Hillebrands, *Phys. Rev. Lett.* **90**, 017201 (2003).
2. B. Hillebrands and J. Fassbender, *Nature* **418**, 493 (2002).
3. A. V. Kimel, A. Kirilyuk, P. A. Usachev, R. V. Pisarev, A. M. Balbashov, and T. Rasing, *Nature* **435**, 655 (2005).
4. E. B. Myers, D. C. Ralph, J. A. Katine, R. N. Louie, and R. A. Buhrman, *Science* **285**, 867 (1999).
5. C. Thirion, W. Wernsdorfer, and D. Maily, *Nat. Mater.* **2**, 524 (2003).
6. G. A. Prinz, *Science* **282**, 1660 (1998).
7. S. A. Wolf, D. D. Awschalom, R. A. Buhrman, J. M. Daughton, S. von Molnár, M. L. Roukes, A. Y. Chtchelkanova, and D. M. Treger, *Science* **294**, 1488 (2001).
8. K. S. Buchanan, A. Krichevsky, M. R. Freeman, and A. Meldrum, *Phys. Rev. B* **70**, 174436 (2004).
9. K. S. Buchanan, X. Zhu, A. Meldrum, and M. R. Freeman, *Nano Lett.* **5**, 383 (2005).
10. L. H. F. Andrade, A. Laraoui, M. Vomir, D. Muller, J. P. Stoquert, C. Estournès, E. Beaurepaire, and J.-Y. Bigot, *Phys. Rev. Lett.* **97**, 127401 (2006).
11. C.-H. Hsia, T.-Y. Chen, and D. H. Son, *Nano Lett.* **8**, 571 (2008).
12. C.-H. Hsia, T.-Y. Chen, and D. H. Son, *J. Am. Chem. Soc.* **131**, 9146 (2009).
13. A. Sukhov and J. Berakdar, *Phys. Rev. Lett.* **102**, 057204 (2009).
14. J. Park, J. Joo, S. G. Kwon, Y. Jang, and T. Hyeon, *Angew. Chem. Int. Ed.* **46**, 4630 (2007).
15. W. Zhou, L. He, R. Cheng, L. Guo, C. Chen, and J. Wang, *J. Phys. Chem. C* **113**, 17355 (2009).
16. S.-H. Wu and D.-H. Chen, *J. Colloid Interface Sci.* **259**, 282 (2003).
17. A. Barman, T. Kimura, Y. Otani, Y. Fukuma, K. Akahane, and S. Meguro, *Rev. Sci. Instrum.* **79**, 123905 (2008).
18. L. Guidoni, E. Beaurepaire, and J.-Y. Bigot, *Phys. Rev. Lett.* **89**, 017401 (2002).
19. J.-Y. Bigot, M. Vomir, and E. Beaurepaire, *Nat. Phys.* **5**, 515 (2009).
20. A. Laraoui, V. Halté, M. Vomir, J. Vénuat, M. Albrecht, E. Beaurepaire, and J.-Y. Bigot, *Eur. Phys. J. D* **43**, 251 (2007).

21. A. Laraoui, J. Venuat, V. Halte, M. Albrecht, E. Beaurepaire, and J.-Y. Bigot, *J. Appl. Phys.* **101**, 09C105 (2007).
22. J.-Y. Bigot, M. Vomir, L. H. F. Andrade, and E. Beaurepaire, *Chem. Phys.* **318**, 137 (2005).
23. W. Hübner and K. H. Bennemann, *Phys. Rev. B* **53**, 3422 (1996).

# CHAPTER 12

---

## Summary and Future Perspectives

---

### 12.1 Summary

In this thesis, we have studied the quasistatic and ultrafast magnetization dynamics of primarily two types of nanostructures: (i) lithographically patterned magnetic nanodot arrays and (ii) chemically synthesized clusters and chains of magnetic nanoparticles. The quasistatic magnetization reversal dynamics is studied by static magneto-optical Kerr effect (SMOKE) measurements and vibrating sample magnetometer (VSM), whereas the ultrafast magnetization dynamics in different time scales is studied by a home-built all optical time-resolved magneto-optical Kerr effect (TRMOKE) microscope with collinear pump-probe geometry. The experimental results are analyzed and interpreted with the aid of finite difference and finite element method based micromagnetic simulations and macrospin modeling of Landau-Lifshitz-Gilbert (LLG) equation.

The quasistatic magnetization reversal dynamics of arrays of 200 nm square permalloy dots show a systematic transition from a strongly collective magnetization reversal to a non-collective reversal dynamics as the interdot separation ( $S$ ) increases from 50 nm to 400 nm. The hysteresis loops of the arrays change significantly with  $S$ . The saturation magnetic field reduces and the remanence increases with the decrease in the interdot separation and attain values very close to those of a  $10 \times 10 \mu\text{m}^2$  blanket permalloy thin film with similar thickness when  $S$  becomes minimum (50 nm). The coercive field also becomes very close to that for the blanket thin film, indicating a transformation to a strongly collective reversal mechanism. In the ultrafast magnetization dynamics, the demagnetization time remains unaffected by the areal density of the array as it is an intrinsic property of material. In contrast, the fast and slow relaxation time shows a significant but non-systematic variation with the areal density, which is attributed to the random size distribution and defects in the

dots of different arrays and variation in the configurations of the nanodots in different arrays and their physical contacts with the Si substrates. The collective precessional magnetization dynamics shows a systematic transition from uniform collective regime to non-collective regime via different weakly collective regimes as the interdot separation ( $S$ ) of arrays of 200 nm dots increases from 50 nm to 400 nm. The intrinsic edge mode – Damon Eshback (EM-DE) mode of 200 nm dots is suppressed by the uniform collective mode when the dots are closely packed with  $S = 50$  nm. For  $S = 50$  nm, the coherent precession of all the elements in the array leads to a lower value of the effective damping ( $a_{eff}$ ) similar to that of an unpatterned thin film. However, as  $S$  increases, the increment of the incoherence of precession due to the decrease in interdot coupling and mode splitting increases the  $a_{eff}$  value. The reason behind that is the variation of magnetostatic coupling among the nanodots with the interdot separation. Further, the strongly collective dynamics undergoes a transition to a weakly collective regime with the decrease in the bias field magnitude for array of 200 nm dots with 50 nm edge-to-edge separation. The reason behind this is the increase in the nonuniformity in the magnetic ground states of the nanodots with the decrease in the bias field. Consequently the  $a_{eff}$  also increases with the decrease in the bias field. The collective dynamics is found to be anisotropic with the variation in the azimuthal angle of in-plane bias field. As the azimuthal angle of the bias field is varied from  $0^\circ$  to  $45^\circ$  *w.r.t.* the symmetric axis, a systematic transition from a uniform collective dynamics to non-collective dynamics is observed in strongly coupled regime ( $S = 50$  nm), whereas no clear trend is observed in the weakly coupled regime ( $S = 100$  nm). As the dot size decreases from 200 nm down to 50 nm, an increase in the resonant frequency is observed for the intrinsic dynamics as well as for the collective dynamics. With the decrease in dot size, the centre mode (CM) of the dots are suppressed by dominating edge modes (EM) of the dots and consequently a crossover from upper branch of resonance frequency to lower branch is observed for the intrinsic dynamics as well as for the collective dynamics. The ultrafast magnetization dynamics of array of 50 nm dots with interdot separation = 50 nm shows that the demagnetization time remains same as the arrays of 200 nm dots, but the fast remagnetization time changes due to change in spin-orbit coupling with dot size. The precessional magnetization dynamics reveals that in the single nanomagnet regime the dynamics of 50 nm dots are governed by the edge mode (EM) of the dot. As the interdot separation decreases, the resonant frequency increases due to the increment of interdot coupling and damping of precession also increases due to the increase of mutual dynamic dephasing of slightly out-of-phase precession of the neighbouring dots. For 50 nm separation, the single resonant mode splits into two closely spaced collective

modes of the array and the apparent damping increases drastically. From the analysis of the experimental data for the arrays of 50 nm dots the main contribution to the magnetostatic interaction are found to be quadrupolar in nature. The study of ultrafast magnetization dynamics of array of circular dots show that the ultrafast demagnetization time remains same as the square dots, whereas the fast remagnetization time changes significantly. The intrinsic and collective precessional dynamics of circular dots are significantly different than that of the square dots due to the modification in the ground state of magnetization as well as the stray field profiles for the circular dots. However, a crossover from higher frequency branch to lower branch is also observed here as the dot size decreases down to 50 nm. In the collective regime ( $S = 50$  nm), the intrinsic CMs of larger dots ( $W = 200$  nm and 100 nm) are suppressed either by an uniform collective dynamics of the array (for  $W = 200$  nm) or by a coherent precession of CMs of constituent element (for  $W = 100$  nm), while the intrinsic EMs are modified to the backward volume magnetostatic (BWVMS) modes of constituent dots. For the smallest dot ( $W = 50$  nm), the intrinsic edge mode is suppressed by uniform collective mode in the array.

We have investigated the magnetization reversal and ultrafast magnetization dynamics of chains and clusters of chemically synthesized single domain dipole and exchange coupled Ni nanoparticles of four distinct geometries. For clusters of randomly arranged Ni nanoparticles, the experimental  $M-H$  data were better reproduced by a periodic arrangement of partially overlapped nanoparticles as opposed to single nanoparticles and cluster of randomly arranged nanoparticles. As opposed to a coherent rotation of magnetization expected for single domain nanoparticles, the magnetization reversal of the whole cluster occurs through the appearance of various collective domain states of the cluster including C-state, vortex-like state and flower-like state, although the constituent particles in the cluster maintain primarily single domain states. Various domain structures occur in the cluster due to the incoherence of the magnetization reversal between the constituent particles in the cluster. In case of parallel chains, the overall geometry controls the reversal mechanism, and the magnetic hysteresis loops with magnetic field applied along the long-axis and short-axis of the chains show magnetic easy-axis and hard-axis like behaviours. Micromagnetic simulations show that the reversal mechanism is modified due to the magnetostatic interaction between the chains and formation of local flux closure like structures are observed during the magnetization reversal, which causes low remanence, smaller coercive field and larger saturation field for the loops with the magnetic field applied

perpendicular to the length of the Ni nanochains. We have compared the reversal behavior of four distinct geometries. The magnetization reversal of the clusters and chains is dominated by the interparticle exchange and the shape anisotropy of the overall clusters and occurs through the formation of various local magnetic configurations. In chain-like structures, the fanning- and curling-like modes of magnetization reversal cause the smallest saturation field, and the largest coercive field and remanence. However, in more entangled structures such as branched chains and random clusters, formation of more stable magnetic configurations such as vortices causes a larger saturation field, but a smaller coercive field and remanence. We have also studied the ultrafast magnetization dynamics of single domain Ni nanoparticles with distinctly different local microstructural arrangements. The ultrafast magnetization dynamics show that the ultrafast demagnetization time does not depend on the sample geometry as it is an intrinsic property of material. However, a variation in the fast relaxation time ( $\tau_1$ ) is observed due to the finite size and shape distribution of the nanoparticles and also a variation in the surface properties. A significant variation in the slow relaxation time ( $\tau_2$ ) is also observed, which is mainly attributed due to the variation of interface properties between the nanoparticles and the Si substrate. We have also measured the picosecond precessional dynamics for those samples. The precessional frequency spectra for long chains with single particle along the width show a systematic decrease in the resonance frequency with the decrease in the bias field magnitude, where mainly three resonant frequency branches are observed. The decrease in the frequency of each branch is steeper than as expected from the Kittel formula for uniform magnetization. This is because the bias field values were below the saturation field value and the magnetization also decreases with the decrease in bias field. The precessional frequency spectra for samples with different geometries also show a significant variation. In general, the resonant frequency decreases as we go from parallel chains ( $S_1$ ) to random agglomerate of nanoparticles ( $S_4$ ). This is qualitatively attributed to the decrease of local magnetization value due to formation of more closure domain structures as the sample is varied from  $S_1$  to  $S_4$ . The observed resonant modes are basically nonuniform collective modes of the ensembles of nanoparticles.

## 12.2 Future Perspectives

The collective magnetization dynamics of arrays of magnetic nanodots and chains and clusters of nanoparticles is an important problem with future prospects of applications in various nanomagnetic devices. For example, applications in magnonic crystals and spin wave

logic devices demand the detailed understanding of the spin wave spectra. Mode splitting, band formation, tunability of bandgaps, control on propagation velocity, anisotropy in the spin wave propagation *w.r.t.* the relative orientation of the bias field with the lattice symmetry and variation in Gilbert damping and extrinsic contributions to the damping due to dynamic dephasing are some of the important issues in magnonics and spin wave logic. Hence, more detailed understanding of the spin wave dynamics in magnetic nanodot arrays and possible control of above properties would open up exciting new prospects in these fields.

Luckily, the collective magnetization dynamics of magnetic nanodot arrays is a multidimensional problem with many control parameters. The dynamics of magnetic nanodots strongly depends upon their static magnetic configurations. For thin magnetic films, the magnetization is uniform over the film and the dynamics is mainly determined by intrinsic material parameters like saturation magnetization, magnetic anisotropy, exchange stiffness constant and external parameters like magnitude and direction of the applied magnetic fields. The magnetization of confined magnetic elements deviates from the bias magnetic field even in presence of a large enough magnetic fields thus creating demagnetized regions. These demagnetized regions play important roles in determining the magnetic ground states, quasistatic magnetization reversal and the precessional dynamics of magnetization. They offer different potentials to the propagating spin waves and also spatially localize them within the demagnetized regions. In addition, the interdot magnetostatic interaction in ordered arrays of nanomagnets gets affected by the shape of the elements. This is because the profile of the stray magnetic field depends on the shapes of the boundaries of the elements as well as the internal magnetic field and one may tailor the stray magnetic field to any complicated nature beyond the dipolar and higher order multipolar terms.

The periodicity of the lattice determines the Brillouin zone and the allowed wave vectors for the magnonic modes. In addition to the periodicity of the lattice, the interdot magnetostatic interactions in the lattices should play a very important role in determining its collective magnonic modes and further tailoring of this interaction field offers exciting prospects in magnonics. The variation of lattice symmetry is an attractive option, by which the magnetostatic fields of highly complex nature can potentially be introduced but it has not yet been tried in the context of the spin wave dynamics of magnonic crystals. Investigation of magnonic spectra in nanodot lattices with variable lattice symmetry and the effects of

reduction of lattice symmetry, symmetry breaking and quasi-symmetric and defective crystals will provide a wealth of information on the propagating and localized spin waves.

In addition, advents of new techniques for studying magnetization dynamics with very high spatio-temporal resolution will enable the study of the intrinsic dynamics of smaller single nanomagnets as well as their dynamics under the magnetostatic interaction of the neighbouring elements when placed in arrays of various lattice constants and lattice symmetries.